UNIVERSITÉ DU QUÉBEC À MONTRÉAL

L'ÉLONGATION EMBRYONNAIRE PRÉCOCE DU *CAENORHABDITIS ELEGANS* : CARACTÉRISATION DE LA VOIE PIX-1 / PAK-1.

THÈSE

PRÉSENTÉE

COMME EXIGENCE PARTIELLE

DU DOCTORAT EN BIOCHIMIE

PAR

EMMANUEL MARTIN

SEPTEMBRE 2016

REMERCIEMENTS

Ce fut une aventure incroyable, nuancée par des rencontres diverses et variées ; une aventure humaine qui

La première personne que je souhaite remercier, et non la moindre, pour m'avoir accueilli dans son laboratoire est la Dre Sarah Jenna. Sarah, merci de m'avoir pris en stage à l'été 2010, moi petit étudiant français qui souhaitait voir du pays, et surtout merci de m'avoir proposé de poursuivre un doctorat au sein de ton laboratoire. Ces quatre années et demie ont été pour moi une expérience extraordinaire, autant d'un point de vue professionnel que personnel, et cela grâce à toi. Merci d'avoir été là pour moi tout au long de cette thèse, dans les bons moments, et surtout dans les moins bons. Quand les résultats n'étaient pas au rendez-vous, quand la motivation était au plus bas, quand j'avais de gros doutes par rapport à mon sujet, tu as toujours été là, avec ton attitude positive pour me remonter le moral et me permettre de repartir de l'avant. Ta persévérance et ton optimisme sont sources d'inspiration, et je pense avoir mûri en ce sens à tes côtés. Merci également de m'avoir permis de présenter mes résultats dans de nombreux congrès internationaux – Madison (USA), Los Angeles (USA), Nara (Japon), Banff. Je te suis reconnaissant pour tout, et te remercie mille fois encore !!

Par ailleurs, je tiens à exprimer ma profonde gratitude aux membres de mon jury, le Dr Nicolas Pilon, la Dre Claire Benard et la Dre Christelle Gally, d'avoir accepté de lire et d'évaluer mon travail de thèse, et ce pendant la période de vacances. Merci beaucoup !

Je voudrais maintenant remercier mes collègues de laboratoire présents et passés. Je pense à Germain « mon ami de rando », Karim, Marie-Hélène, Barbara et notre dernier arrivé Grégoire, qui va poursuivre mes travaux et à qui je souhaite bon courage. Evidemment, un merci tout particulier à Benjamin, qui est dans le même bateau que moi depuis le début. Ben, j'ai apprécié toutes nos discussions sur nos projets de recherche respectifs, même si ceux-ci sont bien différents. Cela m'a permis de m'ouvrir à d'autres horizons.

Je pense également à Denis Flipo qui m'a aidé pour mes premières acquisitions en microscopie confocale. Je pense aussi à Hervé Barrière. Toutes nos discussions et les heures passées à « jouer » sur le microscope avec toi m'ont donné le goût de

découvrir et d'approfondir mes connaissances dans ce domaine. J'ai découvert plus qu'un simple outil d'imagerie, une passion.

Un énorme merci à ma fiancée et future femme Caroline pour son soutien indéfectible, ses encouragements, sa bonne humeur… Tu as été une source de motivation énorme depuis que nous nous sommes rencontrés. Tu as toujours su trouver les mots justes pour m'apaiser et me faire relativiser. Merci aussi à ma petite Marianne d'avoir pointé le bout de son nez à la fin de mon doctorat. Tu as rendu cette fin de thèse moins banale qu'elle n'aurait du l'être en parsemant mes nuits de sommeil de pleurs et de changements de couche. Je suis heureux et fiers que tu sois entrée dans nos vies.

Finalement, je tiens à dire un grand merci à ma famille, et particulièrement à ma mère qui m'a toujours soutenu dans ce que j'ai entrepris. Je sais que cela n'a pas été facile de me voir partir de l'autre côté de l'océan mais tu m'as toujours dis de faire ce qui était le mieux pour moi, et maintenant, je sais que tu es une mamie heureuse. Merci à ma grand-mère pour ses colis de biscuits, de foie-gras, de chocolat, le tout accompagnés de ses cartes-postales. Cela a été d'un grand réconfort pendant les longs mois d'hiver canadien.

Merci à tous !!

TABLE DES MATIÈRES

LISTE DES FIGURES

Figures Supplémentaires

LISTE DES TABLEAUX

LISTE DES ABBRÉVIATIONS, SIGLES ET ACRONYMES

ABD	actin binding domain
AJM-1	adherens junction marker 1
aPKC	atypical protein kinase C
ARHGEF	Rho guanine-nucleotide exchange factor
Arp2/3	actin-related protein 2/3 (*C. elegans* : ARX2/3)
BG	bandelette germinative
C-terminal	carboxy-terminal
CAF	complexe d'adhésion focale
CARMIL	capping protein, Arp2/3 and myosin-I linker (*C. elegans* : CRML-1)
CCC	complexe cadhérine-caténine – catenin-cadherin complex
Cdc42	cell division control protein 42 (*C. elegans* : CDC-42)
CdGAP	Cdc42 GTPase-activating protein
CeAJ	*C. elegans* adherens junction
CGC	*Caenorhabditis* Genetics Center
DAC	DLG-1/AJM-1 complex
DH	GEF/dbl homology
DIC	differential interference contrast (microscopy)
DLG-1	Drosophila discs large homologue 1
DOCK180	dedicator of cytokinesis
DTC	distal tip cells
E-cadherine	epidermal cadherin
ECT2	epithelial cell transforming 2
Emb	embryonic lethality
EPLIN	epithelial protein lost in neoplasm
F-actine	filaments d'actine
FB	filamentous actin bundles
FHOD-1	formin homology domain 1
GAP	guanine nucleotide activating protein
GBD	GIT-binding domain
GDI	guanine nucleotide-dissociation inhibitors
GDP	guanosine diphosphate
GEF	guanine nucleotide exchange factor
GFP	green fluorescent protein

GIT1	G protein- coupled receptor kinase interactor 1 (*C. elegans* : GIT-1)
GTP	guanosine triphosphate
GTPase	guanosine triphosphatase
HDs	hémidesmosomes
HMP-1/2	humpback dorsal lumps 1/2
HMR-1	hammerhead embryonic lethal 1
L1/2/3/4	*C. elegans* larval stage (1-4)
LIN-26	abnormal cell lineage 26
Lva	larval arrest
mCherry	monomeric cherry fluorescent protein
mDia	mammalian diaphanous-related formin
MEC	matrice extracellulaire
MIG-2	mitogen inducible gene 2
MLC	myosin light chain (*C. elegans* : MLC-4 and MLC-5)
MLCK	myosin light chain kinase
MRCK	myotonin-related Cdc42-binding kinase (*C. elegans* : MRCK-1)
MYPT	myosin phosphatase targeting protein (*C. elegans* : MEL-11)
N2	*C. elegans* wild type (Bristol)
NGM	nematode growth media
NMY-1/2	non-myosin heavy chain 1 and 2
OP-50	*Escherichia coli* strain OP50 / *C elegans* feeding bacteria
PAK1	p21-activated kinase (*C. elegans* : PAK-1)
Par6	partitioning defective protein 6
PCR	polymerase chain reaction
PIX (α ou β)	PAK-interactive exchange factor (*C. elegans* : PIX-1)
POPX2	partner of PIX 2 (*C. elegans* : FEM-2)
PP1cδ	protéine serine/thréonine phosphatase 1 de type c delta
Rac1	Ras-related C3 botulinum toxin substrate 1 (*C. elegans* : CED-10)
RhoA	Ras homolog gene family, member A (*C. elegans* : RHO-1)
ROCK	Rho-associated protein kinase (*C. elegans* : LET-502)
SH3	Src homology 3
TAM	transition amiboïdo-mésemchymateuse
TEA	trans epidermal attachment
TEM4	tumor Endothelial Marker 4 (ARHGEF17)
TMA	transition mesenchymo-amiboïdale
TOCA1	transducer of Cdc42-dependent actin assembly protein 1
UNC-73/Trio	UNCoordinated protein

VAB-10	variable abnormal morphology 10
VASP	vasodilator-stimulated phosphoprotein
WASp	Wiskott-Aldrich syndrome protein (*C. elegans* : WSP-1)
WAVE	WASp-family verprolin homology protein (*C. elegans* : WVE-1)
wt	*wild type*
ZB	PDZ-binding domain

LISTE DES SYMBOLES ET DES UNITES

bp	paires de base – base pairs
kb	kilobase
°C	degré Celsius
µl	microlittre
µm	micromètre
M	molaire
min	minute
mM	millimolaire
ng	nanogramme
nm	nanomètre

RÉSUMÉ

La morphogenèse des tissus est essentielle pour le développement des métazoaires. Elle requiert une coordination d'évènements cellulaires variés, tels que l'adhésion, la migration et le remodelage du cytosquelette d'actine, qui dépendent de la régulation des GTPases Rho. La compréhension des évènements morphogénétiques est un problème multi-échelle qui se traduit par une intégration des niveaux moléculaire, cellulaire, tissulaire et organique. En outre, faire le lien entre les réseaux de régulation protéique et la morphogénèse reste un défit majeur. Le nématode *Caenorhabditis elegans* est un modèle de choix dans l'étude du développement embryonnaire et de la morphogenèse.

Au laboratoire, nous étudions l'élongation embryonnaire du *C. elegans*, une étape tardive du développement qui permet à l'embryon ovoïde d'acquérir sa forme de ver. Spécifiquement, je me suis intéressé à l'étape précoce de l'élongation embryonnaire. Cette étape est dirigée par la contraction des filaments d'actine-myosine au pôle apical des cellules latérales de l'épiderme. Selon le modèle accepté au début de mes travaux, les cellules ventrales et dorsales sont dans un état relâché pendant toute l'élongation précoce. Deux voies de signalisation redondantes dirigent la contraction du cytosquelette, la voie *mel-11/let-502* et la voie *pak-1*. Afin de mieux caractériser les voies contrôlant l'élongation précoce, nous avons développé des méthodes permettant l'analyse des embryons à l'échelle de l'organisme ainsi qu'à l'échelle cellulaire. Ces analyses nous ont révélé que PIX-1/β-PIX, une GEF pour les GTPases Rac et Cdc42, contrôle l'élongation précoce dans la voie PAK-1, en parallèle de la voie MEL-11/LET-502. Elles ont aussi montré que PIX-1 et PAK-1 régulent principalement la réduction de la largeur de la tête à ce stade, alors que LET-502 contrôle la réduction de la largeur de la tête et de la queue de l'embryon. Spécifiquement, PIX-1 et PAK-1 régulent le remodelage des jonctions apicales et la formation de lamellipodes polarisés dans les cellules dorsales antérieures. LET-502 contrôle le remodelage des jonctions apicales et la morphologie de protrusions de type amiboïde dans les cellules latérales. Cette étude révèle donc que l'adoption d'un programme *pix-1/pak-1* ou *let-502* par la cellule définit son comportement et sa morphologie au cours de l'élongation. Enfin, nous avons montré que la dominance cellulaire d'un programme est contrôlée par l'antagonisme entre *pix-1/pak-1* et *let-502*.

En conclusion, ce travail démontre que les voies *pix-1/pak-1* et *let-502* agissent de façon redondantes et synergiques à l'échelle de l'organisme, et antagonistes à l'échelle cellulaire. Ce travail apporte des modifications majeures au modèle précédemment établi permettant d'expliquer la base moléculaire de l'élongation embryonnaire précoce du *C. elegans*.

MOTS-CLÉS :

GTPases Rho, morphogenèse, épiderme, *C. elegans*, PIX, PAK

ABSTRACT

Tissue morphogenesis is essential for metazoan development. It requires coordination of multiple cellular events such as adhesion, migration and actin remodeling, which are dependent of Rho GTPases regulation. Understanding morphogenic events is a multiscale problem that involves the understanding of molecular processes at both cellular and tissue levels. The morphological simplicity of the epidermis of *Caenorhabditis elegans* embryos makes this system an ideal model to study the molecular and signaling events that control epidermal morphogenesis.

I focused my research work on a late stage of *C. elegans* embryonic development, called embryonic elongation. This stage allows the transformation of an ovoid embryo into a vermiform larva. This step is known to be driven by the contraction of acto-myosin bundles at the apical pole of the lateral epidermal cells, while ventral and dorsal cells are in relaxed state. Two parallel and redundant pathways control this contraction, the *mel-11/let-502* and the *pak-1* pathways. During my PhD, we demonstrated that PIX-1/β-PIX, a Rac- and Cdc42-specific GEF, regulates early elongation in the PAK-1 pathway and in parallel with MEL-11/LET-502. To better characterize these pathways, we developed novel methods to characterize morphogenic processes at the organism as well as the cell levels. Applying these methods to early elongation revealed that PIX-1 and PAK-1 mainly control the reduction of the head width of the embryos, while LET-502 regulates their head and the tail width. When characterized at a single cell level, PIX-1 and PAK-1 were found to regulate apical junction remodeling and production of polarized lamellipodia from dorsal anterior cells towards their lateral neighbors. In addition, LET-502 was found to control remodeling of apical junctions between lateral cells and morphology of amoeboid-like protrusion produced by these cells towards their dorsal neighbors. This study revealed that adoption of a *pix-1/pak-1* or a *let-502* program by cells defines their behavior and morphology during early elongation. Finally, we showed that the adoption of a specific program is controlled by the *pix-1/pak-1* and *let-502*.

In conclusion, this work showed that the *pix-1/pak-1* and *let-502* pathways act in a redundant and synergistic manner at the organism level, while being antagonistic at a single cell level. This work also brought major modifications compared to the previously accepted model, allowing a better spatial characterization of molecular and cellular events controlling early embryonic elongation in *C. elegans*.

KEYWORDS:

Rho GTPases, morphogenesis, epidermis, *C. elegans*, PIX, PAK

CHAPITRE I

INTRODUCTION

1.1 Introduction générale

La détermination de la forme et de la structure des tissus et des organes, aussi appelée morphogenèse, est cruciale pour le développement des métazoaires. Ce mécanisme dépend d'évènements cellulaires variés tels que le changement de forme des cellules, l'adhésion et la migration. Tous ces évènements sont finement régulés, en réponse à des stimuli externes chimiques ou mécaniques, par des voies de signalisation intracellulaire. Les membres de la famille des GTPases Rho jouent un rôle essentiel dans cette transduction du signal. Ils vont notamment contrôler le remodelage du cytosquelette d'actine, le trafic vésiculaire et l'adhésion cellule-cellule et cellule-substrat (Etienne-Manneville et Hall, 2002). La compréhension des évènements morphogéniques est cependant un problème multi-échelle qui se traduit par une intégration des niveaux moléculaires, cellulaires, tissulaires et organiques. Le lien entre la régulation des protéines de signalisation et la morphogénèse n'est toujours pas complètement compris.

Les modèles eucaryotes unicellulaires et les cellules d'organismes multicellulaires en culture sont de bons modèles pour étudier le comportement des cellules en isolation ou en communauté homogène. Cependant, l'étude des mécanismes cellulaires impliqués dans le développement embryonnaire permet de mieux comprendre le comportement de ces cellules dans leur contexte tissulaire, leurs interactions avec d'autres types cellulaires et avec leur environnement en trois dimensions. Le nématode *Caenorhabditis elegans* possède des qualités remarquables qui en font un

modèle clé dans l'étude du développement embryonnaire et de la morphogenèse. C'est en effet un organisme pluricellulaire simple, facile à manipuler génétiquement en laboratoire, dont le temps de génération est court (environ 2-3 jours, Figure 1.1) et la progénie nombreuse. La simplicité et la transparence de ce modèle ont, en outre, permis de suivre son développement embryonnaire par microscopie et d'identifier le lignage cellulaire complet de l'organisme en développement, du stade une cellule au stade adulte (959 cellules pour un hermaphrodite adulte) (Sulston et Horvitz, 1977 ; Kimble et Hirsh, 1979 ; Sulston *et al.*, 1983). De plus, les études génétiques utilisant des mutants ayant des anomalies développementales ont permis d'identifier et de caractériser de nombreux gènes impliqués dans le développement embryonnaire.

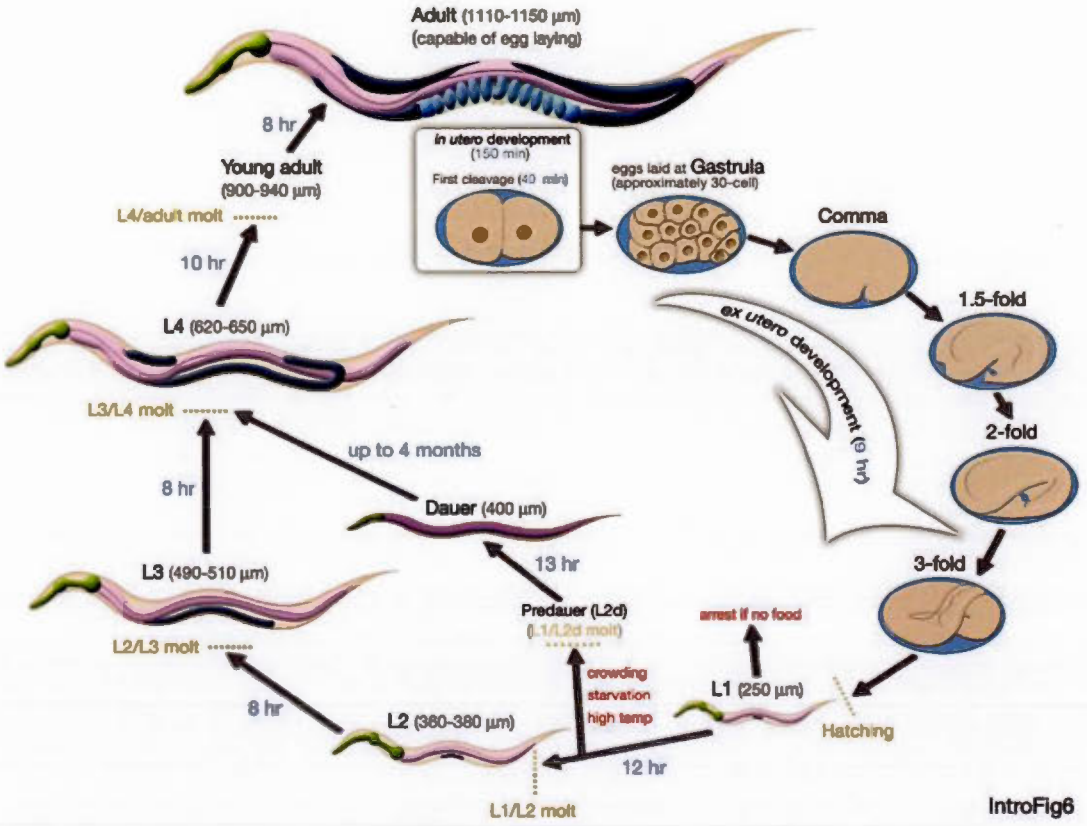

Figure 1.1 : Cycle de vie du *C. elegans* à 20°C. 0 minute correspond à la fertilisation. Les nombres en bleu indiquent la durée de temps pour passer au stade suivant. La longueur de l'animal à chaque stade est indiquée entre parenthèse à côté du nom du stade. Figure extraite du Wormatlas.

De nombreux processus développementaux sont conservés entre les nématodes et les mammifères ; 40% des gènes humains ont en effet un très proche homologue chez le nématode (Shaye et Greenwald, 2011). Spécifiquement, les GTPases Rho identifiées dans le génome du *C. elegans* présentent 60 à 90% d'identité de séquence protéique avec leur plus proche homologue chez l'homme. Ceci fait du *C. elegans* un modèle de choix pour étudier la fonction de ces protéines dans le contrôle du développement embryonnaire et de la morphogenèse des tissus et organes.

1.2 La morphogenèse épithéliale

1.2.1 Principes généraux

Un épithélium se définit à la fois comme une barrière de protection de l'organisme multicellulaire contre le milieu extérieur, et comme une interface favorisant les échanges entre deux milieux chimiques différents. Il se compose d'une ou plusieurs couches de cellules polarisées, étroitement connectées les unes aux autres et à la matrice extracellulaire (MEC) par divers complexes jonctionnels. Au cours du développement, les épithéliums subissent des transformations pour passer d'une couche cellulaire en deux dimensions en une architecture tridimensionnelle formant ainsi les tissus et les organes : c'est ce que l'on appelle la morphogenèse épithéliale. Les mécanismes de morphogenèse épithéliale peuvent être classés en quatre groupes majeurs. On distingue ainsi : (i) les modifications de forme cellulaire où chaque cellule individuelle réorganise son cytosquelette, entraînant un remodelage du tissu épithélial sans pour autant modifier la position relative des cellules ; (ii) l'intercalation cellulaire et la fusion qui implique un changement de position des cellules les unes par rapport aux autres au sein du tissu ; (iii) la migration cellulaire impliquant le déplacement d'une ou d'un groupe de cellules dans le tissu, et (iv) la division cellulaire et la mort cellulaire dont la régulation spatio-temporelle joue un

rôle important dans la formation des tissus (Fristrom, 1988 ; Schock et Perrimon, 2002b ; Pilot et Lecuit, 2005 ; Quintin *et al.*, 2008). L'ensemble de ces processus implique un remodelage du cytosquelette des cellules impliquées, ainsi que de leurs jonctions cellule-cellule et cellule-substrat.

1.2.2 Les jonctions cellulaires

Différents types de complexes jonctionnels sont impliqués dans l'interaction d'une cellule épithéliale avec ses voisines et avec la MEC. Du pôle apical au pôle basal, on distingue, chez les vertébrés (Figure 1.2) : (i) les jonctions serrées qui assurent l'étanchéité de l'épithélium empêchant ainsi aux fluides de s'infiltrer entre les cellules ; (ii) les jonctions adhérentes qui forment une ceinture d'adhérence entre chacune des cellules ; (iii) les desmosomes qui sont également des structures adhésives et qui servent d'ancrage aux filaments intermédiaires ; (iv) les jonctions communicantes qui permettent l'échange de petites molécules entre les cellules, et enfin (v) les points de contact entre la cellule et la MEC (hémidesmosomes et complexes d'adhésion focale) (Giepmans et van Ijzendoorn, 2008). Les jonctions les plus étudiées dans l'étude de la morphogenèse épithéliale sont les jonctions adhérentes et les adhésions focales.

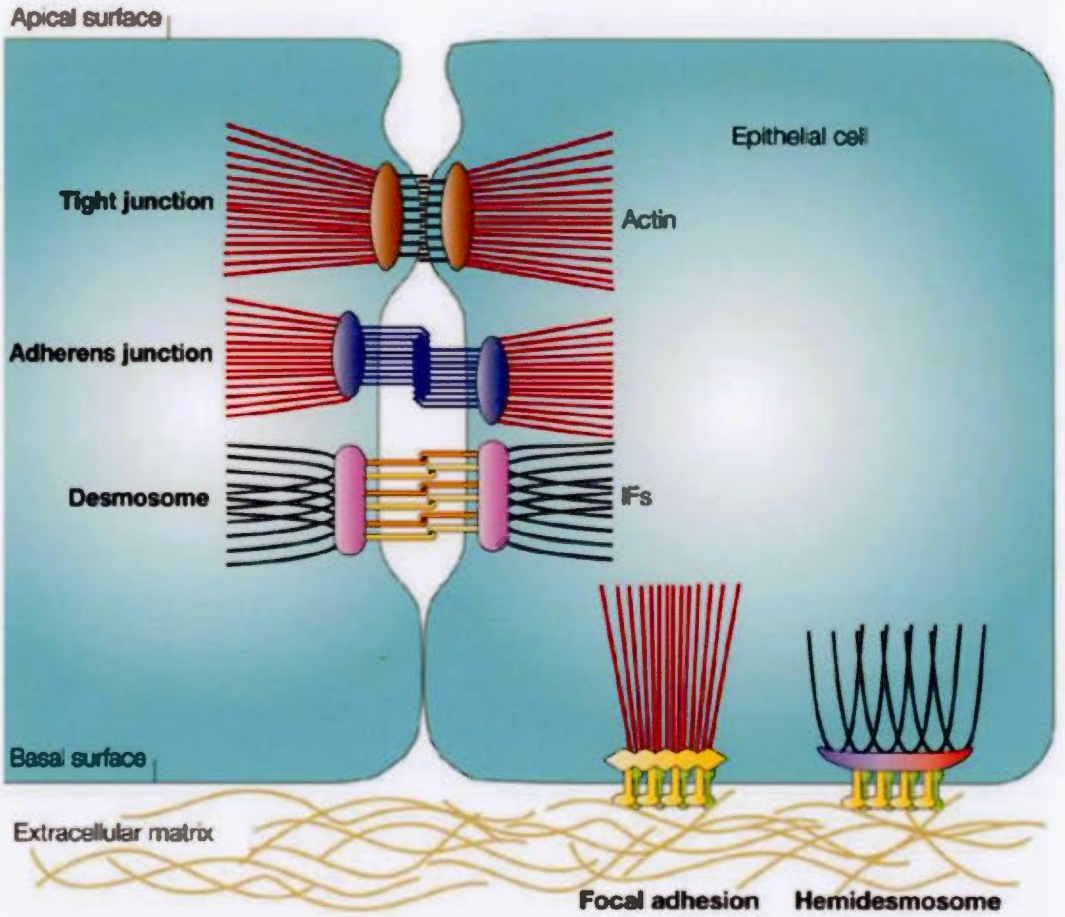

Figure 1.2 : Les jonctions cellulaires épithéliales chez les mammifères. Les cellules épithéliales sont connectées entre elles par divers complexes jonctionnels. Du pôle apical au pôle basal sont retrouvés : les jonctions serrées, les jonctions adhérentes et les desmosomes. A la membrane basale, les cellules adhèrent à la matrice extracellulaire par l'intermédiaire des hémidesmosomes et des complexes d'adhésion focale. Figure extraite de Jefferson *et al.*, 2004.

Les jonctions adhérentes sont des structures apicales ayant plusieurs fonctions, dont entre autres la stabilisation de l'adhésion cellule-cellule et la régulation du cytosquelette d'actine. Ces jonctions impliquent des protéines intrinsèques (transmembranaires), les cadhérines, et plus particulièrement la cadhérine épithéliale : E-cadhérine. Le domaine extracellulaire de cette protéine établi une interaction homotypique avec celui des cadhérines situées dans la membrane plasmique de la cellule voisine (Gumbiner, 2000). Son domaine intracellulaire interagit avec la p120-caténine et la β-caténine, formant ainsi le complexe cadhérine-caténine. Ce complexe est ensuite capable d'interagir avec les filaments d'actine (F-actine), les microtubules, et leurs régulateurs. L'interaction spécifique avec la F-actine, se fait par l'intermédiaire de l'α-caténine qui elle-même interagit avec la formine, la vinculine et l'EPLIN (Figure 1.3) (Watabe-Uchida *et al.*, 1998 ; Kobielak *et al.*, 2004 ; Abe et Takeichi, 2008 ; Meng et Takeichi, 2009). Sous l'action de certaines protéines, ou en réponse à une force appliquée sur la jonction, les protéines impliquées dans les jonctions adhérentes régulent l'organisation et la contraction des filaments d'actine-myosine ainsi que la structure des jonctions (Baum et Perrimon, 2001 ; Perez-Moreno *et al.*, 2003 ; Drees *et al.*, 2005 ; le Duc *et al.*, 2010 ; Yonemura *et al.*, 2010 ; Baum et Georgiou, 2011). La régulation des E-cadhérines et de l'organisation du cytosquelette d'actine par les GTPases Rho sera détaillée dans la section 1.3.3. Au pôle basal de la cellule se trouvent des points d'ancrage entre les cellules et la MEC. Les complexes jonctionnels impliqués dans cet ancrage dépendent des intégrines et sont de deux types : les hémidesmosomes et les complexes d'adhésion focale (CAFs), qui se lient respectivement, du côté cytosolique, aux filaments intermédiaires et au cytosquelette d'actine. Les CAFs sont d'un intérêt tout particulier dans la morphogenèse car ils peuvent passer d'un état hautement dynamique et faiblement adhérent, favorisant la migration cellulaire, à un état faiblement dynamique et fortement adhérent, favorisant la stabilité. (*cf* section 1.5.2.1). La plasticité observée au niveau de ces jonctions implique le remodelage du cytosquelette d'actine d'une façon similaire à ce qui est observé pour les jonctions adhérentes.

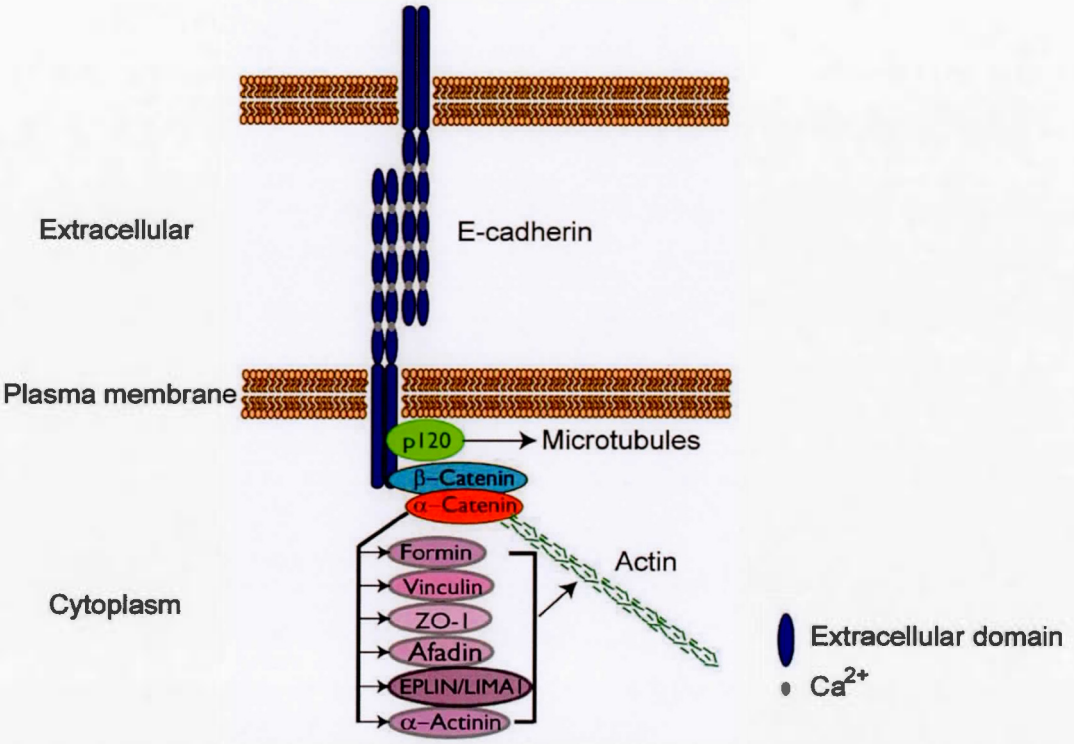

Figure 1.3 : Structure du complexe cadhérine-caténine. Les jonctions adhérentes facilitent l'adhésion cellule-cellule *via* une interaction homotypique entre des molécules d'E-cadhérine se trouvant sur des cellules adjacentes. Le complexe cytoplasmique composé de l'α-caténine, la β-caténine et la p120-caténine (p120) lie les homodimères d'E-cadhérine au cytosquelette d'actine et aux protéines associées à l'actine (en violet sur le schéma). Figure extraite de Baum et Georgiou, 2011.

1.2.3 Les modifications de forme cellulaire

Les processus les plus étudiés de la morphogenèse épithéliale sont ceux impliquant un changement de forme des cellules. Différents types de mécanismes ont été caractérisés dans le cas où le changement de forme affecte uniquement un pôle de la cellule (apical ou basal) ou s'il suit une polarité planaire.

Le premier changement qui peut s'opérer est l'aplatissement (*flattening*) et, à l'inverse, la « colonnarisation » (*columnarization*) des cellules (Figure 1.4). L'aplatissement des cellules se caractérise par un rétrécissement de la cellule dans son axe apico-basal (le long de la membrane latérale) et par une augmentation de la surface apicale et basale de cette même cellule, augmentant ainsi la surface globale de l'épithélium ; la « colonnarisation » à l'effet inverse. Ces deux changements sont retrouvés de façon simultanée au niveau de deux populations de cellules épithéliales au cours de l'ovogenèse de *Drosophila melanogaster* (Deng et Bownes, 1998 ; Dobens et Raftery, 2000 ; Wu *et al.*, 2008 ; Kolahi *et al.*, 2009 ; Baum et Georgiou, 2011). En effet, entre les stades 8 et 10 du développement ovarien, les cellules folliculaires, initialement cuboïdes, subissent des changements morphogéniques majeurs. Le sous-groupe de cellules folliculaires postérieures, qui recouvre l'ovocyte, acquiert une morphologie en colonne. Cette « colonnarisation » est principalement imputée à l'activité du complexe actine-myosine au pôle apical de ces cellules (Zarnescu et Thomas, 1999 ; Wang et Riechmann, 2007). Dans le même temps, les cellules les plus antérieures s'aplatissent pour s'adapter au déplacement des cellules nourricières de la lignée germinale au cours de la croissance de l'ovocyte (Figure 1.4B) (Kolahi *et al.*, 2009).

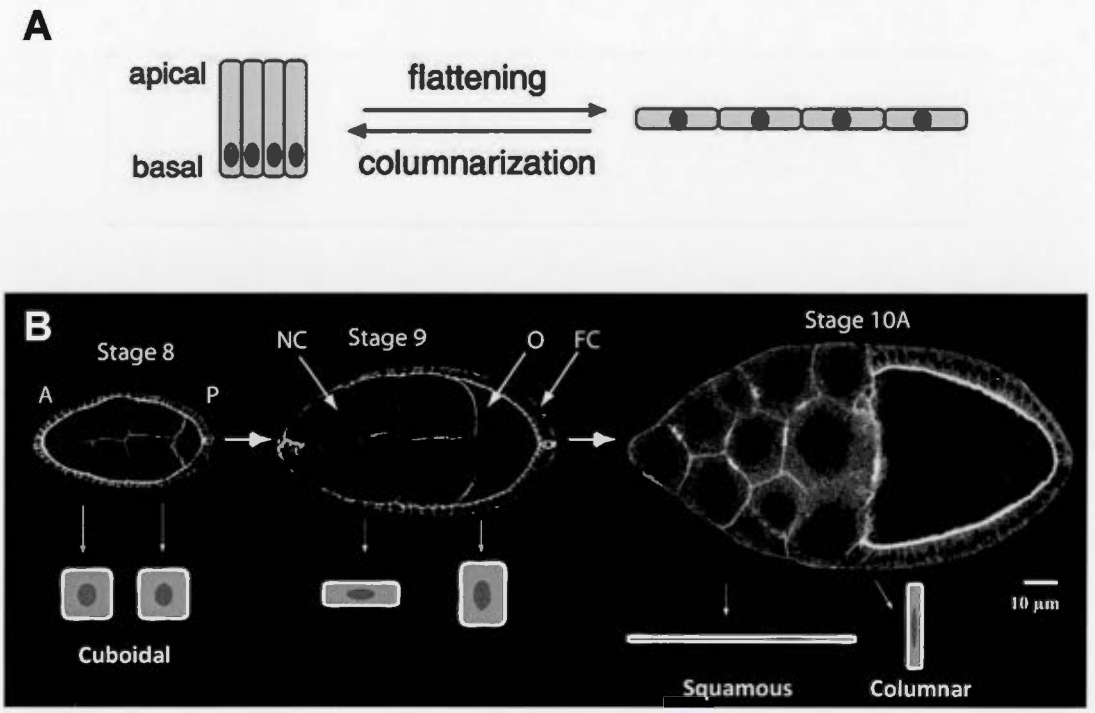

Figure 1.4 : Aplatissement et formation en colonne des cellules épithéliales. (A) Représentation schématique de l'aplatissement et de la « colonnarisation » des cellules. (B) Images, en coupe sagittale, des stades 8, 9 et 10A du développement de la chambre ovarienne de *Drosophila melanogaster*, marquées pour l'E-cadhérine. Sont retrouvées : les cellules nourricières (NC), l'ovocyte (O), et les cellules folliculaires (FC) formant la paroi. Ces dernières, initialement cuboïdes au stade 8, subissent des changements morphologiques jusqu'au stade 10A où deux populations différentes sont présentes : des cellules squameuses et des cellules en colonne. Figures extraites de Schock et Perrimon, 2002b ; Kolahi *et al.*, 2009.

La deuxième modification pouvant avoir lieu est l'élongation des cellules dans leur plan apical (x-y). Ce changement se caractérise par un raccourcissement des membranes dans un axe (x) et l'allongement des membranes dans l'autre axe (y) (Figure 1.5A). L'élongation des cellules épithéliales aboutit en général à l'élongation du tissu. C'est un mécanisme que l'on retrouve notamment pendant l'élongation embryonnaire du *C. elegans*. A ce stade, les cellules de l'épiderme réduisent en taille dans l'axe dorso-ventral et s'allongent dans l'axe longitudinal, entrainant ainsi une réduction du diamètre de l'embryon et une augmentation de sa longueur pour acquérir sa forme définitive de ver (Priess et Hirsh, 1986) (Figure 1.5B).

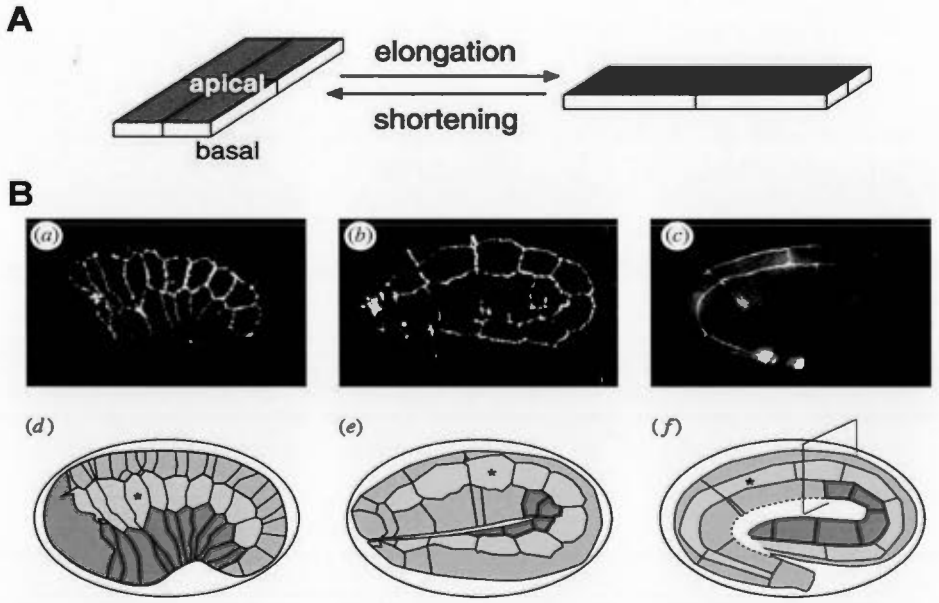

Figure 1.5 : Elongation et rétrécissement des cellules épithéliales. (A) Représentation schématique de l'élongation et du rétrécissement cellulaire. (B) L'élongation embryonnaire du *C. elegans*. (a-c) Vue latérale d'un embryon de *C. elegans* au début de l'élongation précoce (a), au stade 2-fold (b) et 3-fold (c), marqué avec un anticorps contre la protéine jonctionnelle AJM-1::GFP. (d-f) Dessin des images montrées en (a-c). L'étoile indique la même cellule aux différents stades. Figures extraites de Schock et Perrimon, 2002b ; Ciarletta *et al.*, 2009.

Ce mécanisme est dû d'une part à la contraction des filaments d'actine-myosine dans les cellules latérales de l'épiderme (Shelton *et al.*, 1999 ; Piekny *et al.*, 2003 ; Diogon *et al.*, 2007 ; Gally *et al.*, 2009 ; Chan *et al.*, 2015) (voir section 1.4.3), et d'autre part à la mécano-transduction entre les cellules de l'épiderme et les muscles sous-jacents (Zhang *et al.*, 2011). L'ensemble de ces processus est régulé par les GTPases Rho. Le phénomène inverse de raccourcissement est observé chez *D. melanogaster* lors de la régression de la bandelette germinative (BG) par exemple (Schock et Perrimon, 2002a ; Lynch *et al.*, 2013). Ce processus semble également faire intervenir le remodelage du cytosquelette d'actine et la modulation de la contraction de la myosine, et implique les GTPases Rho (Schock et Perrimon, 2002a).

Autre modification de forme cellulaire, l'invagination est un mécanisme fréquemment observé au cours de l'embryogenèse et de l'organogenèse chez les animaux. Nous la retrouvons lors de la formation du tube neural et de la morphogenèse de la placode cristallinienne et otique chez la souris, mais aussi lors de la gastrulation de la drosophile. Au cours de ce dernier processus, certaines cellules subissent une constriction de leur pôle apical entrainant la formation d'une « gouttière » au sein de l'épithélium (Leptin et Grunewald, 1990 ; Sawyer *et al.*, 2010 ; Martin et Goldstein, 2014 ; Chauhan *et al.*, 2015 ; Kondo et Hayashi, 2015) (Figure 1.6). Cette constriction est majoritairement due à la contraction pulsatile de la myosine (Martin *et al.*, 2009 ; Borges *et al.*, 2011 ; Plageman *et al.*, 2011), elle-même régulée par une compartimentalisation des GTPases Rho, RhoA et Rac1, et de leurs régulateurs le long de l'axe apico-basal des cellules subissant la déformation (Simoes *et al.*, 2006 ; Chauhan *et al.*, 2011) (voir section 1.3.4.2 pour une description détaillée de cet antagonisme).

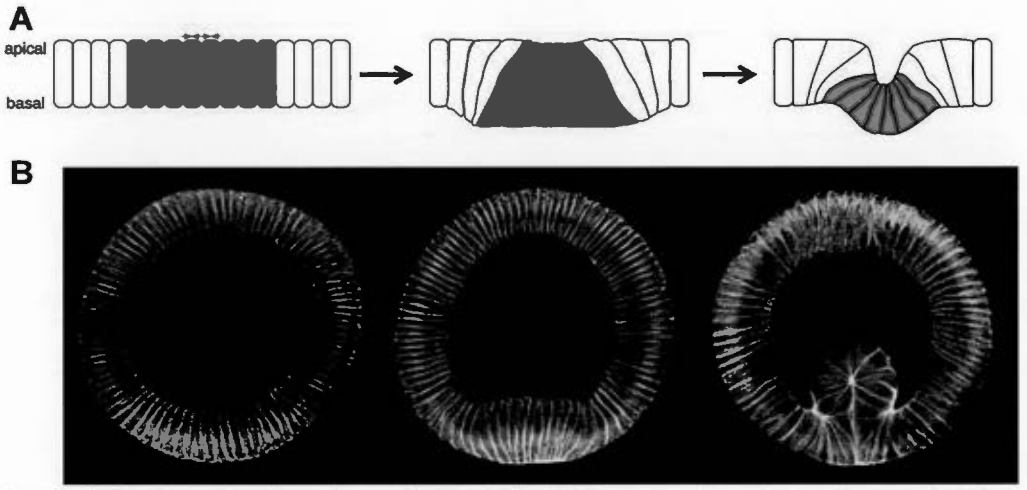

Figure 1.6 : Invagination des cellules épithéliales. (A) Représentation schématique de l'invagination cellulaire. (B) Coupe transversale d'un embryon de *D. melanogaster* en cours de gastrulation illustrant le phénomène d'invagination au cours de la morphogenèse (marquage membranaire). Figures extraites de Schock et Perrimon, 2002b et de la page Internet d'Eric Wieschaus.

1.2.4 L'intercalation cellulaire

Un grand groupe de modifications menant à la morphogenèse épithéliale implique le repositionnement des cellules les unes par rapport aux autres comme par exemple au cours de l'intercalation cellulaire. Ce processus entraine une élongation du tissu dans un axe et un rétrécissement dans l'axe orthogonal (Figure 1.7).

L'intercalation cellulaire est associée à un remodelage actif des jonctions adhérentes. On retrouve de l'intercalation de cellules épithéliales au cours de l'extension de la bandelette germinative de la drosophile, lors de la formation des tubes épithéliaux dans la formation de la cochlée de la souris, ou encore du rein du xénope (Walck-Shannon et Hardin, 2014). Si l'on considère le plan apical des cellules épithéliales, caractérisé par deux axes perpendiculaires x et y, leur intercalation implique un rétrécissement puis une disparition des jonctions situées le long de l'axe x (verticales) et une création de jonctions le long de l'axe y (horizontales), le long duquel de fait l'élongation du tissu (Figure 1.7A).

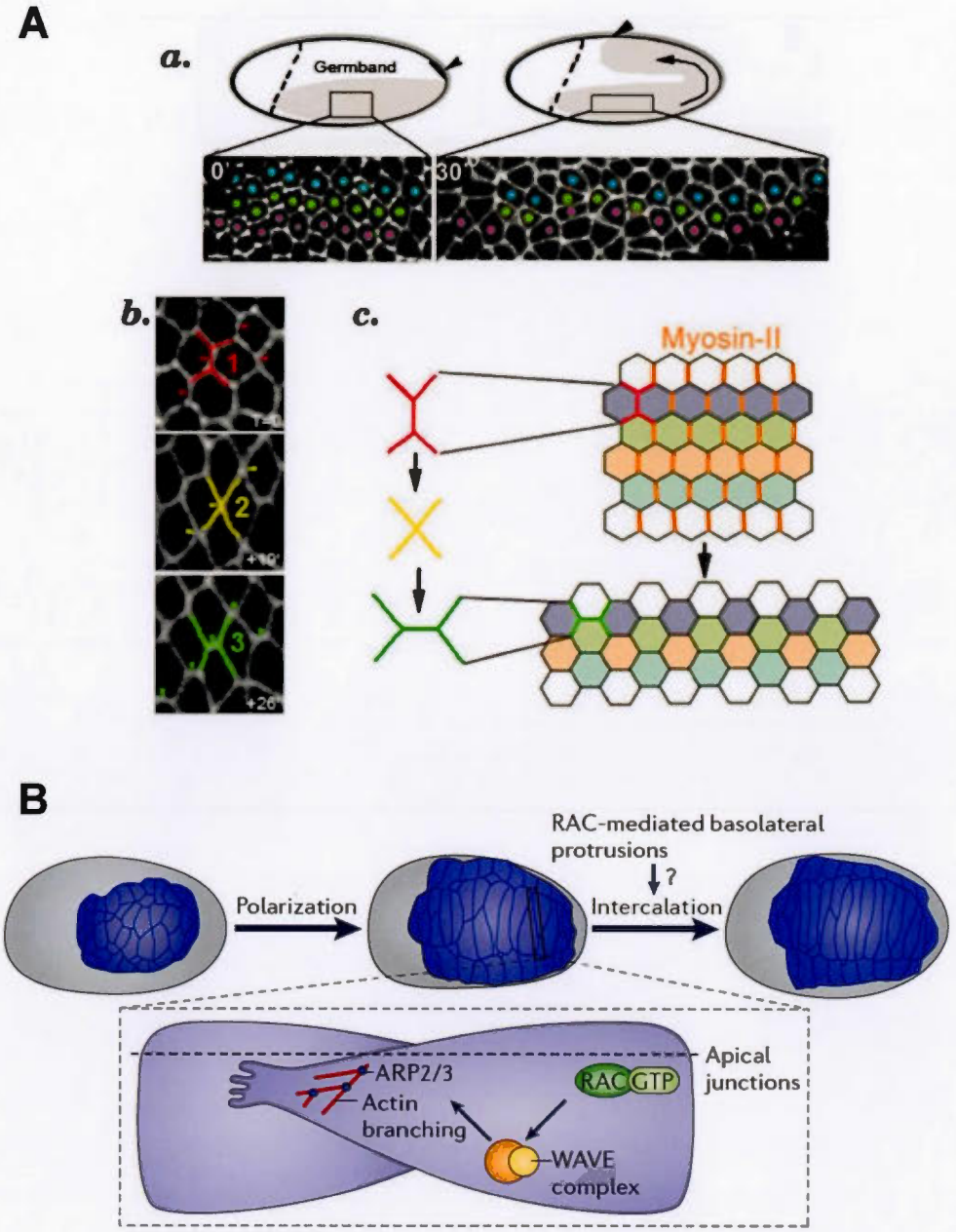

Figure 1.7 : L'intercalation cellulaire. (A) L'intercalation cellulaire au cours de l'élongation de la bandelette germinative chez *D. melanogaster* est associée à un remodelage actif des jonctions apicales (marquage à l'E-cadhérine) et dépend de la contraction de la myosine II. (B) La formation des protrusions basolatérales dirige l'intercalation dorsale du *C. elegans* et dépend de la GTPase Rac1, de son effecteur WAVE et du complexe de nucléation de l'actine ARP2/3. Figures extraites de Bertet *et al.*, 2004 ; Walck-Shannon et Hardin, 2014.

Ce processus a été particulièrement bien étudié chez la drosophile au cours de l'extension de la bandelette germinative. Dans ce système, la réduction de taille des jonctions verticales est engendrée par la contraction du système actine-myosine, elle-même associée à une accumulation polarisée de la myosine, de l'actine et de leurs régulateurs/activateurs au niveau de ces jonctions (Bertet *et al.*, 2004 ; Rauzi *et al.*, 2008 ; Rauzi *et al.*, 2010). Les jonctions horizontales accumulent des protéines jonctionnelles (Bertet *et al.*, 2004 ; Zallen et Wieschaus, 2004 ; Blankenship *et al.*, 2006), un processus qui apparait étroitement lié à l'endocytose de ces protéines aux jonctions verticales (Levayer *et al.*, 2011 ; Levayer et Lecuit, 2013). Ces mécanismes d'endocytose et de contraction, qui permettent respectivement de réduire l'adhésion et la taille des jonctions verticales, et qui mènent à l'intercalation cellulaire, semblent eux-mêmes régulés par des voies de signalisation impliquant la GTPase RhoA, son régulateur Rho GEF2, et son effecteur ROCK (*Rho-associated protein kinase*) (Levayer *et al.*, 2011).

Il est important de noter que, dans certains modèles cellulaires et développementaux, l'intercalation des cellules dépend de la production de protrusions basolatérales. C'est le cas de l'intercalation dorsale des cellules de l'hypoderme des embryons de *C. elegans* (Figure 1.7B ; Williams-Masson *et al.*, 1998 ; Walck-Shannon *et al.*, 2015). Dans ce système, les cellules produisent des protrusions de façon polarisée (Williams-Masson *et al.*, 1998 ; Walck-Shannon *et al.*, 2015). Ces protrusions, hautement dynamiques, dépendent d'une signalisation impliquant les GTPases CED-10/Rac et MIG-2/RhoG, leur régulateur positif UNC-73/Trio, et leurs effecteurs respectifs WVE-1/WAVE (*WASP-family verprolin-homologous protein*) et WSP-1/WASP (*Wiskott-Aldrich syndrome protein*). La polarisation de ces protrusions semble dépendre d'un régulateur négatif de Trio, CRML-1/CARMIL (Capping Arp2/3 Myosin I Linker), qui s'accumule aux membranes latérales où il inhibe toute activité protrusive (Walck-Shannon *et al.*, 2015). Comment ce mécanisme est couplé

à la réorganisation des jonctions adhérentes au cours de l'intercalation est encore inconnu.

Ces mécanismes d'intercalation médiolatérale décris ci-dessus sont les mécanismes d'intercalation les mieux compris à ce jour. Il est important de noter qu'il existe un autre type d'intercalation, nommé intercalation radiale, au cours de laquelle les cellules se repositionnent dans l'épaisseur d'un épithélium multicouche, et qui mène, par exemple, à l'épibolie (Solnica-Krezel et Sepich, 2012 ; Walck-Shannon et Hardin, 2014) (Figure 1.8A). De plus, des processus reminiscents de l'intercalation cellulaire, et qui dépendent du remodelage des jonctions adhérentes, peuvent intervenir dans la morphogenèse. Il s'agit des phénomènes de fusion, d'ingression et d'égression (Figure 1.8B), mais ils ne seront pas détaillés ici.

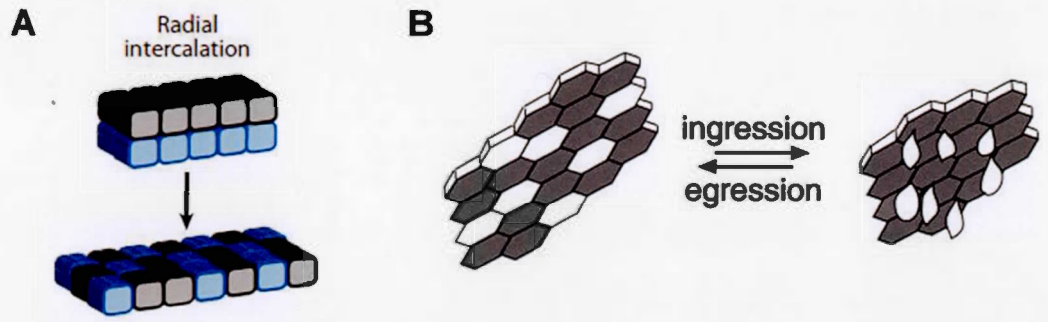

Figure 1.8 : Mécanismes d'intercalation radiale, d'ingression et d'égression. (A) Représentation schématique de l'intercalation radiale dans laquelle deux couches cellulaires s'intercalent, aboutissant à une couche cellulaire unique plus étalée. (B) Représentation schématique des mécanismes d'ingression et d'égression cellulaire. Figures extraites de Schock et Perrimon, 2002b ; Solnica-Krezel et Sepich, 2012.

1.2.5 La migration cellulaire

La morphogenèse peut également impliquer la migration collective et coordonnée des cellules dans le plan apical de l'épithélium. Cette migration implique le maintien des jonctions entre les cellules de l'épithélium. Cette migration collective est par exemple retrouvée dans la formation et la régénération de la peau, dans le développement des tubules et des glandes (ex. : formation de la trachée et des glandes salivaires chez *D. melanogaster* (Samakovlis *et al.*, 1996 ; Pirraglia et Myat, 2010)), et également au cours de la fermeture dorsale de la drosophile ou de la fermeture ventrale du nématode (Williams-Masson *et al.*, 1997 ; Jacinto *et al.*, 2002). La migration collective requiert une coordination entre les mécanismes d'adhésion cellulaire – cellule-matrice extracellulaire *via* les intégrines, et cellule-cellule *via* les cadhérines – , le remodelage du cytosquelette d'actine, et le maintien de la polarité apico-basale des cellules. La migration collective de cellules épithéliales nécessite également un contrôle et une adaptation aux forces mécaniques appliquées au niveau des différentes jonctions et permettant une coordination des mouvements cellulaires au sein de la colonie en cours de migration. Ce processus est appelé mécano-couplage entre les cellules. Ces processus sont régulés de façon spatio-temporelle par les GTPases Rho, en particulier RhoA, Rac1 et Cdc42, leurs régulateurs et leurs effecteurs (revue de Zegers et Friedl, 2014).

1.2.6 La division cellulaire et la mort cellulaire

Le dernier groupe de mécanismes contribuant à la morphogenèse est la division et la mort cellulaire. Dans la plupart des cas, la division cellulaire est incompatible avec les autres mécanismes de morphogenèse, cependant, elle peut parfois y contribuer comme c'est le cas pour le développement d'organes tubulaires, tels que les poumons et le rein par exemple (Lechner et Dressler, 1997 ; Muglia *et al.*, 1999). La mort cellulaire par apoptose est, quant à elle, plus souvent associée aux mécanismes de

morphogenèse. Elle est retrouvée chez les mammifères pour l'individualisation des doigts (Mori *et al.*, 1995). On la retrouve également au cours de la fermeture du tube neural des vertébrés et dans la formation des articulations chez la drosophile (Weil *et al.*, 1997 ; Manjon *et al.*, 2007). Son rôle ne se limite pas uniquement à éliminer des cellules afin, par exemple, de générer des canaux dans un processus de tubulogenèse. En effet, il a récemment été montré que les cellules apoptotiques peuvent induire de la tension dépendante de la myosine à la surface apicale de l'épithélium au cours de la formation de la patte de la drosophile, et que cette tension entraine la formation d'un pli dans l'épithélium entrainant, à terme, une articulation fonctionnelle (Monier *et al.*, 2015 ; Monier et Suzanne, 2015).

1.3 Les GTPases Rho

1.3.1 Généralités

La famille des GTPases Rho est une famille de petites protéines G (20 – 25 kDa) appartenant à la superfamille des Ras, laquelle compte environ 150 membres. Chez les mammifères, on dénombre 20 GTPases Rho, toutes documentées pour leur rôle dans la régulation du cytosquelette d'actine. Parmi elles, douze sont considérées comme des GTPases « classiques », et les huit autres sont décrites comme « atypiques » puisqu'elles ne sont pas activées et régulées de façon traditionnelle (Figure 1.9 ; Heasman et Ridley, 2008). Dans cette section, seules les GTPases classiques seront décrites et plus particulièrement les trois GTPases les mieux caractérisées RhoA, Rac1 et Cdc42.

Les GTPases Rho sont des protéines de signalisation qui régulent un nombre important de processus cellulaires tels que l'organisation du cytosquelette d'actine et des microtubules, l'expression génique, et le trafic vésiculaire. Ces protéines agissent comme des interrupteurs moléculaires et existent sous deux états distincts. D'une part

un état actif lié au GTP dans lequel elles interagissent avec leurs effecteurs afin de transduire des signaux reçus de facteurs de croissance, de cytokines et de molécules d'adhésion. D'autre part, une conformation inactive liée au GDP, et dans laquelle elles ne sont pas capables d'interagir avec leurs effecteurs. Le cycle des GTPases entre ces deux états est étroitement régulé au sein des cellules afin d'assurer la fonction de signalisation de ces protéines.

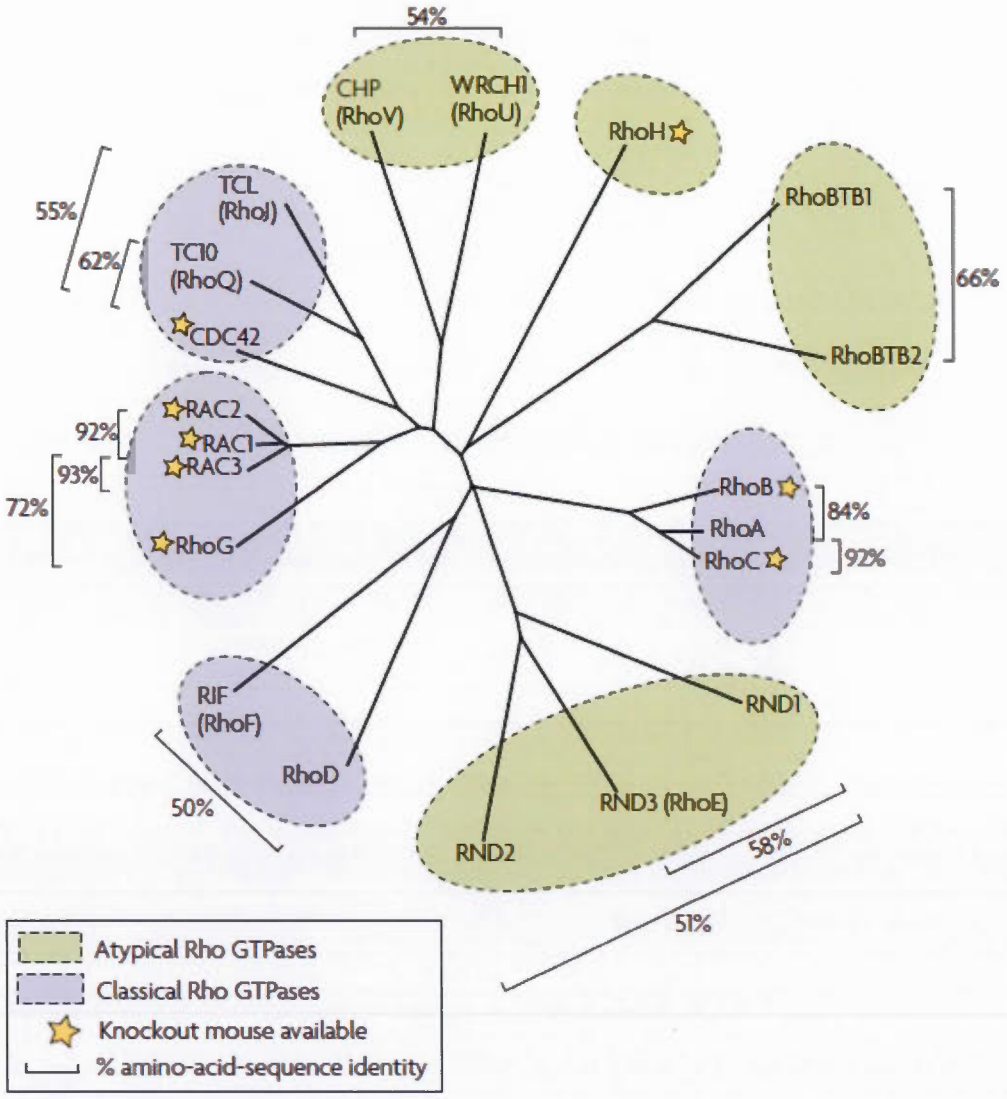

Figure 1.9 : Classification des Rho GTPases. Arbre phylogénique basé sur l'alignement de la séquence protéique des 20 GTPases Rho. Figure extraite de Heasman et Ridley, 2008.

1.3.2 Régulation des GTPases Rho

De façon classique, les GTPases Rho cyclent entre un état actif (lié au GTP) et inactif (lié au GDP). Ce cycle GDP–GTP est finement régulé par trois familles de protéines. Les « *guanine nucleotide-exchange factors* » (GEFs) sont des régulateurs positifs des GTPases qui catalysent l'échange du GDP en GTP en réponse à un stimulus externe et ainsi activent les GTPases. Les « *GTPase-activating proteins* » (GAPS), à l'inverse, stimulent l'activité intrinsèque d'hydrolyse du GTP des petites protéines G, les rendant inactives. Enfin, les « *guanine nucleotide-dissociation inhibitors* » (GDIs) inhibent l'activation des GTPases en les séquestrant dans un état inactif dans le cytoplasme (Figure 1.10) (Van Aelst et Symons, 2002 ; Tcherkezian et Lamarche-Vane, 2007).

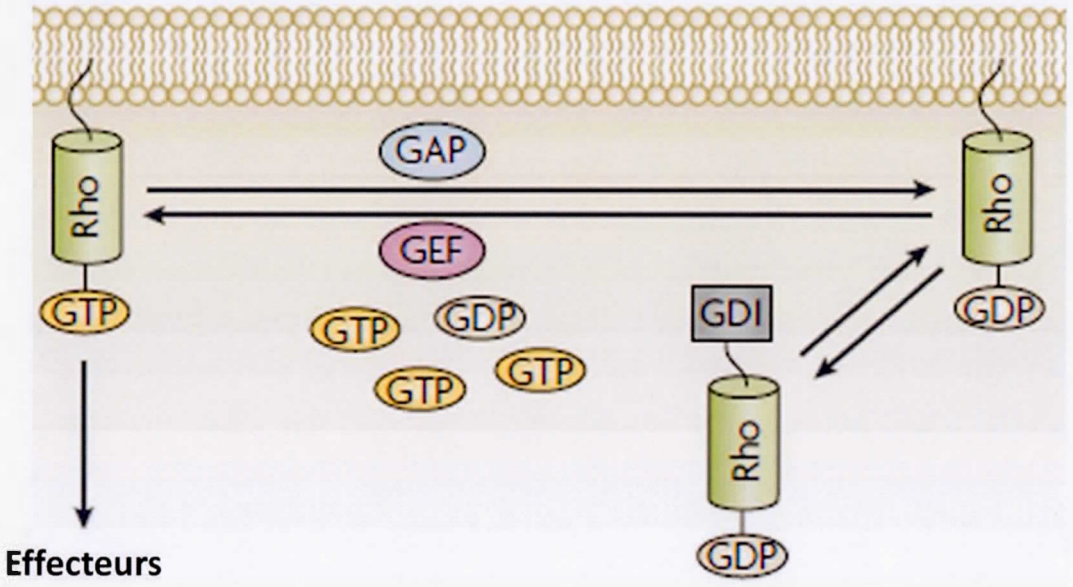

Figure 1.10 : Régulation des Rho GTPases. Les GTPases Rho sont finement régulées par les GEFs, les GAPs et les GDIs qui entrainent respectivement leur activation (état lié au GTP), leur inactivation (état lié au GDP), et leur séquestration sous la forme inactive dans le cytoplasme. Figure adaptée de Heasman et Ridley, 2008.

Ces trois familles de régulateurs jouent un rôle important dans l'activation spatio-temporelle des GTPases Rho, c'est pourquoi elles doivent également être régulées. La régulation de l'activité catalytique des GEFs et des GAPs peut impliquer un domaine d'autoinhibition contenu dans la structure primaire de la protéine. Ce type de domaine est retrouvé dans la GEF Vav1 (Aghazadeh *et al.*, 2000) ou dans la GAP α-chimaerin (Ahmed *et al.*, 1993). L'activité de ces protéines peut aussi être régulée par phosphorylation comme observée pour CdGAP, dont la phosphorylation inhibe son activité catalytique (Tcherkezian *et al.*, 2005). La régulation de la localisation subcellulaire des GEFs et GAPs, et particulièrement leur adressage aux membranes biologiques *via* leur interaction avec d'autres molécules de signalisation, peut également contrôler leur activité catalytique. C'est par exemple le cas de la GEF Tiam1 qui se localise exclusivement aux adhésions cellule-cellule *via* son interaction avec la protéine de polarité Par3, et qui permet une activation de Rac1 spatialement restreinte (Mertens *et al.*, 2005). Les GTPases Rho peuvent aussi être régulées par des processus contrôlant leur adressage aux membranes. Cet adressage nécessite une modification post-traductionnelle consistant en un ajout d'un groupement géranyl-géranyl ou farnesyl en C-terminal de la protéine (Casey et Seabra, 1996 ; Winter-Vann et Casey, 2005). Cet ajout permet, à terme, leur passage du cytosol à la membrane cible. Dans ce contexte, les Rho GDIs jouent un rôle important car elles peuvent séquestrer le groupement lipidique dans une poche hydrophobe et ainsi disloquer les GTPases des membranes (Bustelo *et al.*, 2007). Un autre niveau de contrôle peut être exercé sur les GTPases Rho, il s'agit de la régulation transcriptionnelle (Bustelo *et al.*, 2007). Dans ce cas-ci, les GTPases sont soit exprimées dans un type cellulaire spécifique, ou alors leur expression dépend d'un stimulus. A titre d'exemple, alors que Rac1 est ubiquitaire, Rac2 est exprimée uniquement dans les cellules hématopoïétiques (Didsbury *et al.*, 1989) et Rac3 dans les neurones et le système nerveux central (Bolis *et al.*, 2003), restreignant ainsi leur activité.

1.3.3 Fonctions des GTPases Rho

1.3.3.1 Principales fonctions des GTPases Rho

Une fois transloquées à la membrane et activées, les GTPases Rho peuvent exercer leur rôle sur une pléthore d'effecteurs incluant des kinases, des phosphatases, des lipases et des protéines liées à l'actine (Zhao et Manser, 2005 ; Bustelo *et al.*, 2007). Cela leur confère un vaste champ d'action sur bon nombre de processus cellulaires clés tels que la réorganisation du cytosquelette d'actine et des microtubules, l'expression génique et le trafic vésiculaire. Parce qu'elles régulent ces processus, les GTPases Rho contrôlent le cycle cellulaire, la division cellulaire, la différenciation, la migration, l'adhésion, et donc tous les différents types de morphogenèse décrits précédemment.

Le premier processus pour lequel les GTPases Rho ont été identifiées comme des régulateurs majeurs, et qui est d'un intérêt tout particulier dans ce travail, est la réorganisation du cytosquelette d'actine. Au début des années 1990, les études menées sur des fibroblastes en culture par le groupe de Alan Hall ont permis d'identifier successivement RhoA, Rac1, puis Cdc42 dans la régulation de la formation de trois structures dépendantes de la réorganisation des filaments d'actine : les fibres de stress, les lamellipodes et les filopodes (Ridley et Hall, 1992 ; Ridley *et al.*, 1992 ; Nobes et Hall, 1995). Depuis, de nombreuses études ont permis de mieux qualifier le rôle des GTPases Rho dans la réorganisation du cytosquelette d'actine et dans la morphogenèse. Dans les sections suivantes seront détaillés trois processus majeurs :

(1) le remodelage des jonctions adhérentes, lesquelles sont des points d'ancrage essentiels de l'actine.

(2) le contrôle de la contraction des câbles d'actine-myosine.

(3) la régulation des différents types de protrusions, évènement essentiel à la mobilité cellulaire.

1.3.3.2 Le remodelage des jonctions adhérentes par les GTPases Rho

Comme cela a été évoqué précédemment, les jonctions apicales jouent un rôle très important dans les processus morphogéniques. Les GTPases Rho sont des régulateurs essentiels à la formation, à la maintenance et au désassemblage de ces jonctions.

In vitro comme *in vivo*, l'étape initiale de la formation des jonctions réside dans l'accumulation des E-cadhérines au niveau du contact primordial entre les cellules, et requiert l'activation de Rac1 et de Cdc42 (Figure 1.11) (Raich *et al.*, 1999 ; Jacinto *et al.*, 2000 ; Ehrlich *et al.*, 2002 ; Kovacs *et al.*, 2002 ; Lambert *et al.*, 2002). L'activation des GTPases induit la polymérisation de l'actine grâce à une machinerie qui implique leur effecteurs WAVE, WASp et le complexe de nucléation de l'actine ARP2/3 (*actin-related proteins ARP2 and ARP3*). Elle induit aussi la formation de lamellipodes et de filopodes, favorisant ainsi la formation de nouveaux contacts jonctionnels entre les cellules voisines. Les GTPases Rho permettent également le remodelage local de la membrane et le recrutement de protéines cibles comme la cortactine ou la formine (Katsube *et al.*, 1998 ; Kobielak *et al.*, 2004), favorisant ainsi l'extension de la zone de contact cellule-cellule. L'extension des jonctions est également assurée par Rac1 et Cdc42 *via* leur action sur la polymérisation de l'actine (Figure 1.11). Une GEF spécifique pour Rac1, TIAM1, a été montré essentielle à l'établissement des jonctions apicales, notamment les jonctions serrées, dans les cellules épithéliales (Chen et Macara, 2005). D'autres GEFs, telles que Tuba, une GEF pour Cdc42, et Asef, une GEF pour Rac1, ont aussi été montrées comme impliquées dans la formation des adhésions cellule-cellule (Kawasaki *et al.*, 2003 ; Otani *et al.*, 2006). L'activation de Cdc42 par Dbl3 joue également un rôle important au cours de cette phase d'extension car elle permet la mise en place de la polarité apico-basale et l'extension apicale des jonctions *via* l'activation du complexe Par6-aPKC (Zihni *et al.*, 2014).

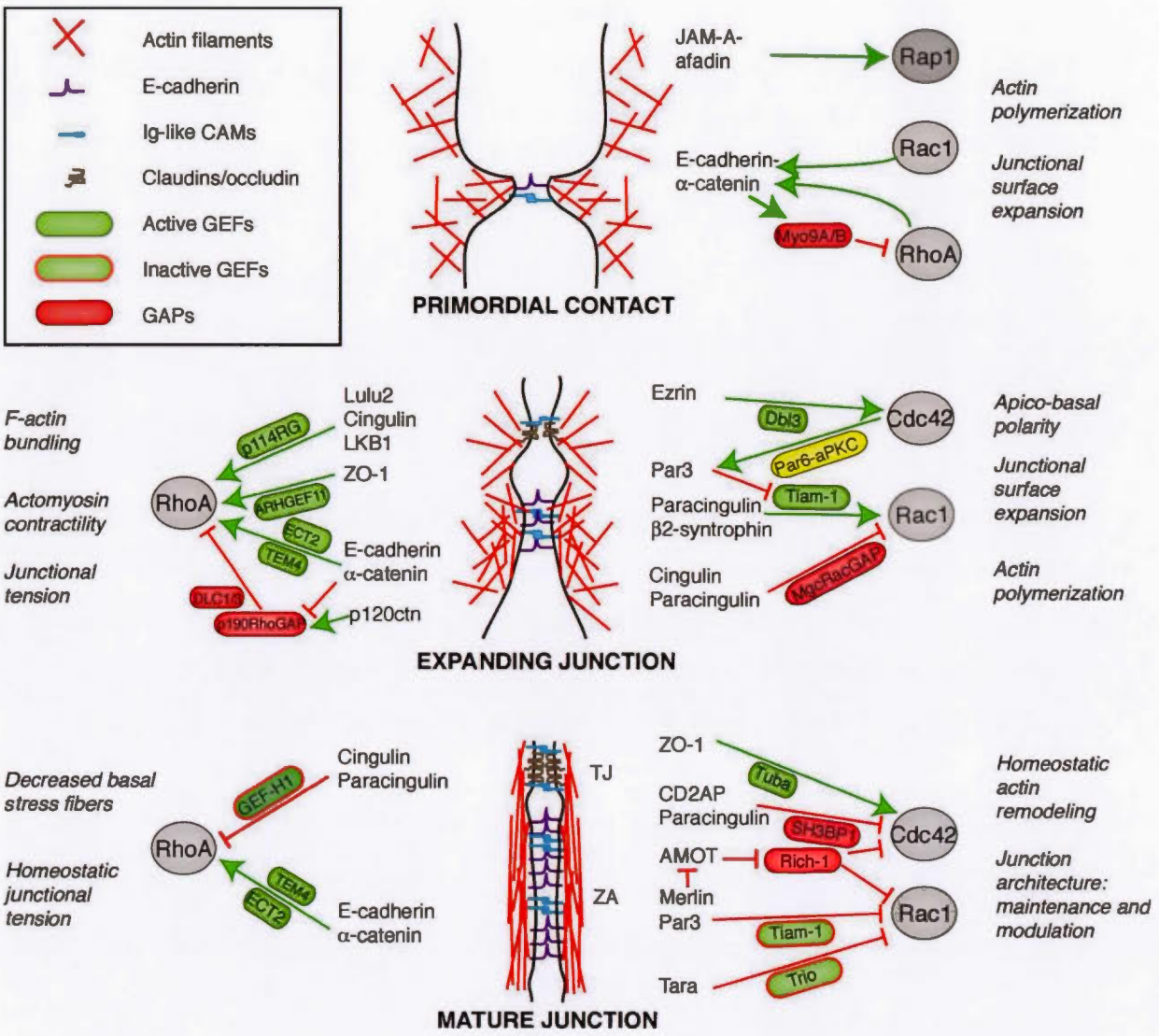

Figure 1.11 : Assemblage et maturation des jonctions adhérentes. Schéma montrant les étapes de formation et de maturation des jonctions apicales (de haut en bas) dans les cellules épithéliales, ainsi que les différentes protéines impliquées dans ces processus. Les lignes et les flèches vertes et rouges représentent respectivement l'activation et l'inhibition. Les principaux effets de la régulation des Rho GTPases sur l'organisation et la fonction du cytosquelette sont indiqués de part et d'autre du schéma. Figure extraite de Citi *et al.*, 2014.

RhoA joue également un rôle important dans le processus d'extension et de stabilisation des jonctions. En effet, par l'intermédiaire des GEFs TEM4, ARHGEF11, p114RhoGEF et ECT-2, RhoA est activée au niveau des jonctions apicales où elle promeut un assemblage et une contraction des filaments d'actine-myosine (Figure 1.11) (Terry *et al.*, 2011 ; Itoh *et al.*, 2012 ; Ratheesh *et al.*, 2012 ; Ngok *et al.*, 2013 ; Priya *et al.*, 2013), deux mécanismes menés par deux effecteurs distincts. En effet, mDia (Diaphanous-related formin-1) permet la nucléation de l'actine alors que ROCK entraine la contraction des câbles d'actine-myosine (Sahai et Marshall, 2002 ; Kobielak *et al.*, 2004). La contraction de ces filaments génère de la tension qui renforce, regroupe et stabilise les adhésions (Shewan *et al.*, 2005). Cependant, RhoA ne doit pas être suractivée car si la tension dépasse un certain seuil, cela provoque un désassemblage des jonctions (Sahai et Marshall, 2002). Une telle augmentation de tension dépendante d'une suractivation de RhoA a été, par exemple, associée à une transition morphologique de cellules épithéliales en culture (Bhowmick *et al.*, 2001 ; Tavares *et al.*, 2006 ; Cho et Yoo, 2007). Cette transition se caractérise par le passage d'une morphologie épithéliale à une morphologie mésenchymateuse, et est appelée transition épithélio-mésenchymateuse.

Une fois que les jonctions sont établies et matures, d'autres protéines et régulateurs de GTPases Rho sont impliqués dans le maintien de ces jonctions, leur remodelage, et dans le contrôle de la tension à laquelle elles sont soumises. Cdc42 joue un rôle primordial dans cette régulation. Comme cela a été montré *in vitro* dans des cellules mammifères (Akhtar et Hotchin, 2001 ; Izumi *et al.*, 2004), et *in vivo* chez *D. melanogaster* (Georgiou *et al.*, 2008 ; Harris et Tepass, 2008) et le *C. elegans* (Balklava *et al.*, 2007), l'activité de Cdc42, couplée à son rôle avec les protéines Par, est primordiale pour réguler l'endocytose des jonctions, et donc leur recyclage. Confirmant ce point, certains effecteurs de Cdc42 sont décrits pour leur rôle dans la formation des vésicules d'endocytose et le trafic des E-cadhérines. On peut par exemple citer N-WASP/WASp, associée au complexe de nucléation de l'actine

Arp2/3 (Merrifield *et al.*, 2004 ; Galletta *et al.*, 2008), TOCA1/CIP4/FBP17 (Kamioka *et al.*, 2004 ; Leibfried *et al.*, 2008 ; Fricke *et al.*, 2009) et PAK1 (Pirraglia *et al.*, 2010). Le remodelage des jonctions adhérentes semblent aussi être couplé à la tension au cours de la morphogenèse. Chez la drosophile, il a par exemple été montré que l'accumulation de la myosine II est couplée à l'endocytose au niveau des jonctions qui rétrécissent (Figure 1.12) (Levayer *et al.*, 2011 ; Yashiro *et al.*, 2014).

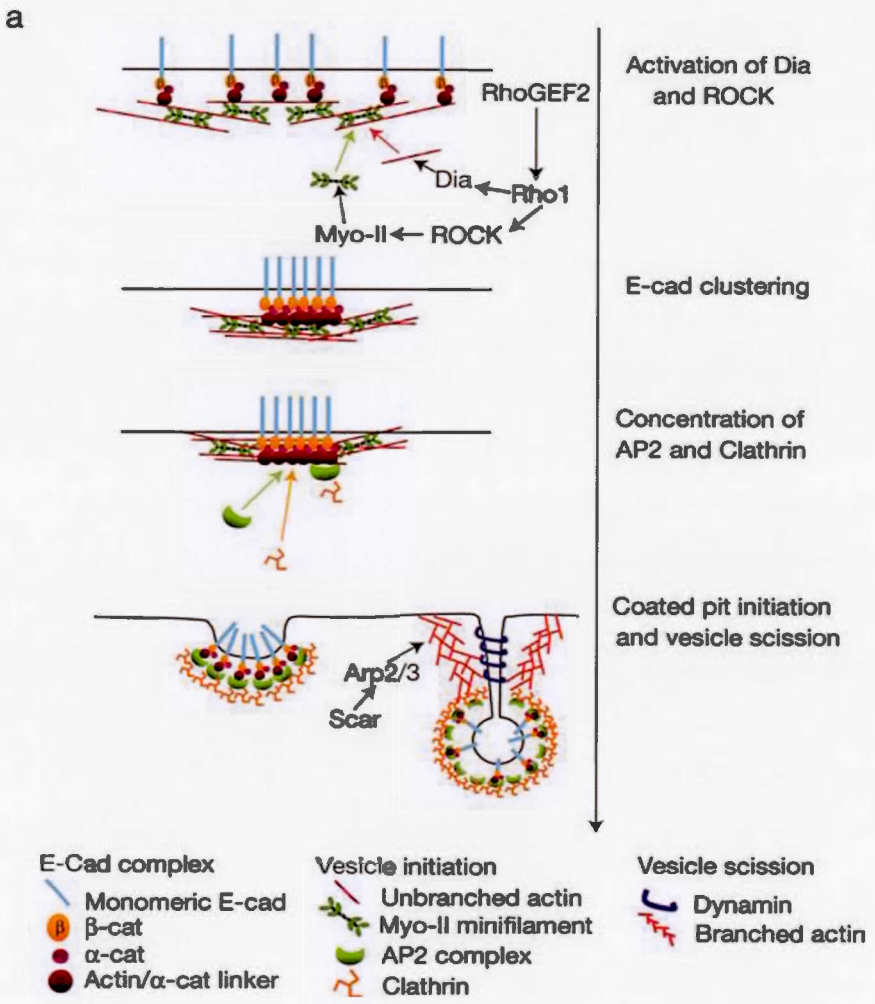

Figure 1.12 : Remodelage des jonctions adhérentes chez *D. melanogaster*. Schéma récapitulatif de la séquence d'évènements entrainant l'endocytose des E-cadhérines telle que décrite dans la section 1.3.3.2. Figure extraite de Levayer *et al.*, 2011.

En effet, sous l'impulsion de RhoGEF2, RhoA active ROCK et mDia, ce qui entraine un remodelage du cytosquelette d'actine et la contraction de la myosine II. Ces deux processus provoquent un regroupement local des E-cadhérines entrainant lui-même le recrutement de la machinerie d'endocytose clathrine-dépendante, puis leur internalisation (Levayer *et al.*, 2011 ; Engl *et al.*, 2014) (Figure 1.12). Tout cela montre qu'il y a une interdépendance entre l'assemblage/désassemblage des jonctions apicales, la modulation de l'assemblage et de la contraction des filaments d'actine-myosine, et les GTPases Rho.

1.3.3.3 L'appareil contractile d'actine-myosine

Comme cela vient d'être évoqué, une fois les jonctions assemblées, l'appareil de contraction actine-myosine se met en place et devient actif. Dans cette partie du chapitre sera décrite la régulation de la contraction des filaments d'actine-myosine par les GTPases Rho.

La contraction et le relâchement des filaments d'actine-myosine à lieu à travers la modulation de la phosphorylation des chaînes légères de myosine (MLC, *myosin light chain*) et est régulée par des kinases et une phosphatase (Figure 1.13). Cette phosphatase est un trimère composé d'une sous-unité catalytique PP1cδ, d'une sous-unité M20 et de la sous-unité MYPT qui confère la spécificité à la sous-unité catalytique. Son rôle est de déphosphoryler les chaines légères de la myosine, d'inhiber leur contraction et donc d'empêcher la génération de tension (Dent *et al.*, 1992 ; Moorhead *et al.*, 1998). La contractilité de la myosine non musculaire II est régulée par RhoA, Cdc42 et Rac1 *via* l'activation de leurs effecteurs respectifs ROCK, MRCK (*myotonin-related Cdc42-binding kinase*), et PAK1 (*p21 protein (Cdc42/Rac)-activated kinase 1*) (Sanders *et al.*, 1999 ; Totsukawa *et al.*, 2000 ; Dong *et al.*, 2002) (Figure 1.13).

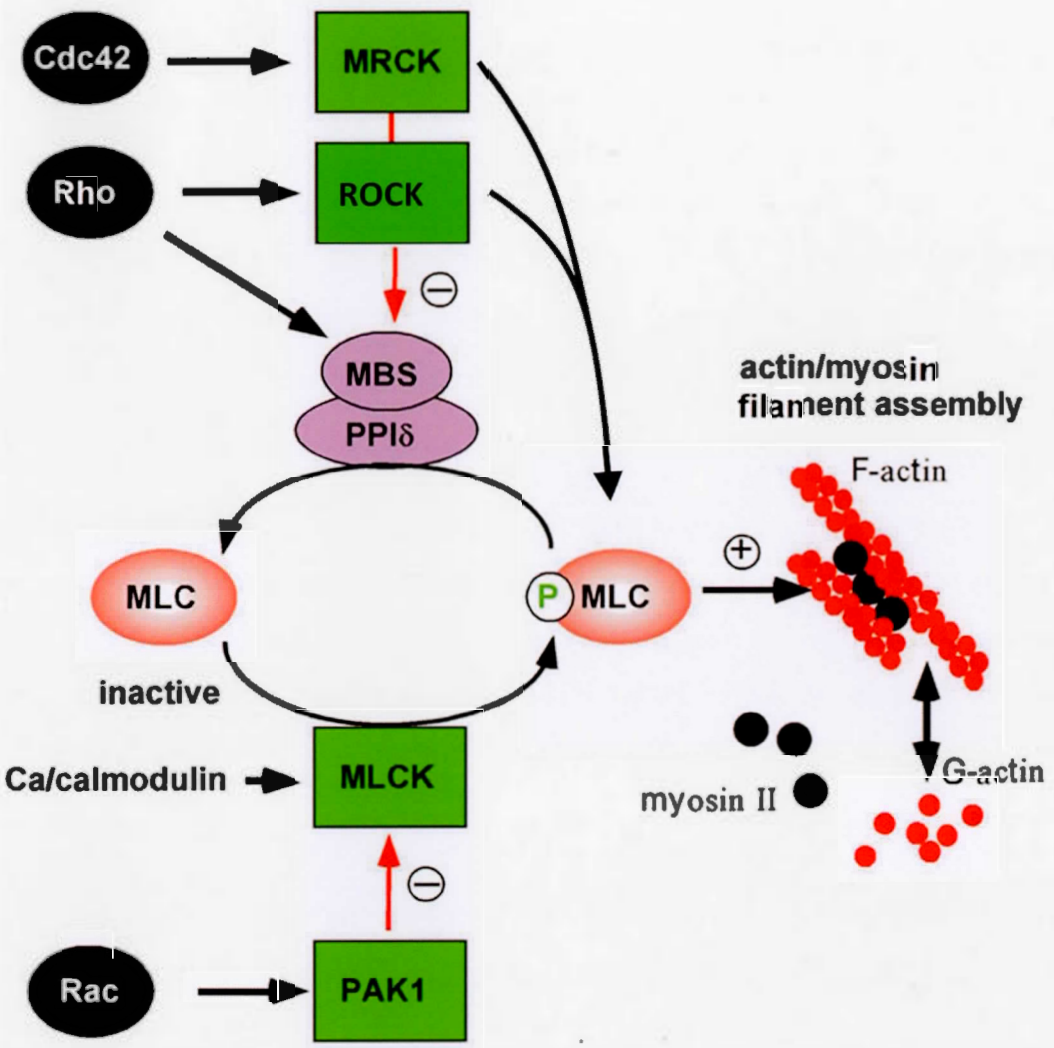

Figure 1.13 : Régulation de l'appareil contractile actine-myosine. La phosphorylation des chaînes légères de myosine (MLC) est régulée par 3 kinases activatrices (MRCK, ROCK et MLCK), une kinase inhibitrice (PAK1), et une phosphatase (PP1δ-MBS), elles-mêmes régulées par les GTPases RhoA, Rac1 et Cdc42. Les flèches noires et rouges indiquent respectivement l'activation et l'inhibition. Figure adaptée de Zhao et Manser, 2005.

Lorsqu'activée par RhoA, ROCK phosphoryle les MLC provoquant la contraction de la myosine (Amano *et al.*, 1996). Cependant, l'activité de ROCK ne se limite pas uniquement à cela car cette protéine peut également inhiber la phosphatase de la MLC en phosphorylant la sous-unité MYPT, et ainsi engendrer davantage de contraction de la myosine (Kimura *et al.*, 1996). En addition à RhoA, Cdc42 est également capable de stimuler la phosphorylation de la MLC. Cdc42 peut effectivement activer son effecteur MRCK qui en retour phosphoryle la MLC (Leung *et al.*, 1998). A l'instar de ROCK, MRCK peut également inhiber la myosine phosphatase et ainsi favoriser l'activité de la myosine II (Tan *et al.*, 2001). La GTPase Rac1 intervient aussi dans la modulation de la phosphorylation de la MLC par l'intermédiaire de son effecteur PAK1. Le rôle de PAK1 est cependant controversé. Chez les mammifères, il semble que PAK1 agisse négativement sur la contraction de la myosine en phosphorylant et inhibant MLCK (*myosin light chain kinase*) (Sanders *et al.*, 1999) (Figure 1.13). Cette dernière est une kinase spécifique pour la MLC dont l'activité est régulée par le calcium et la calmoduline. Chez le *C. elegans*, par contre, PAK-1 apparait comme un activateur de la contraction de la myosine (Gally *et al.*, 2009).

1.3.3.4 La régulation des différents types de protrusions par les GTPases Rho

La migration cellulaire est un mécanisme essentiel pouvant conduire la morphogenèse épithéliale. Elle nécessite des changements de forme de la cellule impliquant le remodelage du cytosquelette, des adhésions cellule-substrat et de la MEC. On distingue deux grands types de migration : la migration individuelle des cellules, elle-même divisée en migration mésenchymateuse et amiboïde, et la mobilité des cellules en cohorte appelée migration collective (Figure 1.14).

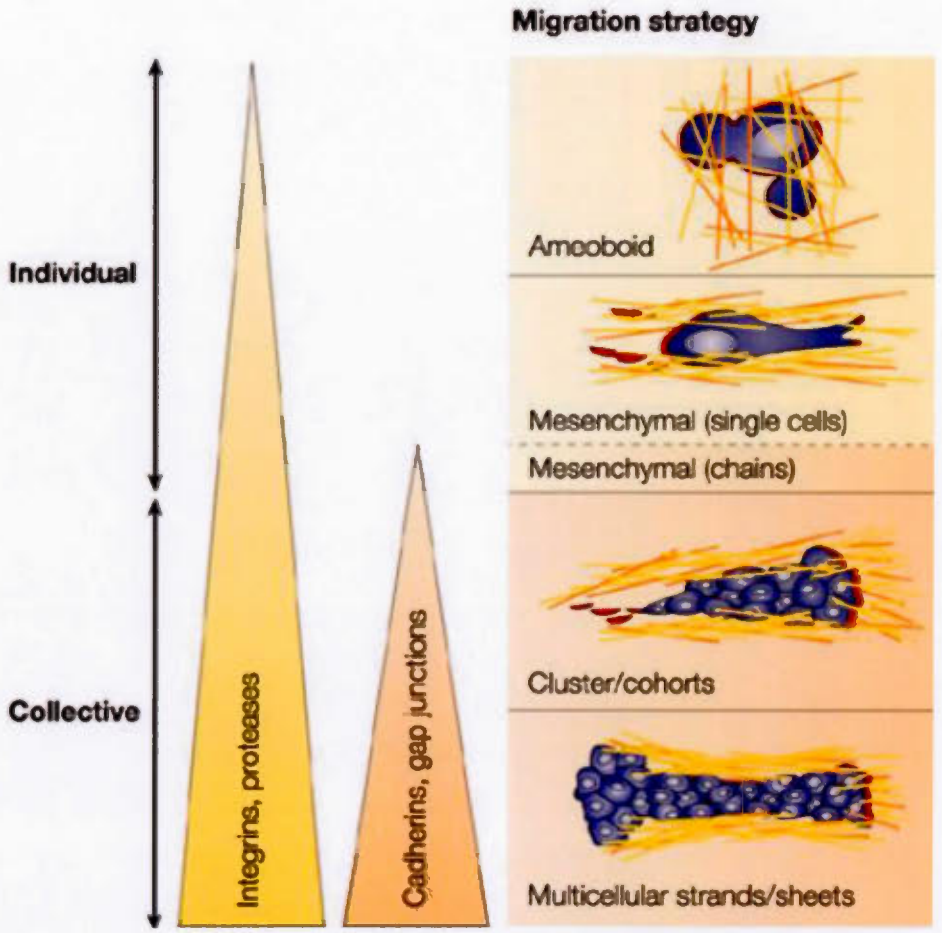

Figure 1.14 : Les différentes stratégies de migration. On distingue deux grands types de migration : la migration individuelle des cellules, divisée en migration amiboïde et mésenchymateuse, et la migration collective. Ces différentes stratégies migratoires se distinguent par le niveau d'interaction cellule-matrice extracellulaire (intégrines et protéases ; triangle jaune), et cellule-cellule (Cadhérines ; triangle orange). Figure adaptée de Friedl et Wolf, 2003.

Ces différents procédés de mobilité cellulaire sont dépendants de la formation de protrusions au front migratoire de la cellule ou de la colonie de cellules migratrices. Dans cette section, nous allons décrire ces différents types de protrusions en fonction du mode de migration utilisé ainsi que leur régulation par les GTPases Rho. Sous le terme protrusion sont regroupés les lamellipodes, les filopodes et les « *blebs* », respectivement régulés par Rac1, Cdc42 et RhoA. Les lamellipodes et les filopodes sont des protubérances de la membrane riches en actine polymérisée. Elles impliquent des complexes d'adhésion entre la cellule et son substrat, et sont principalement impliquées dans les modes de migration de type mésenchymateux et collectifs. La migration amiboïde dépend, pour sa part, de la formation de *blebs* et est grandement dépendante de la contractilité du cytosquelette d'actine-myosine au niveau de ces protrusions (revue de Ridley, 2011).

Les lamellipodes sont des extensions de la membrane plasmique plates et fines, et dépendantes de la formation d'un réseau branché de filaments d'actine. Cette réorganisation du cytosquelette est dépendante de l'activation de Rac1, et à lieu à l'avant des cellules ayant une mobilité mésenchymateuse, ainsi qu'au niveau des cellules meneuses dans la migration collective. L'activation localisée de Rac1 est le point clé de la formation de ces protubérances, et dépend des GEFs telles que Tiam1, β-PIX et DOCK180 (D'Amico *et al.*, 2010 ; Goicoechea *et al.*, 2014 ; Ridley, 2015). Une fois activée, Rac1 peut interagir avec son effecteur Scar/WAVE qui, en retour, active le complexe de nucléation des filaments d'actine Arp2/3 (Figure 1.15). Ce complexe Arp2/3 est un initiateur de la formation de nouveaux filaments d'actine le long de filaments déjà existants, dans le but de former un réseau d'actine branchée (Amann et Pollard, 2001). La polymérisation de l'actine peut aussi être assurée par VASP (Havrylenko *et al.*, 2015) *via* son interaction avec WAVE.

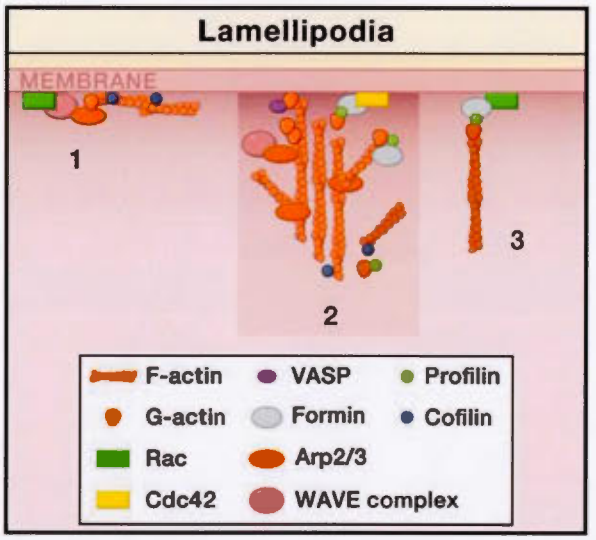

Figure 1.15 : Structure et formation des lamellipodes. (1) Le sectionnement des filaments d'actine par la cofiline laisse des extrémités franches libres qui servent de sites pour (2) la polymérisation de l'actine. Cette polymérisation est dépendante de l'activation de la GTPase Rac1 qui active le complexe de nucléation de l'actine Arp2/3 *via* WAVE. VASP et la formine peuvent aussi contribuer à la polymérisation de l'actine. La formine permet l'allongement des filaments d'actine de façon dépendante ou (3) indépendante du complexe Arp2/3. Figure extraite de Ridley, 2011.

Ces deux voies (Arp2/3 et VASP) sont d'ailleurs importantes dans la formation des lamellipodes par les cellules de l'hypoderme migrant collectivement au cours de la fermeture ventrale du *C. elegans* (Sawa *et al.*, 2003 ; Withee *et al.*, 2004 ; Havrylenko *et al.*, 2015). En plus de Rac1, les GTPases Cdc42 et RhoA sont également actives au niveau des lamellipodes (Machacek *et al.*, 2009). Le rôle de Cdc42 dans la migration serait d'assurer la bonne localisation de l'activité de Rac1 en jouant sur la localisation des GEFs spécifiques pour Rac1 et le trafic vésiculaire (revue de Etienne-Manneville, 2004), deux processus importants pour l'établissement et le maintien la polarité antéro-postérieure lors de la migration. Quant à RhoA, elle est retrouvée active au bout du lamellipode où elle initie supposément la polymérisation de l'actine par l'intermédiaire de la formine Dia (Kurokawa et Matsuda, 2005). Cependant, son rôle est controversé car il a aussi été montré que RhoA et ses effecteurs doivent avoir une activité réduite pour permettre l'extension des lamellipodes (Vial *et al.*, 2003), et qu'une forte activité de RhoA peut

inhiber ce type de migration voire même entrainer une migration de type amiboïde (Petrie et Yamada, 2012). L'hypothèse la plus crédible quant au rôle de ces GTPases au cours de la formation des lamellipodes est que Cdc42, Rac1 et RhoA fonctionneraient séquentiellement au niveau des protrusions, permettant la polymérisation de l'actine, la contraction de la myosine, la formation des adhésions focales et leur maturation.

La migration amiboïde réfère à une reptation rapide des cellules dans leur environnement tridimensionnel. C'est un type de migration pendant lequel les cellules n'ont pas besoin d'adhérer fortement aux tissus environnants pour se mouvoir. Elle est dépendante de la contraction des filaments d'actine-myosine corticaux, et est associé à une très forte activité de la voie RhoA/ROCK (Charras et Paluch, 2008 ; Petrie et Yamada, 2012). En effet, la régulation spatiale des niveaux de contraction des filaments d'actine-myosine dans la cellule génère un flux de cytoplasme entrainant la formation de *blebs* à l'avant de la cellule suivie d'une rétraction à l'arrière (Figure 1.16) (Lammermann et Sixt, 2009). Ce type de déplacement est dépendant de l'activation de RhoA.

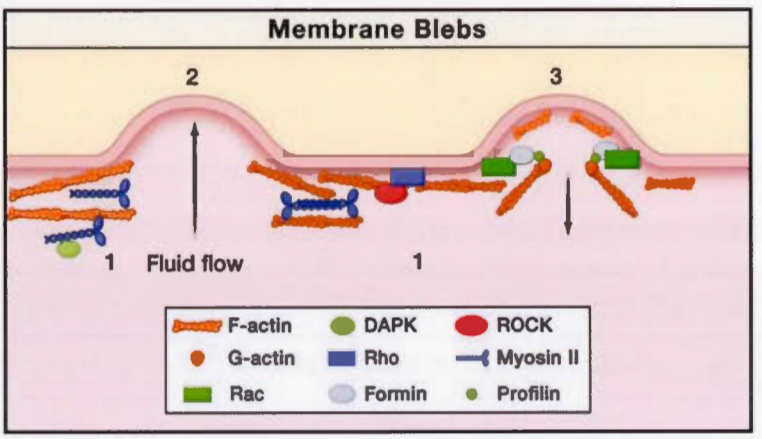

Figure 1.16 : Structure et formation des blebs. Les blebs sont induits par (1) la contractilité des filaments d'actine-myosine, dépendante de la voie RhoA/ROCK, à la membrane, et par (2) un flux de cytoplasme déformant la membrane. (3) La rétraction des blebs fait suite à la polymérisation de l'actine dépendante de la GTPase Rac1à la membrane de ce bleb. Figure extraite de Ridley, 2011.

L'activation de la voie Rac1 entraine par contre un changement vers un mode de migration lamellipode-dépendant. Il existe une interchangeabilité élevée entre la migration basée sur les *blebs* et celle basée sur les lamellipodes. Au cours du développement précoce du poisson zèbre, par exemple, les cellules individuelles du mésoderme émettent des *blebs* qui adoptent par la suite une morphologie de type lamellipode au cours du développement (Row *et al.*, 2011).

Ces deux mécanismes migratoires, lamellipodes ou *blebs*-dépendants, peuvent également impliquer un autre type de protubérances de la membrane : les filopodes. Ce sont de longues et fines extensions membranaires riches en filaments d'actine non branchée formant des faisceaux (Figure 1.17).

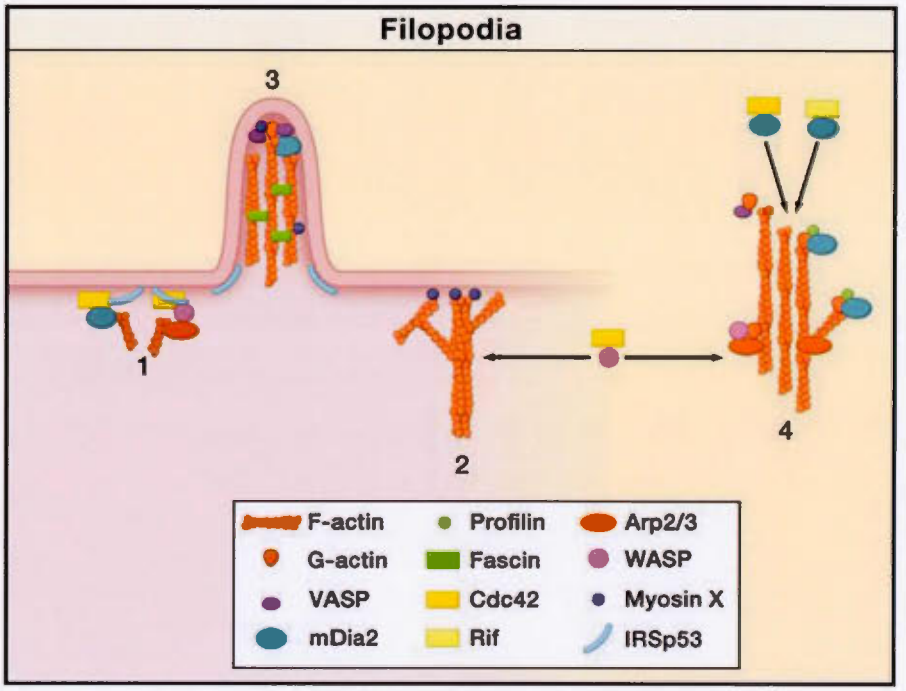

Figure 1.17 : Structure et formation des filopodes. (1-2) La formation des filopodes est initiée par une courbure de la membrane induite par IRSp53, laquelle recrute Cdc42 et ses effecteurs Dia et WASP pour stimuler la polymérisation de l'actine. Les filaments d'actine peuvent aussi provenir des lamellipodes. (3-4) VASP et Dia jouent un rôle important dans le processus d'extension du filopode en permettant la nucléation de l'actine à la pointe du filopode. Figure extraite de Ridley, 2011.

Il a été montré que non seulement les filopodes peuvent initier des contacts cellule-cellule, mais qu'ils jouent en rôle important dans la direction de la migration, le chimiotactisme et la concentration de Rac1 actif à l'avant des cellules. Cdc42 semble être la principale GTPases Rho impliquée dans la formation des filopodes de par son action sur le complexe de nucléation Arp2/3 *via* N-WASP (Miki *et al.*, 1998) et sur les formines Dia (Peng *et al.*, 2003). Le rôle de ces dernières est de promouvoir la nucléation de filaments d'actine non branchée (Figure 1.17). D'autres protéines comme la fascine, dont l'activité est stimulée par la voie RhoA/ROCK, peuvent également contribuer à la formation des filopodes (Jayo *et al.*, 2012).

A travers cette présentation rapide des différents types de protrusions impliquées dans la migration cellulaire, il est remarquable de voir à quel point le phénotype migratoire est dépendant des GTPases Rho et de leur coordination au sein de la cellule.

1.3.4 Antagonisme RhoA / Rac1

Par le biais des quelques fonctions des GTPases Rho décrites précédemment, nous pouvons voir l'importance de la régulation spatio-temporelle des GTPases Rho au cours de la morphogenèse des épithéliums. Un aspect important de cette régulation consiste en l'antagonisme observé entre les GTPases Rho, et en particulier entre RhoA et Rac1. Plusieurs exemples ont permis de mettre cet antagonisme mutuel en évidence (revue de Guilluy *et al.*, 2011). Ces études ont permis de montrer que l'activation d'une de ces GTPases provoque l'inhibition systématique de l'autre entrainant leur exclusion spatiale et/ou temporelle (Parri et Chiarugi, 2010 ; Pertz, 2010 ; Guilluy *et al.*, 2011). Récemment, il a même été montré que cette diaphonie (ou *crosstalk*) entre RhoA et Rac1 est responsable de l'hétérogénéité morphologique observée au sein d'une population isogénique de cellules en culture (Sailem *et al.*, 2014). Ce *crosstalk* est en réalité dû à une double boucle de rétrocontrôle négatif où RhoA inhibe Rac1 et Rac1 inhibe RhoA. Dans certains cas, cette inhibition mutuelle

peut entrainer la bistabilité (Kholodenko, 2006). Un système bistable se caractérise par une interchangeabilité entre deux états stables mais biochimiquement distincts, et dans lequel chacun des deux états stables entraîne un phénotype spécifique. Cette bistabilité du système Rho/Rac a été modélisée dans plusieurs études (Kholodenko, 2006 ; Jilkine *et al.*, 2007 ; Semplice *et al.*, 2012 ; Tsyganov *et al.*, 2012) et récemment prouvée dans une lignée de cellule cancéreuse (Byrne *et al.*, 2016). Dans cette dernière étude, les auteurs se sont intéressés à la plasticité du phénotype migratoire, c'est-à-dire au passage d'un phénotype mésenchymateux à amiboïde, et inversement, et ont montré que PAK, entre autres, joue un rôle clé dans cette plasticité. Différents types de régulation peuvent effectivement mener à ce *crosstalk* ou cette bistabilité : une régulation de l'activité des GTPases Rho *via* les GEFs et les GAPs, une régulation de l'expression et de la stabilité des protéines, et une régulation des voies de signalisation en aval. Tous ces points ont fait l'objet d'une revue (Guilluy *et al.*, 2011) et ne seront pas détaillés ici. Cependant, pour appuyer ces propos et bien comprendre l'enjeu de cet antagonisme réciproque entre Rho et Rac, deux exemples seront détaillés. Un premier exemple portant sur un mécanisme cellulaire individuel, la plasticité migratoire, et un second sur un évènement morphogénique, l'invagination.

1.3.4.1 Exemple 1 : la plasticité migratoire et la bistabilité du système RhoA/Rac1

L'inhibition réciproque de RhoA et Rac1 est régulée par différents mécanismes et peut entraîner soit des transitions amiboïdo-mésenchymateuse (TAM), soit mesenchymo-amiboïdale (TMA) (Figure 1.18A).

L'inhibition de Rac1 par RhoA, qui favorise la migration amiboïde, peut par exemple être le résultat de l'activation de FilGAP, une GAP pour Rac1 (Saito *et al.*, 2012 ; Nakamura, 2013). En effet, la phosphorylation de FilGAP par ROCK active cette protéine (Ohta *et al.*, 2006) qui peut ainsi catalyser l'hydrolyse du GTP par Rac1 et

mener à son inactivation (conversion vers une forme liée au GDP), favorisant ainsi la TMA. De manière similaire, ArhGAP22 est capable d'inhiber Rac1 de façon RhoA-dépendante, et bien que son activation soit dépendante de ROCK, elle n'est pas activée par phosphorylation mais *via* la contraction cellulaire (Sanz-Moreno *et al.*, 2008) (Figure 1.18B).

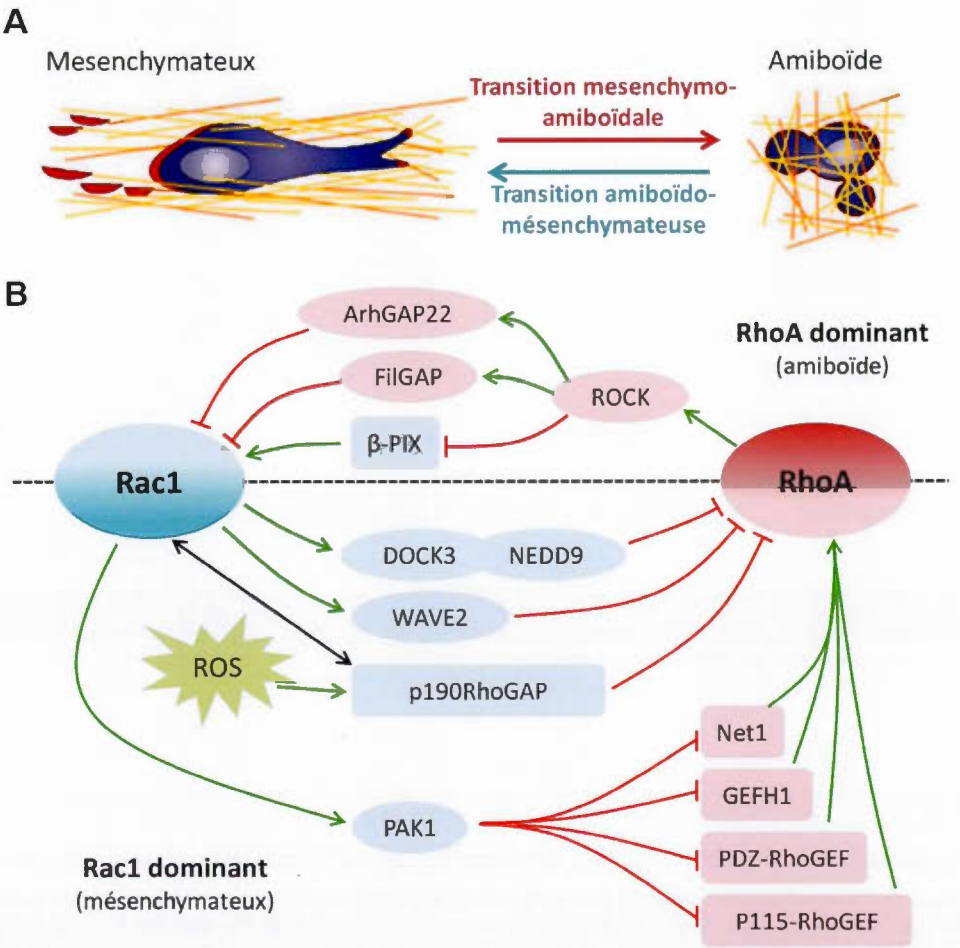

Figure 1.18 : La plasticité migratoire. (A) Schéma représentant la transition mésenchymo-amiboïdale et la transition amiboïdo-mésenchymale. (B) Modèle moléculaire de l'antagonisme RhoA/Rac1 dans la plasticité migratoire. Les protéines permettant une dominance de Rac1 ou de RhoA sont respectivement sur fond bleu et sur fond rouge. Les flèches vertes indiquent l'activation et les lignes rouges indiquent l'inhibition. La double flèche noire indique une interaction directe entre Rac1 et p190RhoGAP. Figure (A) adaptée de Friedl et Wolf, 2003.

D'autres voies de régulation impliquant la tension mécanique issue de l'activité de ROCK sur la myosine peuvent diminuer l'activité de Rac1. On peut par exemple citer la GEF β-PIX dont le rôle est d'activer Rac1 au niveau des complexes d'adhésion focale naissants, favorisant ainsi la formation des lamellipodes. Une étude protéomique utilisant un inhibiteur de la myosine II, la blebbistatine, a montré que β-PIX est recrutée aux adhésions focales en présence de la drogue, suggérant que sous une activité contractile élevée, β-PIX se dissocierait de ces adhésions (Kuo *et al.*, 2011).

La TAM est elle aussi favorisée par certaines GEFs et GAPs. p190RhoGAP est une de ces protéines. En effet, elle est capable d'inhiber l'activité de RhoA lorsqu'elle est activée par Rac1 soit par une interaction directe (Bustos *et al.*, 2008), soit indirectement *via* la production d'espèces réactives de l'oxygène (ROS) qui favorise la phosphorylation et l'activité de p190RhoGAP (Nimnual *et al.*, 2003). Dans des cultures de cellules de mélanome, il a aussi été montré que DOCK3, une GEF pour Rac1, NEDD9, une protéine adaptatrice liant DOCK3, et WAVE2 favorisent le phénotype mésenchymateux en augmentant l'activité de Rac1 et en diminuant la contractilité de la myosine (Sanz-Moreno *et al.*, 2008). De plus, PAK1, déjà présentée comme importante dans la bistabilité, est également essentielle pour inhiber l'activité de RhoA et ainsi maintenir un phénotype mésenchymateux. Son inhibition favorise donc la TMA (Byrne *et al.*, 2016). PAK1 agirait entre autre en phosphorylant des GEFs spécifiques pour RhoA telles que p115-RhoGEF, Net1, PDZ-RhoGEF, GEF-H1, ce qui inhibe leur activité catalytique et donc diminue l'activité de RhoA (Zenke *et al.*, 1999 ; Barac *et al.*, 2004 ; Alberts *et al.*, 2005 ; Rosenfeldt *et al.*, 2006) (Figure 1.18B).

1.3.4.2 Exemple 2 : L'antagonisme RhoA/Rac1 au cœur de l'invagination cellulaire

Le processus d'invagination au sein d'un tissu épithélial est initié par un groupe de cellules dont le pôle apical se contracte, et est finement régulé par l'antagonisme RhoA/Rac1, lequel détermine la morphologie du sillon formé. Il y a une dizaine d'années, Simoes et ses collègues ont montré que la compartimentalisation des régulateurs de RhoA dirige l'invagination durant la morphogenèse. En effet, dans cette étude chez *D. melanogaster*, ils montrent que les GEFs RhoGEF2 et RhoGEF64C sont exclusivement apicales et favorisent l'activité de Rho, et donc la contraction de la myosine à ce niveau. A l'inverse la RhoGAP Cv-c est retrouvée dans le domaine basolatéral des cellules, excluant ainsi toutes fonctions de RhoA (Simoes *et al.*, 2006). Ceci est confirmé par une étude plus récente montrant qu'une balance entre les activités de Rac1 et de RhoA est essentielle à l'invagination au cours de la morphogenèse de la placode cristallinienne chez la souris (Chauhan *et al.*, 2011). Ici, les auteurs montrent que la perte de RhoA entraine une courbure du sillon moins prononcée que dans le contrôle, et que les cellules formant le sillon sont plus grandes. La perte de Rac1, à l'inverse, réduit la hauteur des cellules et favorise une courbure plus importante (Figure 1.19A-C). En outre, l'analyse de divers marqueurs de l'activité de RhoA et de Rac1 montre des niveaux d'activité soit basale ou apicale pour ces deux GTPases. Finalement les auteurs arrivent à un modèle (Figure 1.19D) où l'activité de RhoA est apicale et entraine la contraction de la myosine, alors que l'activité de Rac1 est basale et favorise l'élongation de la cellule ; ces deux processus étant nécessaires à la courbure du sillon. Cette étude est donc en accord avec la localisation cellulaire des RhoGEFs et RhoGAPs décrite par Simoes.

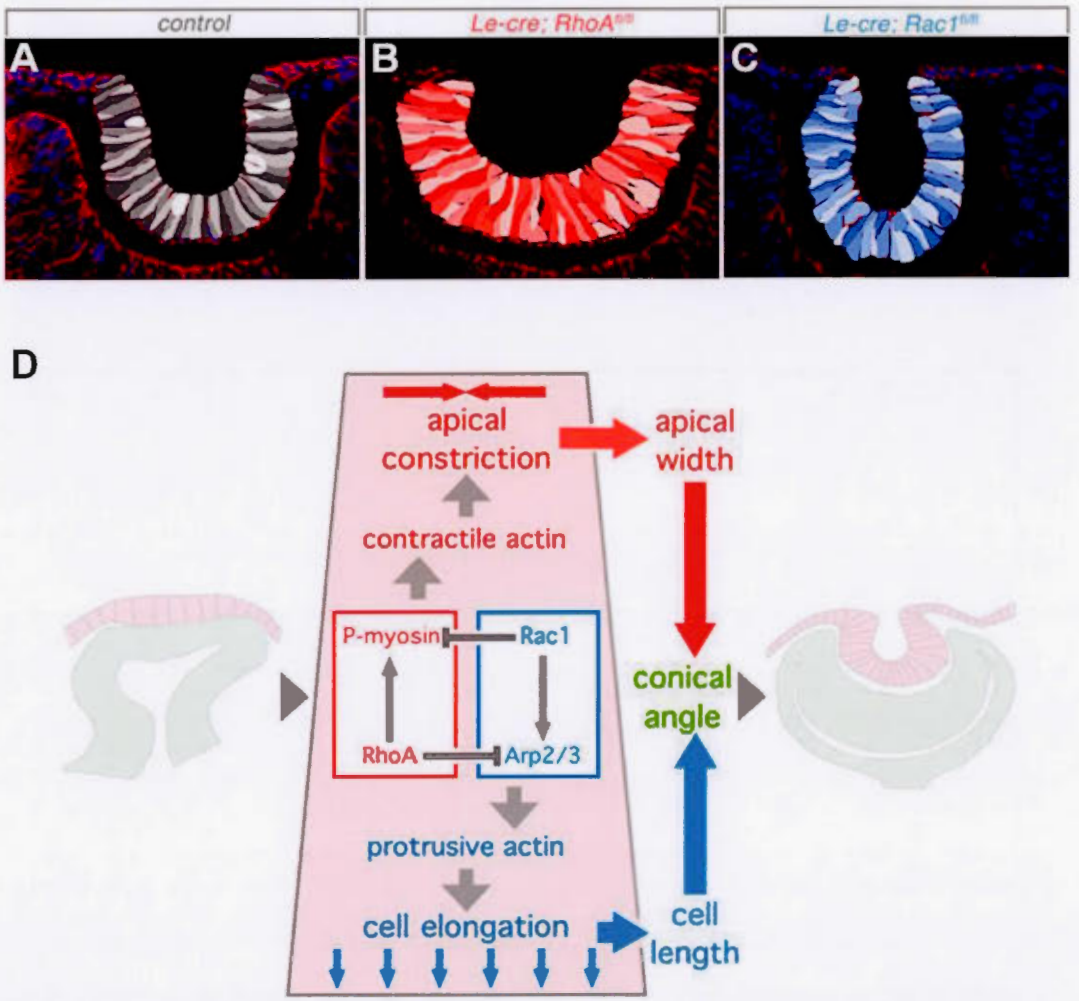

Figure 1.19 : L'antagonisme Rho/Rac régule le mécanisme d'invagination des épithéliums. (A-C) Rac1 et RhoA ont des effets opposés sur la courbure du sillon. Profil du sillon au cours de la formation de la placode cristallinienne dans des souris (A) contrôles, (B) mutantes pour RhoA, ou (C) Rac1. Les mutations RhoA et Rac1 sont retrouvées uniquement dans la placode cristallinienne *via* la recombinaison Cre-Lox. Dans ce cas précis cette recombinaison utilise des allèles conditionnels $RhoA^{fl/fl}$ et $Rac1^{fl/fl}$ *floxés* et de la recombinase Cre exprimée spécifiquement dans la placode cristallinienne (Le-Cre). (D) Schéma récapitulatif de l'antagonisme RhoA/Rac1 au cours de l'invagination des épithéliums. La GTPase Rac1 est active au pôle basal de la cellule où elle promeut l'élongation cellulaire et inhibe la phosphorylation de la myosine. A l'inverse, la GTPase RhoA est active au pôle apical où elle promeut la contraction de la myosine et inhibe l'élongation cellulaire. Cette compartimentalisation permet un contrôle précis de l'invagination cellulaire. Figures extraites de Chauhan *et al.*, 2011.

A travers ces deux exemples, nous remarquons que les cellules peuvent adopter un destin soit RhoA soit Rac1 (phénotype migratoire), ou bien compartimentaliser l'activation de ces deux GTPases au niveau subcellulaire pour permettre des processus morphogéniques. Ces deux possibilités impliquent une inhibition mutuelle et une activité balancée de RhoA et Rac1.

1.4 La morphogenèse du *C. elegans*

Le développement de l'embryon de *C. elegans* dure environ 800 minutes depuis le stade une cellule jusqu'à l'éclosion (Figure 1.20). Pendant la première partie du développement, soit pendant les quatre premières heures environ, les cellules se multiplient puis commencent à se différencier. A la fin de la gastrulation, les cellules de l'épiderme – aussi appelé hypoderme[1] – sont différenciées et se répartissent en trois groupes de cellules : i) l'hypoderme dorsal constitué de deux rangées de dix cellules jointes au niveau de la ligne médiane dorsale, ii) deux rangées de cellules latérales flanquant l'hypoderme dorsal de part et d'autre, et iii) l'hypoderme ventral accolé à l'extrémité ventrale des cellules latérales. C'est à ce stade que la morphogenèse épithéliale s'amorce. Celle-ci est composée des quatre phases suivantes : l'intercalation dorsale, la fermeture ventrale, l'élongation précoce et l'élongation tardive (Figure 1.20).

[1] D'après Chisholm et Hsiao, 2012, cette dénomination ne devrait plus être utilisée et remplacée par « épiderme » qui est un terme plus approprié d'un point de vue biologique. Cependant, le terme d'hypoderme persiste encore dans la littérature et dans la nomenclature cellulaire du *C. elegans*.

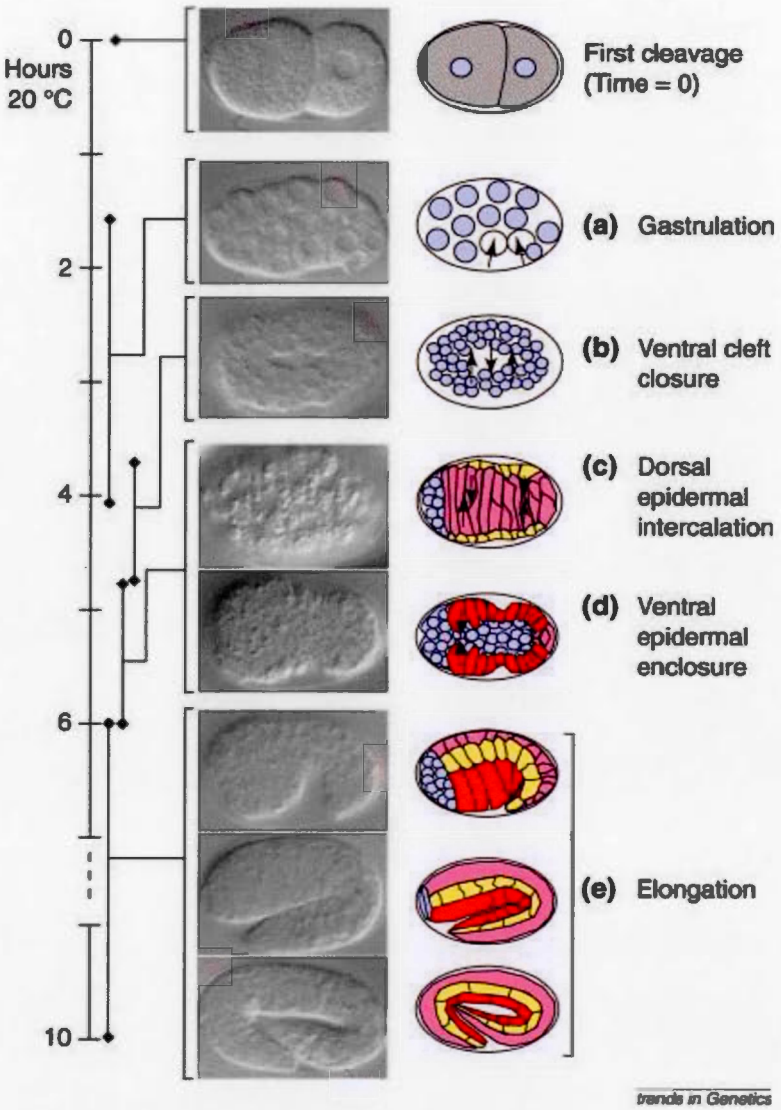

Figure 1.20 : Vue chronologique de l'embryogenèse du *C. elegans*. La morphogenèse de l'épiderme, composé des cellules dorsales (rose), latérales (jaunes) et ventrales (rouge), se passe entre 290 et 520 minutes environ après la première division et inclus l'intercalation dorsale (c), la fermeture ventrale (d) et l'élongation (e). Figure adaptée de Chin-Sang et Chisholm, 2000.

1.4.1 Vue générale des différentes étapes de la morphogenèse

La première étape de la morphogenèse est l'intercalation dorsale. Au cours de cette étape, les deux rangées de dix cellules dorsales présentent initialement s'intercalent pour ne former qu'une seule rangée de cellules dorsales (Figure 1.21A, cellules de couleur verte). Ce mécanisme semble être dépendant de la formation de protrusions basolatérales polarisées (Williams-Masson *et al.*, 1998 ; Walck-Shannon *et al.*, 2015), et a été décrit précédemment à la section 1.2.3.

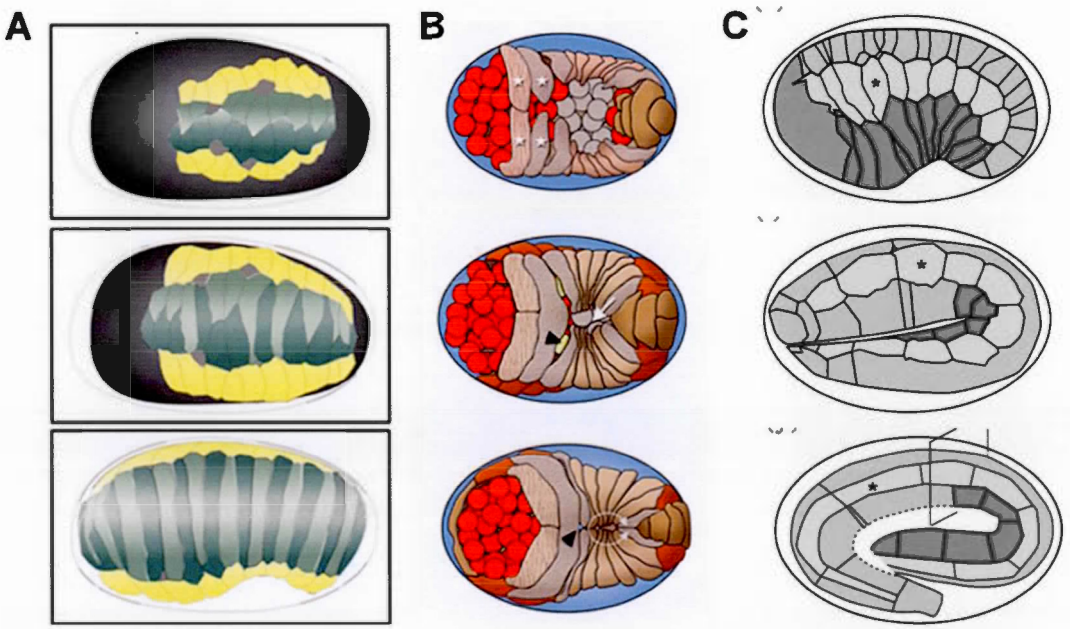

Figure 1.21 : Représentation schématique de la morphogenèse épithéliale du *C. elegans*. Schéma dans le temps (de haut en bas) représentant (A) l'intercalation dorsale, (B) la fermeture ventrale, et (C) l'élongation. Les étoiles blanches en (B) représentent les cellules ventrales antérieures ; la pointe de flèche noire montre la cellule du pore excréteur, et la flèche blanche pointe la poche ventrale L'étoile noire en (C) indique la même cellule aux différents stades de l'élongation. Figures extraites du WormBook, WormAtlas et Ciarletta *et al.*, 2009.

Dès la fin de l'intercalation dorsale, la fermeture ventrale commence. Durant cette phase, les cellules ventrales migrent collectivement pour se rejoindre au niveau de la ligne médiane ventrale et ainsi envelopper l'embryon d'une couche d'hypoderme. Cette étape se déroule en deux phases et suivant deux mécanismes distincts. Tout d'abord, les cellules ventrales antérieures – ou cellules meneuses – vont projeter de larges protrusions riches en actine leur permettant de migrer en direction de la ligne médiane ventrale où elles vont former, après contact, des jonctions avec leurs voisines contralatérales (Figure 1.21B, étoiles blanches). Puis dans un second temps, les cellules postérieures, aussi appelées cellules de la poche (*pocket cells*), vont utiliser un mécanisme dépendant de la contraction – la fermeture en « cordon de bourse » (*purse-string*) – pour migrer et ainsi complètement envelopper l'embryon d'épiderme (Figure 1.21B) (Williams-Masson *et al.*, 1997). A l'issue de cette étape, l'élongation va débuter.

L'élongation embryonnaire est un événement morphogénique permettant le passage d'un embryon ovoïde en une larve vermiforme (Figure 1.21C). Ce processus se traduit par une élongation de l'embryon le long de son axe longitudinal et par une réduction de sa circonférence. Cet événement est guidé par les cellules de l'hypoderme, lesquelles subissent des changements morphologiques notables au cours de cette étape. Elle se divise en deux phases successives que sont l'élongation précoce et l'élongation tardive (Figure 1.21C, de haut en bas). Brièvement, la phase précoce, du stade *comma* jusqu'à 1,75-*fold*, est connue pour être menée par la contraction des filaments d'actine-myosine dans les cellules latérales de l'hypoderme alors que l'élongation tardive implique des mécanismes de mécano-transduction entre les cellules dorsales et ventrales de l'hypoderme et les muscles sous-jacents (Zhang *et al.*, 2011).

Tous ces évènements morphogéniques sont dépendants de la réorganisation du cytosquelette d'actine et du remodelage des jonctions apicales. Ces jonctions diffèrent

entre les cellules épithéliales du *C. elegans* et celles des vertébrés. Leur structure sera brièvement décrite plus bas.

1.4.2 Les jonctions des cellules épithéliales chez le *C. elegans*

De manière similaire aux vertébrés et à la drosophile, on retrouve, chez le nématode, différents complexes d'adhésion. La fonction de ces complexes est conservée mais leur organisation diffère entre les nématodes, les arthropodes et les vertébrés.

On retrouve tout d'abord des jonctions apicales (CeAJs, *C. elegans apical junctions*) qui se divisent en deux complexes distincts : le complexe cadhérine-caténine (CCC) et le complexe DLG-1/AJM-1 (DAC) (Figure 1.22).

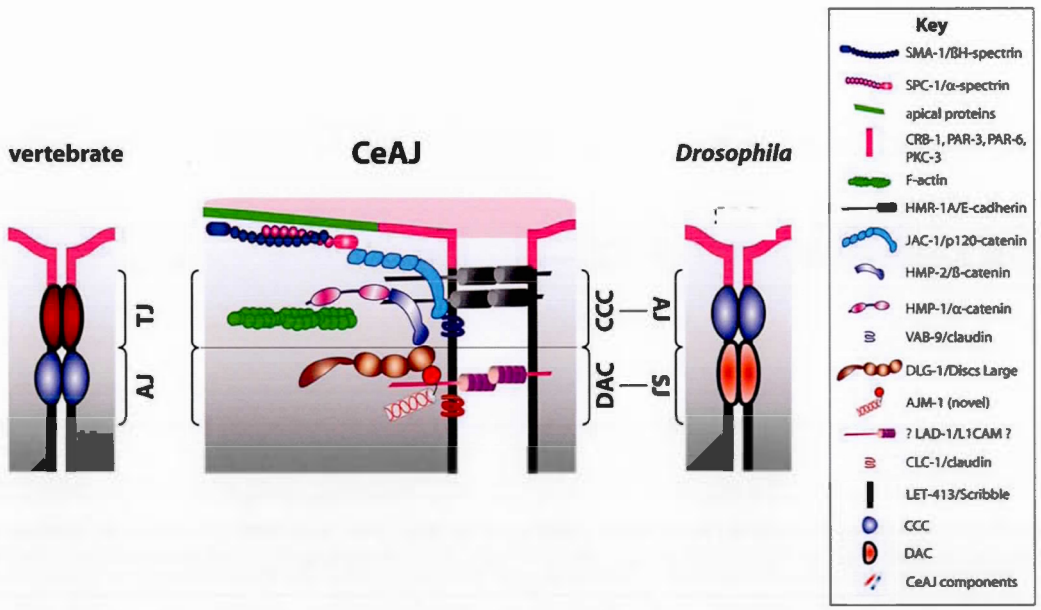

Figure 1.22 : Jonctions apicales du *C. elegans*. Représentation schématique de la composition moléculaire des jonctions apicales du *C. elegans* (CeAJ). La légende est représentée à droite. Comme chez les vertébrés (à gauche) et la drosophile (à droite), les cellules épithéliales du *C. elegans* contiennent deux complexes d'adhésion distincts : le complexe cadhérine-caténine (CCC), qui s'apparente aux jonctions adhérentes (AJ) et le complexe DLG-1/AJM-1 (DAC) qui s'apparente aux jonctions serrées (TJ) et aux jonctions septate (SJ). Figure adaptée du WormBook.

Le CCC est composé de la cadhérine HMR-1, la β-caténine HMP-2, l'α-caténine HMP-1 et la p120-caténine JAC-1 (Costa *et al.*, 1998 ; Pettitt *et al.*, 2003), et est le point d'ancrage des câbles d'actine circonférentielle qui permettent l'élongation du nématode. D'autres protéines ont été associées à ce complexe. Parmi elles, on retrouve notamment VAB-9 (Simske *et al.*, 2003), une claudine normalement associée aux jonctions serrées chez les vertébrés, et qui régule l'attachement des câbles d'actine circonférentielle aux CeAJs chez le nématode (Simske *et al.*, 2003). Les complexes DAC ont une localisation plus basale que les CCC et joueraient un rôle dans l'adhésion et la perméabilité de l'hypoderme. Il se compose principalement de DLG-1, une kinase guanylate associée à la membrane (MAGUK) qui joue un rôle dans la formation des jonctions adhérentes, dans l'organisation du cytosquelette d'actine, et qui permet le recrutement d'autres protéines (Firestein et Rongo, 2001). Parmi ces autres protéines, on retrouve principalement AJM-1 qui s'apparente à la cinguline et à AMOTL1 – deux protéines associées aux jonctions serrées chez les vertébrés (Cox et Hardin, 2004). De façon intéressante, il a été montré que les protéines AMOT se lient à l'actine et qu'elles pourraient potentiellement jouer un rôle de senseur de la tension (Mana-Capelli *et al.*, 2014). Pour résumer, ces deux complexes, en plus d'assurer la maintenance de l'intégrité de l'hypoderme (Costa *et al.*, 1998 ; Simske *et al.*, 2003), semblent jouer un rôle important dans l'organisation du cytosquelette d'actine.

On retrouve également chez le *C. elegans* des structures qui s'apparentent aux complexes d'adhésion focale (CAFs) et aux hémidesmosomes, respectivement appelées corps denses et organites fibreux, à la différence près que seul les corps denses, liant le cytosquelette des muscles et la lamine basale située entre les muscles et l'hypoderme, sont intégrines-dépendants (Figure 1.23). Les organites fibreux, à la membrane des cellules de l'hypoderme ventral et dorsal, sont des structures liant mécaniquement les muscles à la cuticule, et qui maintiennent l'intégrité de l'hypoderme via l'ancrage des filaments intermédiaires (Francis et Waterston, 1991 ;

Hresko *et al.*, 1999 ; Bosher *et al.*, 2003 ; Hetherington *et al.*, 2011). Les corps denses, structurellement très similaires aux CAFs (Figure 1.23), sont donc présents aux membranes des cellules musculaires (Francis et Waterston, 1985). Aucun équivalent de CAF n'a encore été identifié aux membranes de l'hypoderme.

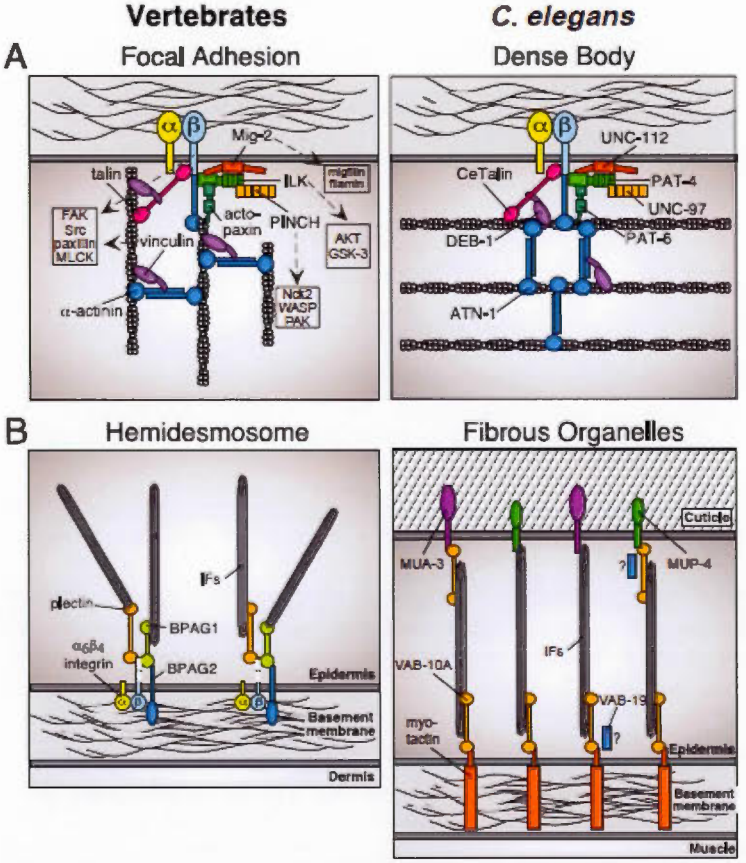

Figure 1.23 : Structure des jonctions cellule-matrice extra-cellulaire chez le *C. elegans*. (A) Structure moléculaire des complexes d'adhésion focale et des corps denses retrouvés respectivement chez les vertébrés et chez le nématode. (B) Structure moléculaire des hémidesmosomes et des organites fibreux retrouvés respectivement chez les vertébrés et chez le *C. elegans*. Figure adaptée de Cox et Hardin, 2004.

1.4.3 Régulation de l'élongation précoce par les GTPases Rho

L'élongation précoce est une étape tardive du développement embryonnaire qui est régulée par l'état de contraction des filaments d'actine-myosine dans les cellules de l'hypoderme. Au cours de cette étape, les filaments d'actine, tout comme la myosine, s'organisent en câbles circonférentiels et parallèles dans les cellules ventrales et dorsales alors qu'ils forment un réseau en maille dans les cellules latérales (Priess et Hirsh, 1986 ; Gally *et al.*, 2009). Cette organisation de l'actine filamenteuse s'accompagne d'un niveau de contraction de la myosine différent dans ces cellules. Aucun lien de cause à effet n'a cependant été établi entre ces deux observations. Le modèle accepté par la communauté scientifique au commencement de notre étude suggérait que le niveau de contraction de la myosine était élevé dans les cellules latérales au cours de l'élongation précoce, tandis que les cellules ventrales et dorsales était dans un état relâché (Priess et Hirsh, 1986 ; Piekny *et al.*, 2003 ; Ciarletta *et al.*, 2009 ; Gally *et al.*, 2009) ; ces états de contraction et de relâchement étant eux-mêmes dépendants de l'état de phosphorylation des chaines légères de la myosine.

Le principal régulateur de la contraction de la myosine est la GTPase RHO-1/RhoA. Celle-ci, lorsque liée au GTP, active la kinase LET-502/ROCK qui en retour phosphorylerait les chaines légères de myosine MLC-4 (rMLCs) (Gally *et al.*, 2009) (Figure 1.24). Une fois phosphorylées, MLC-4 provoquent la contraction des chaînes lourdes de myosine NMY-1 et NMY-2 (Piekny *et al.*, 2003). Durant l'élongation précoce, LET-502 est exprimée dans toutes les cellules de l'hypoderme (Piekny *et al.*, 2003) mais se retrouve principalement activée dans les cellules latérales. Cette restriction d'activité spatiale est due à l'activité de la GAP RGA-2 qui inhibe RHO-1 dans les cellules ventrales et dorsales (Diogon *et al.*, 2007) et à celle de la GEF RHGF-2 qui active cette GTPase dans les cellules latérales (Chan *et al.*, 2015) (Figure 1.24). Le niveau de phosphorylation des chaines légères de la myosine est également contrôlé par la phosphatase MEL-11/MYPT qui déphosphoryle MLC-4,

rendant la myosine NMY-1/2 inactive (Figure 1.24). Cette protéine est également exprimée dans toutes les cellules de l'hypoderme, cependant, son activité est inhibée dans les cellules latérales par LET-502/ROCK. En effet, la phosphorylation de MEL-11 par LET-502 entraîne sa séquestration à la membrane plasmique, où elle se retrouve incapable d'exercer son activité sur la myosine (Piekny *et al.*, 2003). Ces deux protéines, MEL-11 et LET-502, explique donc l'état d'activation de la myosine observé dans les cellules latérales *versus* dorsales/ventrales. Cependant, bien que la mutation de chacun des gènes codants ces protéines prise individuellement soit létale (Wissmann *et al.*, 1997 ; Wissmann *et al.*, 1999), le double mutant *mel-11; let-502* présente un phénotype moins pénétrant, suggérant que la contraction peut être contrôlée par une voie parallèle et redondante à la voie MEL-11/LET-502 (Piekny *et al.*, 2000).

Conformément à cette idée, il été montré que l'activation de la myosine peut être régulée par deux autres kinases, PAK-1/PAK1 et MRCK-1/MRCK, en plus de LET-502/ROCK (Gally *et al.*, 2009). Ces trois kinases agissent de manière redondante au cours de l'élongation, cependant, leur mécanisme d'action semble un peu diverger. Tout d'abord, d'après les études d'interaction génétique, MRCK-1 agirait en amont de MEL-11/MYPT, ayant ainsi un rôle d'inhibiteur de l'activité phosphatase de myosine de MEL-11 (Figure 1.24). Dans ce rôle, il assurerait la promotion de la contraction de la myosine de façon indirecte. En accord avec ceci, et bien que retrouvée dans toutes les cellules de l'hypoderme, MRCK-1 est plus fortement exprimée dans les cellules latérales, où la contraction de la myosine est la plus intense. La kinase PAK-1, quant à elle, semble avoir une action directe sur le niveau de phosphorylation de MLC-4 en parallèle de la voie MEL-11/LET-502 (Gally *et al.*, 2009) (Figure 1.24). Il est par contre important de noter que la mutation de *pak-1* seule ne présente qu'un défaut d'élongation mineure alors que le triple mutant *mel-11; let-501; pak-1* est 100% létal, suggérant que PAK-1 a un rôle prépondérant uniquement en absence de MEL-11/LET-502. Bien qu'il n'y ait pas d'évidence

formelle, l'implication de MRCK-1 et PAK-1 laisse suggérer que les GTPases CDC-42/Cdc42 et/ou CED-10/Rac sont nécessaires à l'élongation embryonnaire.

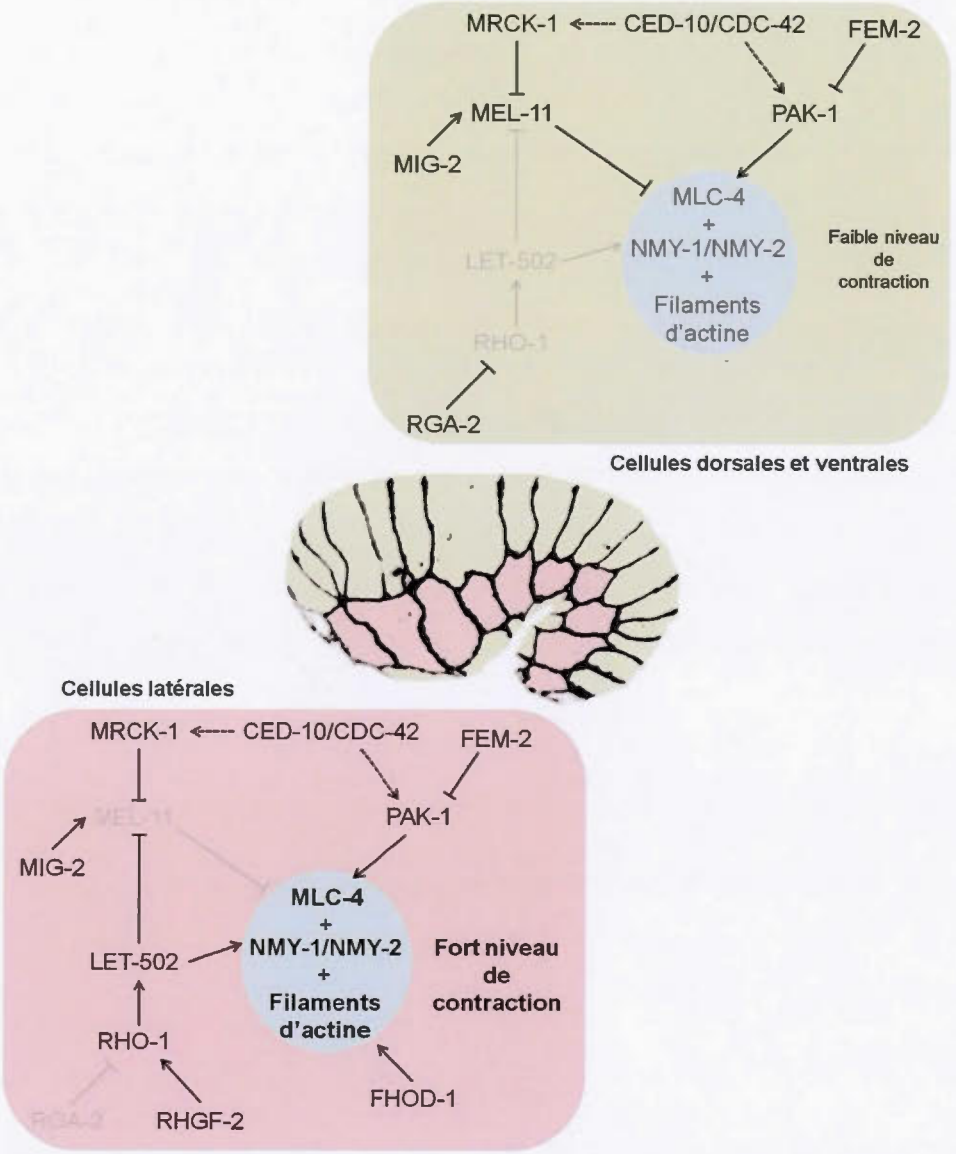

Figure 1.24 : Modèle moléculaire de l'élongation embryonnaire précoce du *C. elegans*. L'élongation précoce est dirigée par la contraction de l'actine-myosine dans les cellules latérales de l'hypoderme (en rouge), alors que les cellules dorsales et ventrales (en vert) sont dans un état relâché. Les protéines inactives ou faiblement actives sont grisées. Les flèches pointillées représentent des activations non confirmées chez le *C. elegans*. Ce modèle est basé sur la littérature de 1997 à aujourd'hui mais n'inclut pas le travail de cette thèse.

D'autres régulateurs de l'élongation précoce ont également été identifiés. On peut tout d'abord citer la Rho GTPase MIG-2 qui d'après les études d'interaction génétique se situerait en amont de LET-502 ou MEL-11 (Wissmann *et al.*, 1999 ; Piekny *et al.*, 2000). Il y a ensuite la sérine/thréonine phosphatase FEM-2/POPX2 (Piekny *et al.*, 2000). Les études d'interaction génétiques montrent que la mutation de *fem-2* n'aggrave pas la mutation de *pak-1*, suggérant que FEM-2 agirait dans la même voie que PAK-1 (Vanneste *et al.*, 2013). En outre, chez les mammifères, l'orthologue de FEM-2, POPX2, inactive l'activité kinase de PAK1 (orthologue de PAK-1) en le déphosphorylant (Koh *et al.*, 2002), ce qui confirme que FEM-2 régulerait PAK-1 dans une voie parallèle à MEL-11/LET-502. Toujours dans l'optique de décrire la régulation des filaments d'actine-myosine, la formine FHOD-1 a été montrée essentielle à la mise en place du réseau en maille dans les cellules latérales de l'hypoderme. Cette protéine, impliquée dans la nucléation de l'actine, est uniquement exprimée dans les cellules latérales et son absence se traduit par une désorganisation des microfilaments d'actine (Vanneste *et al.*, 2013). Il est suggéré que RHO-1 régulerait la structure du cytosquelette de l'actine *via* FHOD-1.

Tout cela montre qu'au moins deux voies parallèles impliquant les GTPases Rho contrôlent l'élongation embryonnaire précoce du *C. elegans via* la régulation de la structure et de la contraction des filaments d'actine-myosine. Cependant des questions subsistent, et notamment, l'importance d'avoir deux voies de signalisation contrôlant la phosphorylation des MLC, dont l'une est dominante et l'autre mineure, reste à expliquer.

1.5 PIX et PAK

1.5.1 Structure et régulation

1.5.1.1 PAK, *p21-activated protein kinases*

Les protéines PAKs ont été les premières kinases régulées par les Rho GTPases à être identifiées dans les années 1990 (Manser *et al.*, 1994). Ce sont des Sérine/Thréonine kinases dépendantes de l'activité de Rac1 et Cdc42, qui jouent un rôle central dans un nombre important de processus cellulaires incluant, entre autres, la mobilité cellulaire, la morphologie et la dynamique du cytosquelette (Bokoch, 2003). Chez l'humain, il existe six différentes formes de la protéine PAK divisées en PAK conventionnelles (ou groupe I) – PAK1-3 – et non-conventionnelles (ou groupe II) – PAK4-6. Ici, nous nous intéresserons uniquement aux PAKs conventionnelles dont l'orthologue principal chez le *C. elegans* est PAK-1, protéine étudiée dans le cadre de ce travail. Chez le *C. elegans*, deux autres protéines PAKs sont également retrouvées ; il s'agit de MAX-2 et PAK-2. L'analyse de la séquence montre que MAX-2 s'apparente aux PAKs conventionnelles ; cependant, le motif de reconnaissance du domaine SH2 et le domaine de liaison à PIX-1 sont absents (Lucanic *et al.*, 2006), et le domaine de liaison à Rac1 et Cdc42 est aussi moins conservé. La protéine PAK-2 appartient, elle, aux PAKs du groupe II (Hofmann *et al.*, 2004 ; Lucanic *et al.*, 2006).

Structurellement parlant, ces protéines sont composées d'un domaine de liaison aux GTPases Cdc42 et Rac appelé le domaine CRIB (*Cdc42/Rac-interacting binding domain*), un domaine d'auto-inhibition (AID) qui chevauche le domaine CRIB, et un domaine kinase qui confère à la protéine son activité catalytique. En outre, on retrouve trois régions riches en proline capables de lier les domaines SH3 de diverses protéines telles que Nck et Grb2, et un domaine d'interaction avec la GEF pour Cdc42/Rac, α/β-PIX (Figure 1.25A).

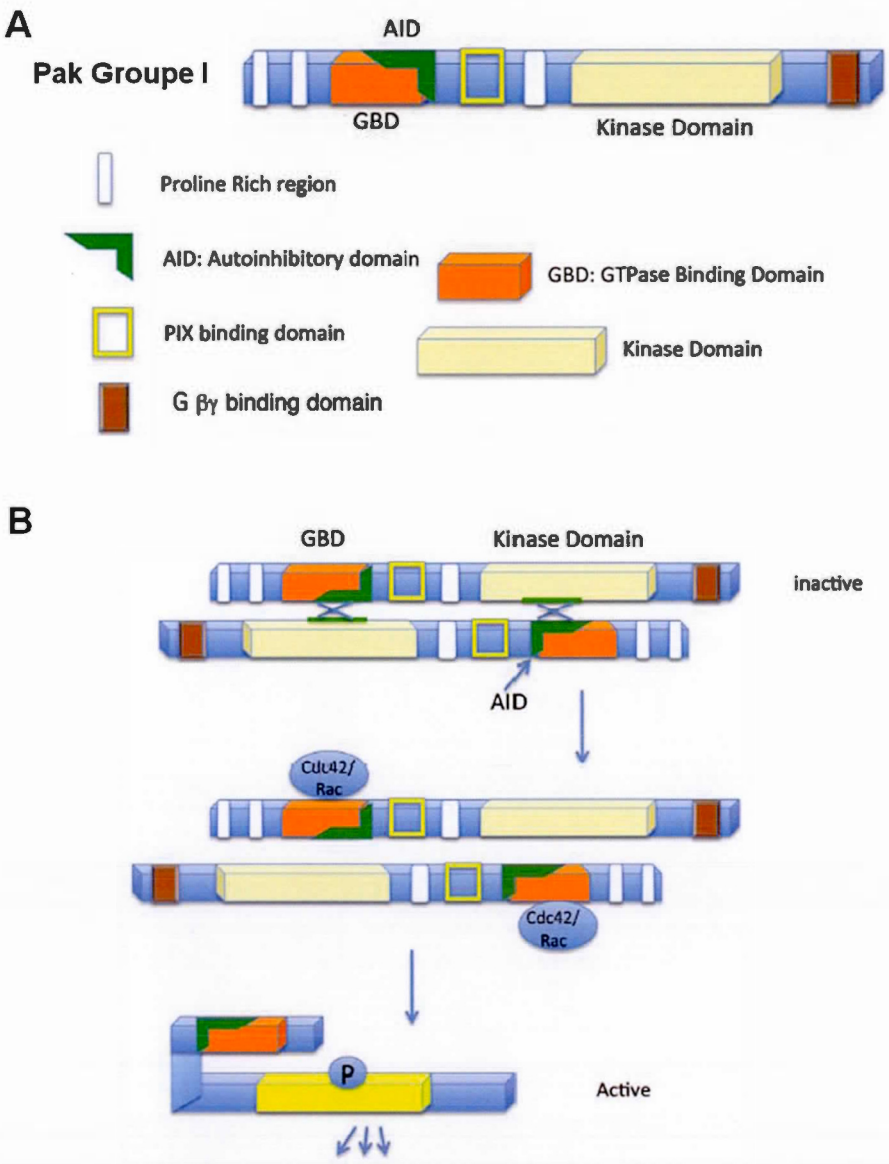

Figure 1.25 : Structure et mécanisme d'activation des PAKs conventionnelles. (A) Représentation schématique de la structure protéique et des différents domaines retrouvés dans les PAKs du groupe I (PAK1, 2 et 3). (B) Modèle du mécanisme d'activation des PAK du groupe I. Figures extraites de Rane et Minden, 2014.

Le domaine d'auto-inhibition joue un rôle important dans la régulation de PAK. Les protéines PAKs du groupe I fonctionnent en effet en dimère, où le domaine d'autoinhibition de la première protéine lie, en *trans*, le domaine kinase de la seconde, et vice et versa, provoquant leur inhibition respective (Figure 1.25B) (Parrini *et al.*, 2002). Leur activation se produit lorsque Cdc42 ou Rac1 se lie au domaine CRIB. Dès lors, cela provoque un changement de conformation du domaine d'auto-inhibition ayant pour effet de rompre l'interaction avec le domaine kinase et d'entrainer une auto-phosphorylation (Lei *et al.*, 2000). C'est l'auto-phosphorylation de la boucle d'activation du domaine catalytique qui permet le passage à un état actif, même si d'autres sites sont aussi phosphorylés (Yu *et al.*, 1998 ; Gatti *et al.*, 1999 ; Zenke *et al.*, 1999).

Bien que PAK1-3 soient considérées comme des effecteurs de Cdc42 et Rac1/2/3, il existe des mécanismes d'activation indépendants de ces GTPases. La liaison de la protéine Nck à PAK1 peut par exemple entrainer le recrutement de PAK1 à la membrane et stimuler son activité kinase (Lu *et al.*, 1997). L'activité de PAKs peut aussi être stimulée par protéolyse (Rudel et Bokoch, 1997). Par ailleurs, la Arf GAP GIT1 (*G-protein-coupled receptor kinase-interacting target 1*) peut s'associer avec PAK1-3 *via* α/β-PIX et favoriser l'activité catalytique des PAKs (Loo *et al.*, 2004). De même, α-PIX, en se liant à PAK1, est capable de l'activer, de manière GTPases dépendante ou indépendante (Daniels *et al.*, 1999). Ces trois protéines forment une plateforme PIX/GIT/PAK et jouent un rôle prépondérant dans l'adhésion focale (Zhao *et al.*, 2000). En outre, les deux phosphatases POPX1 et POPX2 ont été identifiées pour leur capacité à déphosphoryler PAK1 (Koh *et al.*, 2002) et donc l'inactiver. Ces protéines, en se liant avec β-PIX et PAKs, forment un complexe qui explique le cycle rapide d'activation et d'inactivation des PAKs (Zhan *et al.*, 2003).

1.5.1.2 PIX, *PAK-interactive exchange factor*

Les protéines PIX, aussi appelée Cool, ont été identifiées pour la première fois par leur interaction avec PAK1 (Bagrodia *et al.*, 1998 ; Manser *et al.*, 1998). Il existe au moins deux isoformes de la protéine PIX : α-PIX/Cool2/ARHGEF6, retrouvée dans les muscles, les cellules neuronales et les cellules hématopoïétiques, et β-PIX/Cool1/ARHGEF7 exprimée de façon ubiquitaire. C'est cette dernière qui est l'orthologue de PIX-1 chez le *C. elegans*. La protéine β-PIX, tout comme PIX-1, possède une activité GEF envers Cdc42 et Rac due à la présence des domaines DH (*Dbl homology* – domaine catalytique) et PH (*Pleckstrin homology* – domaine de recrutement aux membranes) en tandem (Figure 1.26). Divers domaines d'interaction avec d'autres protéines sont également présents au sein de la protéine (Figure 1.26). Parmi ces domaines, on retrouve un domaine SH3 qui lui permet de se lier à PAK1-3 (Bagrodia *et al.*, 1998 ; Manser *et al.*, 1998), à l'ubiquitine ligase c-Cbl (Flanders *et al.*, 2003) et à Rac1 (ten Klooster *et al.*, 2006), un domaine d'interaction à GIT1/2 (GBD ; *GIT binding domain*) (Turner *et al.*, 1999 ; Zhao *et al.*, 2000), un motif *coiled-coil* (CC) permettant la dimérisation (Kim *et al.*, 2001), une région riche en proline (PR) favorisant l'interaction avec les phosphatases POPX1 et POPX2 (Koh *et al.*, 2002), et un motif de liaison au domaine PDZ pour l'interaction avec Scribble et Shank (Park *et al.*, 2003 ; Audebert *et al.*, 2004). Ces deux dernières protéines jouent un rôle dans l'endocytose et l'exocytose des récepteurs et dans le maintien de la polarité de cellules épithéliales (Bilder et Perrimon, 2000 ; Legouis *et al.*, 2000 ; Park *et al.*, 2003 ; Audebert *et al.*, 2004 ; Lahuna *et al.*, 2005 ; Zhang, Maximov, *et al.*, 2005). Toutes ces interactions possibles jouent directement sur la localisation de α/β-PIX et sur leur fonction. Par ailleurs, l'activité GEF de β-PIX est inhibée par la présence d'un motif T1 au sein de la protéine, et cette inhibition peut être levée *via* la phosphorylation de la tyrosine 442 par Src. Cette phosphorylation, qui active l'activité GEF de β-PIX envers Cdc42, peut entrainer la formation d'un complexe Cdc42/β-PIX/Cbl qui joue un rôle important dans le contrôle de la croissance

cellulaire (Feng *et al.*, 2006), et favorise également la migration et l'invasion cellulaire (Feng *et al.*, 2010).

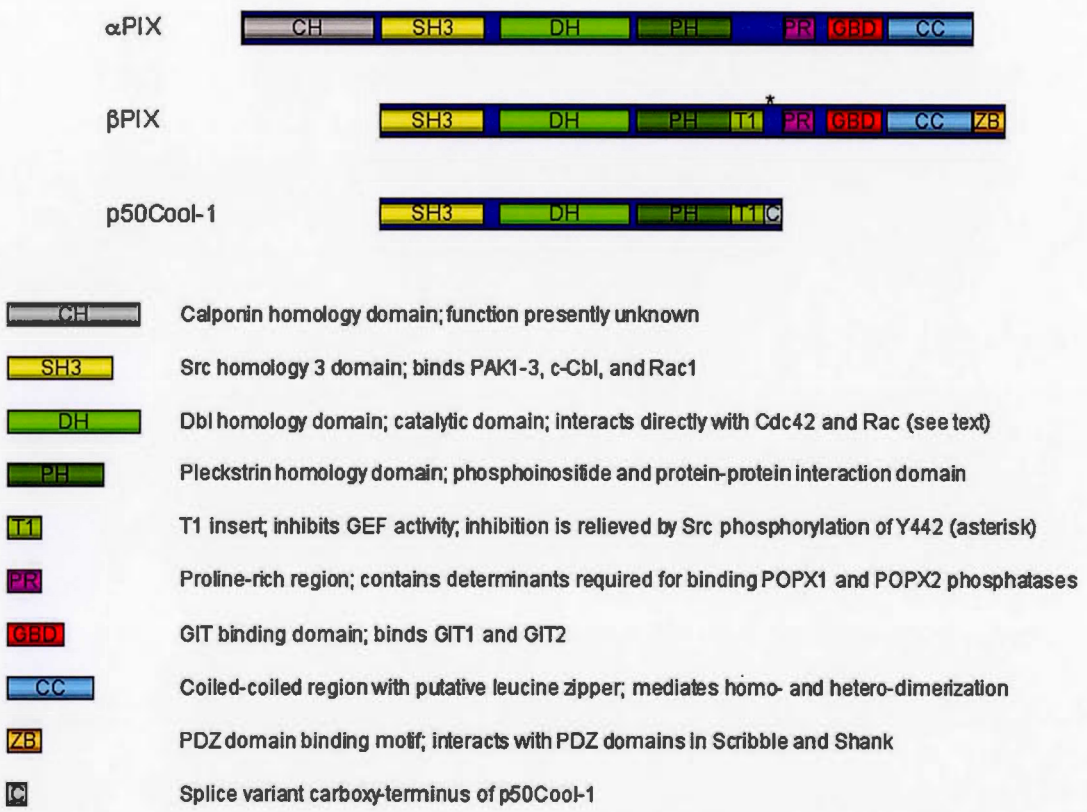

Figure 1.26 : Structure des protéines PIX. Représentation schématique et comparaison de la structure protéique et des différents domaines de α-PIX, β-PIX et p50Cool-1. Figure extraite de Frank et Hansen, 2008.

1.5.2 Fonctions du complexe β-PIX–PAK1 dans les processus de morphogenèse

Nous venons de voir que les protéines β-PIX et PAK1 interagissent ensemble, formant un complexe capable de réguler spatio-temporellement l'activité des GTPases Cdc42 et Rac1. Ensemble ces protéines régulent de nombreux processus cellulaires dont la dynamique des membranes, le réarrangement du cytosquelette d'actine et le remodelage des jonctions adhérentes. Ces trois mécanismes sont étroitement couplés aux mécanismes morphogéniques et sont donc importants dans le cadre de cette étude. Nous avons, par ailleurs, évoqué plus haut la fonction de PAK1 sur la contraction de la myosine (*cf* section 1.3.3.3) et nous ne reviendrons pas sur cette fonction dans cette partie.

La fonction de β-PIX–PAK1 la mieux caractérisée à ce jour est le rôle dans la migration cellulaire et notamment au niveau des complexes d'adhésion focale (CAFs). Dans ce contexte, nous nous intéresserons à décrire l'assemblage de ces CAFs ainsi que leur maturation tout en intégrant le rôle de β-PIX–PAK1. Puis, nous aborderons un rôle nouveau conféré à ces deux protéines : le remodelage des jonctions apicales.

1.5.2.1 Les complexes d'adhésion focale (CAFs) et la migration cellulaire

Nous avons vu précédemment que la migration cellulaire joue un rôle important dans la morphogenèse et qu'elle dépend de contacts entre la cellule et la MEC lors de la formation de lamellipodes. Les principaux médiateurs de ce contact cellule-MEC sont les intégrines. Ces intégrines sont formées d'un hétérodimère composé d'une chaine α et d'une chaine β, et font partie intégrante d'un complexe multimérique, composé d'au moins 180 protéines (Zaidel-Bar *et al.*, 2007 ; Zaidel-Bar et Geiger, 2010), qui les connectent au cytosquelette d'actine (Burridge *et al.*, 1988 ; Jockusch *et al.*, 1995). Parmi ces contacts cellule-MEC dépendants des intégrines, trois groupes

d'adhésion, différant par leur niveau de maturation, se distinguent. Ce sont respectivement les adhésions naissantes, les complexes focaux et les adhésions focales (Figure 1.27).

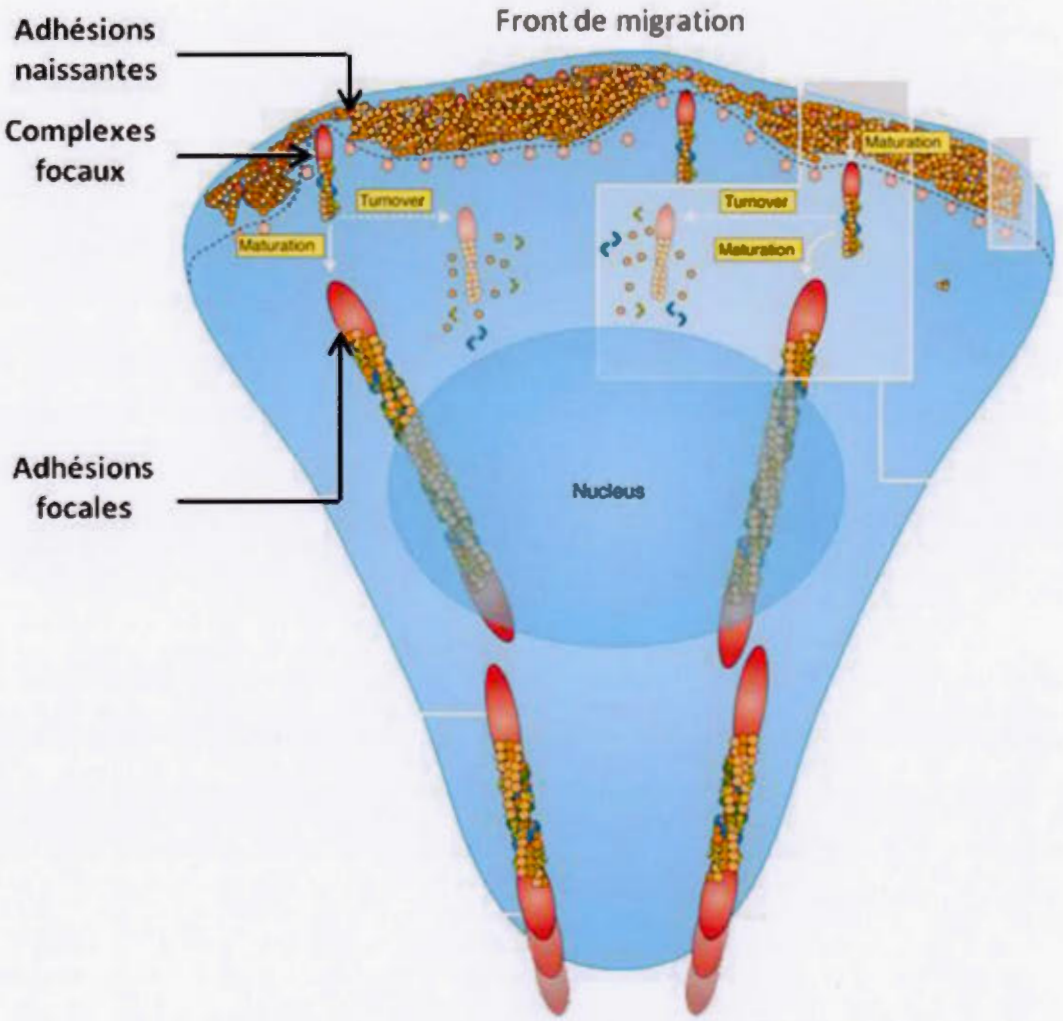

Figure 1.27 : Les complexes d'adhésion cellule-matrice extracellulaire dépendants des intégrines. Représentation schématique d'une cellule en migration (front de migration en haut) présentant les différents complexes d'adhésion cellule-MEC en fonction de leur niveau de maturation. Sont représentés les adhésions naissantes, les complexes focaux et les adhésions focales. La ligne pointillée sépare le lamellipodium (au dessus de la ligne) du corps cellulaire (en dessous de la ligne). Figure adaptée de Vicente-Manzanares et Horwitz, 2011.

Les adhésions naissantes se forment initialement à l'avant du front de migration dans une région appelée le lamellipodium (Cramer *et al.*, 1997 ; Ponti *et al.*, 2004). Ces adhésions naissantes sont des petites adhésions transitoires dont le cycle d'assemblage/désassemblage est très rapide (Zaidel-Bar *et al.*, 2003 ; Nayal *et al.*, 2006 ; Alexandrova *et al.*, 2008 ; Choi *et al.*, 2008) et qui génèrent la force de propulsion nécessaire à la migration cellulaire (Beningo *et al.*, 2001). La formation de ces adhésions naissantes requiert une activité de polymérisation de l'actine mais ne dépend pas de la contraction de la myosine (Vicente-Manzanares *et al.*, 2007 ; Alexandrova *et al.*, 2008 ; Choi *et al.*, 2008). Dès que ces adhésions se retrouvent à l'arrière du lamellipodium, elles peuvent soit se désassembler, soit subir un processus de maturation en complexes focaux. Ces derniers sont des complexes plus larges que les précédents et, bien que structurellement similaires aux adhésions naissantes, deviennent dépendants de la contraction de la myosine (Choi *et al.*, 2008). Ils peuvent également soit se désassembler, soit croitre pour former des adhésions focales. Ces adhésions focales sont de gros complexes d'adhésion matures qui, sous l'action de la contraction de la myosine, ralentissent le flux d'actine rétrograde normalement observé dans les lamellipodes (Guo et Wang, 2007 ; Alexandrova *et al.*, 2008), et inhibe ainsi la migration cellulaire (Burnette *et al.*, 2011). Le recyclage rapide des adhésions naissantes et des complexes focaux favorisent, quant à lui, la migration cellulaire. C'est dans ce processus d'assemblage et de désassemblage que β-PIX et PAK1 jouent un rôle important.

L'assemblage des adhésions naissantes nécessite la présence de diverses protéines phosphorylées telles que la FAK (*focal adhesion kinase*), Src, la paxilline, la p130CAS, la vinculine, etc, (Kirchner *et al.*, 2003 ; Ballestrem *et al.*, 2006), afin d'assurer le recrutement de protéines additionnelles et la polymérisation de l'actine (Figure 1.28).

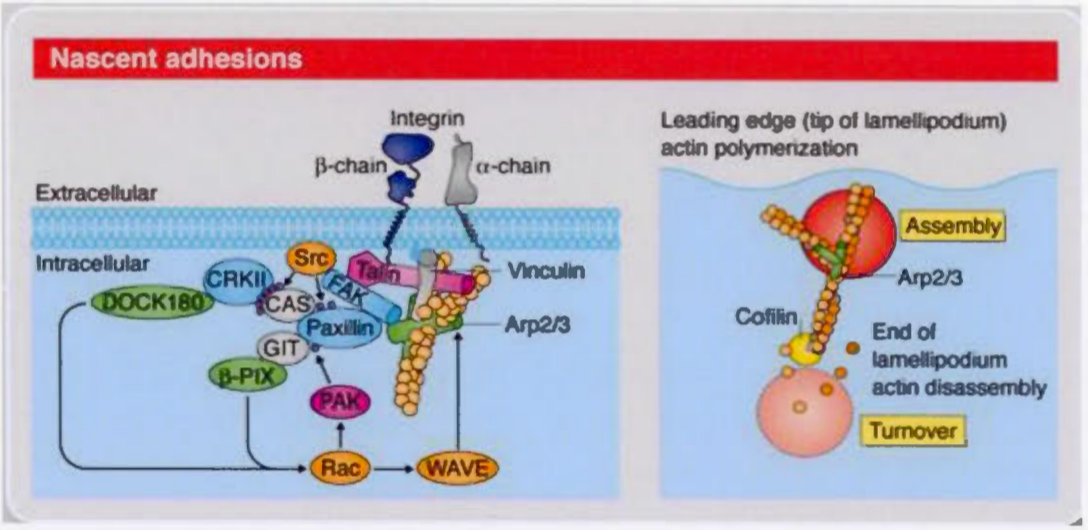

Figure 1.28 : Structure moléculaire des adhésions naissantes. Représentation schématique de la structure et de la composition moléculaire des adhésions naissantes (à gauche). A droite est représenté le rôle de la cofiline sur le turnover des adhésions naissantes. Figure adaptée de Vicente-Manzanares et Horwitz, 2011.

Il a en effet été montré que la phosphorylation de p130CAS est un évènement initiateur au recrutement et à l'activation de Rac1, et à la formation des lamellipodes découlant de cette activation (Sharma et Mayer, 2008). Au niveau des complexes naissants, la paxilline est également phosphorylée par PAK sur la sérine 273 (Nayal *et al.*, 2006). Cette phosphorylation entraine le recrutement de la protéine adaptatrice GIT1, qui se retrouve ciblée à la bordure protrusive (Manabe *et al.*, 2002). GIT1 recrute ensuite β-PIX qui en retour s'associe à la forme active de la protéine PAK1. A ce niveau, β-PIX peut être phosphorylée par FAK, augmentant l'affinité de β-PIX pour Rac1 (Chang *et al.*, 2007) et permettant ainsi de localiser l'activité de la GTPase Rac1 au front de migration (Nishiya *et al.*, 2005 ; Zhang, Webb, *et al.*, 2005 ; Nayal *et al.*, 2006). Le recrutement de β-PIX, PAK1 et Rac1 au front de migration est également assuré par la protéine de polarité Scribble (Osmani *et al.*, 2006 ; Dow *et al.*, 2007 ; Nola *et al.*, 2008). L'activité locale de Rac1 entraine ensuite la

polymérisation de l'actine au niveau des complexes naissants *via* WAVE et le complexe de nucléation ARP2/3 (Figure 1.28). Cette polymérisation de l'actine est également favorisée par PAK dont l'activité est antagoniste à l'activité de dépolymérisation de l'actine par la cofiline (Delorme *et al.*, 2007).

Les protéines β-PIX et PAK1 interviennent donc dans l'assemblage des adhésions naissantes au niveau du lamellipodium. Cependant, afin d'assurer le bon déroulement de la migration cellulaire, le complexe β-PIX–PAK1 joue également un rôle important dans l'assemblage/désassemblage des CAFs (Figure 1.29).

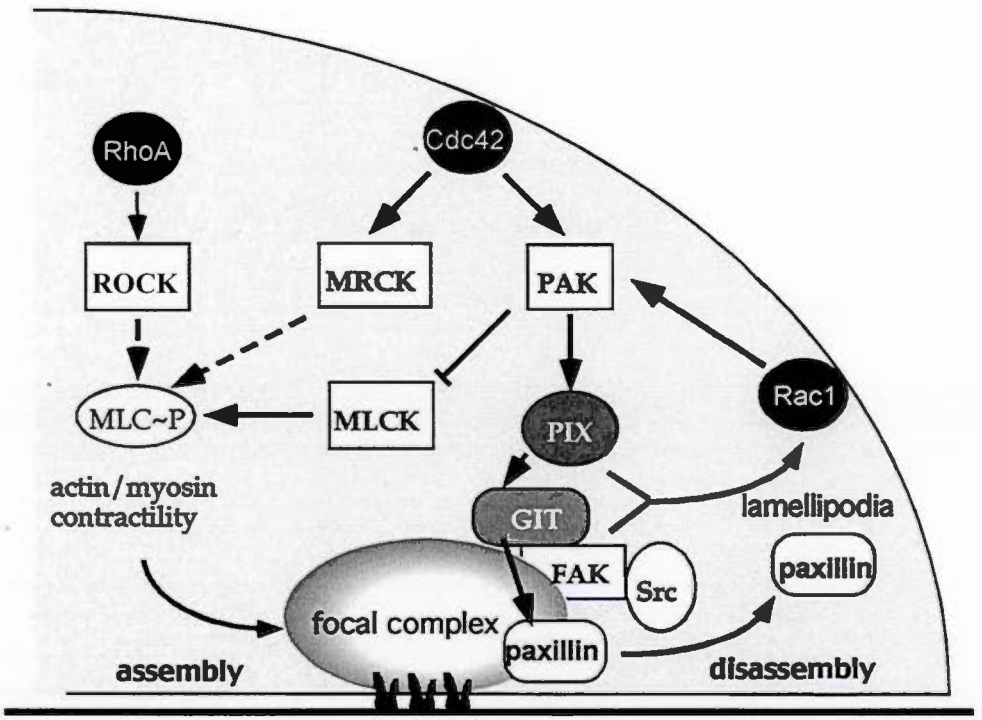

Figure 1.29 : Modèle moléculaire de l'assemblage et du désassemblage des CAFs. L'assemblage et la maturation des complexes focaux est facilité par la contraction de la myosine induite par RhoA/ROCK, Cdc42/MRCK et MLCK. L'activation du complexe PIX/GIT/PAK dissocie la paxilline des complexes focaux, ce qui entraine leur désassemblage. Le désassemblage des CAFs peut aussi être induit par l'inhibition de la contraction des filaments d'actine-myosine par PAK, en aval de Cdc42 et Rac1. Figure extraite de Zhao *et al.*, 2000.

Plusieurs études montrent en effet que le complexe PIX/GIT/PAK favorise la libération de la paxilline, déstabilisant ainsi les adhésions focales et favorisant la migration (Zhao *et al.*, 2000 ; Nayal *et al.*, 2006 ; Hammer *et al.*, 2015). Il est également montré que le recyclage des CAFs peut se produire *via* l'inhibition de la phosphorylation de la MLC par PAK1, diminuant ainsi la contraction de la myosine (Zhao *et al.*, 2000 ; Delorme-Walker *et al.*, 2011). Une telle diminution de la contraction de la myosine favorise le recrutement de β-PIX au niveau des complexes d'adhésion, qui lui-même augmente localement l'activité de Rac1 et favorise ainsi la migration cellulaire (Kuo *et al.*, 2011). Ce dernier point décrit parfaitement l'antagonisme qui existe entre l'effecteur spécifique de RhoA, ROCK, et la protéine β-PIX au niveau des CAFs. En effet, lorsque ROCK est actif, il entraine une contraction de la myosine au niveau des adhésions focales, et son inhibition, ou l'inhibition de la myosine II par la blebbistatine, entraine le recrutement de β-PIX à ces mêmes adhésions afin d'engendrer leur déstabilisation et leur recyclage (Kuo *et al.*, 2011).

Dans le contexte que nous avons décris ci-dessus, le complexe β-PIX-PAK1 a donc une activité pro-migratoire en favorisant le recyclage des CAFs et en inhibant leur maturation. Récemment, il a été montré qu'en plus de ce rôle dans le roulement des CAFs et dans la polarité migratoire, β-PIX a un rôle dans la génération de stress mécanique induisant la migration collective. En effet, il a été montré dans des myoblastes de souris que la présence de P-cadhérine aux jonctions cellule-cellule entraine le recrutement de β-PIX à ces jonctions. Ce recrutement spécifique de β-PIX provoque l'activation locale de la GTPase Cdc42, induisant de ce fait une augmentation de la tension mécanique intra et intercellulaire qui coordonne la migration collective des cellules (Plutoni *et al.*, 2016).

1.5.2.2 B-PIX et PAK1 dans la formation et le remodelage des jonctions apicales.

Depuis quelques années maintenant, il est admis que les intégrines et les cadhérines communiquent et coordonnent leurs fonctions afin de réguler les mécanismes d'adhésion cellulaire, de migration et de contraction. Il n'est donc pas étonnant de voir que ce sont, en partie, les mêmes protéines qui régulent à la fois le remodelage des intégrines et celui des jonctions apicales. Pour illustrer ces propos, dans les expériences de fermeture de brèche (*wound healing*), il a été montré que β-PIX et PAK1 joue un rôle primordial dans la répression de la migration cellulaire et de la prolifération lorsque les cellules entrent en contact ; c'est ce que l'on appelle l'inhibition de contact. En effet, lorsque les cellules migrent, β-PIX et PAK1 se localisent au front de migration, comme nous l'avons vu dans la section précédente. Et lorsque que les cellules entrent en contact, ces deux protéines sont redistribuées au niveau des contacts cellule-cellule, inhibant la migration et la prolifération cellulaire (Zegers *et al.*, 2003). Cette redistribution de β-PIX et PAK1 aux jonctions cellule-cellule est dépendante des cadhérines (Liu *et al.*, 2010) et de Scribble (Frank *et al.*, 2012), et a pour conséquence d'entrainer la maturation des CAFs et d'empêcher l'apoptose des cellules épithéliales confluentes (Frank *et al.*, 2012). La formation du complexe Scribble, associé à β-PIX et GIT1, est également importante pour la polarité épithéliale. Chez la drosophile, il a été montré que la mutation de Scribble/Scrib provoque une perte de polarité épithéliale, résultant d'une mauvaise localisation des jonctions adhérentes, accompagnée d'une perte de l'intégrité tissulaire (Bilder *et al.*, 2000). Dans les cellules épithéliales mammifères, il a été montré que Scribble intéragit avec la β-caténine et les E-cadhérines et qu'elle stabilise les jonctions adhérentes (Navarro *et al.*, 2005 ; Yates *et al.*, 2013). La protéine β-PIX pourrait jouer un rôle dans ce contexte. En effet, lorsque liée au complexe Scribble, elle activerait la GTPase Cdc42 (Osmani *et al.*, 2006) qui elle-même agirait sur le complexe de polarité Par entrainant ultimement une activation de Rac1, et permettant l'initiation et la maintenance de la polarité épithéliale (Joberty *et*

al., 2000 ; Nishimura *et al.*, 2005 ; Ngok *et al.*, 2014). Il est également montré que Scribble assure la stabilité des complexes E-cadhérine en inhibant l'endocytose de ces jonctions (Qin *et al.*, 2005 ; Lohia *et al.*, 2012). Bien que β-PIX et PAK1 jouent également un rôle dans le maintien des jonctions adhérentes, comme cela a été montré dans les expériences de fermeture de brèche (Zegers *et al.*, 2003 ; Liu *et al.*, 2010 ; Frank *et al.*, 2012) et durant l'épibolie du poisson zèbre (Tay *et al.*, 2010), leur rôle dans l'endocytose des jonctions adhérentes est opposé à ce maintien. En effet, au cours de la formation des glandes salivaires de *D. melanogaster*, PAK1 active l'endocytose des E-cadherines, permettant de définir au final la forme et la taille de la lumière de ces glandes (Pirraglia *et al.*, 2010). Dans un contexte non-épithélial cette fois, β-PIX et PAK1 ont été montrées essentielles à l'induction de la perméabilité vasculaire *via* l'endocytose des VE-cadherines (Gavard et Gutkind, 2006 ; Stockton *et al.*, 2007). Ces études montrent donc que β-PIX et PAK1 favorisent l'endocytose des jonctions adhérentes.

La fonction de β-PIX et PAK1 sur le remodelage des jonctions adhérentes reste controversée, certaines études montrant que ce complexe déstabilise les jonctions cellule-cellule alors que d'autres sont en faveur d'un maintien de ces jonctions. Il est donc important de ne pas généraliser le rôle de ces protéines et d'étudier au cas par cas suivant le type et le contexte cellulaire.

1.5.3 Fonctions de β-PIX/PIX-1 et PAK1/PAK-1 chez *C. elegans*

Les protéines β-PIX et PAK1 sont très bien conservées chez *C. elegans*, et sont respectivement appelées PIX-1 et PAK-1. Ici, nous allons décrire les différentes fonctions de PAK-1 et PIX-1 connues à ce jour.

Comme suggérés par la localisation d'un rapporteur GFP fusionné à PAK-1 (Iino et Yamamoto, 1998), cette protéine semble avoir plusieurs rôles chez *C. elegans*. Elle a en effet été retrouvé au sein des neurones moteurs, dans les cellules musculaires, dans

les gonades et dans les cellules de l'hypoderme des embryons en cours d'élongation (Chen *et al.*, 1996 ; Iino et Yamamoto, 1998). Il a en effet été montré que PAK-1 agit sur l'orientation des axones en aval de CED-10/Rac1 et MIG-2/RhoG (Lucanic *et al.*, 2006 ; Quinn *et al.*, 2008), ainsi que dans la migration neuronale (Kennedy *et al.*, 2013). Elle a aussi été impliquée dans l'élongation des gonades au sein d'un complexe PIX-1/GIT-1/PAK-1 qui agit indépendamment des GTPases et en parallèle d'une voie de signalisation dépendante des GTPases (Lucanic et Cheng, 2008 ; Peters *et al.*, 2013). PIX-1 a également un rôle dans la formation des protrusions et dans la migration des neuroblastes, de façon redondante à la GEF UNC-73/Trio (Dyer *et al.*, 2010). Cependant les rôles de PIX-1 et PAK-1 qui nous intéressent plus particulièrement sont ceux qui ont été examinés au cours de la morphogenèse de l'épiderme.

En 1996, Chen et ses collègues ont amorcé le processus de compréhension de la protéine PAK-1 (ou CePAK) au cours de la morphogenèse embryonnaire du *C. elegans* (Chen *et al.*, 1996). Au cours de leurs investigations, ils ont montré que, à l'instar de la protéine mammifère, PAK-1 est capable de lier les formes actives des GTPases Rac-1/CED-10 et Cdc42/CDC-42. Leur étude a également mis en avant que *pak-1* est largement exprimée pendant l'embryogenèse du nématode et que la protéine se retrouve localisée spécifiquement aux jonctions apicales se situant entre les cellules de l'hypoderme des embryons au cours de l'élongation précoce (Chen *et al.*, 1996). Cette localisation est en accord avec le rôle conféré à PAK-1 au cours de cette étape. En effet, pendant l'élongation précoce, l'activation de PAK-1 entraine la phosphorylation de chaines légères de myosine, en parallèle de LET-502/ROCK et MRCK-1/MRCK, ayant pour effet la contraction de la myosine II, processus essentiel au déroulement de cette étape (Gally *et al.*, 2009). Toujours au cours de l'embryogenèse, PAK-1 est également impliquée dans la mécano-tranduction entre les muscles et l'hypoderme au cours de l'élongation tardive (Zhang *et al.*, 2011). A ce stade, PAK-1, tout comme la protéine PIX-1, est localisée au niveau de structures

trans-épidermales appelées hémidesmosomes (HDs) (Chen *et al.*, 1996 ; Zhang *et al.*, 2011). Sous l'influence de la tension musculaire, la protéine adaptatrice GIT-1 est maintenue aux HDs où elle interagit supposément avec PIX-1 qui en retour active CED-10/Rac1. Cette activation de CED-10/Rac1 entraine elle-même l'activation de PAK-1. PAK-1 phosphoryle ensuite les filaments intermédiaires des HDs, ce qui entraine la maturation des HDs et favorise l'élongation (Zhang *et al.*, 2011).

1.6 Problématique et hypothèses de travail

L'étude de la morphogenèse des épithéliums utilisant des cellules mammifères en culture a été extrêmement utile pour identifier les mécanismes moléculaires contrôlant la déformation cellulaire et la régulation des complexes d'adhérence lors de ces déformations (Schock et Perrimon, 2002b). Cependant, ces études ne permettent pas de comprendre la régulation spatiotemporelle de ces mécanismes, et particulièrement ceux contrôlés par les GTPases Rho lors de la morphogenèse de tissus épithéliaux dans le contexte d'un organisme multi-cellulaire. Le but des recherches effectuées dans le laboratoire du Dr Jenna est d'acquérir une telle compréhension. Ainsi l'objectif général de mon doctorat vise à étudier le rôle des GTPases Rho au cours de l'élongation embryonnaire précoce du *Caenorhabditis elegans*, et plus particulièrement caractériser la voie de signalisation impliquant la GEF et l'effecteur spécifique de Rac1 et Cdc42, PIX1/PIX-1 et PAK1/PAK-1.

Au cours de l'élongation embryonnaire précoce du *C. elegans*, PAK-1 a été décrite comme une kinase phosphorylant les chaines légères de myosine et favorisant ainsi la contraction de l'appareil actine-myosine ; cependant peu de choses est connu quant à ses partenaires et son mécanisme d'action à ce stade. Durant l'élongation tardive, par contre, PAK-1 agit au niveau des hémidesmosomes avec PIX-1. Au sein du laboratoire, des études préliminaires ont montré que les mutants *pix-1* présentent une

morphologie similaire aux mutants *pak-1* et nous nous demandons si ces protéines PIX-1 et PAK-1 agissent ensemble au cours de la morphogenèse du *C. elegans*, et plus particulièrement pendant l'étape d'élongation embryonnaire précoce.

La première partie de cette thèse vise donc à décrire le rôle général de *pix-1* et *pak-1* au cours de l'élongation embryonnaire précoce du *C. elegans*. Nous montrons que *pix-1* contrôle l'élongation précoce dans la même voie que *pak-1* et en parallèle de la voie *mel-11/let-502*. Nous avons ensuite développé de nouvelles méthodes d'analyse de la morphogenèse embryonnaire afin de caractériser le rôle de ces deux voies. Ainsi, nous démontrons que ces deux voies agissent différemment sur la morphogenèse le long de l'axe antéro-postérieur de l'embryon. En effet, *let-502* semble réduire autant la tête que la queue de l'embryon alors que *pix-1* et *pak-1* agissent principalement sur la réduction de la tête. Nous observons également que PIX-1 est exprimée dans les cellules de l'hypoderme mais que son expression doit être réduite dans les cellules dorsales postérieures pour permettre une élongation efficace. Ces données suggèrent donc que l'élongation embryonnaire précoce est contrôlée par deux voies parallèles dont le rôle est régulé le long de l'axe antéro-postérieur et dorso-ventral.

Dans une seconde partie, nous avons caractérisé plus en détail le rôle de la voie *let-502* et de la voie *pix-1/pak-1* au cours de l'élongation précoce. Nous avons pour cela développé de nouvelles techniques d'imagerie confocale et d'analyses pour étudier la morphogenèse, non plus à l'échelle de l'organisme entier, mais à l'échelle cellulaire. En mesurant la réduction/élongation de taille des jonctions apicales, l'anisotropie des jonctions, la densité des clusters jonctionnels et la forme des protrusions, nous montrons qu'un antagonisme existe entre la voie *let-502* (*Rho-like*) et *pix-1/pak-1* (*Rac-like*) à l'échelle cellulaire. Cela se traduit par la domination de la voie *Rho-like* dans les cellules latérales antérieures, et par la domination de la voie *Rac-like* dans les cellules dorsales antérieures. Nous montrons pour la première fois une hétérogénéité cellule-cellule contrôlée par l'antagonisme RhoA/Rac1 au cours d'un évènement de

morphogenèse épithéliale, et nous montrons également que cette hétérogénéité est nécessaire à une morphogenèse embryonnaire correcte.

CHAPITRE II

pix-1 CONTRÔLE L'ÉLONGATION EMBRYONNAIRE PRÉCOCE DU *CAENORHABDIDTIS ELEGANS* EN PARALLÈLE DE *mel-11* ET *let-502*.

Le travail de ce chapitre a été publié, en avril 2014, de la revue *PLoS One* 9(4) : e94684. (Voir la version publiée en Annexe A)

Contribution des auteurs :

Emmanuel Martin : conception, design, acquisitions, analyse et interprétation des résultats, rédaction du manuscrit, montage des figures et révision de l'article ; expériences : mesure de la taille des embryons à la fin de l'élongation précoce (Figure 1D), mesure des ratios tête/queue (Figure 2 et 3D), croisements des transgéniques, toute l'imagerie confocale et les quantifications qui s'y rapportent (Figure 4, 5, 6). *Sharon Harel* : conception, design, acquisitions, analyse et interprétation des résultats, rédaction du manuscrit, montage des figures ; expériences : analyse phénotypique des larves L1 des différents mutants (Figure 1B et 3C), mesure du temps d'élongation précoce (Figure 1C), croisements et interactions génétiques (Table 2). *Bernard Nkengfac* : Interactions génétiques (Table 1 et 2). *Karim Hamiche* : génération des vers transgéniques sajEx1[*pix-1p ::pix-1 ::gfp* + *rol-6*], sajIs2[*pix-1p ::pix-1 ::gfp* + *unc-119R*] ; expériences : létalité embryonnaire Table 1. *Mathieu Neault* : acquisition des larves L1 des différents mutants (Figure 1A et 3A et B). *Sarah Jenna* : conception, design, analyse et interprétation des résultats, rédaction du manuscrit, montage des figures et révision de l'article.

NOTE : Les références de l'article sont incluses dans la bibliographie générale.

2.1 Résumé

Le changement de forme des cellules est un mécanisme crucial pour le développement des métazoaires. Au cours de l'embryogenèse du *Caenorhabditis elegans* par exemple, les cellules épithéliales changent de forme pour permettre à des embryons ovoïdes de se transformer en larves. Ce processus est divisé en deux phases : l'élongation précoce et tardive. L'élongation précoce implique la contraction des câbles circonférentiels d'actine dans les cellules latérales de l'épiderme (ou hypoderme). Les gènes régulant l'élongation précoce sont répartit en deux voies de signalisation parallèles. La première voie implique un effecteur spécifique de *rho-1*/RhoA, *let-502*/ROCK, et la sous-unité régulatrice de la phosphatase de myosine *mel-11* ; alors que dans la seconde voie, on retrouve un effecteur spécifique de CDC42 et Rac, *pak-1*. L'élongation tardive est, elle, menée par la mécano-transduction entre les cellules ventrales et dorsales de l'hypoderme et les muscles sous-jacents. Elle implique une « *Guanine-nucleotide Exchange Factor* » (GEF) spécifique de Rac et CDC42 *pix-1*, la GTPase *ced-10*/Rac, et *pak-1*. Dans cette étude, nous montrons que *pix-1* contrôle l'élongation précoce en parallèle de *let-502/mel-11*, comme cela a déjà été montré pour *pak-1*. Nous montrons aussi que *pix-1*, *pak-1* et *let-502* contrôlent la vitesse d'élongation ainsi que la morphologie antéropostérieure des embryons. Plus spécifiquement, *pix-1* et *pak-1* contrôle la largeur de la tête, alors que *let-502* contrôle à la fois la largeur de la tête et de la queue. Ces résultats suggèrent que la fonction de *let-502* est requise tout au long de l'axe antéropostérieur de l'embryon, alors que la fonction de *pix-1* et *pak-1* est principalement requise dans la partie antérieure de l'embryon. Allant dans le sens de cette hypothèse, nous montrons enfin qu'un faible niveau d'expression de *pix-1* dans les cellules dorsales postérieures de l'hypoderme est requis pour permettre une vitesse d'élongation normale au cours de l'élongation précoce.

Manuscrit

pix-1 CONTROLS EARLY ELONGATION IN PARALLEL WITH *mel-11* AND *let-502* IN *CAENORHABDITIS ELEGANS.*

Emmanuel Martin*#, Sharon Harel*#, Bernard Nkengfac*, Karim Hamiche*, Mathieu Neault*, and Sarah Jenna*

Department of Chemistry, Pharmaqam, Biomed, Université du Québec à Montréal (UQÀM), Montréal, Québec, H3C 3P8, Canada

* Corresponding Author: jenna.sarah@uqam.ca

2.2 Abstract

Cell shape changes are crucial for metazoan development. During *Caenorhabditis elegans* embryogenesis, epidermal cell shape changes transform ovoid embryos into vermiform larvae. This process is divided into two phases: early and late elongation. Early elongation involves the contraction of filamentous actin bundles by phosphorylated non-muscle myosin in a subset of epidermal (hypodermal) cells. The genes controlling early elongation are associated with two parallel pathways. The first one involves the *rho-1*/RHOA-specific effector *let-502*/Rho-kinase and *mel-11*/myosin phosphatase regulatory subunit. The second pathway involves the CDC42/RAC-specific effector *pak-1*. Late elongation is driven by mechanotransduction in ventral and dorsal hypodermal cells in response to body-wall muscle contractions, and involves the CDC42/RAC-specific Guanine-nucleotide Exchange Factor (GEF) *pix-1*, the GTPase *ced-10*/RAC and *pak-1*.

In this study, *pix-1* is shown to control early elongation in parallel with *let-502/mel-11,* as previously shown for *pak-1*. We show that *pix-1*, *pak-1* and *let-502* control the rate of elongation, and the antero-posterior morphology of the embryos. In particular, *pix-1* and *pak-1* are shown to control head, but not tail width, while *let-502* controls both head and tail width. This suggests that *let-502* function is required throughout the antero-posterior axis of the embryo during early elongation, while *pix-1/pak-1* function may be mostly required in the anterior part of the embryo. Supporting this hypothesis we show that low *pix-1* expression level in the dorsal-posterior hypodermal cells is required to ensure high elongation rate during early elongation.

Keywords: *Caenorhabditis elegans*, morphogenesis, elongation, PIX, PAK, ROCK

2.3 Introduction

In mammals, the CDC42/RAC-specific Guanine-nucleotide exchange factor (GEF) α/β-PIX and the CDC42/RAC-specific effector kinase PAKs were shown to control cell migration, cell polarity, cytoskeleton remodeling and focal adhesion complex assembly/disassembly dynamics (Frank et Hansen, 2008). Their involvement in the control of epithelium morphogenesis and migration of epithelial sheets has also been recently established in mammals (Hunter et Zegers, 2010), and in model organisms such as *Drosophila melanogaster* and *Caenorhabditis elegans* (Harden *et al.*, 1999 ; Gally *et al.*, 2009 ; Zhang *et al.*, 2011). Study of epithelial morphogenesis in *C. elegans* appears as an excellent model to better understand the function of α/β-PIX and PAKs during complex morphogenic events in living organisms.

In the nematode *C. elegans,* embryonic elongation involves the extension of the embryo along its longitudinal axis and a reduction of its transverse diameter, resulting in a 4-fold increase in length. This morphogenetic event involves dramatic changes in the shape of the epidermal (hypodermal) cells. Elongation is divided into an early and a late phase. The early phase, from comma to 1.75-fold stage – corresponding to embryos that are 1.75-fold in length compared to non-elongated embryos –, occurs through contraction of filamentous actin bundles (FBs) in hypodermal cells (Priess et Hirsh, 1986). The hypodermis is composed of ventral, lateral (seam cells) and dorsal cells, which are linked by adherens junctions (Keller, 2006b). Contraction of FBs during early elongation is thought to be high in the seam cells and low in dorsal and ventral hypodermal cells (Priess et Hirsh, 1986 ; Piekny *et al.*, 2003).

The late phase of elongation involves mechanotransduction signaling from the body-wall muscles to the dorsal and ventral hypodermal cells (Zhang *et al.*, 2011). At the 1.5-fold stage of development, muscle cells form connections, called trans-epidermal attachment structures (TEAs), with the dorsal and ventral hypodermis (Ding *et al.*, 2004). As embryos develop to the 1.75-fold stage, the muscles become functional and

start contracting, thus inducing chemical changes in the overlying hypodermal cells through mechanical tension applied on the TEAs (Zhang *et al.*, 2011).

The signal transduction pathways that regulate early and late elongation have been extensively investigated over the last 15 years. Interestingly, many genes controlling morphological changes of the hypodermis during elongation are effectors or regulators of Rho GTPases (Piekny *et al.*, 2000 ; Diogon *et al.*, 2007 ; Gally *et al.*, 2009 ; Zhang *et al.*, 2011). Rho GTPases are molecular switches controlling a wide-range of cellular functions involving cell shape changes, cell migration, cell proliferation and differentiation (Takai *et al.*, 2001). They cycle between an "ON" GTP-bound form and an "OFF" GDP-bound form. When bound to GTP, they interact with specific effectors. They are regulated by three families of proteins: Guanine nucleotide-Exchange Factors (GEFs); GTPase-Activating Proteins (GAPs); and Guanine nucleotide-Dissociation Inhibitors (GDIs). To date, although three Rho GTPases (*rho-1*/RHOA, *ced-10*/RAC and *mig-2*/RHOG) have been implicated in pathways controlling elongation, only three of their regulators (GAPs and GEFs) have been shown to be involved in this process (Piekny *et al.*, 2000 ; Diogon *et al.*, 2007 ; Zhang *et al.*, 2011 ; Lin *et al.*, 2012), suggesting that others remain to be identified.

In hypodermal cells, contraction of the FBs during early elongation depends on the regulation of myosin-light-chain (MLC-4/MLC) phosphorylation by three serine-threonine kinases, the RHO-1/RHOA-effector kinase LET-502/ROCK, the *C. elegans* ortholog of the CDC42-effector myotonic dystrophy kinase MRCK-1/MRCK and the CDC42/RAC-effector kinase PAK-1/PAK1. These kinases act antagonistically with the MEL-11/PP-1M and are organized in two parallel pathways: The *let-502 /mel-11* pathway including *mrck-1* and a second pathway involving *pak-1* (Piekny *et al.*, 2000 ; Piekny *et al.*, 2003 ; Gally *et al.*, 2009). Downstream of these pathways, MLC-4/MLC phosphorylation leads to non-muscle myosin filament assembly and contractility, while its dephosphorylation is associated with relaxation.

LET-502/ROCK is an essential component of the *let-502/mel-11* pathway and an essential regulator of elongation (Wissmann *et al.*, 1997). It is activated downstream of the Rho GTPase RHO-1/RHOA (Spencer *et al.*, 2001), that may itself be activated by the GEF RHGF-2 (Lin *et al.*, 2012) and inactivated by the GAP RGA-2 (Diogon *et al.*, 2007). Inactivation of RHO-1 by RGA-2, occurs in ventral and dorsal hypodermal cells during early elongation leading to inactivation of LET-502/ROCK and reduction of FB contractions in these cells (Diogon *et al.*, 2007). RHO-1/RHOA and LET-502/ROCK may then be activated in the lateral hypodermal cells where most of the FB contractions may occur during early elongation. Consistent with this model, expression of MLC-4/MLC in the lateral cells can rescue *mlc-4 loss-of-function*-associated elongation defects, while expression of MLC-4/MLC in ventral and dorsal cells cannot (Gally *et al.*, 2009). In seams cells, MEL-11/PP-1M may be inhibited by LET-502/ROCK and MRCK-1/MRCK presumably through phosphorylation (Piekny *et al.*, 2003 ; Gally *et al.*, 2009).

The second pathway involves the CDC42/RAC-effector PAK-1, the PP2C phosphatase FEM-2/POPX2 and a RHO/RAC-specific GTP-nucleotide exchange factor (GEF) UNC-73/TRIO. The function of these two later proteins in the regulation of MLC-4 phosphorylation and/or PAK-1 function remains unknown (Piekny *et al.*, 2000 ; Piekny *et al.*, 2003 ; Gally *et al.*, 2009 ; Vanneste *et al.*, 2013).

To date, the genes controlling the *pak-1* pathway during early elongation remain unknown. Moreover, the biological significance of the functional redundancy of the *mel-11/let-502* and *pak-1* pathways is not clear. This redundancy is intriguing since it does not appear to add robustness to the elongation system: a single perturbation in any component of the *mel-11/let-502* pathway induces a high proportion of embryonic lethality (Piekny *et al.*, 2000). This suggests that the *mel-11/let-502* and *pak-1* pathways have unique functions during elongation that remain to be identified.

The CDC42/RAC-specific GEF, PIX is a well-known activator of PAKs in several organisms (Frank et Hansen, 2008). In *C. elegans, pix-1* codes for a protein homologous to the mammalian β-PIX (Figure S1). It contains a Src-homology 3 (SH3); a GEF/dbl homology (DH); a GIT-binding (GBD), and a PDZ binding (ZB) domains (Figure S1). These conserved domains are shown in mammals to mediate β-PIX interaction with PAK1-3, the Rho GTPases CDC42 and RAC, the phosphatases POPX1/2, the ARFGAP GIT, the tumor suppressor Scribble and the postsynaptic density protein Shank (Frank et Hansen, 2008). In *C. elegans*, PIX-1 was shown to activate PAK-1 in a GTPase-independent manner in migrating distal tip cells (DTC) during gonad morphogenesis in larvae (Lucanic et Cheng, 2008). In this system, PAK-1 activation still appears to be at least partially dependent on CED-10/RAC Peters *et al.*, 2013. PIX-1 was also shown to activate PAK-1 through the GTPase CED-10/RAC in hypodermal cells during late elongation of embryos (Zhang *et al.*, 2011).

In this study, we demonstrate that *pix-1* controls early elongation in parallel with *mel-11/let-502*. Our data suggest that *pix-1* is a novel component of the *pak-1* pathway while retaining some function during early elongation independent from *pak-1*. We show that the *pix-1/pak-1* pathway controls the antero-posterior morphology of the embryo during early elongation through regulating head width, while *let-502*/ROCK controls both the head and tail width. Our study proposes a novel model for early elongation where the *mel-11/let-502* and *pix-1/pak-1* pathways have redundant and complementary functions to shape the antero-posterior axis of the embryo.

2.4 Results

2.4.1 *pix-1* and *pak-1* control early elongation

To investigate the role of *pix-1* during early elongation, we examined the phenotypes of *pix-1(gk416)* and *pix-1(ok982)* embryos. As controls, we characterized the elongation phenotypes of *pak-1(ok448)* and *let-502(sb118ts)* mutant embryos, which display early elongation defects (Piekny *et al.*, 2000 ; Gally *et al.*, 2009. *pix-1(gk416)* and *pak-1(ok448)* are null alleles Lucanic et Cheng, 2008 ; Gally *et al.*, 2009. *pix-1(ok982)* contains a 1002 bp deletion spanning exons 8 to 11 and may code for a protein that retains the N-terminal SH3 and RhoGEF/DH domains of PIX-1 (Figure S2.1). *let-502(sb118ts)* is a thermosensitive allele coding for the RHO-1/RHOA-effector kinase LET-502/ROCK. This allele shows no obvious phenotypes at 20°C, but displays strong elongation defects and L1-larval arrest characteristic of strong hypomorphic and null *let-502* alleles at 25.5°C (Piekny *et al.*, 2000) (Figure 2.1).

Phenotypic characterisation of animals carrying *pix-1(gk416), pix-1(ok982)* and *pak-1(ok448)* alleles revealed low penetrance embryonic lethality (Emb) and early larval arrest (Lva) confirming previous findings (Table 2.1) (Zhang *et al.*, 2011). Measurements of *pix-1(gk416), pix-1(ok982), pak-1(ok448)* and *let-502(sb118ts)* arrested larvae showed that they were significantly shorter than synchronized *wt* L1 larvae at 25.5°C (T-test, $p < 0.01$) (Figure 2.1A and B). To better characterize the elongation defects associated with the *pix-1*, *pak-1* and *let-502* alleles, we measured the duration of early elongation using four-dimensional light microscopy. To do so, embryos were collected through dissection of hermaphrodites grown at 25.5°C, and embryonic development was imaged at 23-24°C. The duration of early elongation was measured from the 1.2-fold stage to the beginning of late elongation – when body wall muscles started contracting (Figure 2.1C). Animals carrying *let-502(sb118ts)* (n=10), *pix-1(gk416)* (n=25) and *pak-1(ok448)* (n=20) alleles developed significantly slower than *wt* animals (n=17) during early elongation (Figure 2.1C).

We also measured the length of the embryos at the end of early elongation (Figure 2.1D), and found that mutant embryos were significantly shorter than *wt* embryos (Figure 2.1D). These data demonstrate that the elongation rate of *pix-1*, *pak-1* and *let-502* mutant embryos is significantly reduced during early elongation, and provide the first evidence of a requirement for *pix-1* at this stage. They also confirm the involvement of *pak-1* during early elongation (Gally *et al.*, 2009).

Interestingly, *pix-1* and *pak-1* arrested larvae had very similar morphologies and behavior. For example, they were thin and clear when compared to *let-502* arrested larvae (Figure 2.1A). Furthermore, they appeared to have different antero-posterior morphologies when compared to *wt* and *let-502* larvae. When the width of the head (H3, Figure 2.2A and B) and the width of the tail (T3, Figure 2.2A and B) were measured and combined as a head/tail width ratio (H3/T3, Figure 2.2B), *pix-1(gk416), pix-1(ok982)* and *pak-1(ok448)* had significantly higher ratios than *wt* and *let-502* larvae (H3/T3, Figure 2.2B, data not shown). This indicates that *pix-1* and *pak-1* mutant arrested larvae present a morphological alteration characterized by an inflated anterior part of their body when compared to their posterior part. These mutants arrested larvae also had severe pharynx pumping defects and were completely paralyzed, although pumping in L3 escapers was similar to *wt* larvae (Figure S2.2). While these later phenotypes may be physiological consequences of primary developmental phenotypes, they support the fact that a similar array of phenotypes is observed in *pix-1* and *pak-1* mutant animals. These data support then the hypothesis that *pix-1* and *pak-1* could be part of the same developmental pathway. This also suggests that *pix-1* and *pak-1* control the relative width of the head vs. the tail of developing embryos, a process that does not seem to require *let-502*.

2.4.2 *pix-1* and *pak-1* control the head to tail width of the embryos during early elongation

Since *pix-1* and *pak-1*are also involved in the control of late elongation, we investigated whether their function during early elongation is required to control the head to tail width of the animal. To do so, we measured the H/T ratio of *pix-1(gk416)*, *pak-1(ok448)* and *let-502(sb118ts)* embryos at the beginning, 1.2-fold stage (H1/T1, Figure 2.2A and B), and at the end of the early elongation (H2/T2, Figure 2.2A and B). These experiments were done using the same populations of embryos characterized previously (Figure 2.1C and D). While no change, or a reduced H/T ratio was observed in *pix-1, pak-1* and *let-502* mutants when compared to *wt* animals at the beginning of early elongation (H1/T1, Figure 2.2A), all three mutants showed a significantly higher H/T ratio than *wt* embryos at the end of early elongation (T-test *p-values* <0.006; H2/T2, Figure 2.2A). This shows that the inflated head vs tail morphology observed in *pix-1* and *pak-1* arrested larvae is also observed at the end of early elongation in *pix-1*, *pak-1* and *let-502* mutant embryos, suggesting that *pix-1*, *pak-1* and *let-502* control the head to tail width of the embryos at that stage. We then measured the reduction of head (H) and tail (T) width during early elongation. To do so, we compared the width of the head and the width of the tail of the embryos at the beginning and the end of early elongation (H1/H2 and T1/T2 respectively; Figure 2.2C). In *wt* embryos the head and the tail appeared to be 1.4- and 1.16-fold wider at the beginning than at the end of early elongation (Figure 2.2C). This shows that the head width reduces more than the tail width during early elongation in *wt* animals. We found that the head width of the *pix-1* and *pak-1* mutant embryos reduced significantly less during early elongation than *wt* embryos (Figure 2.2C left panel). We also found that the tail width reduced similarly in *pix-1* and *pak-1* mutant embryos than in *wt* embryos. Interestingly, the degrees of head and tail width reduction in *let-502(sb118ts)* embryos were significantly lower than *wt* embryos and not significantly different than 1, suggesting that in *let-502* mutant animals neither

the head, nor the tail width of the animal reduce during early elongation (Figure 2.2C).

Together, these data suggest that the higher reduction of the head versus the tail width of the embryo during early elongation requires *pix-1*, *pak-1* and *let-502* function. These three genes appear to be required for reduction of the head width of the embryo, while only *let-502* may be required for reduction of the tail width.

2.4.3 *pix-1* and *pak-1* control early elongation in parallel with *mel-11/let-502* pathway

pak-1 was previously proposed to control early elongation in parallel with the *mel-11/let-502* pathway (Gally *et al.*, 2009). To assess whether *pix-1* also controls early elongation in parallel with the *mel-11/let-502* pathway, we tested whether *pix-1(gk416)* genetically interacts with *mel-11(it26)* and *let-502(sb118ts)* temperature sensitive mutants, as reported for *pak-1* (Gally *et al.*, 2009). At 18ºC, 98% of *mel-11(it26)* mutant embryos rupture during elongation as previously described (Table 2.2, line 3) (Piekny *et al.*, 2000). The penetrance of this phenotype is increased to 100% at 25.5ºC. As previously shown, *mel-11(it26); pak-1(ok448)* double mutant embryos display phenotypes similar to *mel-11(it26)* at both 18ºC and 25.5ºC (Table 2.2 line 10) (Gally *et al.*, 2009). Interestingly, the *mel-11(it26)*-associated embryonic rupturing is completely suppressed by *pix-1(gk416)* at 18ºC and 25.5 ºC (Table 2.2, line 4). A small fraction of *mel-11(it26); pix-1(gk416)* hatched larvae arrest at the L1 stage with characteristic *pix-1* phenotypes, and a penetrance similar to *pix-1(gk416)* at 18ºC (Table 2.2, line 2 and 4). Surprisingly, at 25.5ºC, 9.7% of *mel-11(it26); pix-1(gk416)* embryos arrest between 1.2- and 2-fold stages without rupturing and 40.3% of them display late elongation defects and stop developing without hatching (Table 2.2, line 4). These results show that *pix-1(gk416)* suppresses both the expressivity – the embryos arresting at 1.2-2 fold stages without rupturing – and the penetrance of

mel-11 early elongation defects at 25.5°C. Considering *mel-11(it26)* to be null at 25.5°C Wissmann *et al.*, 1999, these data suggest that *pix-1* functions in parallel with *mel-11* during early elongation. The aggravation of *pix-1* associated late elongation defects in a *mel-11(it26)* background is somewhat intriguing and provides the first evidence suggesting an involvement of *mel-11* in late elongation, in parallel with *pix-1*.

We then assessed whether *pix-1(gk416)* and *pak-1(ok448)* interacts with *let-502(sb118ts)* at 25.5°C. As previously shown, few *let-502(sb118ts)* embryos arrest between the 1.2- and 2-fold stage at restrictive temperature and the vast majority of the animals hatch as non-elongated larvae (Table 2.2, line 5, Figure 2.1A) (Piekny *et al.*, 2000). 89% and 100% of *let-502(sb118ts)* embryos arrest between 1.2- and 2-fold stages in *pix-1(gk416)* and *pak-1(ok448)* backgrounds, respectively at 25.5°C (Table 2.2, line 6 and 11). In addition, *let-502(sb118ts); pix-1(gk416)* hatched larvae arrested with more severe elongation defects than *let-502(sb118ts)* animals (Table 2.2, line 6; Figure 2.3A and C), while their head/tail width ratio is not significantly different than *wt* as observed for *let-502(sb118ts)* arrested larvae (Figure 2.3D). These results suggest that *pix-1* functions in parallel with *let-502* to control elongation, as previously shown for *pak-1* (Gally *et al.*, 2009), and that the loss of *let-502* function suppress the higher H/T ratio observed in *pix-1* mutant arrested larvae when compared to *wt*. Interestingly, the aggravation of *let-502* defects by *pix-1(gk416)* appears to be weaker than that observed for *pak-1(ok448)*, suggesting that *pix-1* is redundant with a yet unidentified gene in parallel with *let-502*.

To assess if *pix-1* functions in parallel with the *let-502/mel-11* pathway, we generated *mel-11(it26); let-502(sb118ts); pix-1(gk416)* triple mutants. At 18°C, *mel-11(it26); let-502(sb118ts)* display similar elongation defects to *mel-11(it26)* single mutant embryos due to the thermosensitive nature of *let-502(sb118ts)* (e.g. *wt* phenotype at 18°C; Table 2.2, compare lines 3 and 7). At non-restrictive temperature, a reduced number of *mel-11(it26); let-502(sb118ts); pix-1(gk416)* animals arrest during early

elongation when compared to *mel-11(it26); let-502(sb118ts)* (Table 2.2, compare lines 7 and 8). This is consistent with our data showing suppression of *mel-11(it26)* early elongation defects by *pix-1(gk416)* (Table 2.2 line 4). At 25.5 °C, *mel-11(it26); let-502(sb118ts)* are viable and embryos display 24% early elongation arrest (Table 2.2 line 7). At restrictive temperature, elongation defects are aggravated in *mel-11(it26); let-502(sb118ts); pix-1(gk416)* triple mutants in comparison to *mel-11(it26); let-502(sb118ts)* double mutants (Table 2.2, compare lines 7 and 8) : 43.1% embryos arrested during early elongation (compared to 24% in *mel-11(it26); let-502(sb118ts)*), and 31% of animals hatched as non-elongated larvae presenting *pix-1* mutant-associated morphology (compared to 0% in *mel-11(it26); let-502(sb118ts);* Figure 2.3B and C*)*. Interestingly, *mel-11(it26); let-502(sb118ts); pix-1(gk416)* arrested larvae present a H/T width ratio significantly higher than *wt* and similar to that observed in *pix-1(gk416)* arrested larvae (Figure 2.3D). This suggests that in *mel-11(it26)* background, loss of *let-502* function is not anymore able to suppress *pix-1*-induced H/T ratio defect.

As previously shown, 100% of *mel-11(it26); let-502(sb118ts); pak-1(ok448*) embryos failed to hatch and displayed early elongation arrest (Table 2.2, line 12) (Gally *et al.*, 2009). These results suggest that *pix-1* functions in parallel with the *let-502/mel-11* pathway during early elongation, as shown for *pak-1*. However, the increased phenotypic severity observed in *pak-1 vs. pix-1* mutants suggests that *pix-1* functions redundantly with a gene or a group of genes in parallel with *mel-11/let-502* during early elongation. The different relationship observed between *mel-11* and *pix-1* or *pak-1* mutants also suggests that *pix-1* and *pak-1* have independent functions during early elongation. Whether this is the case during late elongation, could not be ascertained from our data.

2.4.4 PIX-1::GFP is homogeneously distributed in the cytoplasm and at cell periphery of hypodermal cells

pix-1 was previously shown to be involved in mechanotransduction signaling in ventral and dorsal hypodermal cells upon muscle contraction during late elongation events (Zhang *et al.*, 2011). The localisation of PIX-1 at the TEA in dorsal and ventral hypodermal cells supports this function (Zhang *et al.*, 2011). Our data suggest that *pix-1* also controls early elongation events. These events are thought to be directed by the contraction of filamentous actin bundles (FBs) at the cell periphery and at the most apical part of the lateral hypodermal cells (Gally *et al.*, 2009). To better understand the function of PIX-1 during early elongation, we characterized its subcellular localization in hypodermal cells during early elongation. To do so, we examined the localisation of PIX-1::GFP expressed under the control of the *pix-1* endogenous promoter in *pix-1(gk416)* animals immuno-stained with MH27 antibodies (staining of hypodermal adherens junctions; Figure 4) or expressing the filamentous actin-binding probe VAB-10_{ABD}::mCherry in hypodermal cells (Figure S2.4). Confocal microscopy analysis revealed that during early elongation, PIX-1::GFP is expressed in the dorsal (Figure 2.4A-C, Figure S2.4A-F), lateral (Figure 2.4D-F) and ventral hypodermal cells (Figure 2.4G-I, Figure S2.4D-F). Throughout early elongation, PIX-1::GFP is located at the TEA in dorsal and ventral hypodermal cells, as previously reported (Figure 2.4 E, arrow-head) (Zhang *et al.*, 2011) and is also homogeneously distributed in the cytoplasm and at the cell periphery of all expressing cells (Figure 2.4, Figure S2.4). Interestingly, at the comma stage, PIX-1::GFP expression appears to be reduced in several posterior dorsal hypodermal cells (Figure 4 B, arrowhead). Concomitant with the fusion of these cells, around the 1.2-fold stage, the expression of PIX-1::GFP appears to be reduced in the fused cells (Figure 2.5A).

2.4.5 High expression of *pix-1* in dorsal posterior hypodermis is detrimental for early elongation

Considering that *pix-1* controls reduction of the head but not the tail width of the embryos during early elongation, we were intrigued by the reduction of the expression of PIX-1::GFP in the dorsal-posterior hypodermal cells in the transgenic animals. We then quantified PIX-1::GFP expression in dorsal-anterior (DA), dorsal-posterior (DP), ventral-anterior (VA), ventral-posterior (VP), lateral-anterior (LA) and lateral-posterior (LP) hypodermal cells (Figure 2.5A). This study revealed a significant lower ratio of DP/DA and DP/V expression when compared to LP/LA, VP/VA, DA/V and DA/L ratios, which were not significantly different than 1 (Figure 2.5B). Similar data were obtained using two independent transgenic lines expressing translational fusions of PIX-1::GFP under the control of the *pix-1* endogenous promoter, one transgenic line carrying an extrachromosomal array (*pix-1(gk416);sajEx1*) and one stable transgenic line carrying an integrated array (*unc-119(ed3);pix-1(gk416);sajIs1* see Methods). We also found that all measured ratios were constant throughout early elongation (Figure S2.5).

We then assessed whether the *sajEx1[pix-1p::pix-1::GFP,rol-6]* transgene could rescue elongation defects in *pix-1(gk416)* animals. We found that the transgene significantly rescued the larval arrest phenotype (Lva) of *pix-1(gk416)* from 8.5% (N=1216) to 2.0% (N=917) (Table 1; T-test, *p-value* = 0.03). Using time-lapse microscopy, we also measured the elongation rate of wild-type (*wt*), *pix-1(gk416)* and *pix-1(gk416);sajEx1[pix-1p::pix-1::GFP, rol-6]* embryos and found that the transgene did not significantly rescue the elongation rate of mutant animals (Figure 2.6B). This suggests that while the expression of PIX-1::GFP fusion protein is sufficient to support PIX-1 function during early elongation (rescuing Lva), it was not as efficient as the endogenous protein.

We then observed the elongation rate of embryos at the single animal level and attempted to see if there was any correlation between a given expression pattern of the transgene and the ability of the transgene to efficiently rescue the mutant elongation rate defect. We found that transgenic embryos with similar elongation rates to *wt* embryos (elongation $\geq$ 288nm/min, Figure 2.6D) had DP/DA and DP/V ratios of PIX-1::GFP intensity that were significantly lower than embryos that elongated slower (elongation < 288nm/min, *p-value* < 0.01; Figure 2.6D). No significant difference was observed for the LP/LA, VP/VA DA/V and DA/L ratios between the two populations of embryos (Figure 2.6D). These data show that PIX-1::GFP expression was significantly reduced in dorsal-posterior cells when compared to dorsal-anterior and ventral cells in rescuing animals. Such reduction of PIX-1::GFP expression in dorsal-posterior cells was not observed in non-rescuing animals. Importantly, animals presenting a DP/DA ratio higher than 0.5, elongated almost 3 times slower than *wt* animals (Figure 2.6A). Overall, the speed of early elongation appeared to be negatively correlated to the DP/DA ratio of PIX-1::GFP expression (Spearman correlation coefficient $R^2 > 0.427$; *p-value* < 0.002; Figure 2.6C), but not to any other PIX-1::GFP intensity ratio measured in hypodermal cells (Figure S2.6). Similar results were obtained using two independent *pixp::pix-1::GFP* expressing transgenic lines, one carrying an extrachromosomal array (*pix-1(gk416);sajEx1*), and a stable transgenic line carrying an integrated array (*unc-119(ed3);pix-1(gk416);sajIs1)*. These data suggest that transgenic animals expressing PIX-1::GFP homogeneously in dorsal-anterior, lateral and ventral hypodermal cells, but two times less in dorsal-posterior cells, elongate at a *wt*-rate during early elongation. However, animals expressing the transgene in dorsal-posterior cells at a similar/higher level when compared to other cells elongated significantly slower.

PIX-1::GFP is expressed in cells other than the hypodermis, and we cannot exclude the possibility that differential expression of PIX-1::GFP in other cells may affect the rescuing ability of the transgene. To test this possibility, we generated transgenic

animals expressing PIX-1::GFP under the control of the hypodermal specific promoter, *lin-26p*. This promoter is thought to drive the expression of coding sequences only in hypodermal cells and in a homogenous manner (Gally *et al.*, 2009). We confirmed this later assumption through measurements of the DP/DA fluorescence intensity ratios in *lin26p::vab-10(ABD)::GFP* and *lin-26p::vab-10(ABD)::mCherry* transgenic animals carrying integrated arrays expressing actin-binding fluorescent probes in all hypodermal cells under the control of *lin-26p* (Gally *et al.*, 2009). We showed that these ratio were not significantly different than 1 (Figure 2.5C and D).

As observed with *pix-1p::pix-1::GFP* expressing animals, transgenic animals carrying an integrated array expressing PIX-1::GFP under the control of *lin-26p* segregated into two populations. The embryos of the first population displayed an elongation rate similar to *wt* (elongation rate $\geq$ 288nm/min, Figure S2.7) and had DP/DA and DP/L intensity ratios that were significantly lower than the second population of embryos that elongated slower (elongation rate < 288nm/min, Figure S2.7). As shown for transgenic animals expressing *pix-1p::pix-1::GFP*, all animals expressing PIX-1::GFP under the control of *lin-26p* express similar levels of the transgene in DA, L and V cells (Figure S2.7). These data support our hypothesis that a DP/DA PIX-1::GFP expression ratio higher than 0.5 may hinder early elongation.

To determine if the lower DP/DA, DP/L and DP/V intensity ratios observed in embryos with a *wt*-like elongation rate were due to a reduced expression of PIX-1::GFP in DP cells or to an increased expression of PIX-1::GFP in DA, L and V cells, we measured the fluorescence intensity of PIX-1::GFP in DA and DP cells in *lin-26p::pix-1::GFP* expressing animals. We found that the PIX-1::GFP fluorescence intensity was not significantly different in the DA cells of embryos developing at a *wt*-rate when compared to those developing at slower rates (Figure 2.6E). However, PIX-1::GFP fluorescence intensity appeared to be significantly lower in the DP hypodermal cells in the subpopulation of embryos that elongated faster. This

phenomenon was observed in two independent stable transgenic lines. These data suggest that the DP/DA ratios in embryos that elongated at a *wt*-rate was not due to an increased expression of PIX-1::GFP in the DA cells, but to decreased PIX-1::GFP expression in the DP cells.

Altogether, these data suggest that homogenous expression of PIX-1::GFP in dorsal-anterior, lateral and ventral hypodermal cells, and decreased expression in dorsal-posterior cells significantly rescued the elongation defects observed in the *pix-1(gk416)* animals. They also suggest that expression of the transgene in dorsal-posterior cells above a threshold corresponding to half the expression in the other hypodermal cells decreases the efficiency of early elongation. This suggests that *pix-1* may be submitted to a tight control of its expression level in hypodermal cells, particularly to decrease its level in the dorsal-posterior cells.

2.5 Discussion

Embryonic elongation transforms the ovoid embryo into the long, thin vermiform nematode. This morphogenetic process occurs in two phases. The early elongation is driven by the contraction of Filamentous actin Bundles (FBs) in hypodermal cells. The late elongation is driven by a mechanotransduction pathway in the dorsal and ventral hypodermis resulting from contraction of the underlying muscle cells.

Two parallel pathways control early elongation. One pathway involves two kinases: the RHO-1/RHOA effector LET-502/ROCK and the ortholog of the CDC-42-effector human myotonic dystrophy kinase MRCK-1/MRCK (Piekny *et al.*, 2000 ; Piekny *et al.*, 2003). Both kinases are thought to inhibit the function of MEL-11/PP-1M thus permitting phorphorylation of myosin-light chain (MLC-4/MLC) and contraction of FBs. The second pathway involves the CDC42/RAC-effector PAK-1, the PP2C phosphatase FEM-2/POPX2 and a RHO/RAC GTP nucleotide-exchange factor

(GEF) UNC-73/TRIO. The function of these two later genes in the regulation of MLC-4/MLC phosphorylation and/or PAK-1 function remains unknown (Piekny *et al.*, 2000 ; Piekny *et al.*, 2003 ; Gally *et al.*, 2009 ; Vanneste *et al.*, 2013). Downstream of the two parallel pathways LET-502/ROCK and PAK-1 are thought to phosphorylate MLC-4/MLC in the hypodermal cells and to control contraction of FBs. This contraction is assumed to be high in the lateral and low in the ventral and dorsal hypodermal cells during early elongation (Diogon *et al.*, 2007).

In this study, we show that the CDC42/RAC-GEF *pix-1* controls early elongation in parallel with the *mel-11/let-502* pathway. Our data suggest that *pix-1* controls this process as part of the *pak-1* pathway in parallel with a gene (or a group of genes) that remains to be identified. *pix-1* may also function independently from *pak-1*. Our data suggest that PIX-1/PAK-1 and LET-502/ROCK have different function along the antero-posterior axis of the embryo during early elongation: PIX-1, PAK-1 and LET-502/ROCK appear to control the constriction of the head while only LET-502/ROCK controls the constriction of the tail of the elongating embryo. Our study also revealed that PIX-1::GFP fusion protein is homogeneously distributed in the cytoplasm and at the cell periphery of hypodermis during early elongation. We showed that this fusion protein rescues the reduced elongation rate observed *pix-1(gk416)* in a subset of transgenic animals expressing the transgene homogenously in dorsal-anterior, lateral and ventral cells and at a lower level in dorsal-posterior cells. Our results also suggest that PIX-1 expression above a certain threshold in dorsal-posterior hypodermal cells is detrimental for early elongation.

2.5.1 *pix-1* functions with unidentified genes in parallel with *mel-11/let-502*.

pix-1 and *pak-1* mutants have similar elongation phenotypes and both aggravate the elongation defects observed in *mel-11; let-502* double mutant suggesting that these two genes control together a subset of developmental mechanisms in parallel with

mel-11; let-502 during early elongation. However, *pix-1* mutant aggravates elongation defects associated with *mel-11; let-502* to a lesser extent than the *pak-1* mutant. This suggests that *pix-1* functions with other genes that act in parallel with *mel-11/let-502* pathway (Figure 2.7).

In both mammals and *C. elegans* βPIX/PIX-1 was shown to activate PAK-1 kinase activity in a GTPase-dependent (canonical) or GTPase-independent (non-canonical) manner (Lucanic et Cheng, 2008 ; Zhang *et al.*, 2011 ; Peters *et al.*, 2013). M. Labouesse's laboratory (IGBMC, Illkirch, France) showed using GTPase pull-down assays that the level of activation of the Rho GTPase CED-10/RAC was significantly lower in *pix-1(gk416)* than in *wt* embryos, suggesting that PIX-1 regulates CED-10/RAC activity during embryonic development (Zhang *et al.*, 2011). We can then hypothesize, that PIX-1 may activate PAK-1 in a canonical manner through CED-10/RAC during early elongation as shown during late elongation (Zhang *et al.*, 2011). Supporting this hypothesis, CED-10/RAC was located at both cell junctions and at the TEA within hypodermal cells in elongating embryos (Chen *et al.*, 1996 ; Zhang *et al.*, 2011). However, we cannot exclude the possibility that PIX-1 may also activate PAK-1 during early elongation in a GTPase-independant/non-canonical manner as shown during gonad morphogenesis (Lucanic et Cheng, 2008 ; Peters *et al.*, 2013). Interestingly, the RHO/RAC specific GEF *unc-73*/TRIO was also shown to control early elongation in parallel to *mel-11/let-502* (Piekny *et al.*, 2000). The allele used in that study, *rh40,* consists of a missense mutation that eliminates its exchange activity towards CED-10/RAC, RAC-2/RAC and MIG-2/RHOG without affecting its activity towards RHO-1/RHOA (Steven *et al.*, 1998 ; Spencer *et al.*, 2001). A UNC-73/TRIO - CED-10/RAC - PAK-1 pathway would then be an excellent candidate pathway controlling early elongation in parallel with a non-canonical PIX-1 – PAK-1 or a canonical PIX-1 - CED-10/RAC - PAK-1 pathway (Figure 7). Careful study will be required to test these hypotheses and to better understand the molecular mechanisms involving PIX-1 and controlling the activity of PAK-1 during early elongation.

2.5.2 *pix-1* may control early elongation in a *pak-1* dependent manner.

While *pix-1* and *pak-1* may be part of the same pathway in parallel with *mel-11/let-502, mel-11(it26)*-inducing embryo rupturing is suppressed by *pix-1(gk416)* but not by *pak-1(ok448)* (Table 2). This intriguing genetic interaction between *pix-1* and *mel-11*/PP-1M during elongation is similar to that observed between *fem-2*/POPX2 and *mel-11*/PP-1M, another gene shown to be part of the *pak-1* pathway (Vanneste *et al.*, 2013).

It was shown that the *fem-2* null allele induces weak larval arrest with non-elongated larvae similar to that observed in *pix-1* and *pak-1* mutants Piekny *et al.*, 2000. The *fem-2* mutant can also aggravate *mel-11*; *let-502* double mutants and suppress the *mel-11* rupturing phenotype (Piekny *et al.*, 2000 ; Vanneste *et al.*, 2013. This suggests that *pix-1*, and *fem-2*/POPX2 function together to control early elongation in parallel with *mel-11/let-502*. Interestingly, the PP2C-like serine/threonine phosphatases, POPX2/Protein Phosphatase 1F, the closest homolog of FEM-2 in mammals, was shown to interact with β-Pix (ortholog of PIX-1) and to dephosphorylate and inactivate PAK1 (ortholog of PAK-1) kinase activity in mammalian cells (Koh *et al.*, 2002). It was suggested that the β-PIX - POPX2 complex controls the activation/inactivation turnover of PAK1 in mammalian cells (Huang *et al.*, 1998 ; Koh *et al.*, 2002). Considering that these proteins are highly conserved between *C. elegans* and mammals, we hypothesize that PIX-1, FEM-2/POPX2 and PAK-1 may have functional relationships similar to their homologs in mammals. Following this hypothesis, PIX-1 and FEM-2/POPX2 may control the activation/inactivation turnover dynamics of PAK-1 during early elongation. Considering that *pix-1* and *fem-2* mutant have similar interactions with *mel-11* and *let-502* during early elongation, this hypothesis suggests that a reduced or a sustained activation of PAK-1 alters similarly early elongation process. While this hypothesis would explain the genetic data obtained with *pix-1*, *fem-2* and *pak-1* mutants during elongation, it still remains

to be confirmed through a careful analysis of a possible relationship existing between PAK-1 activation/inactivation dynamics and the regulation of myosin contraction in *C. elegans* hypodermal cells during early elongation.

2.5.3 *pix-1* may control early elongation in a *pak-1* independent manner.

Considering the molecular analysis of *mel-11(it26)* allele (Wissmann *et al.*, 1999), we cannot exclude the possibility that this allele may not be completely null even at 25.5°C. We can then hypothesize that *pix-1* may function together with *pak-1* in parallel with *mel-11* and may also function upstream of *mel-11* independently of *pak-1*. This would constitute an alternative explanation for the suppression of *mel-11(it26)*-inducing rupturing by *pix-1* but not by *pak-1* allele. Interestingly, the kinase MRCK-1/MRCK, whose mammalian ortholog, is an effector of CDC-42 (Wilkinson *et al.*, 2005) was shown to control early elongation upstream of *mel-11* (Gally *et al.*, 2009). CDC-42 being expressed in hypodermal cells during early elongation (Chen *et al.*, 1996), and being also a potential target of PIX-1 GEF activity, we can hypothesize that PIX-1 may activate MRCK-1 through CDC-42 upstream of MEL-11 and may also activate PAK-1 in parallel with *mel-11/let-502* (Figure 7).

2.5.4 The *pix-1/pak-1* pathway mainly controls the constriction of the head of the embryos during early elongation

Observation of the head to tail morphology of the elongating embryo showed that the anterior part of the embryo at 1.2-fold stage is much wider than the posterior part. This suggests that contraction forces applied on the anterior part of the embryo is higher than in the posterior part at that stage. We showed that the mechanism leading to a faster reduction of the head width during early elongation is dependent on *pix-1*, *pak-1* and *let-502*/ROCK and that reduction of the tail width is dependent on *let-502*/ROCK but neither on *pix-1* nor on *pak-1*. This suggests that contraction forces

controlled by *let-502*/ROCK are required for the embryo morphogenesis along the antero-posterior axis, while those controlled by the *pix-1/pak-1* pathway may mostly be required in the anterior part of the embryo. This also suggests that either the *pix-1/pak-1* pathway induces contractions mostly in the anterior part of the embryo, or this pathway is redundant with another pathway (in addition to *let-502/mel-11)* specifically involved in the control of contractions in the posterior part of the embryo. Interestingly, we found that animal expressing PIX-1::GFP at a reduced level in the dorsal posterior cells present an elongation rate similar to *wt*. Higher expression of PIX-1::GFP in the dorsal-posterior cells is also shown to be detrimental for the elongation rate of embryos during early elongation. This suggests that the function of *pix-1* is required at a low level in the dorsal-posterior hypodermal cells to ensure optimal elongation rate. This supports the hypothesis that the *pix-1/pak-1* pathway may induce more contractions in the anterior part of the embryo than in the posterior part. However, this hypothesis will have to be tested through careful measurement of contraction forces induced by the *let-502/mel-11* and *pix-1/pak-1* pathways in individual sets of hypodermal cells during early elongation.

We also showed that loss of *let-502* function suppresses the increased head/tail width ratio observed in *pix-1* arrested larvae when compared to *wt* and that this suppression occurs only in embryos expressing an active *mel-11* (Figure 3D). These data support our observations that *let-502; pix-1* arrested larvae display *let-502* morphology, while *let-502; mel-11; pix-1* larvae display *pix-1* morphology (Table 2). To explain these results, we may hypothesize that loss of *let-502* may induce a severe reduction of contraction forces in hypodermal cells due to the activation of *mel-11*. This activated *mel-11* may then strongly suppress the contraction forces induced by the *pix-1/pak-1* pathway and consequently the difference of contraction forces applied on the head and tail during early elongation. According to this hypothesis, in absence of both *let-502* and *mel-11*, deletion of *pix-1* function is associated with the arrest of larvae displaying a similar increase of H/T width ratio than observed in single *pix-1(gk416)*

mutants. These data confirm that MEL-11 function antagonizes both contraction forces induced by LET-502 and those induced by the PIX-1/PAK-1 pathway (Figure 7) (Wissmann *et al.*, 1997 ; Gally *et al.*, 2009).

In summary, our study demonstrates a function for *pix-1* during early elongation within the *pix-1/pak-1* pathway in parallel with *mel-11/let-502*. At that stage, *let-502* may drive the contraction forces leading the reduction of the embryo circumference along the antero-posterior axis, while the *pix-1/pak-1* pathway may mainly control the contraction forces applied on the anterior part of the embryo.

2.6 Methods

2.6.1 Strains and Culture Methods

Control N2 and other animals were maintained in standard conditions at 20°C Brenner, 1974. Worm strains carrying the following mutations and markers: *pix-1(gk416) X, pix-1(ok982) X, pak-1(ok448) X, mcIs40 [lin-26p::ABDvab-10::mcherry + myo-2p::gfp]* and *mcIs50 [lin-26p::ABDvab-10::gfp + myo-2p::gfp],* were obtained from the *Caenorhabditis Genetic Center* (CGC). Mutant strains were backcrossed at least 3 times against wild-type (*wt*) animals prior to analysis. Strains carrying *let-502(sb118) I, mel-11(it26) unc-4(e120)/mnC1 II* and *mel-11(it26) unc-4(e120) II; let-502(sb118) I,* were kindly provided by Dr Paul Mains (University of Calgary, Calgary, Canada). *Mel-11(it26) unc-4(e120) II; let-502(sb118) I* were maintained at 25.5°C. *mel-11(it26) unc-4(e120) II; let-502(sb118) I; pix-1(gk416) X* and *mel-11(it26) unc-4(e120) II; let-502(sb118) I; pak-1(ok448) X* were generated after crossing *mel-11(it26) unc-4(e120) II; let-502(sb118) I* hermaphrodites with *pix-1(gk416) X* or *pak-1(ok448) X* males. Genotyping of F2 progeny was done through isolation of Unc F2 (*mel-11(it26) unc-4 (e120) II homozygotes)* at 15°C. Mutations in *pix-1* and *pak-1* genes were identified using Polymerase chain Reaction (PCR) and

let-502(sb118) I homozygotes were identified through scoring of embryonic lethality (Emb) and larval arrest (Lva) phenotypes of populations grown at 18°C and 25.5°C.

2.6.2 Generation of Transgenic animals

pix(gk416); sajEx1[pix-1p::pix-1::GFP;rol-6(su1006)] animals were generated by injection. Translational PIX-1::GFP fusion construct (*pix-1p::pix-1::gfp*) was obtained from Dr Chen HJ's laboratory (University of California Davis, Davis, California, USA) (Lucanic et Cheng, 2008) and injected at 15 ng/µl with pRF4 (containing *rol-6(su1006)* at 50 ng/µl) in *pix(gk416)* animals. Rol transgenic animals were isolated and expression of PIX-1::GFP was assessed by fluorescent microscopy. *Unc-119(ed3); pix-1(gk416); sajIs1[pix-1p::pix-1::gfp; unc-119^{R}]* was generated using biolistic bombardment. To do so, constructs were generated through amplification of the *pix-1* promoter (1.6 kb upstream of the initiation codon), amplification using reverse-transcription and PCR using thermoscript II (life technologies) kit of *pix-1* cDNA (from the ATG the codon in 5`of the endogenous stop codon, including the intron between exon 1 and 2). Both DNA fragments were inserted using gateway recombination in pDONRP4P1R and pDONR201 respectively and recombined together in pMB14. This construct was integrated by biolistic bombardment in *unc-119(ed3); pix-1(gk416)* strain, using a PDS-1000/He system with the Hepta adaptor (Bio-Rad) as previously reported (Berezikov *et al.*, 2004). *Unc-119(ed3); pix-1(gk416); sajIs2[lin-26p::pix-1::GFP]* and *unc-119(ed3); pix-1(gk416); sajIs3[lin-26p::pix-1::GFP]* were independent, stable transgenic lines generated also using biolostic bombardment. It contains 5kb of the *lin-26* promoter, the *pix-1* coding sequence including the intron between exon 1 and 2, and the GFP coding sequence in pMB14 vector. This construct was also integrated by biolistic bombardment in *unc-119(ed3); pix-1(gk416)* strain, using a PDS-1000/He system with the Hepta adaptor (Bio-Rad).

Transgenic animals expressing PIX-1::GFP together VAB-10(ABD)::mCherry were obtained through crossing *pix(gk416); sajEx1*, *unc-119(ed3); pix-1(gk416); sajIs1*, *unc-119(ed3); pix-1(gk416); sajIs2* and *unc-119(ed3); pix-1(gk416); sajIs3* hermaphrodites with *mcIs40[lin-26p::ABDvab-10::mcherry+myo-2p::gfp]* males. Stable lines expressing GFP, mCherry transgenes and carrying *pix-1(gk416)* allele were isolated from the F2 progeny.

2.6.3 Phenotyping mutant animals and 4-dimensional microscopy

To score Emb and Lva phenotypes, worms were synchronized by hypochlorite treatment. After synchronisation 10-20 worms were deposited on NGM agar with OP50 as a source of food Worms were allowed to lay eggs at 18°C or 25.5°C for 4 to 5 hours and were washed off the plate with M9 medium. After 24 and 48 hours dead eggs and arrested L1 larvae were counted and observed at high magnification. The stage of embryonic arrest was confirmed in mutant animals using four-dimension microscopy. Embryos dissected from adult hermaphrodites were mounted on 3% agarose pads in M9 buffer and coverslips were sealed with drawing gum (pébéo). Elongation was recorded using 4-dimensional microscopy (3D and time), which recorded a Z-stack every 2 minutes during 10 hours at 23-24°C using a Leica DM5500 microscope equipped with a 63X oil immersion objective upon differential interference contrast illumination (DIC). Images were captured using the Leica LAS AF imaging software. These recording were used to measure the duration of early elongation for at least 20 eggs from 1.2- to the end of early elongation – identified as the moment when body-wall muscles start contracting, the length of the embryos at the end of early elongation, the width of the head (measured at equidistance from the tip of the nose to the pharynx-intestinal valve), the width of the tail (measured at equidistance from the pharynx-intestinal valve to the distal extremity of hyp10) at 1.2-fold and at the end of early elongation in the different mutant animals. These measurements were done using Leica LAS AF6000 imaging analysis tools. The

reproducibility of these measurements were tested as detailed in the supplementary Figure 3. Length and head/tail width measurements were also done on mutant arrested larvae and wild-type (*wt*) L1 arrested by starvation after hypochlorite treatment. The head/tail ratio was calculated as the ratio of the head width with the tail width in µm per animal. The head (and tail) width reduction ratio was calculated as the ratio of the head width (or tail width) at 1.2-fold stage over the head width (or tail width) at the end of early elongation. Statistical significance was calculated using unpaired Student's T-test.

2.6.4 Immunostaining of embryos

For indirect immunofluorescence, embryos were fixed using 3% paraformaldehyde at room temperature for 10 minutes. Following washes with PBS (137 mM NaCl, 2.7 mM KCl, 4.3 mM Na_2HPO_4, 1.47 mM KH_2PO_4 Adjust to a final pH of 7.4.), embryos were incubated 10 minutes in cold methanol, and extensively washed with PBS. Fixed embryos were incubated overnight at 4°C with appropriate dilutions of primary antibodies in culture media (4X eggs salt, 0.5% Hepes 1M, 5% goat serum). Mouse anti-MH-27 antibodies (The Developmental Studies Hybridoma Bank, University of Iowa) were used at 1:10 dilution, rabbit anti-GFP antibodies were used at 1:500 (Invitrogen). After three washes with culture media (4X egg salt, 0.5% HEPES 1M, goat serum 5%), embryos were incubated at room temperature for 1h with 1:200 dilution of either anti-mouse IgG conjugated to TRITC or anti-rabbit IgG conjugated to FITC (Jackson ImmunoResearch) in 1X-PBS. Embryos were washed three times with culture media and incubated with 100 ng/ml of DAPI for 1 minute at room temperature, washed with water, resuspended in 40 µl of Mowiol (sigma Aldrich) and mounted on slides.

2.6.5 Confocal fluorescence microscopy

The expression pattern of PIX-1::GFP in living animals was observed using a Nikon A1R confocal microscope with 100X oil CFI NA 1.45 Plan Apochromat λ objective. All images were captured with a pinhole size of 59.1 µm, with a calibration of 0.12 µm/pixel (radial resolution of 0.20 µm) and a Z-step of 0.15 µm. Images were captures using NIS-element software (Nikon). Deconvolution was done using Autoquant 3X, 3D deconvolution software. Orthogonal views, and fluorescence quantifications were generated using ImageJ software. For fluorescence quantification, individual Z-steps were extracted from Z-stacks recording of elongating embryos. DP, DA, LP, LA, VP, VA hypodermal cells were selected using ImageJ 'polygon selections' tool. Nuclei of cells in these areas were also selected using the same tool. The Raw intensities of selected areas were measured using area and gray value function. Raw Intensities of nuclei were subtracted to raw intensities of selected hypodermal sections. The pixel mean value was then calculated dividing this adjusted raw intensity by the area size selected excluding also size of nuclei. Intensity ratios and raw intensities were calculated and used using the resulting value. Comparison of raw intensities between different animals was done on image captured within a week, to limit the impact of laser fluctuation. This fluctuation was controlled through comparison of intensities obtained for the same sample at different days. Fluorescence intensity was compared on images captured using the same laser power and adjusted photomultiplier tube (PMT). Statistical significance of quantification was assessed using the unpaired student T-test. Spearman correlation coefficients and statistical tests for significance of correlation between two quantitative variables were calculated using spearman cor.test function in R (Bioconductor).

2.7 Acknowledgments

Thanks to Dr Paul Mains (University of Calgary, Calgary, Canada), to Dr Michel Labouesse (IGBMC, Illkirch, France) for sharing biological material. Thanks to Alexander Parker (university of Montreal, Montréal, Canada) for technical support for generation of transgenic animals by injection. Thanks to Dr Alisa Piekny (U. Concordia, Montréal, Canada) for discussions and helpful comments on the manuscript. Thanks to Claire Jacquelin, and Maria Corrimaya (UQAM, Montréal, Canada) for technical support. Some of the strains were provided by the *Caenorhabditis* Genetics Center, which is funded by NIH Office of Research Infrastructure Programs (P40 OD010440)

2.8 Tables

Table 2.1 : Embryonic lethality and arrest of non-elongated larvae in *pix-1 and pak-1* mutants

Allele	18°C			25.5 °C		
	Emb (%)	Lva (%)	n	Emb (%)	Lva (%)	n
Wt	0	0	709	0.5	0	2367
pix-1 (ok982)	6	7	1140	11	15	679
pix-1 (gk416)	1	6	713	2.14	8.5	1216
pix-1(gk416);sajEx1[pix-1p ::pix-1::GFP; rol-6]	-	-	-	1.2	2.0	917
pak-1(ok448)	1	12	2502	3	25.6	264

Table 2.2 : Genetic interactions of *pix-1* and *pak-1* with *mel-11* and *let-502* mutants

		18°C			25.5°C		
	Genotype	early elongation arrest (%)	Lva (%)	n	early elongation arrest (%)	Lva (%)	n
1	*wt*	0	0	531	0	0	323
2	*pix-1(gk416)*	0	5	420	0	8,5*	1190
3	*mel-11(it26)*	98$	0	508	100$	0	65
4	*mel-11(it26); pix-1(gk416)*	0	3	100	9,7$$	40,3***	62
5	*let-502(sb118ts)*	0	0	645	7,9	91,2**	353
6	*let-502(sb118ts); pix-1(gk416)*	18,1	2,5	764	89	11**	373
7	*mel-11(it26); let-502(sb118ts)*	96	0	905	24	0	487
8	*mel-11(it26); let-502(sb118ts); pix-1(gk416)*	29,8	2,2	359	43,1	31*	297
9	*pak-1(ok448)*	0	12	1714	0	25,8*	256
10	*mel-11(it26); pak-1(ok448)*	98	0	763	100	0	931
11	*let-502(sb118ts); pak-1(ok448)*	1	90	2417	100	0	2003
12	*mel-11(it26); let-502(sb118ts); pak-1(ok448)*	100	0	1066	100	0	891

Early elongation arrest include embryos arresting between comma and 1.75-fold with or without rupturing

* arrested larvae present a *pix-1(gk416)* specific morphology (Figure 1A)

** arrested larvae present a *let-502 (sb118ts)* specific morphology (Figure 1A)

*** late elongation arrest without hatching

$ all arrested embryos rupture

$$ 0% rupture

2.9 Figures

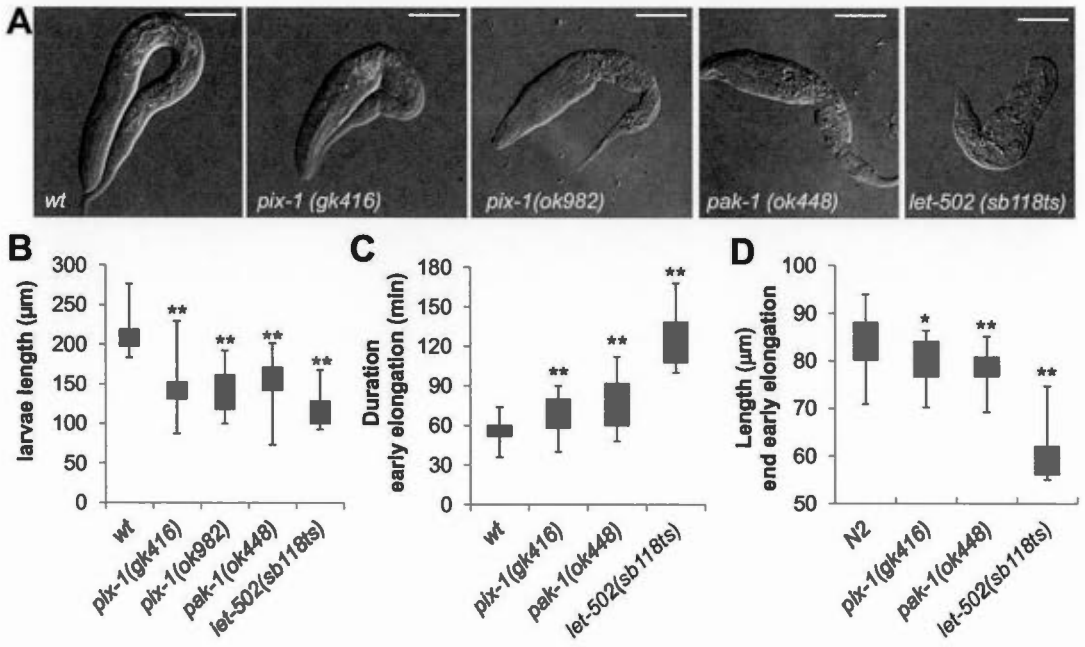

Figure 2.1 : *pix-1* and *pak-1* control early elongation.

A) Arrested larvae of *pix-1(gk416)*, *pix-1(ok982)*, *pak-1(ok448)* and *let-502(sb118ts)* mutants grown at 25.5°C. Bar = 25 µm. **B)** Box-plot representing the distribution of sizes of arrested larvae in mutant populations grown at 25.5°C. The box-plot represents the min, max, 25th, 50th (median) and 75th percentile of the population. Distribution of *wild-type* animals (*wt*) has been established using N2 L1 larvae synchronized by starvation after hypochlorite treatment. **C)** Box-plot representing the distribution of the duration in minutes of early elongation for *wt* and mutants embryos. Embryos are collected through dissection of hermaphrodites grown at 25.5°C. Embryonic development is recorded at 23-24°C. **D)** Box-plot representing the distribution of the length of embryos (in µm) at the end of early elongation. The same population of embryos was used to generate data presented in panel C and D. Student's T-test *p-values* are indicated

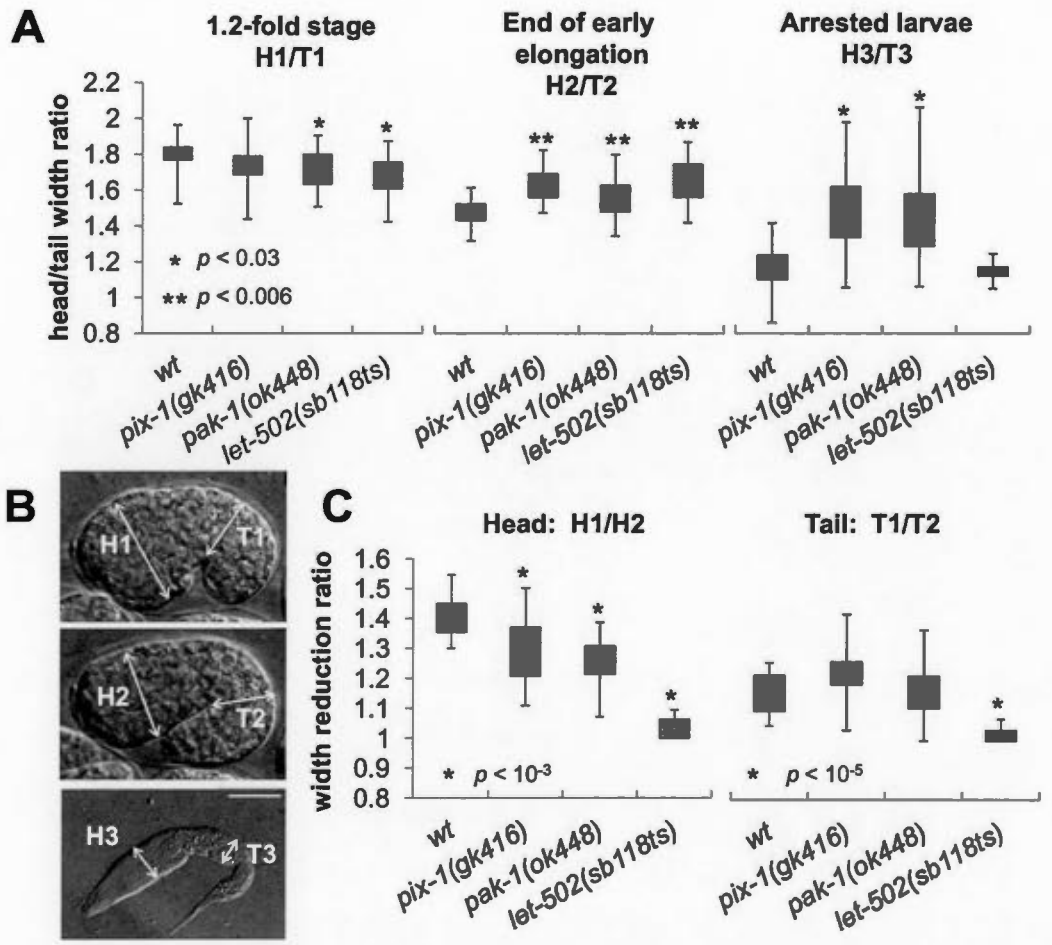

Figure 2.2 : *pix-1, pak-1* and *let-502* control the head to tail width ratio of elongating embryos.

Head (H) and tail (T) width are measured on 1.2-fold stage embryos (H1 and T1); at the end of early elongation (H2 and T2) and in arrested larvae (H3 and T3). In all panels of this figure animals were grown at 25.5°C. Embryos were collected through dissection of hermaphrodite grown at 25.5°C. Embryonic development is then recorded using 4-dimensional microscopy at 23-24°C. **A)** Distribution of ratio between the head and tail width of embryos at 1.2-fold stage (H1/T1; left panel), at the end of early elongation (H2/T2; middle panel) and of arrested larvae (H3/T3; right panel) in *wt*, *pix-1(gk416)*, *pak-1(ok448)* and *let-502(sb118ts)* mutants. **B)** Localisation of measured areas in embryos and larvae **C)** Distribution of the head (H1/H2) and tail (T1/T2) width reduction ratios during early elongation. The box-plots represent the min, max, 25th, 50th (median) and 75th percentiles of the populations. Student's T-test *p-values* are indicated

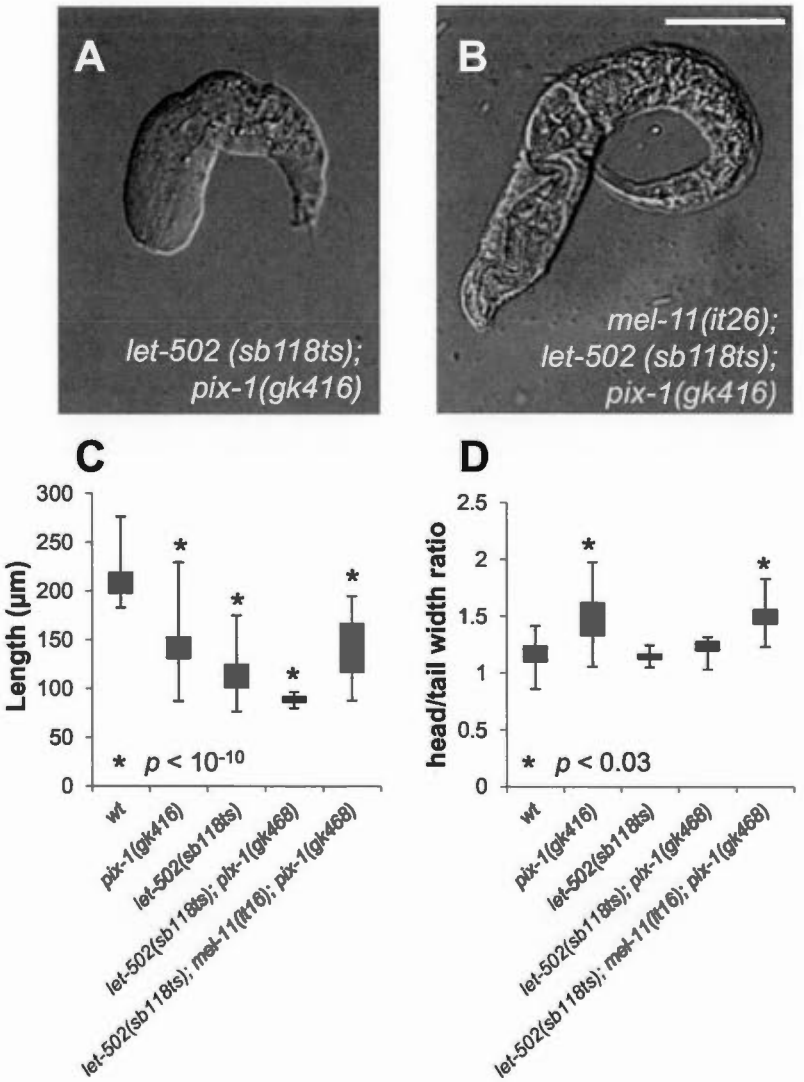

Figure 2.3 : *pix-1(gk416)* controls early elongation in parallel with *mel-11/let-502*.

A) Morphology of *let-502 (sb118ts); pix-1(gk416)* and **B)** *mel-11(it26); let-502 (sb118ts); pix-1(gk416)* arrested larvae grown at 25.5°C. **C)** Distribution of sizes of arrested larvae in mutants' populations, at 25.5°C. Distribution of wild-type animals (*wt*) has been established using N2 L1 larvae synchronized by starvation after hypochlorite treatment. **D)** Distribution of ratio between the head and tail width of arrested larvae in mutant populations. The box-plot represents the min, max, 25th, 50th (median) and 75th percentiles of the population. Student's T-test *p-values* are indicated

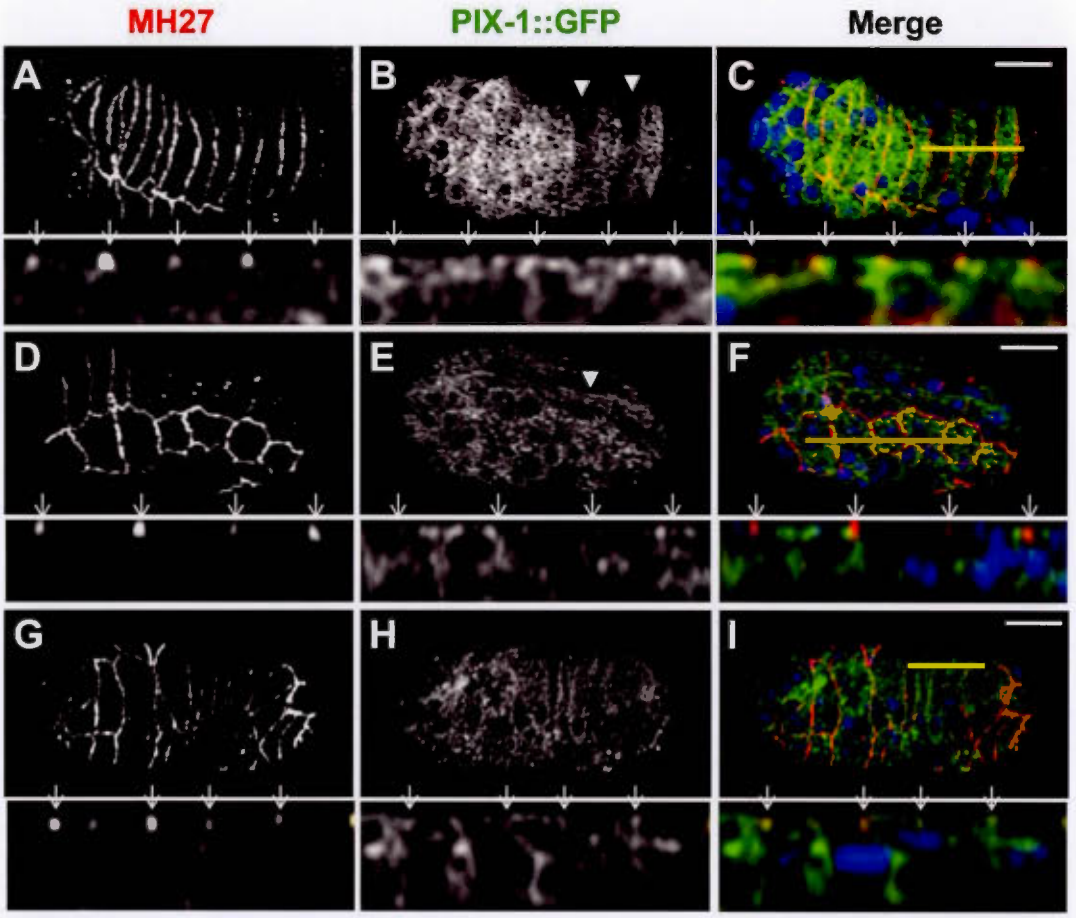

Figure 2.4 : PIX-1 is homogeneously distributed in the cytoplasm and at the cell periphery of hypodermal cells.

A-I) Immunostaining of *pix-1(gk416); sajEx1[pix-1p::pix-1::gfp]* expressing embryos with MH27 antibodies (**A, D, G** and red in merge panel **C, F, I**) and anti-GFP antibodies (**B, E, H** and green in merge panel **C, F, I**). Lower panel of each view correspond to orthogonal views of embryos Z-sectioning. Position of Z-sectioning is indicated in upper panel by a yellow line in dorsal (**A-C**) and lateral (**D-F**) and ventral (**G-I**) hypodermis. In orthogonal views, arrows point to adherens junctions which partially colocalize with PIX-1::GFP immunostaining. Arrowheads show the decrease in PIX::GFP expression every other cell in the dorsal-posterior hypodermis (at comma stage) in picture **B** (upper panel); Arrow-head indicates dorsal trans-epithelial attachment structures (TEA) in picture **E** (upper panel). Scale bars: 10 µm.

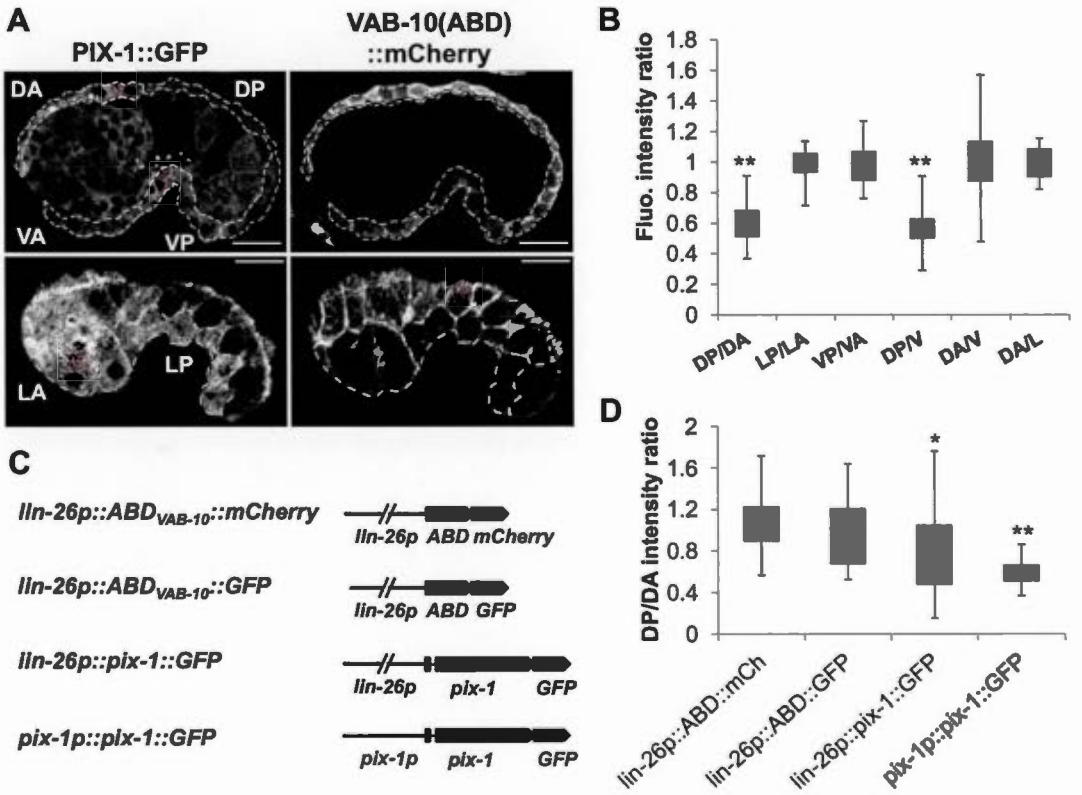

Figure 2.5 : PIX-1::GFP is differentially expressed in hypodermal cells during elongation.

A) Confocal lateral projections of *pix-1(gk416); sajEx1[pix-1p::pix-1::GFP]; mcIs40 [lin-26p::ABDvab-10::mcherry + myo-2p::gfp]* embryos. Dorsal-anterior (DA, upper panel), dorsal-posterior (DP, upper panel), ventral-anterior (VA, upper panel), ventral-posterior (VP, upper panel), lateral-anterior (LA, lower panel) and lateral-posterior (LP, lower panel) hypodermis are surrounded by dashed line and have been identified using *lin-26p::vab-10(ABD)::MCHERRY* hypodermal markers. **B)** Distributions of the dorsal-posterior/dorsal-anterior (DP/DA), lateral-posterior/lateral-anterior (LP/LA), ventral-posterior/ventral-anterior (VP/VA), dorsal-posterior/ventral (DP/V); dorsal-anterior/ventral (DA/V), dorsal-anterior/lateral (DA/L) rates of fluorescence intensity measured in *pix-1(gk416); sajEx1[pix-1p::pix-1::GFP; rol-6]; mcIs40 [lin-26p::ABDvab-10::mcherry + myo-2p::gfp]* embryos between comma and 1.75-fold stages (n = 26 embryos). Similar results were also obtained in *pix-1(gk416); sajIs1[pix-1p::pix-1::GFP; unc-119^{R}]; mcIs40 [lin-26p::ABDvab-10::mcherry + myo-2p::gfp]*. The box-plots represent the min, max, 25th, 50th

(median) and 75th percentiles of the populations. ** T-test comparing ratios to 1 $p <$ 0.01. **C)** Schematic representation of *pix-1::GFP* and ABD_{VAB-10} (control) constructs used to measure the DP/DA intensity ratio reported in panel **D**. DP/DA of animals carrying *mcIs40* (*lin-26p::ABD::mCh* expressing), *mcIs50* (*lin-26p::ABD::GFP* expressing), *sajIs2* (*lin-26p::pix-1::GFP* expressing) or *sajEx1* (*pix-1p::pix-1::GFP* expressing). ratios** T-test comparing DP/DA ratios measured on *pix-1::GFP* expressing embryos to ratio measured in ABD_{VAB-10} expressing transgenics, p <0.01. The box-plots represent the min, max, 25th, 50th (median) and 75th percentiles of populations.

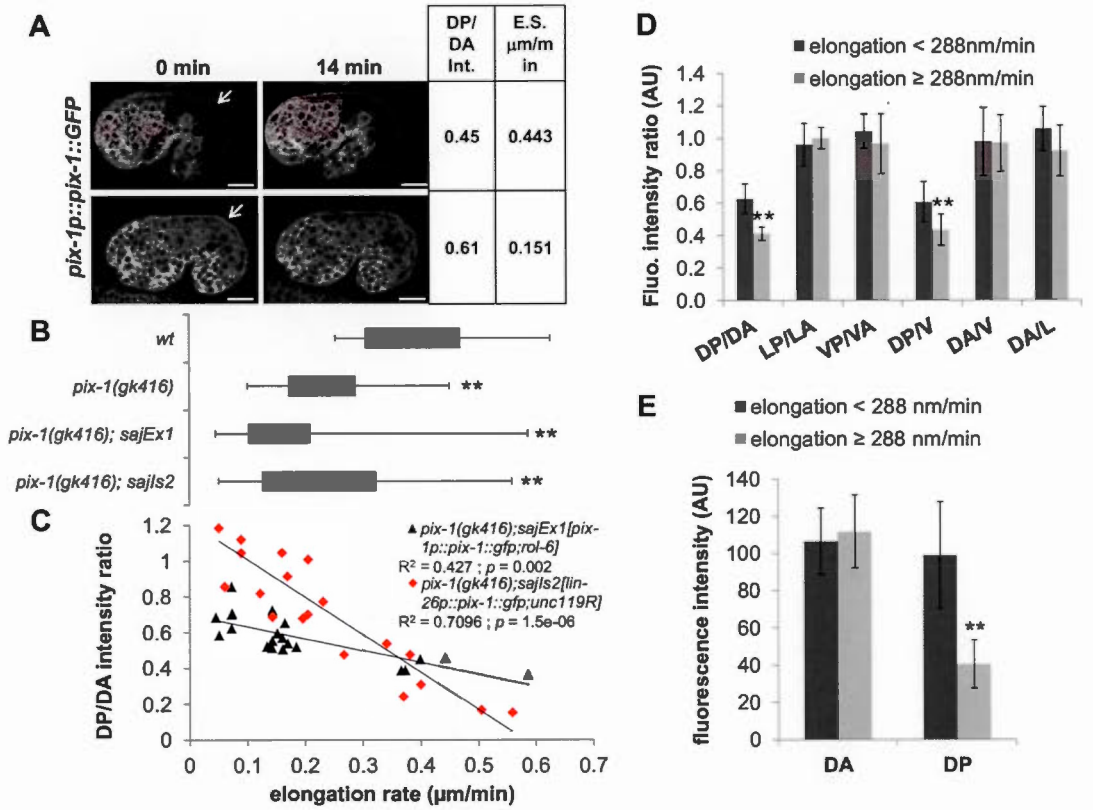

Figure 2.6 : High expression of PIX-1::GFP in dorsal posterior hypodermis is detrimental for elongation rate of embryos.

A) Confocal projections of *pix-1(gk416); sajEx1[pix-1p::pix-1::GFP, rol-6]* at t = 0 min and t = 14 min. The DP/DA fluorescence intensity ratio and elongation rate (in µm/min) are indicated. Arrows indicate the dorsal-posterior hypodermis. Scale bar: 10 µm. **B)** Distribution of elongation rate in µm/min of *wild-type (wt)*, *pix-1(gk416)*, and *pix-1(gk416)* animals carrying *sajEx1[pix-1p::pix-1::GFP, rol-6]* or *sajIs2[lin-26p::pix-1::GFP, unc-119^R]* during early elongation. Elongation rate was measured from 4-dimensional recording of embryonic development between comma and the end of early elongation upon DIC illumination. Box-plots represent the min, max, 25th, 50th (median) and 75th percentile of the populations. ** T-test p <0.01 vs *wt*. **C)** Scatter plot representing the relationship between the dorsal-posterior/dorsal-anterior (DP/DA) intensity ratio of PIX-1::GFP and the elongation rate in µm/min during early elongation of *pix-1(gk416)* embryos carrying *sajEx1[pix-1p::pix-1::GFP, rol-6]* or *sajIs2[lin-26p::pix-1::GFP, unc-119^R]* (n=20 for each line). The spearman correlation (R2) between the elongation rate and the DP/DA ratio are indicated, as

well as the *p-values* rejecting the null hypothesis being that the two values are not significantly correlated. Similar results were obtained for *pix-1(gk416)* animals carrying *sajIs1* and *sajIs3* (see methods). **D)** DP/DA, lateral-posterior/lateral-anterior (LP/LA), ventral-posterior/ventral-anterior (VP/VA), dorsal-posterior/ventral (DP/V), dorsal-anterior/ventral (DA/V) and dorsal-anterior/lateral (DA/L) fluorescence intensity ratio measured for *pix-1(gk416); sajEx1[pix-1p::pix-1::GFP, rol-6]* embryos elongating at a *wt*-rate (elongation ≥ 288nm/min) or elongating slower (elongation < 288nm/min) during early elongation. Bar correspond to the mean and error bars to the standard deviation. ** T-test p-value <0.01. **E)** PIX-1::GFP fluorescence intensity (AU) was measured in DA and DP hypodermal cells of embryos elongating at a *wt*-rate (elongation ≥ 288nm/min) or elongating slower (elongation < 288nm/min) during early elongation (see methods). ** T-test p-value <0.01.

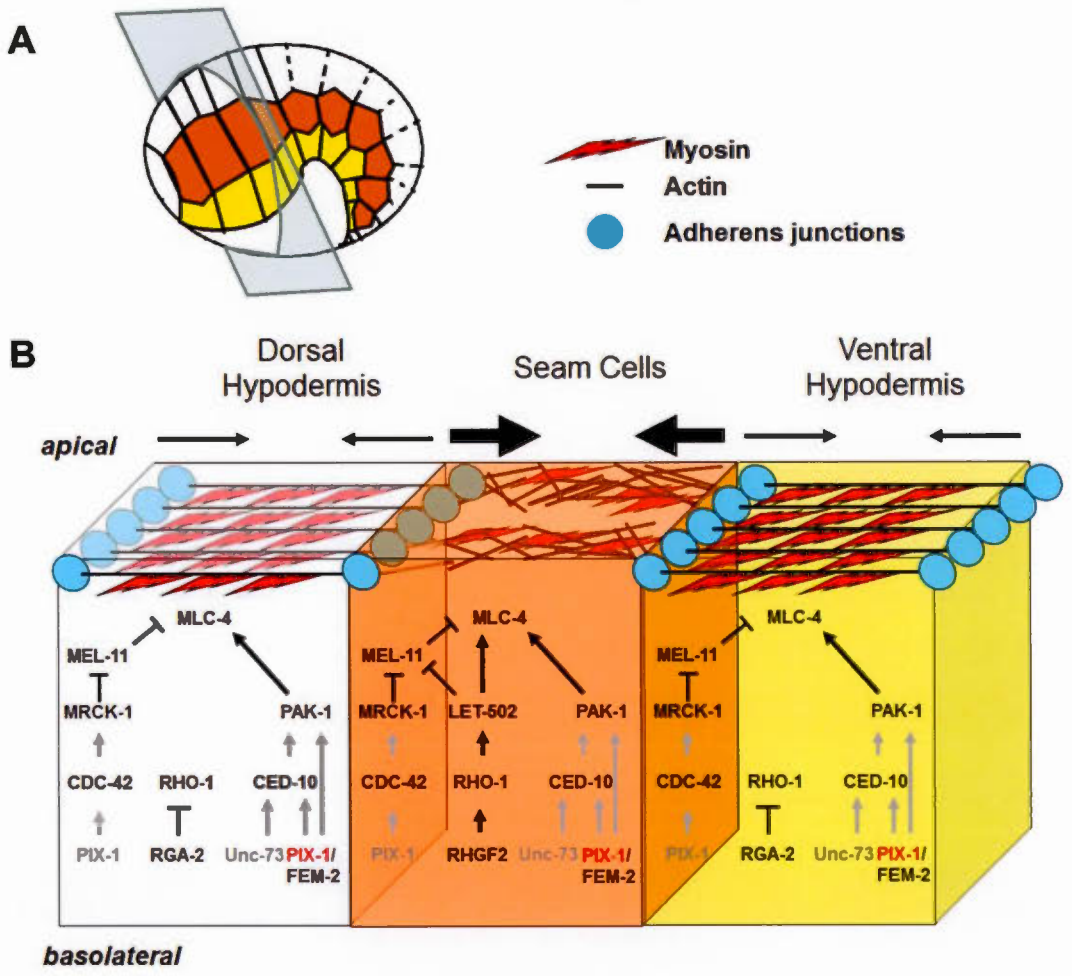

Figure 2.7 : Model for signaling pathways controlling embryonic elongation.

A) Schematic representation of an embryo during early elongation. Anterior is at the left and dorsal side on the top. Dorsal (white), lateral (orange) and ventral (yellow) hypodermal cells are represented. The blue plan indicates the location of the transversal sectioning of the hypodermal cells represented in panel **B**. **B)** Signaling pathways in the dorsal (white), lateral (orange) and ventral (yellow) hypodermis in the anterior part of the embryo during early elongation. In this model PIX-1 is expressed at similar level in all hypodermal cells of the anterior part of the embryo. While homogenous expression of PIX-1::GFP in these cells rescues elongation defects of *pix-1(gk416)*, we cannot exclude the possibility that *pix-1* may be required only in a subset of these cells. In PIX-1-expressing cells, PAK-1 is activated in a

GTPase-dependant (through activation of CED-10 by PIX-1 and/or UNC-73) or in a GTPase-independent manner (by PIX-1 directly). LET-502 is activated only in seam cells through activation of RHO-1 by RHGF-2. PIX-1 may also activate MRCK-1 through CDC-42 upstream of MEL-11. Following this model, the contraction pressure applied on the actin cytoskeleton is similar in ventral and dorsal hypodermis and higher in seams cells. Arrows represent relative contraction forces within each cell.

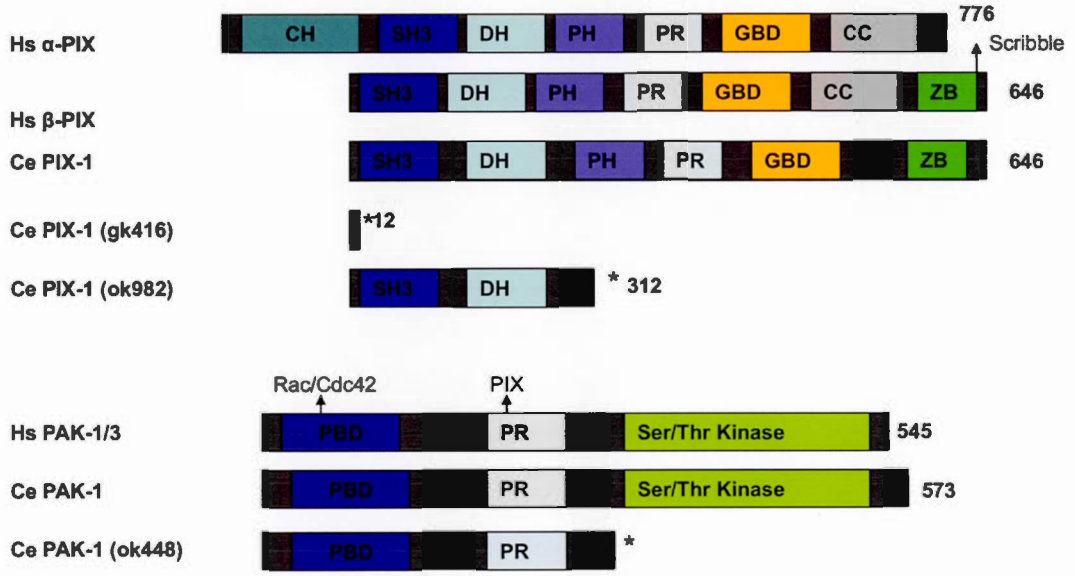

Supplementary Figure 2.1 : Schematic representation of human (Hs) and C. elegans (Ce) PIX and PAKs.

Modular structure has been identified using the SMART tool (www.smart.org) or by alignment of consensus sequence using CLUSTALW. Binding-domains for protein partners reported in the literature are indicated. Proteins coded by C. elegans mutant alleles are indicated. * indicate the location of translation arrest. CH: calponin homology domain; SH3: src homology domain; DH: dbl homology domain; PH: Pleckstrin homology domain; PR: Proline Rich sequence, GBD: GIT-binding domain, CC: coil-coiled domain, ZB: PDZ binding domain, PBD: GTPase binding domain; Ser/Thr kinase: serine threonine kinase domain.

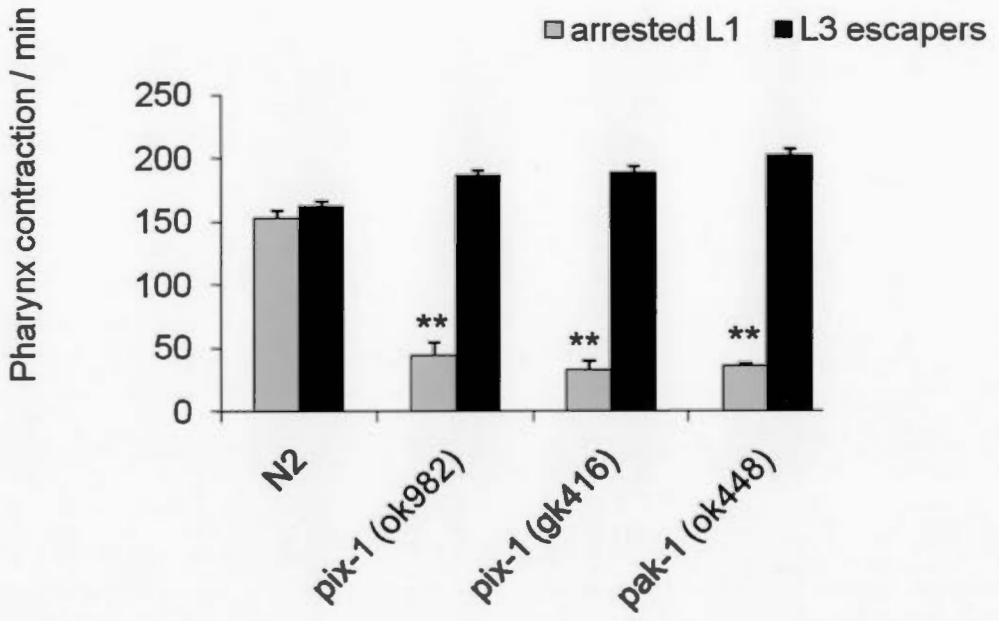

Supplementary Figure 2.2 : pix-1(ok982) and pak-1(ok448) arrested larvae present severe pharynx pumping defects.

48 hours after egg-laying, pharynx pumping rates were counted on arrested L1 animals and escaper L3 animals moving freely on a bacterial lawn. At least 10 animals per genotype were examined during 15-sec periods. N=3. ** T-test p (mutant/N2) <0.001.

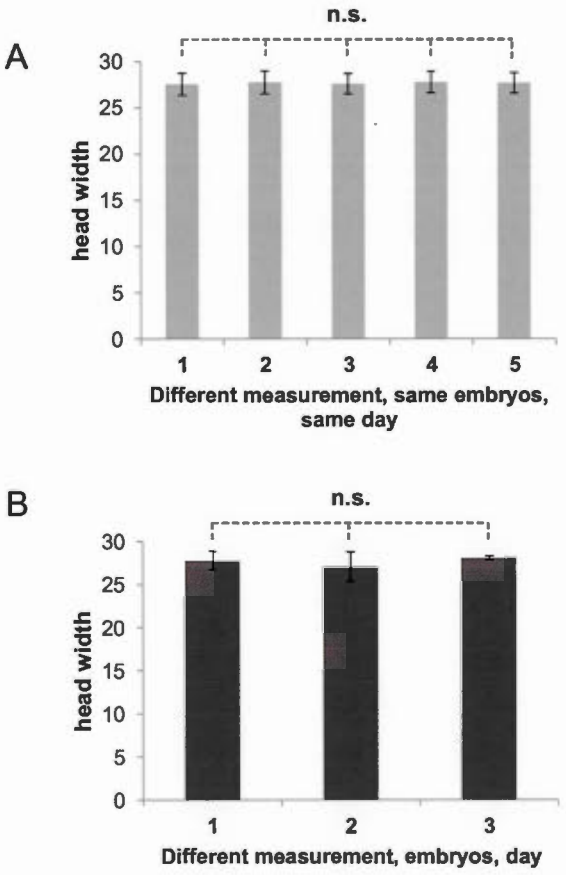

Supplementary Figure 2.3 : Establishment of embryo width measurement as a robust metrics to characterize embryonic elongation.

A) We tested the robustness and reproducibility of head width measurement of embryos. To do so, head width was measured five times on a given population of wt embryos at 1.2-fold stage (n=12 embryos). Means and standard deviation were calculated and Brown-Forsythe test (using R statistical package) was used to test for homogeneity of variances among the five different groups of measurement. This test revealed no significant variance difference amongst the measurements (F-test p-value > 0.5). **B)** The repeatability and batch effect of our measurements were assessed through measurement of the head width of wt embryos at 1.2-fold stage from 4D-recording done at three different days (n=12 embryos). Means and standard deviation were calculated and Brown-Forsythe test was used to test for homogeneity of variances among the three different groups of measurements. This test revealed no significant variance difference amongst the measurements (F-test p-value > 0.5). Similar results were obtained for tail width measurements and for measurement done at different stages of early elongation (data not shown).These data indicate that the significant differences observed between genotypes using head-width, tail-width and head/tail width ratio measurements are not due to measurement variability and batch effect.

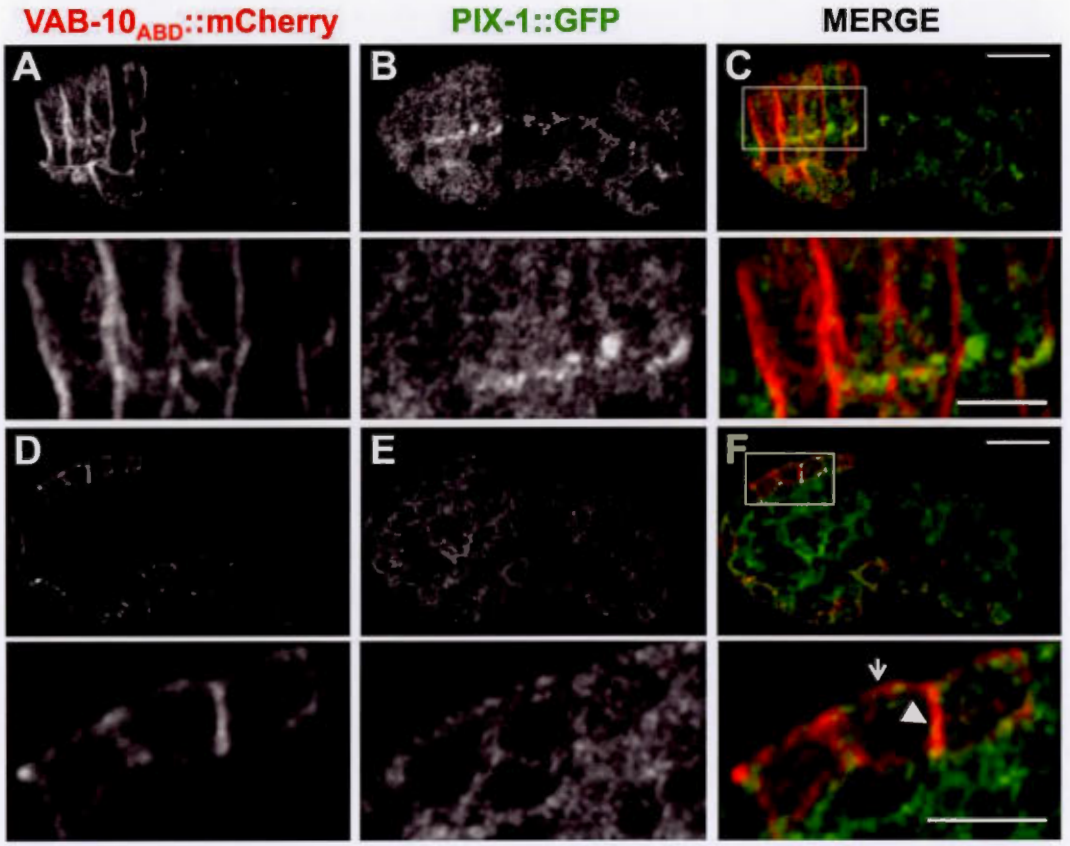

Supplementary Figure 2.4 : PIX-1 is homogeneously distributed in the cytoplasm and at the cell periphery of hypodermal cells during early elongation.

Confocal microscopy analysis of *pix-1(gk416)* embryos carrying *sajEx1[pix-1p::pix-1::gfp; rol-6]; mcIs40[lin-26p::ABDvab-10::mCherry + myo-2p::gfp]. PIX-1::GFP* is observed in **B** and **E** (green in **C, F**) and *VAB-10$_{ABD}$::mCherry* in **A** and **D** (red in **C, F**). Embryos are oriented anterior to the left and dorsal up. Enlarged views (lower panels) show areas indicated by white rectangles in upper panels. Apical and basolateral membrane are indicated by arrow and arrowhead, respectively (**L**, lower panel). Scale bars upper panels: 10 µm; lower panels 5 µm.

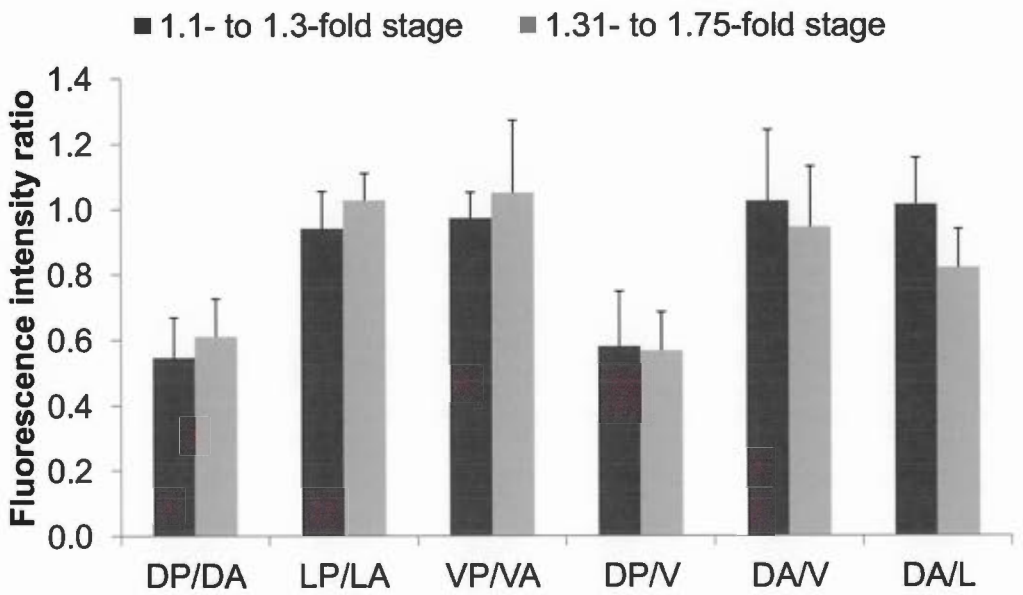

Supplementary Figure 2.5 : PIX-1::GFP intensity ratio are constant throughout early elongation.

Dorsal-posterior/dorsal-anterior (DP/DA), lateral-posterior/lateral-anterior (LP/LA), ventral-posterior/ventral-anterior (VP/VA), dorsal-posterior/ventral (DP/V), dorsal-anterior/ventral (DA/V) and dorsal-anterior/lateral (DA/L) fluorescence intensity ratio were measured as detailed in methods and in Figure 5 in *pix-1(gk416); unc-119; sajIs2[lin-26p::pix-1::GFP,unc-119^{R}]* embryos during early elongation. Bar correspond to the mean and error bars to the standard deviation. * T-test < 0.05.

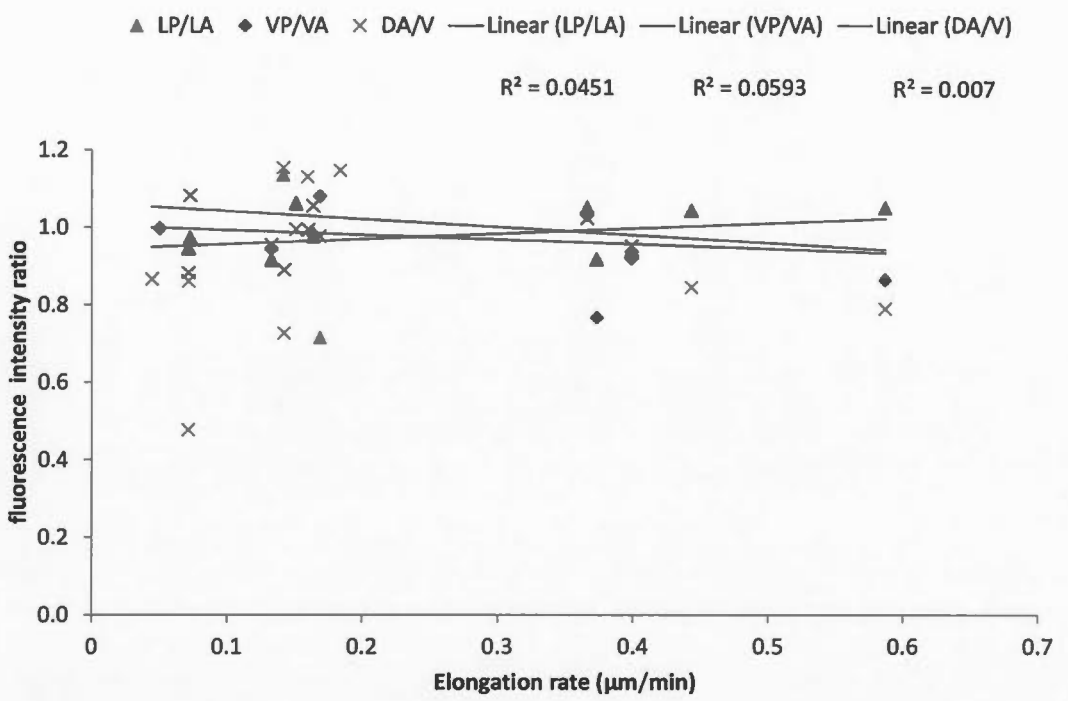

Supplementary Figure 2.6 : Only DP/DA ratio inversely correlates with the elongation rate of the embryos during early elongation.

Scatter plot representing the relationship between the lateral-posterior/lateral-anterior (LP/LA), ventral-posterior/ventral-anterior (VP/VA), dorsal-posterior/dorsal-anterior (DP/DA) and dorsal-anterior/ventral (DA/V) intensity ratio of PIX-1::GFP and the elongation rate in µm/min during early elongation of *pix-1(gk416); sajEx1[pix-1p::pix-1::GFP, rol-6]* embryos (n=20). The spearman correlation (R2) between the elongation rate and the PIX-1::GFP intensity ratio are indicated, as well as the *p-values* rejecting the null hypothesis being that the two values are not significantly correlated. Similar results were obtained from two independent transgenic lines.

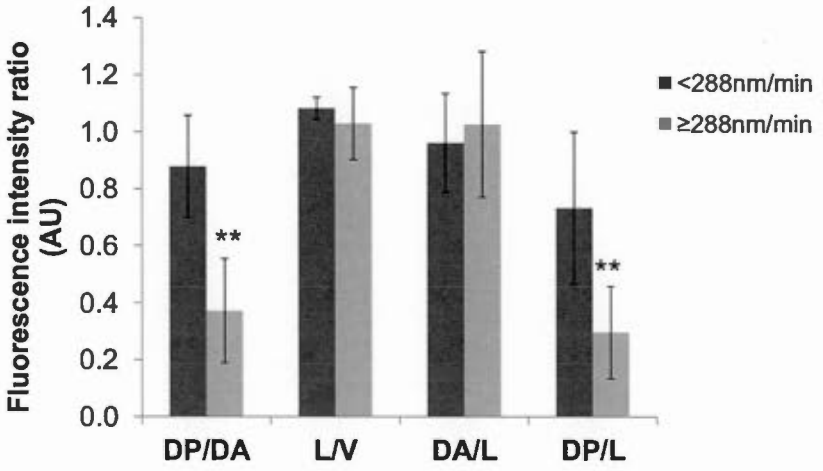

Supplementary Figure 2.7 : High expression of PIX-1::GFP in dorsal-posterior hypodermis is detrimental for elongation rate of embryos.

Dorsal-posterior/dorsal-anterior (DP/DA), lateral/ventral (L/V), dorsal-anterior/lateral (DA/L) and dorsal-posterior/lateral (DP/L) fluorescence intensity ratio were measured as detailed in methods and in Figure 5 in *pix-1(gk416); unc-119; sajIs2[lin-26p::pix-1::GFP;unc-119^{R}]* embryos elongating at a *wt*-rate (elongation ≥ 288nm/min) or elongating slower (elongation < 288nm/min) during early elongation. Bar correspond to the mean and error bars to the standard deviation. ** T-test p-value <0.01.

CHAPITRE III

DÉVELOPPEMENT DE NOUVEAUX PARAMÈTRES POUR CARACTÉRISER L'ÉLONGATION EMBRYONNAIRE DU NÉMATODE *CAENORHABDITIS ELEGANS*

Le travail de ce chapitre a été publié, en mars 2016, dans *The Journal of Visualized Experiments* (*JoVE*) (109), e53712. (Voir la version publiée en Annexe B).

Dans le chapitre II nous avons développé des méthodes permettant une analyse morphologique précise des embryons en élongation précoce. Pour cela, nous avons mis au point la mesure du ratio tête/queue, de la longueur des embryons à la fin de l'élongation précoce, et de la longueur des larves arrêtées au stade L1. Le présent chapitre est un article de méthode décrivant étape par étape, depuis l'acquisition jusqu'à l'analyse des résultats, la marche à suivre effectuer ces différentes mesures.

Contribution des auteurs :
Emmanuel Martin : conception, design, acquisitions, analyse et interprétation des résultats, rédaction du manuscrit, montage des figures et révision de l'article ; expériences : (protocole 1 et 2) mesure longueur des embryons, ratio tête/queue, mesure des larves (Figures 1, 2, 4, 5A). Vidéo : Introduction, captures d'écran protocoles 1 et 2. *Olivier Rocheleau-Leclair* : conception, design, acquisitions, analyse ; expériences : (protocole 3) mesure des larves en utilisant le COPAS (Figure 3). Vidéo : expérience protocole 3, conclusion. *Sarah Jenna* : conception, design, analyse et interprétation des résultats, rédaction du manuscrit, montage des figures et révision de l'article ; expériences : (protocole 3) mesure des larves en utilisant le COPAS et analyses (Figures 3, 5). Vidéo : captures d'écran protocole 3.

NOTE : Les références de l'article sont incluses dans la bibliographie générale.

3.1 Résumé

La dissection des voies de signalisation contrôlant les processus morphogéniques durant le développement embryonnaire nécessite des méthodes de mesure fiables et sensibles. L'élongation embryonnaire du nématode *Caenorhabditis elegans* est un stade développemental tardif qui consiste en une élongation de l'embryon dans son axe longitudinal. Cette étape est contrôlée par la communication intercellulaire entre les cellules de l'hypoderme et les muscles sous-jacents et dépend d'une signalisation qui contrôle la morphologie des cellules de l'hypoderme *via* le remodelage du cytosquelette et des jonctions cellulaires. La mesure de la létalité embryonnaire et de l'arrêt développemental au stade larvaire 1, tout comme l'altération du cytosquelette et des structures d'adhésion cellule-cellule dans l'hypoderme et les muscles sont des phénotypes classiques utilisés depuis plus de 25 ans pour disséquer les voies de signalisation. Cependant les études récentes ont requis de nouveaux paramètres de mesure pour cibler spécifiquement l'élongation précoce ou l'élongation tardive et également caractériser les défauts morphogéniques le long de l'axe antéropostérieur de l'embryon. Dans cet article, nous détaillons un protocole permettant la mesure précise de la longueur et de la largeur des embryons en élongation, ainsi que la longueur de larves synchronisées. Ces méthodes sont des outils utiles pour identifier des gènes contrôlant l'élongation, pour tester si ces gènes contrôlent l'élongation précoce ou tardive, et s'ils sont requis uniformément le long de l'axe antéropostérieur de l'embryon.

Manuscrit

NOVEL METRICS TO CHARACTERIZE EMBRYONIC ELONGATION OF THE NEMATODE *CAENORHABDITIS ELEGANS*

Emmanuel Martin, Olivier Rocheleau-Leclair and Sarah Jenna

Department of Chemistry, Pharmaqam, Biomed, Université du Québec à Montréal (UQÀM), Montréal, Québec, H3C 3P8, Canada

* Corresponding Author: jenna.sarah@uqam.ca

3.2 Abstract

Dissecting the signaling pathways that control the alteration of morphogenic processes during embryonic development requires robust and sensitive metrics. Embryonic elongation of the nematode *Caenorhabditis elegans* is a late developmental stage consisting of the elongation of the embryo along its longitudinal axis. This developmental stage is controlled by intercellular communication between hypodermal cells and underlying body-wall muscles. These signaling mechanisms control the morphology of hypodermal cells by remodeling the cytoskeleton and the cell-cell junctions. Measurement of embryonic lethality and developmental arrest at larval stages as well as alteration of cytoskeleton and cell-cell adhesion structures in hypodermal and muscle cells are classical phenotypes that have been used for more than 25 years to dissect these signaling pathways. Recent studies required the development of novel metrics specifically targeting either early or late elongation and characterizing morphogenic defects along the antero-posterior axis of the embryo. Here, we provide detailed protocols enabling the accurate measurement of the length and the width of the elongating embryos as well as the length of synchronized larvae. These methods constitute useful tools to identify genes controlling elongation, to assess whether these genes control both early and late phases of this stage and are required evenly along the antero-posterior axis of the embryo.

Keywords: morphogenesis, *Caeanorhabditis elegans*, elongation, 4-D microscopy, flow cytometry

3.3 Introduction

For nearly 50 years the nematode *Caenorhabditis elegans* established itself as a powerful model to study important questions in development, neurobiology, evolution, host-pathogen interactions etc. (Corsi *et al.*, 2015) The strength of this model in the study of development lies in: its short life cycle of 3 days; the ease with which these animals can be genetically altered; its transparency that enables the observation of cell displacement and morphology in living animals and its development that is mostly extra-uterine. The developmental stages of the nematode involve embryogenesis and four larval stages (L1 to L4), followed by adulthood. During embryonic development, epidermal morphogenesis drew considerable attention for its ability to enable a better understanding of how epithelial cells migrate as a group, how they reorganize their junctions and modify their individual morphology as well as their relative positioning within a functional epithelium. Epidermal morphogenesis is divided into four stages: dorsal intercalation consisting in the reorganisation of dorsal epidermal cells, referred to as the hypodermis; ventral enclosure, consisting in migration of ventral hypodermal cells towards the ventral midline thus encasing the embryo in an epithelial cell monolayer; early and late elongation transforming the bean-shaped embryo into vermiform larvae. Following morphogenesis, embryos hatch and L1 larvae start feeding using available bacteria in their immediate environment.

Embryonic elongation is therefore a late phase of embryonic development. It consists of the extension of the embryo along its longitudinal axis and a reduction of its transverse diameter. This involves a dramatic modification of the shape of the hypodermal cells. Elongation is divided into an early and a late phase. The early phase starts at the comma stage and ends when body-wall muscles start contracting at 1.75-fold stage in *wild-type* (*wt*) embryos – corresponding to embryos that are 1.75-fold in length compared to non-elongated embryos. Morphogenic processes occurring

at that stage are mainly driven by contraction of filamentous actin bundles (FBs) located at the apical pole of hypodermal cells that drive their elongation along the antero-posterior axis of the embryo (Priess et Hirsh, 1986). Contraction of FBs is control by phosphorylation of myosin-light chains by three kinases LET-502/ROCK, MRCK-1 and PAK-1 [5]. The late phase of the elongation, starts when body-wall muscles become functional and start contracting. It involves mechanotransduction signaling from the body-wall muscles to the dorsal and ventral hypodermal cells and ends when animals hatch (Zhang *et al.*, 2011).

Elongation defects are generally characterized by the percentage of animals dying as embryos (Embryonic lethality; Emb) and those arresting their development as L1 larvae (Larval arrest phenotype; Lva) and being significantly shorter than *wt.* Identification of the stage of developmental arrest requires microscopic observation of dead embryos and arrested Larvae (Piekny *et al.*, 2000 ; Diogon *et al.*, 2007 ; Gally *et al.*, 2009 ; Zhang *et al.*, 2011).

It was recently shown that several genes, such as the Cdc42/Rac regulators and effectors *pix-1* and *pak-1,* control morphogenic processes during both early and late elongation (Zhang *et al.*, 2011 ; Martin *et al.*, 2014). We also recently showed that morphogenic processes differ along the antero-posterior axis of the embryos during early elongation (Zhang *et al.*, 2011 ; Martin *et al.*, 2014). These findings motivated the development of novel metrics specifically targeting early or late elongation stages and other metrics enabling the characterization of the morphology of embryos along their antero-posterior axis during early elongation.

These novel methods consist in measuring the length of embryos at the beginning and at the end of early elongation as well as the width of their heads and tails.(Martin *et al.*, 2014) Two protocols were also developed to measure the length of newly hatched larvae, synchronized at L1 stage (Martin *et al.*, 2014).

The eggshells of the embryos protect them against alkaline hypochlorite treatment while larvae, adults and bacteria present in the culture media are dissolved by the treatment. This treatment is then used to purify embryos from a non-synchronized population containing a majority of well-fed adults (Sulston et Hodgkin, 1988). Food restriction is used to synchronize newly hatched larvae. Measuring the length of these larvae is then used to detect elongation defects. This measurement is preferred over the measurement of arrested larvae on culture plates because larvae that hatch from non-fully elongated embryos can recover to "normal length" when feeding but will maintain their reduced size when arrested in the absence of food.

Here, we present detailed protocols enabling the measurement of the length of elongating embryos as well as the width of their head and tail using time-lapse DIC microscopy and image analysis (Protocol 1). We also provide detailed protocols to measure the length of synchronized larvae using image analysis (Protocol 2) and Flow-Cytometry (Protocol 3).

3.4 Protocol

3.4.1 Characterization of early elongation defects in *wt* and mutant animals

A. Mounting embryos for Normarski DIC microscopy

A.a. Prepare the following culture media and material:

A.a.a. M9 Buffer, dissolve 12.8 g/L $Na_2HPO_4 \cdot 7H_2O$, 3 g/L KH_2PO_4, 5 g/L NaCl, 0.25 g/L $MgSO_4 \cdot 7H_2O$ in distilled water and Autoclave to sterilize

A.a.b. NGM plates, dissolve 3 g/L NaCl, 16 g/L agar, 2.5 g/L bactopeptone in ddH_2O. Autoclave and add 1 m*M* $MgSO_4$, 1 m*M* $CaCl_2$, 1 m*M* phosphate buffer and 5 µg/mL cholesterol. Pour 6ml of NGM per 60 mm dishes. Allow the medium to solify

for 24h at room temperature. Add a few drops of a saturated culture of *E. coli* OP50 bacteria grown in Luria broth (LB). Let the bacteria grow for 48h and store the plates at 4°C.

A.a.c. To generate the worm pick, mount a 0.01" diameter platinum wire on a short Pasteur pipette. Fasten the platinum wire to the extremity of the glass pipet by heating this extremity with a benzene burner. Flatten the extremity of the wire to generate a sort of shovel.

A.b. Grow the worm strain on 60 mm NGM plates with OP50 at 20°C.

NOTE: Thermosensitive alleles may require growing the animals at non-permissive temperatures at up to 25.5°C. Plates should contain many young adults and still plenty of food in order to pursue the protocols.

A.c. Place a microscope slide between two spacer slides covered by two layers of masking tape (Figure 1A).

A.d. Prepare a 3% agarose solution (weight/volume) in M9 buffer by dissolving 0.6 g of agarose powder in 20 ml M9 buffer by heating in the microwave during 30 sec. Allow the solution to cool down for 5 min.

NOTE: The agarose solution can be used for a few days after melting in a microwave. It can also be aliquoted and stored at 4°C for weeks.

A.e. Place a drop of hot 3% agarose solution on the glass slide located between the two spacer-slides. Avoid forming bubbles.

A.f. Rapidly cover the agarose with another slide as shown in Figure 1B and press down gently. The top slide will flatten the agarose drop and generate a pad with the thickness of two layers of masking tape.

A.g. Allow the agarose to solidify for at least 1 min at room temperature or until the embryos are ready to be transferred to the pad.

A.h. Using a worm pick, transfer 20 to 30 well fed young adults from the NGM-plate into a micro-centrifuge tube containing 400 µl of M9 buffer.

A.i. Allow the worms to sediment by gravity for approximately 5 min and remove the supernatant using a micropipette. This step aims to remove the maximum of bacteria picked with the nematodes.

A.j. Add 200 µl of M9 buffer to each tube.

A.k. Using a Pasteur pipette, transfer the content of the tube (buffer and nematodes) to a watch glass.

A.l. Use one or two 25G 5/8" needles to cut the animals at the mid-body section (between the spermatheca and the vulva).

NOTE: A scalpel blade can also be used as an alternative to needle(s). Do this on swimming nematodes and may require some practice. The idea is to use needles as scissors or as a knife depending how many needles are used. Once the animals are cut open, hermaphrodites release their embryos into the buffer

A.m. Concentrate embryos at the center of the watch glass through generation of a circular vortex within the liquid.

A.n. Remove most of the M9 from the watch glass using a micropipette. Leave approximately 30 µl of M9 with the embryos.

A.o. Remove the slide covering the agarose pad (Figure 1B) by sliding it off the pad.

A.p. Cut the pad with a razor blade in order to be able to completely cover it with a coverslip (Figure 1C).

A.q. Using a Pasteur pipette, transfer all the embryos (and worm debris) onto the agarose pad.

A.r. Group the embryos at the center of the pad using an eyelash glued at the extremity of a tip used for 200 µl micropipettes.

A.s. Slowly place a coverslip on the pad avoiding bubble formation and seal it.

NOTE: Several sealers can be used. We use drawing gum found in art and craft stores (usually used as masking gum for aquarelle painting). This gum is used because it is hydrophilic and solidifies reasonably fast and is not toxic for the worms. Slides can also be sealed with nail polish or VALAP (mixture made of Vaseline, Lanolin and Parafin wax).

A.t. Allow the drawing gum dry for approximately 15 min.

B. Recording early elongation using four-dimensional Normarski DIC microscopy

NOTE: The objective of this step is to record early elongation from comma to the beginning of late elongation - defined as the moment when the body-wall muscles start contracting. We also aim to record more than one embryo at the time. Eight hours of recording are usually required to record early elongation for a group of non-synchronized embryos.

B.a. Place the mounted-slide on the stage of a microscope. Ensure that the microscope is equipped with 10X and 60X objectives as well as DIC lenses, prism, camera and capture software enabling time-lapse microscopy and generation of Z-stacks (automated Z-platform).

NOTE: ensure that the temperature is constant between 20 and 23°C in the microscopy room. A heating-cooling chamber may be required on the microscope stage, especially when using thermosensitive mutants.

B.b. Identify a group of embryos at pre-morphogenesis stages using the 10X objective.

B.c. Once located, slide off the 10X objective and add a drop of oil immersion on the slide.

B.d. Using the 60X objective, identify the top and the bottom of embryos to setup the Z-stack imaging parameters.
NOTE: Do not hesitate to set the Z-stack larger than the thickness of the embryos. Set the distance between two adjacent planes as 0.8 µm. This will enable to cover the total depth of the embryos in 35 to 50 Z-plans.

NOTE: If the microscope contains an automated xy platform, embryos located at different locations of the pad could be recorded simultaneously. To do so, record xy

coordinates of each location on the pad you wish to analyze during the course of the experiment. Make sure to select the xy when setting the recording parameter and follow the rest of the protocol as indicated. Thin Z-sectioning of the embryo during recording is not necessarily required for the measurements detailed in this protocol. Recording embryonic development of *wt* and mutant animals with the maximum resolution is however a good practice in order to build a library of recordings able to support additional analyses.

B.e. Set up the time-lapse with 2 minute intervals between two acquisitions lasting 8 hours.

NOTE: The exposure time will depend on the light intensity set for the microscope. Cell movement during early elongation is very slow; exposure-time could be approximately one frame per second or less. If the embryos are at early morphogenesis stages (dorsal intercalation, ventral enclosure), early elongation would be recorded within 1 hour. Make sure light shutter is closed between each acquisition.

B.f. Run the acquisition and save it.

C. Measurement of early elongation defects using image analysis

C.a. Open Fiji-ImageJ software (v1.48o – http://fiji.sc/Fiji). Open the acquisition file using the menu File/Open. Choose the "Hyperstack" viewing mode and press OK. In the Lookup tables, adjust the brightness and contrast (B/C) using the Auto mode and press Apply.

C.b. In the menu select Analyze/Set Measurements, select Perimeter. For each embryo, adjust the Z-scale bar to focus on the pharynx of the embryo as shown in Figure 2 A. This will ensure that you focus on the center of the embryo.

C.c. To measure the length of the embryo, adjust the time scale bar to have the embryo of interest at the start of the early elongation (comma stage; Figure 2A). Note the time ("Time-beginning").

C.d. Choose the segmented line tool. Draw a segmented line from the tip of the mouth of the embryo up to the tip of its tail following the midline of the embryo (Figure 2A). Using the menu tab Analyze/Measure, obtain the length of the drawn line ("Length beginning").

C.e. Repeat this measurement for the same embryo at the end of early elongation (moment when muscles start contracting). Note the time ("Time-end") and measure the length of the embryo ("Length-end") as detailed above (Figure 2B).

C.f. The duration (D) of early elongation and the length increase (L) during this stage are calculated as followed:

D = "Time-end"-"Time-beginning"
L = "Length-end" –"Length-beginning"

C.g. To measure the head width, adjust the time scale bar to have an embryo at the stage of interest (1.2-fold stage or end of early elongation). Choose the straight-line tool. Draw the transversal (dorso-ventral axis) midline of the head. This section is the thickest part of the embryo (Figure 2C). Using the menu Analyze/Measure, obtain the length of the line corresponding to the head width.

C.h. At the same time point, repeat this step by drawing the transversal midline of the tail (Mid-line between the intestinal valve and the tip of the tail; Figure 2C) and measure it to obtain the tail width.

NOTE: Use this measurement to compare embryos at the same stage across different phenotypes. To ensure the reproducibility of this measurement, make sure to find a location located around the mid-line of the tail of the animal that can easily be recognized from one animal to another.

C.i. To calculate the head to tail width ratio, divide the head width by the tail width.

3.4.2 Characterization of late elongation defects using image analysis.

A. Synchronization of L1 larvae using alkaline hypochlorite treatment

A.a. From a non-starved 60 mm plate containing many gravid adults, collect all worms in a micro-centrifuge tube by washing the nematodes off the plate with 1 ml of M9 buffer using a Pasteur pipette

A.b. Sediment nematodes at 3500 x g for 3 min at room-temperature and remove the supernatant using a micropipette without disturbing the worm pellet.

A.c. Add 1 ml of hypochlorite solution to each tube (0.4 *M* hypochlorite, 0.5 *M* NaOH) and shake for 3 min.

NOTE: Alkaline hypochlorite solution should be freshly prepared and embryos in this solution should be agitated gently but continuously to optimize dissolution of the adults and oxygenation of the embryos. After 3 min agitation, most adults should release their eggs into the solution.

A.d. Spin at 3500 x g for 3 min at room-temperature and quickly remove the supernatant using a micropipette without disturbing the pellet.

A.e. Wash four times with 1 ml of M9 buffer followed by centrifugation at 3500 x g for 3 min.

A.f. After the fourth wash, remove the supernatant and resuspend eggs in 700 µl of M9 buffer without pipetting up the eggs (as the eggs would stick to the plastic of the tip).

A.g. Tape the tube on a 3-mm orbital shaker placed in an incubator at the appropriate growth temperature and shake at 600 rpm overnight.

B. Length measurement of synchronized larvae

B.a. Centrifuge arrested L1 larvae at 3500 x g for 3 min at room-temperature and remove the supernatant. Resuspend the larvae in 100 µl of M9 buffer and transfer them onto an agarose pad using a Pasteur pipette (agarose pads should be prepared as described at section 1.1.2 to 1.1.8)
Place a coverslip on the pad.

NOTE: The pad does not need to be sealed with gum for this experiment that involves short acquisition.

B.b. Use a 10X objective and phase contrast illumination to measure the length of the larvae if a high resolution camera is used. Increase the intensity of the light to be able to capture images within a few milliseconds and consequently obtain a clear picture of the larvae (Figure 2D).

NOTE: While the swimming trashes of larvae are reduced by the agarose pad, they are still moving. Therefore, fast recording is essential to obtain a clear image.

B.c. Open Fiji-ImageJ and repeat step 1.3.1. To measure the length of larvae, choose the segmented line tool. Draw a segmented line from the tip of the head up to the tip of the tail following the midline of the larvae (Figure 2D, right panel).

B.d. Using the menu Analyze/Measure, obtain the length of the drawn line corresponding to the length of the larvae in micrometer.

3.4.3 Characterization of late elongation defects using Flow-cytometry

A. Synchronize Larvae.

A.a. Purify embryos using the alkaline hypochlorite treatment as described in section 2.1 from full 100 mm plates of well-fed young adults and let the embryo hatch and the L1 arrest in M9 buffer for 16 to 24 hours at 20 or 25.5°C depending on the strain analyzed.

NOTE: One full plate of well-+ fed adults per strain is sufficient for the analysis described below.

B. Calibration of the worm sorter

NOTE: The flow cytometer used here is a large particle flow cytometer (hereafter referred to as the worm sorter). The worm sorter includes a 670 nm red diode laser, which is located in front of an extinction detector. The worm sorter also contains a multi-line argon laser for fluorescent excitation. The standard instruments have three photomultiplier tubes (PMT) fluorescence detectors used to detect fluorescence emissions in the green, yellow, and red regions of the spectrum. In the protocol described here, TOF will be used to measure the size of the larvae, the red channel will be used to identify dead worms that will be stained with Propidium Iodide (PI). GP (General Purpose) High Fluorescence Control Particles used to calibrate the

instrument and as an internal control in our experiment display high fluorescence in green, yellow and red. They will be the only objects in the sample analysed with high emission detected in the green channel and will subsequently be identified based on this characteristic.

NOTE: Living animals are identified based on the absence of fluorescence in the Green and Red channel as well as on the TOF. Autofluorescent emission from the gut of the larvae is not detectable at L1 stage.

B.a. Switch on the laser block, the computer, the compressor and the worm sorter instrument. Press the START button on the opened worm sorter software as indicated in the instruction manual of the instrument.

B.b. Observe the argon laser control pop-up window. Select RUN mode and wait as the laser powers reach 10 ± 1 mW. Select DONE on the laser control window.

B.c. The flow rate depends on the sheath and the sample pressures. Set it to 5.10 ± 0.02 and 5.51 ± 0.01 respectively. Allow the pressure to equilibrate for at least 15 min and click the PRESSURE OK check box.

B.d. Make sure to eliminate all bubbles present in the flow channel tubules between the sample cup and the analysing chamber. To do so, click ACQUIRE and gently flick the tubule until no bubble is anymore acquired (as seen in the acquisition window).

B.e. Setup of all parameters for fluorescent and TOF measurement and detection as follows:

B.e.a. Scales for TOF, Ext, Green, Yellow and Red should be set to 256. Gain should be set as described in Table 1. PMT Control should be set at 700 for Green and Yellow and to 900 for Red

NOTE: Two excitation filters are available (488 nm and 514 nm) and can be used to excite either Green fluorescent protein (GFP) or Yellow fluorescent protein (YFP) or any fluorochromes excited at these wavelengths with the multiline argon laser. Appropriate filters need to be inserted in the filter chamber of the equipment. We used the 488 nm filter for the following experiment.

B.f. To calibrate the worm sorter, select "run control particles" in tool menu. Put 20 ml of 1X GP (General Purpose) High Fluorescence Control Particles in the cup (these particles are fluorescent particles of precise size, sold by the cytometry manufacturer to calibrate their instrument).

B.g. Click on ACQUIRE button to begin sheath and sample flow.

NOTE: Expect a mean related to the control particle distribution of 21 ± 6 and a coefficient of variation around that mean (C.V.) ≤11. If the C.V. is >11 and the mean is > 27 try to clean the tubules by clicking several times on the clean button or by flicking the flow channel.

C. Acquisition of animal TOF

NOTE: Light scatters when an object passes in the flow cell between the laser source and the extinction detector. The time it takes for the light to be scattered by the flying object (time of flight, TOF) is used to measure the axial length of the object. The extent of light masked by the object (extinction, EXT) is used as a measure of its opacity/optical density.

C.a. Place 10 µl of synchronized wild-type (*wt)* L1 in a watch glass and estimate the percentage of dead-eggs using a dissecting microscope.

NOTE: Synchronized L1 displaying high Emb (higher than 20%) in *wt* should not be used for further analysis.

C.b. Transfer synchronized L1 from the microcentrifuge (approximately 700 µl of M9 containing L1) to a 15 ml conical tube. Add propidium iodide (PI) at a final concentration of 10µg/ml (dilution 1/100th from a 1mg/ml stock solution) and incubate for 30 min at room temperature.

NOTE: Dead eggs and larvae will be stained using PI and detected as highly fluorescent objects using the red channel.

C.c. Add 10 ml of M9 buffer to dilute stained populations. Take 5 ml of the diluted populations and dilute them four times by adding 15 ml of M9. Place this dilution in the sample cup

C.d. Run the sample flow by clicking ACQUIRE and observe the flow rate.

NOTE: In order to have accurate measurement, the flow rate should stay between 15 and 25 objects/sec.

C.e. If necessary, adjust the amount of animals in the cup to reach the desired flow rate.

NOTE: The flow rate will depends on the pressures (sheath and sample) that are constant as indicated in 3.2.3 and on the concentration of larvae in the cup. If the flow

rate is higher than 25 objects/sec add some buffer in the cup. If it is lower than 15 objects/sec add concentrated L1 (from step 3.3.3) in the cup.

C.f. Once the appropriate concentration of object is reached, evaluate the volume in the cup and add $1/4^{th}$ of this volume in High Fluorescent GP Control Particles 4X solution.

C.g. Adjust the gating and sorting parameter. To do so, click "Gating" on the menu and select " TOF vs." and "Green". Click on "Sorting" on the menu and select "TOF vs. " and "Red". Gating and sorting graphics will then appear as shown in Figure 3A.

NOTE: This will allow the visualization of the control particles (emission in Green and Red), dead animals stained by PI and bubbles (emission in Red and not Green) and living animals (no emission in neither Green nor Red channels) (Figure 3A).

C.h. Run the experiment by clicking ACQUIRE. NOTE: To identify small size differences between larvae, analyse around 10,000 objects, so approximately 8,000 animals. Stop the experiment and export the data as .txt format by clicking on STORE

D. Measurement of the relative size of living animals in synchronized populations

D.a. Open the .txt file using a software able to manage large data tables.

D.b. From the analyzed objects extract the TOF values associated with control particles that are characterized by emission in the green channel higher than 100 arbitrary units (this value depends on the parameters set in section 3.2.5). Create a new column and call it "control particles". Create a column containing all the other objects except the control particles called "sample". NOTE: the fluorescence emission

of new particle batch needs to be verified before starting the acquisitions. This will set the fluorescent threshold enabling the identification of control particles over L1s.

D.c. For each analyzed strain identify the portion of the experiment where the flow rate has been altered (due to the presence of a plug of eggs for example). To do so:

D.c.a. Plot the TOF of "control particles" for each sample as a factor of time (Figure 3B).

D.c.b. Draw the linear trendline using the trendline tool and display the equation on the chart. NOTE: The TOF of control particles should be constant over time (horizontal line, Figure 3B). Considering the equation of the linear trendline drawn on the data y=ax+b, ensure that the "a" value is lower that 10^{-4}. All measurements made within time sections displaying a rupture in the alignment of control particle should be removed from the analysis.

D.d. Remove the dead embryos and bubbles (emission higher than 15 in the red) as well as small debris and large egg plugs (TOF lower than 10 and higher than 70 respectively) from the "sample" measurement.

D.e. Plot the "control particles" distribution for each strain analyzed. As seen in Figure 3 C these distributions should overlay almost perfectly. This ensures that TOF measurements obtained for different strains can be compared. NOTE: normalization of sample elements TOF over control particles can be used if the distributions of control particles in a sample do not overlay with that of control samples. Normalized TOF are computed as followed:

D.e.a. Normalize TOF for genotype G = (sample TOF for G) / (average "control particle" TOF for G) * (average "control particle" TOF for *wt*) where *wt* is the control sample.

D.f. Plot Larvae TOF distribution for each strain including control sample, in our case *wt* animals (Figure 3D). Measure the mean and the standard error of the mean (SEM) for each population (Figure 5A and B).

3.5 Representative results

3.5.1 Head-, tail- and head/tail-width ratio are robust metrics.

The protocols described here have been successfully used to characterize the function of regulators and effectors of Rho GTPases *pix-1, pak-1* and *let-502* during early elongation (Martin *et al.*, 2014). *pix-1* and *pak-1* code respectively for a guanine-exchange factor (GEF) and an effector specific for Rac/Cdc42 GTPases whereas *let-502* codes for an effector for RHO-1 (Martin *et al.*, 2014). In this study, *pix-1* and *pak-1* were shown to control epidermal morphogenesis during early elongation (Martin *et al.*, 2014). This study used head and tail width measurement as metrics to demonstrate, for the first time, that hypodermal cells located in the anterior embryo follow different morphogenic programs than those located in its posterior end (Martin *et al.*, 2014). To establish the reproducibility and robustness of these metrics, head width was measured independently five times on 12 wild-type (*wt)* embryos at 1.2-fold stage. Variances among the five different groups of measurement were compared then assessed using the Brown-Forsythe test (using R statistical package) revealing no significant differences amongst the measurements (*F-test p-value* > 0.5; Figure 4A) suggesting that measurements for a group of embryos are reproducible. Assessment of reproducibility and batch effects associated with these measurements was done through measurement of the head width of *wt* embryos at 1.2-fold stage from 4D-DIC imaging done on three different days (n=12 embryos). Across these three measurement groups, the variance was not significantly different and no

significant batch effects were found to impact the head-width measurement results (F-test p-value > 0.5; Figure 4B).

Similar results were obtained for tail width measurements and for measurements done at different stages of early elongation (data not shown). These data established head-width, tail-width and head/tail width ratio as robust metrics to characterize early elongation defects.

3.5.2 Measuring head and tail width as well as length of the embryos allows for the characterization of genes controlling early elongation along the antero-posterior axis of the embryo.

Measurement of the length of the embryos, as well as the width of their head and tail was done on *wt* and mutant embryos carrying null or strong thermosensitive loss-of function alleles for genes controlling early elongation: *pix-1(gk416)*; *pak-1(ok448)* and *let-502(sb118ts)* (Martin *et al.*, 2014). We measured the head/tail (H/T) width ratio of *wt* and mutant embryos at the beginning (1.2-fold stage) and at the end of early elongation at non-permissive temperatures (Figure 4C left and right panel respectively). While at the beginning of early elongation there was no change or a reduced H/T ratio was observed in *pix-1*, *pak-1* and *let-502* mutants when compared to *wt* animals (1.2-fold stage, Figure 2C, left panel), at the end of early elongation all three mutants showed a significantly higher H/T ratio than *wt* embryos (T-test p-values <0.006; Figure 4C; right panel). This demonstrated that *pix-1*, *pak-1* and *let-502* mutant embryos display abnormal antero-posterior morphology at the end of early elongation. Further analysis comparing head width and tail width between 1.2-fold stage and the end of early elongation, using the same measurement parameters revealed that the head width is less reduced in *pix-1*, *pak-1* and *let-502* mutants while the tail width reduces significantly less in *let-502* mutants only (Martin *et al.*, 2014). This revealed that *let-502* controls morphogenic processes similarly along the antero-

posterior axis of the embryo, while *pix-1* and *pak-1* control morphogenic processes occurring mainly at the anterior part of the embryo (Martin *et al.*, 2014). The length difference between the embryos at the end versus the beginning of early elongation (Figure 4D) was also measured. We found that early elongation was significantly reduced in *pix-1*, *pak-1* and *let-502* mutants when compared to *wt* suggesting that alteration of the anterior morphogenesis in *pix-1* and *pak-1* mutants alone is sufficient to significantly reduce the elongation of the embryo.

Protocol 2 and 3 were used to assess the length of arrested larvae in *wt* and mutant backgrounds. The length of these larvae was assessed using both image analysis (Protocol 2) (Martin *et al.*, 2014) and flow-cytometry (Protocol 3; unpublished data). Measurements of larvae length using image analysis results in absolute measurements of animals' length in micrometers in a robust and highly reproducible manner (Figure 5A). This analysis revealed that synchronized mutant larvae display significantly reduced length when compared to *wt* (Figure 5A) (Martin *et al.*, 2014). Measurement of these larvae using the flow-cytometry based protocol (Protocol 3) gave comparable results (Figure 5B). However, it should be noted that the large number of larvae measured using the latter approach significantly increased the statistical robustness of genotype comparison (t-test p-values $< 10^{-24}$). Based on these findings, the flow-cytometry approach may be a better choice over image analysis in order to characterize mutant animals displaying very subtle elongation defects.

3.6 Discussion

This protocol describes novel metrics to characterize early and late phases of embryonic elongation.

In section 1, the critical step is the potential presence of bacteria on the pad. The embryos are hermetically enclosed between the pad and the coverslip during image acquisition. Sealing the slide is required to avoid desiccation of the animals during acquisition that lasts more than two hours. To our knowledge, none of the sealers used to mount agarose pads between slide and coverslip are air-permeable. Consequently, when a large amount of bacteria (or embryos) is present on the pad, they may be deprived of oxygen after a few hours leading to their premature death. Having three-fold embryos – corresponding to embryos that are 3-fold in length compared to non-elongated embryos – recorded along with the embryos of interest will be a good indicator of potential hypoxic conditions, since those embryos will stop moving in their eggshells in the absence of oxygen. No morphological measurements should be done on hypoxic conditions or on dead embryos.

Another critical step when using time-lapse imaging is temperature at which development of the embryo occurs. Thermosensitive mutants are currently used in *C. elegans*. The biological effect of temperature shift may be immediate or delayed depending on the half-life of the protein and the nature of the mutation its carries. Consequently, the temperature at which the embryo is exposed should be constant over time and should be controlled by appropriate ventilation of the microscopy room or a heating-cooling chamber on the microscope stage.

Section 2 is dependent on larvae synchronization using alkaline hypochlorite treatment. Under certain circumstances, this treatment may lead to embryonic lethality (Emb). Emb above 20% in *wt* population suggests an elevated toxicity during hypochlorite treatment that may negatively impact morphogenesis. Synchronized L1 displaying high Emb in *wt* background should not be used for further analysis. This restriction also applies to protocol 3.

We do not recommend the use of anesthetic drugs to immobilize larvae. Levamisol in particular, immobilizes the nematode through induction of muscle tetany that tends to shrink the larvae introducing experimental bias. If exposure time is not quick enough

as a result of the limitations of the microscope, we recommend reducing the motility of larvae by increasing the concentration of the agarose in the pad and reducing the amount of liquid between the pad and the coverslip. Care should be taken however, not to desiccate the larvae, since desiccation will reduce their size.

In section 3, measurement of the length of larvae used comparison of flow rates between analysed samples. To do so, the distribution of control particles needs to be compared. If the distributions fully overlay, the TOF (Time-of-flight) values obtained for corresponding samples can be compared, if not, these values need to be normalized. Normalization of sample-TOF over control particles-TOF (as detailed in 3.4.5.1) has been used successfully as shown for *pak-1(ok448)* (Figure 3C and Figure 5B). Relative length of *pak-1(ok448)* vs *wt* was found to be similar in at least 3 independent experiments with or without normalization (data not shown). However, we recommend, confirming the results obtained with normalization with those obtained without it, especially when comparing larvae with small size differences. It should be noted that measurement of the larvae length using flow-cytometry provides a length relative to a control sample, in this case, *wt* larvae rather than an absolute length in micrometer as for image analysis. This implies that measurements from independent experiments cannot be combined unless computing size ratio over *wt*.

The buffer used for dilution in the sample cup will have an impact on the flow rate. We observed that the sheath buffer recommended by the manufacturer contains detergent that increases the amount of bubbles generated during acquisition. Using M9 buffer, which does not contain detergent, significantly reduced the formation of bubbles but was less efficient in avoiding the plugging of eggs in the tubules of the sorter, which affects the flow rate of samples. Egg plugging is easily detected during the acquisition by a marked decrease of the observable TOF of control particles for a few seconds followed by an elevated TOF- also for a few seconds. Egg plugging may also lead to the obstruction of the channel and the complete arrest of the particle flow (less that 5 objects per second). If this should occur, click on the CLEAN button until

flow rate is restored. Any measurements occurring during these events should be excluded from the data analysis. Sheath buffer may be recommended for experiments involving strains characterized by high rates of dead eggs.

The sample and sheath pressure (set at the step 3.2.3), may change (slightly) over time and should be adjusted manually throughout the experiment in order to ensure a very constant flow rate. Reduction or increase of the low rate will be observable when analysing the results and plotting the TOFs of control particles over time (Figure 3 C). Reduction of the flow rate will result in the increase of the average TOFs of particles over time, while an increase of the flow rate will result in the opposite. Alteration of the flow rate will negatively impact the sensitivity of the method in detecting small size differences between populations of larvae.

Methods aiming to identify genes controlling elongation and requiring time-lapse microscopy recording are generally highly time-consuming and tedious when phenotyping several genotypes. The flow-cytometer-based approach, while requiring equipment not available to all laboratories, is less time-consuming and consequently more efficient when several strains need to be characterized. This method is also more statistically robust compared to measurements using image analysis (assessed by the student's t-test comparing mutant and *wt* TOF distributions; Figure 5A and B). This method may then be highly suitable for strains expressing elongation defects with low expressivity/penetrance.

Several methods using flow-cytometry have been developed in the past to measure fitness of nematodes (Boulier et Jenna, 2009 ; Ramani *et al.*, 2012 ; Verster *et al.*, 2014 ; Andersen *et al.*, 2015). These methods use animals dispensed in a 96-well plates and the Reflex module of the worm sorter. The Reflex module enables direct analysis of nematode population dispensed within 96-well plates. Consequently, these methods are able to characterize hundreds of conditions per day and constitute a robust manner in which to measure the fitness of a non-synchronized population.

They are however, not well suited to identify small size differences between synchronized L1. Measurement of small differences between L1 larvae requires the measurement across a large number of animals, which is incompatible with the use of 96-well plates and of the Reflex module that may efficiently characterize 100 objects at the most per well. The method described here is designed for this purpose at the expense of the throughput, which is significantly reduced. It enables the characterization of 3 to 4 conditions per hour once the instrument is calibrated, which is a marked improvement over using image analysis in protocol 2.

Measurement of head and tail width ratio is the first method that was developed to characterize morphogenic processes occurring unevenly along the antero-posterior axis of the embryo (Martin *et al.*, 2014). When applied to genes shown to control early elongation, these methods will clarify the spatial distribution of signaling pathways controlling morphogenesis at that stage. Measurement of the length of arrested larvae using either image analysis or flow cytometry in combination with measurement of the length of the embryos at the end of early elongation will enable the identification of genes controlling either early or late elongation or both with high sensitivity and precision. These procedures may then contribute significantly to future understanding of the spatial and temporal regulation of signaling pathways controlling embryonic elongation in *C. elegans*. Furthermore, these approaches can also be adapted to study signaling pathways controlling body length such as the insulin and TGF-beta pathways (So *et al.*, 2011 ; Dineen et Gaudet, 2014) and chronic exposure to environmental contaminants (Tan *et al.*, 2015 ; Yu *et al.*, 2015). These measurements can be done at different larval stages or in adults using minor variations of Protocols 2 and 3. Measuring size differences in L1 is more challenging with the worm sorter than larger objects such as L3, L4 larvae or adults. Protocol 3 can then easily be adapted to do these measurements.

3.7 Acknowledgments

This work was supported by grants from the Natural Sciences and Engineering Research Council (NSERC) of Canada and The Canada Foundation for Innovation. Thanks to Dr Paul Mains (University of Calgary, Calgary, Canada) for *let-502(sb118ts)* strain. Some of the strains were provided by the *Caenorhabditis* Genetics Center, which is funded by NIH Office of Research Infrastructure Programs (P40 OD010440).

3.8 Figures

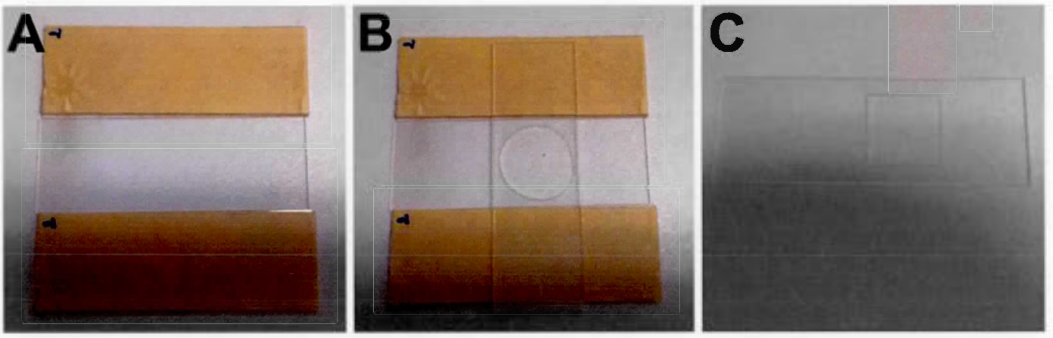

Figure 3.1 : Preparation of an agarose pad.

A, Microscope slide placed between two spacer-slides covered by two layers of masking tape. B, The agarose pad is covered with another slide supported by the two spacer-slides. C, The final shape and size of the agarose pad after cutting with a razor blade to fit the coverslip.

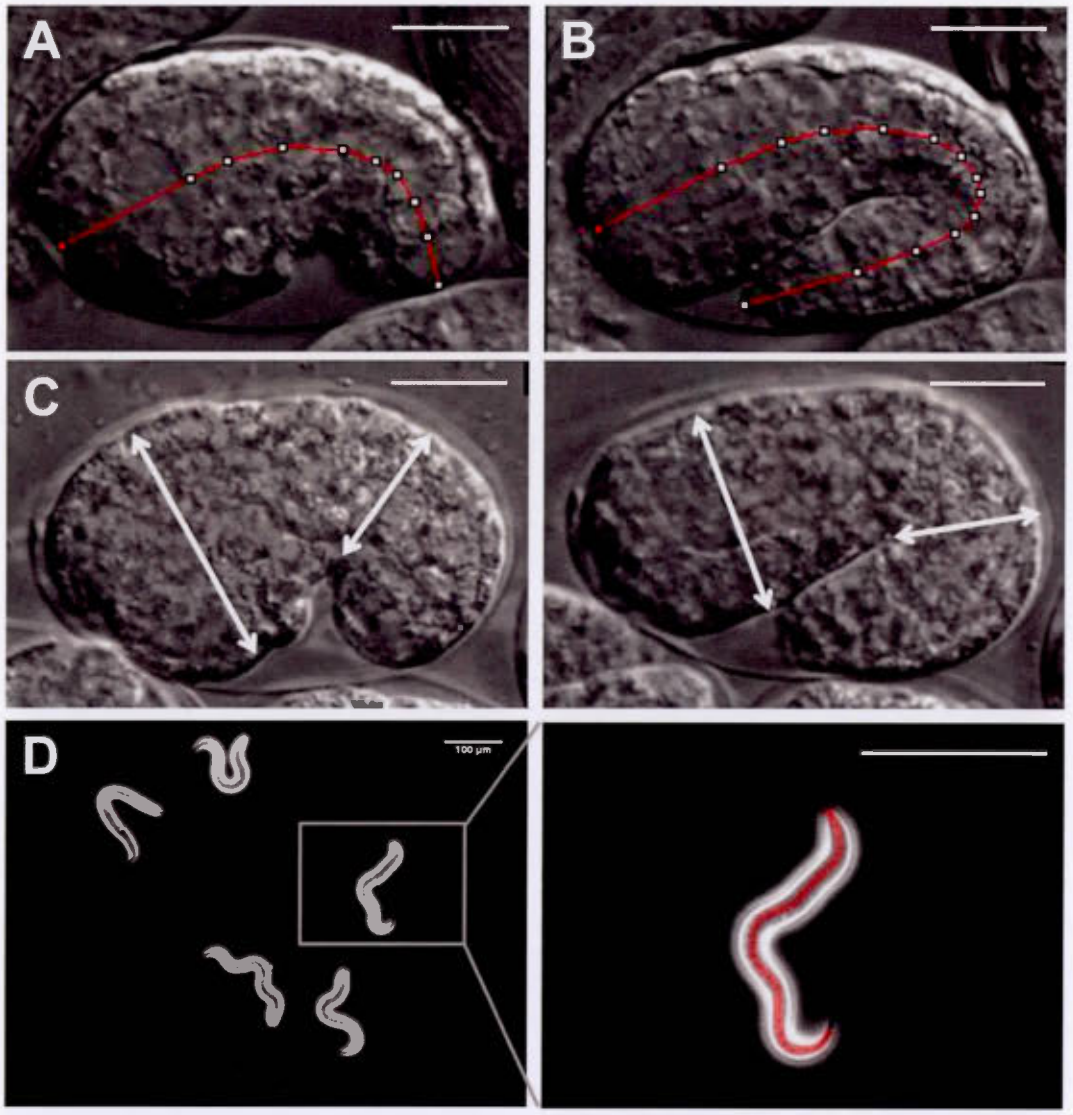

Figure 3.2 : Measurement of early and late elongation defects.

A-B, Measurement of the length of an embryo at comma stage (A) and at the end of early elongation (B). The red line, used to measure the embryos was drawn using the segmented line tool of ImageJ. C, Head and tail width are measured in embryos at 1.2-fold stage (left) and at the end of early elongation (right). Arrows represent the localisation of measured areas (modified from Martin *et al.*, 2014). Scale bar: 20 µm. D, Length of Larvae is measured for synchronized L1-larvae. Right panel is an enlarged view of the captured image (left). The red line was drawn using the segmented line tool of ImageJ. It is used to measure the length of the larva. Scale bar: 100 µm.

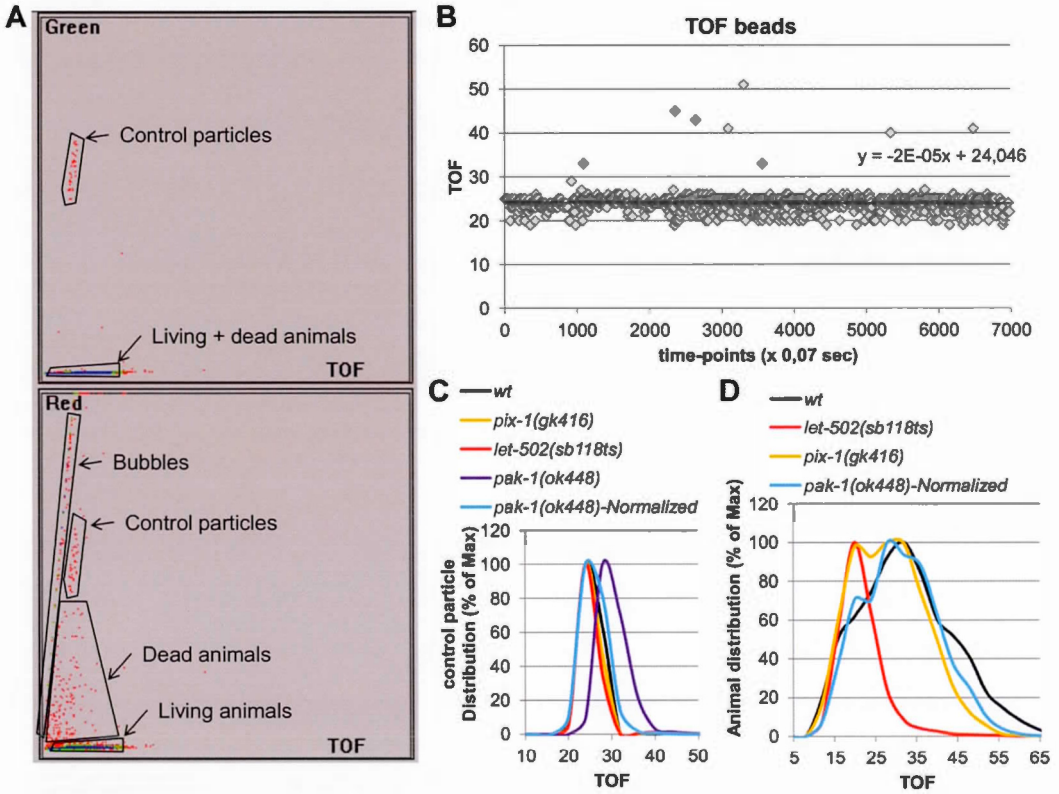

Figure 3.3 : Measurement of the length of synchronized larvae using flow-cytometry.

A, Gating and sorting window of COPAS Biosort showing Green and Red emission of control particles, bubbles, dead and living animals with respect to their Time-Of-Flight (TOF). B, TOF of control particles at different time points for a representative experiment. The slope of the linear function of TOF versus time is around 10^{-5}, indicating that TOF of control particles is constant over time throughout the experiment. C, Distribution of control particle TOFs expressed as a percentage of maximal value of distributions. Non-normalized and normalized control particle distributions are represented for *pak-1(ok448)*. Other distributions are not normalized. D, distribution of TOFs for living animals expressed as a percentage of the maximal value of the distributions. TOFs are not normalized on control particles except for *pak-1(ok448)* as indicated.

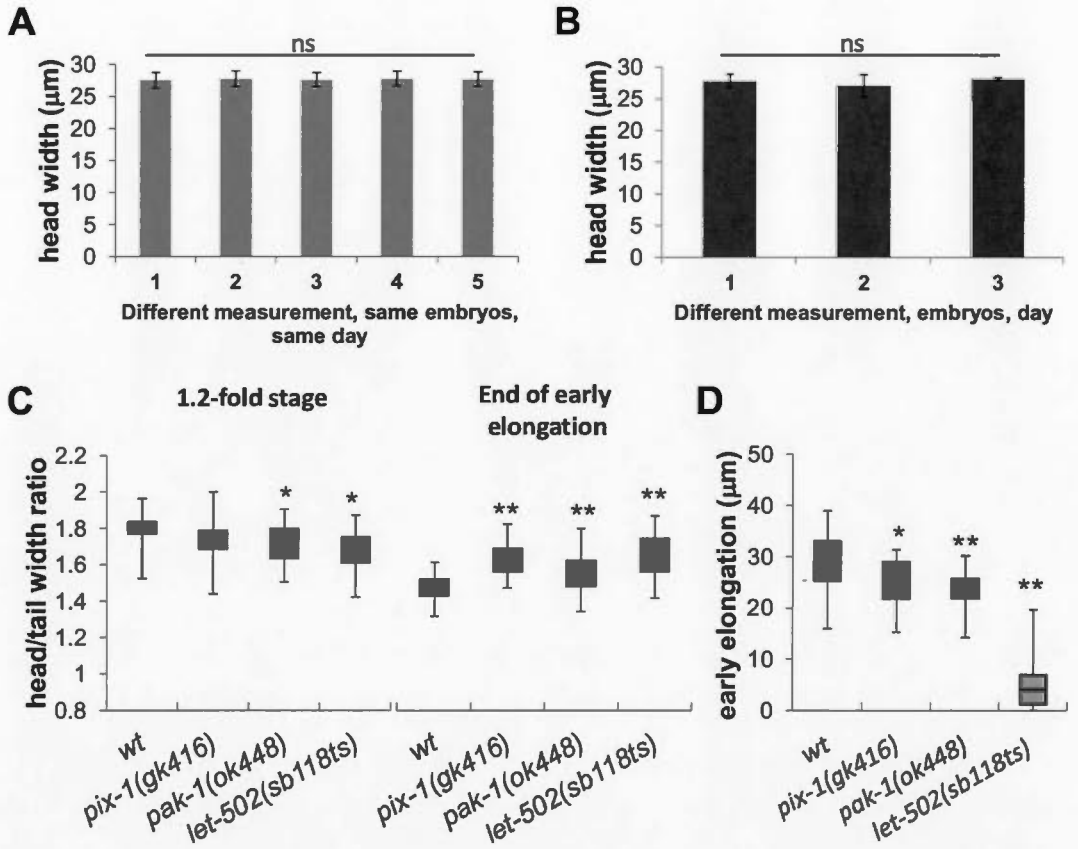

Figure 3.4 : *pix-1, pak-1* and *let-502* mutants present early elongation defects.

A-B, Reproducibility and robustness assessment of head width measurements. A, Five independent measurements of the head width for *wt* embryos at 1.2-fold stage (n=12 embryos). Means and standard deviations (error bars) are indicated. Non significant (ns) differences between measurements were computed using the Brown-Forsythe test (using R statistical package) (F-test *p-value* > 0.5). B, Head width measurement for *wt* embryos at three different days (n=12 embryos). Means and standard deviations are indicated as well; there was no significant difference in variance across the measurements (ns; Brown-Forsythe F-test *p-value* > 0.5). C, Distributions of head/tail width ratio at 1.2-fold stage (left panel), at the end of early elongation (right panel) in *wt*, *pix-1(gk416)*, *pak-1(ok448)* and *let-502(sb118ts)* mutants at 23-24°C. Note that mothers of *let-502ts* embryos used for this study were grown at 25.5°C. D, Distribution of the elongation in *wt*, *pix-1(gk416)*, *pak-1(ok448)* and *let-502(sb118ts)* mutants between comma stage and the start of late elongation. The box-plots represent the min, max, 25th, 50th (median) and 75th percentiles of the populations. * T-test *p-value* < 0.05, ** T-test *p-value* < 0.006 (modified from Martin *et al.*, 2014)

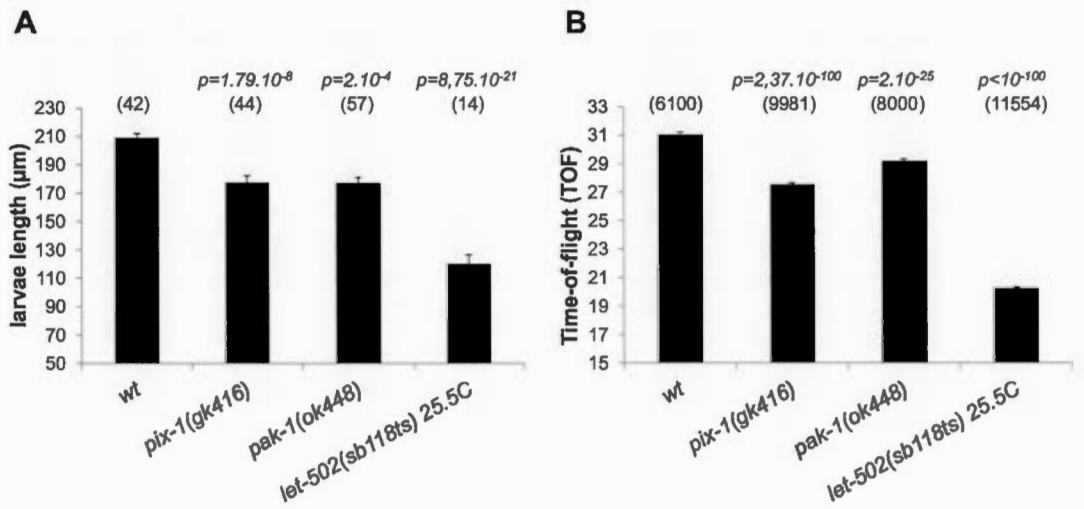

Figure 3.5 : *pix-1(gk416), pak-1(ok448)* and *let-502(sb118ts)* larvae present length defects.

A, Length of larvae measured in *wt*, *pix-1(gk416)*, *pak-1(ok448)* and *let-502(sb118ts)* animals measured using image analysis (Protocol 2). B, Relative larvae length measured using flow-cytometer (Protocol 3). Numbers in brackets correspond to the number of animals used for the measurements. Means of lengths and standard error of the mean (SEM; error bars) are represented. Student's T-test *p-values* are indicated (p).

CHAPITRE IV

L'ANTAGONISME RHO / RAC DÉFINIT L'HÉTÉROGÉNÉITÉ CELLULE-CELLULE PENDANT LA MORPHOGENÈSE DE L'ÉPIDERME CHEZ LE NEMATODE

Le travail de ce chapitre a été soumis pour publication à *Journal of Cell Biology* (*JCB*). Il a récemment été accepté sous réserve de modifications.

Dans le travail du chapitre II, nous avons montré que la répartition des voies de signalisation contrôlant l'élongation embryonnaire précoce – *mel-11/let-502* et *pix-1/pak-1* – n'était pas homogène le long de l'axe antéro-postérieur et dorso-ventral. Dans ce chapitre, nous souhaitons cartographier à l'échelle cellulaire l'activité de ces deux voies de signalisation.

Contributions des auteurs :
Emmanuel Martin : conception, design, acquisitions, analyse et interprétation des résultats, rédaction du manuscrit, montage des figures ; expériences : toutes les expériences de l'article (Figure 1 à 10). *Marie-Hélène Ouellette* : acquisitions de certaines souches exprimant AJM-1::GFP, ABD::mCh pour mesurer l'anisotropie et la taille des protrusions (partie des Figures 4 et 6). *Sarah Jenna* : conception, design, analyse et interprétation des résultats, rédaction du manuscrit, montage des figures.

NOTE : Les références de l'article sont incluses dans la bibliographie générale.

4.1 Résumé

L'antagonisme entre les GTPases Rac1 et RhoA contrôle l'hétérogénéité cellule-cellule dans une population isogénique de cellules en culture *in vitro*, et la morphogenèse épithéliale *in vivo*. Cependant, son implication dans la régulation de l'hétérogénéité cellule-cellule au cours de la morphogenèse n'a jamais été étudiée. Ici, nous avons utilisé une nouvelle méthode d'imagerie afin de caractériser la morphogenèse épithéliale à l'échelle cellulaire au cours de l'élongation embryonnaire précoce du *Caenorhabditis elegans*. Cette étude a révélé qu'une voie Rac-*like*, impliquant la GEF spécifique pour Rac1 et Cdc42 β-PIX/PIX-1 ainsi que leur effecteur PAK1/PAK-1, et une voie RhoA, impliquant ROCK/LET-502, contrôle à la fois le remodelage des jonctions apicales et la formation de protrusions basolatérales dans différents sous-groupes de cellules de l'hypoderme. Dans ce contexte, les protrusions adoptent une morphologie soit de type lamellipode, lequel semble réduire la tension au niveau des jonctions cellule-cellule, soit amiboïde. L'antagonisme cellulaire autonome entre ces voies de signalisation permet aux cellules de passer d'un programme morphogénétique Rac1 à RhoA, et inversement. Cette étude identifie le premier cas d'hétérogénéité cellule-cellule contrôlée par l'antagonisme Rac1/RhoA durant la morphogenèse épithéliale.

Manuscrit

RAC1/RHOA ANTAGONISM DEFINES CELL-TO-CELL HETEROGENEITY DURING EPIDERMAL MORPHOGENESIS IN NEMATODE

Emmanuel Martin*, Marie-Hélène Ouellette* and Sarah Jenna*

Department of Chemistry, Pharmaqam, Biomed, Université du Québec à Montréal (UQÀM), Montréal, Québec, H3C 3P8, Canada

* Corresponding Author: jenna.sarah@uqam.ca

4.2 Abstract

The antagonism between the GTPases Rac1 and RhoA controls cell-to-cell heterogeneity in isogenic populations of mesenchymal cells *in vitro,* and epithelial morphogenesis *in vivo*. Its involvement in the regulation of cell-to-cell heterogeneity during epithelial morphogenesis has, however, never been addressed. We used a novel cell imaging approach to characterize epidermal morphogenesis at a single-cell level during early elongation of *Caenorhabditis elegans* embryos. This study revealed that a Rac1-like pathway, involving the Rac/Cdc42's Guanine-exchange factor β-PIX/PIX-1 and effector PAK1/PAK-1, and a RhoA pathway involving ROCK/LET-502 control the apical junctions remodelling and the formation of basolateral protrusions in distinct subsets of hypodermal cells. In these contexts, protrusions adopt a lamellipodia or an amoeboid morphology, the former one reducing tension building at the cell-cell junctions during morphogenesis. Cell autonomous antagonism between these pathways enables cells to switch between Rac1- and RhoA-like morphogenetic programs. This study identifies the first case of cell-to-cell heterogeneity controlled by Rac1/RhoA antagonism during epithelial morphogenesis.

4.3 Introduction

Morphogenesis of epithelial cells is involved in organogenesis during embryonic development, organ regeneration and metastasis of carcinoma cells. The remodelling of apical junctions leading to apical constriction or anisotropic rearrangement of apical junctions was shown to drive epithelial morphogenesis during gastrulation, planar cell intercalation and elongation in number of genetic models from the nematode to the mouse (reviewed in Munjal et Lecuit, 2014). Junction shrinkage has been mostly investigated during epithelial cells intercalation leading to the elongation of *Drosophila melanogaster* germ band (reviewed in Lecuit et Yap, 2015). Myosin II, as well as its upstream regulator, the RhoA's effector ROCK, play a central role in these processes through the regulation of cadherin endocytosis from adherens junctions (Bertet *et al.*, 2004 ; Levayer *et al.*, 2011 ; Yashiro *et al.*, 2014 ; Collinet *et al.*, 2015). Epithelial morphogenesis was also shown to involve the formation of basolateral protrusions in a polarized manner, which has been proposed to set the polarity of elongation/intercalation in nematodes, arthropods and mouse (Heid *et al.*, 2001 ; Ewald *et al.*, 2008 ; Georgiou et Baum, 2010 ; Williams *et al.*, 2014 ; Walck-Shannon *et al.*, 2015). Studies using epithelial cell culture and developmental systems revealed that myosin contraction at the apical junctions and at the protrusions, which constitute the principal motor for cell-shape changes during morphogenesis, depends on the activation of two main pathways controlled by the Rho GTPases Rac1 and RhoA (Vaezi *et al.*, 2002 ; Yu *et al.*, 2003 ; Vargo-Gogola *et al.*, 2006). Interestingly, pathways involving these two GTPases tend to function in an antagonistic manner (Chauhan *et al.*, 2011 ; Guilluy *et al.*, 2011 ; Vlachos et Harden, 2011). For instance, this antagonism was shown to generate distinct and mutually exclusive Rac1 and RhoA subcellular compartments in placode cells, controlling invagination of the epithelium during lens development in mouse (Chauhan *et al.*, 2011). It was also shown to induce a certain level of heterogeneity within isogenic populations of cells (Yin *et al.*, 2013 ; Sailem *et al.*, 2014). Indeed, invasive carcinoma cells were shown

to switch between a Rac1-dependent mesenchymal to a RhoA-dependent amoeboid migration in response to increased stiffness of their environment (Yamazaki *et al.*, 2009). Recent studies using automated single cell analysis also demonstrated that switch between Rac1 and RhoA programs enables cells of an isogenic population to move within a defined landscape composed of several discrete shapes (Yin *et al.*, 2013 ; Sailem *et al.*, 2014). Importantly, these studies suggested that gene networks have evolved to promote and regulate this morphological heterogeneity that may facilitate population-level behavior and survival when exposed to environmental changes (Yin *et al.*, 2013 ; Sailem *et al.*, 2014). While cell-to-cell heterogeneity within an isogenic population of mesenchymal cells is now well accepted, the presence of such heterogeneity between cells of a polarized epithelium has not yet been observed. Intriguingly, the columnar epithelial cells display an evolutionarily conserved distribution of polygonal shapes with a peak of 40 to 45% hexagons (Lewis, 1928 ; Gibson *et al.*, 2006 ; Gibson et Gibson, 2009). Recent study using human keratinocytes revealed that this rate of hexagons depends on determinist instead of stochastic mechanisms and more particularly, on cell-cell junction remodelling by the RhoA's effectors ROCK1 and ROCK2 (Kalaji *et al.*, 2012). Overall, these studies suggest that distribution of shapes within an epithelium may depend on signaling pathways previously shown to control epithelial morphogenesis. They consequently raise an important and still unaddressed question: is Rac1/RhoA antagonism, controlling both epithelial morphogenesis and cell-to-cell heterogeneity within populations of mesenchymal cells, also defines cell-to-cell heterogeneity during epithelial morphogenesis?

Embryonic elongation is a developmental stage of epidermal morphogenesis in *Caenorhabditis elegans* and is divided into an early and a late phase. Early elongation consists in a reduction of the diameter of the embryo and its elongation along its antero-posterior axis. At that stage, the hypodermis is composed of dorsal, lateral and ventral hypodermal cells (Priess et Hirsh, 1986). Early elongation was proposed to

result from the apical constriction of lateral hypodermal cells (Priess et Hirsh, 1986 ; Keller, 2006a ; Diogon *et al.*, 2007). Rac-1- and RhoA-like pathways involving the Rac/Cdc42's regulator and effector PIX-1/β-PIX and PAK-1/PAK1, and the RHO-1/RhoA's effector LET-502/ROCK respectively were shown to control early elongation in parallel (Piekny *et al.*, 2003 ; Gally *et al.*, 2009 ; Martin *et al.*, 2014). The RHO-1/LET-502 pathway is expected to be active in lateral cells and inactive in dorsal and ventral cells due to the expression of a RHO-1-specific GTPase-activating protein (GAP), RGA-2, in these latter cells (Diogon *et al.*, 2007). The cells expressing active PIX-1 and PAK-1 are still unknown. This pathway was, however, suggested to mostly control morphogenetic processes at the anterior part of the embryo (Martin *et al.*, 2014). Altogether, these studies suggest that the hypodermal cells may use different combinations of Rac1/RhoA signaling pathways along the dorso-ventral and antero-posterior axis of the embryo during early elongation.

We used a novel imaging approach to characterize early elongation at a single cell level. This study revealed that the PIX-1/PAK-1 pathway controls the remodelling of apical junctions and the formation of basolateral protrusions in the dorsal anterior cells, while LET-502 controls similar processes in lateral cells. We also showed that cells can switch between Rac1-like and RhoA-like morphogenetic programs upon genetic alteration of *let-502*, *pix-1* or *pak-1*. We propose a model in which cell-autonomous Rac1/RhoA antagonism defines the morphogenetic program adopted by polarized epithelial cells, and controls cell-to-cell heterogeneity during epithelial morphogenesis.

4.4 Results

4.4.1 Hypodermal cells follow different morphogenetic programs during early elongation.

We developed a novel imaging method to better assess the spatial distribution of cellular and molecular processes controlled by PIX-1/PAK-1 and LET-502 during early elongation. This method uses high-resolution four-dimensional (4D) confocal microscopy to measure the deformation rates (elongation or shrinking) of the cell-cell junctions between hypodermal cells in transgenic animals expressing the junction marker AJM-1::GFP and the filamentous actin (F-actin)-binding probe VAB-10(ABD)::mCherry in the hypodermis. These transgenic animals displayed similar elongation rate and morphology than *wild-type* (*wt*) embryos during early elongation (Figure S1). We measured the deformation rates of transversal and longitudinal cell-cell junctions of dorsal (D), lateral (L) and ventral (V) cells during early elongation (see Materials and methods, Figure S2). The average deformation rates for groups of junctions were represented using rose graphs in which elongating junctions display positive rates (towards the exterior of the graph) and shrinking junctions, negative rates (towards the interior of the graph; bottom panels; Figure 1A-B). Deformation rates for individual junctions were also indicated (Figure 1C and D). This analysis revealed that transversal lateral anterior junctions (light red; Figure 1A) shrank 2.5-fold faster than the posterior ones (dark red, Figure 1A). On the contrary, transversal ventral anterior junctions (light blue, Figure 1A) shrank 3.5-fold less than the posterior ones (dark blue, Figure 1A). A small elongation was also measured for dorsal anterior junctions (green, Figure 1A). Because dorsal posterior cells fuse during early elongation, deformation rate could not be measured for this part of the embryo.

These results suggest that the reduction of the head width of the embryo is mostly associated to the shrinking of transversal junctions of lateral hypodermal cells.

However, these data also suggest that morphogenesis of the posterior part of the embryos depends on the shrinking of the transversal junctions of both lateral and ventral cells. These data deviate from the accepted model suggesting that ventral cells may passively contribute to early elongation (Diogon *et al.*, 2007).

When considering the deformation rate of these junctions individually, we identified two set of junctions which are semi-aligned or aligned along the dorso-ventral axis of the embryo (Figure 1C and D): the D1/L1/V1 junctions linking Dorsal1/2; Lateral H1 and ventral 18/19 to their anterior neighbours and the junctions D2/L2/V2 linking those cells with their posterior neighbours (Figure S3). Interestingly, these junctions appear to deform differently. For example, the L2 junctions shrink significantly more than L1 (T-test *p*-values = 0.046; Figure 1D). These data suggest that hypodermal cells, such as H1 lateral cells, form cell-cell junctions with their anterior and posterior neighbours that are submitted to different morphogenetic mechanisms.

4.4.2 LET-502 and PIX-1/PAK-1 control morphogenesis in different subsets of hypodermal cells.

The results presented above support the hypothesis that hypodermal cells follow different morphogenetic programs during early elongation and that these programs are also modulated at the subcellular level. To better understand the genetic basis of this heterogeneity, we measured the deformation rate (DR) of the hypodermal cell-cell junctions in embryos carrying the strong *loss-of-function let-502(sb118ts)* thermosensitive allele and grown at 25.5°C, in *let-502(RNAi)* and in *wild-type* (*wt*) animals (left and middle panels; Figure 2 A and B). We also computed the relative deformation rates (RDR) of the junctions of mutant/RNAi-treated animals when compared to *wt* (see Material and methods; right panels; Figure 2 A and B). When considered at the organism level, these embryos displayed similar elongation defects (Figure S4). They also displayed similar alteration of junction DR and RDR (Figure

2A and B), consisting in a significant reduction of the shrinking rate of the anterior and posterior transversal lateral junctions and of posterior transversal ventral junctions (red rose graph; Figure 2A-B) when compared to *wt* animals (grey rose graph; t-test *p*-values < 0.045; Figure 2A-B). This analysis also revealed that the RDR of lateral anterior, lateral posterior and ventral posterior cell junctions were similar (around 1.3) in *let-502(sb118ts)* or *let-502(RNAi)* embryos (right panels; Figure 2A and B). This suggests that *let-502* controls the shrinking of transversal membranes of lateral and ventral posterior cells in a similar manner as previously suggested (Martin *et al.*, 2014).

We also measured the DR and RDR of cell-cell junctions in embryos carrying *pix-1(gk416)* and *pak-1(ok448)* null alleles (Figure 2C and D). These embryos displayed a significant RDR over *wt* only at the anterior part of the embryos; consisting in the elongation of transversal dorsal and ventral anterior junctions (t-test *p*-values < 0.01; Figure 2C-D). These results support previous studies suggesting that the *pix-1/pak-1* pathway controls early elongation mostly at the anterior part of the embryo (Martin *et al.*, 2014. Note that D2/V2 junctions display higher RDR than D1/V1 (right panel; Figure 2C and D) suggesting that morphogenetic differences observed for the anterior and posterior junctions of H1 lateral cells (Figure 1D) are also observed at dorsal and ventral cells and involve the function of *pix-1* and *pak-1*.

Altogether, these data suggest that *let-502* controls the deformation of transversal junctions of anterior and posterior lateral cells and ventral posterior cells while *pix-1* and *pak-1* control the deformation of transversal junctions of dorsal and ventral anterior cells. These data also suggest that while *let-502* controls junction shrinking similarly in lateral and ventral posterior cells, *pix-1* and *pak-1* function in a more spatially restricted manner, with a prominent function observed at the D2/V2 transversal junctions.

4.4.3 *let-502* and *pix-1/pak-1* pathways control the reorganization of apical junctions in distinct sets of hypodermal cells.

In order to assess the role played by signaling pathways controlling myosin contraction on apical junction remodelling, we identified a novel metric enabling a quantitative assessment of myosin-dependent remodelling of cell-cell junctions. The anisotropy of fluorescently-tagged junction proteins – being the ratio of the maximal versus the minimal intensity of fluorescence measured along the junctions – was shown to correlate significantly with myosin-dependent tension applied to the junctions in mammalian systems (Engl *et al.*, 2014). We thus measured the anisotropy of AJM-1::GFP at the transversal lateral junctions of *wt* embryos (Figure 3A-B). This revealed that AJM-1::GFP anisotropy significantly anti-correlated with the shrinking rate of these junctions (Spearman correlation = -0.98; *p*-value = $3.9.10^{-4}$; Figure 3B). We also measured the anisotropy of AJM-1::GFP at the lateral anterior transversal junctions (L1, L2 and L3) in *wt* embryos and embryos carrying a thermosensitive allele of the myosin heavy-chain coding gene *nmy-2(ne1490ts)*, at both permissive and restrictive temperature (18°C and 25°C respectively; Figure 3A and C). This study revealed that AJM-1::GFP anisotropy was significantly reduced of at the junctions upon inactivation of *nmy-2* (Figure 3A and C). Therefore, these data identify the measurement of AJM-1::GFP anisotropy at the cell-cell junctions as a powerful metric to measure myosin contraction-dependent remodelling of apical junctions during early elongation.

We subsequently measured AJM-1::GFP anisotropy at the transversal junctions between anterior hypodermal cells in *wt*, *let-502(RNAi)*, *pix-1(gk416)* and *pak-1(ok448)* embryos (Figure 4A-C). This anisotropy was significantly reduced at D2 junctions between dorsal cells in *pix-1(gk416)* and *pak-1(ok448)* but not in *let-502(RNAi)* embryos (Figure 4A). In contrast, it was significantly reduced at L1 and L2 junctions between lateral cells in *let-502(RNAi)* but not in *pix-1* and *pak-1* mutants

(Figure 4B). No significant variation of AJM-1::GFP anisotropy was observed at ventral anterior junctions of tested animals (Figure 4C). These data suggest that *pix-1* and *pak-1* control the D2 junctions remodelling between anterior dorsal cells while *let-502* controls the L1 and L2 junctions remodelling between lateral anterior cells.

4.4.4 Dorsal and lateral hypodermal cells produce convergent lamellipodia and amoeboid-like protrusions during early elongation.

Epithelial morphogenesis was shown to involve the formation of basolateral protrusions during both dorsal intercalation and ventral enclosure in *C. elegans* (Williams-Masson *et al.*, 1997 ; Williams-Masson *et al.*, 1998). However, the potential involvement of such protrusions during early elongation has never been investigated. Photobleaching of the F-actin-binding probes VAB-10(ABD)::mCherry in a selected subset of cells was used to observe the formation of potential protrusions by dorsal, lateral and ventral anterior hypodermal cells. This revealed that dorsal 1/2 cells produce polarized and highly dynamic flat protrusions reminiscent of lamellipodia towards the lateral H1 cells (Figure 5A). This study also revealed that lateral H2 cells produce a unique and deep protrusion located underneath the transversal junction between the dorsal 1/2 and the dorsal 3 hypodermal cells (Figure 5B). To characterize better the morphology and the behaviour of this protrusion, we generated transgenic animals carrying an integrated array *sajIs50* expressing a soluble photoconvertible fluorescent protein, Kaede (Ando *et al.*, 2002), under the control of the hypodermal specific *lin-26p* promoter. Pulses of blue-light illumination of H2 lateral cells induced the photoconversion of Kaede green fluorescent proteins into strong red fluorescent proteins as previously shown (Ando *et al.*, 2002). This spectral isolation of H2 cell confirmed that H2 produced a unique basolateral protrusion towards the dorsal cells which displays a thin neck emerging from the cell body (arrow, Figure 5C and D) followed by a deep cytoplasmic extension (arrow-head; Figure 5C and D) in which was transferred part of the cytoplasm (Figure 5E; Movie

1). Interestingly, these features are usually observed for protrusions used during amoeboid migration of macrophages or invasive carcinoma in mammals (Carr *et al.*, 2013) but, to our knowledge, have never been observed in polarized epithelial cells.

In summary, these data suggest that dorsal cells produce large flat lamellipodia-like protrusions towards the lateral cells while H2 lateral cells produce deep amoeboid-like protrusions towards the dorsal cells. No protrusion was observed between lateral and ventral cells.

4.4.5 *pix-1/pak-1* and *let-502* control the formation and shape of lamellipodia and amoeboid-like protrusions respectively

We subsequently assessed whether *pix-1, pak-1* and *let-502* control the protrusive activity of dorsal and lateral hypodermal cells. Using the same selective photobleaching strategy described above, we measured the size of the protrusions produced by dorsal and lateral cells. Protrusions formed by dorsal cells spread along the longitudinal junction between dorsal 1/2 and lateral H1 cells. Therefore, we normalized the length of the protrusion on the length of this junction (see Materials and methods). The resulting spreading rate of the protrusions was significantly reduced in *pix-1(gk416), pak-1(ok448)* and *let-502(RNAi)* embryos when compared to *wt* (Figure 6A and C). We also assessed the distribution of the protrusion along the longitudinal junction (see Materials and methods; Figure S5). This revealed that protrusions disappeared specifically at the posterior part of this junction in *pix-1(gk614)* and *pak-1(ok448)* embryos (Figure 6D), suggesting that *pix-1* and *pak-1* control the formation and the spreading of protrusions produced by dorsal cells specifically towards the posterior part of H1 lateral cells.

We characterized the protrusive activity of lateral cells by measuring the area covered by the protrusion on a Z-stack projection (white dashed line; Figure 7A). This measurement revealed that the protrusion produced by H2 was significantly more

spread in *let-502(RNAi)* embryos when compared to *wt*, and *pix-1(gk416)* embryos (Figure 7A and B). A slight but significant increase of the protrusion surface was also observed in *pak-1(ok448)* embryos. However, this later surface increase was not correlated with the spreading of the protrusion along the antero-posterior axis as observed for *let-502(RNAi)* animals (Figure 7A), suggesting that deletion of *pak-1* did not significantly change the morphology of the protrusion produced by the lateral cells.

Altogether these data suggest that *let-502* controls the morphology of the amoeboid-like protrusions produced by H2 towards the D2 junction, while *pix-1* and *pak-1* control the formation and spreading of basolateral lamellipodia towards the L2 junction. *let-502* may also control part of the protrusive activity of dorsal cells uniformly along the longitudinal junctions between dorsal and lateral cells. Therefore, these data suggest that *pix-1/pak-1* and *let-502* control the formation of convergent protrusions along the aligned D2/L2 junctions and that their function are prominent in either dorsal or lateral cells.

4.4.6 *pix-1* and *pak-1* functions contribute to the reduction of AJM-1::GFP accumulation at D2/L2 vertice

D2 and L2 junctions display faster shrinking rate (Figure 1D) and more elevated myosin-dependent apical remodelling than D1 and L1 (Figure 4A and B), suggesting that the vertex located at the intersection of these junctions (D2/L2 vertex) is submitted to a higher tension than D1/L1 vertex (Figure 8A and B). Considering that *pix-1/pak-1* and *let-502* control the formation of convergent protrusions along the aligned D2/L2 junctions, we assessed whether the formation of these protrusions may impact differently on the tension applied on D1/L1 and D2/L2 vertices. We showed above a significant correlation between the anisotropy of AJM-1::GFP at cell-cell junction and intracellular myosin contraction (Figure 3). Other groups have also

demonstrated that junction proteins tend to accumulate at a cell-cell junction in response of increasing tension and traction forces (Engl *et al.*, 2014). Consistent with these studies, we observed that AJM-1::GFP strongly accumulate at D1/L1 and D2/L2 junction vertices where tension is expected to be the strongest along the longitudinal junctions between Dorsal 1/2 and lateral H1 cells in *wt* embryos (black line; Figure 8C). Interestingly, AJM-1::GFP accumulation was similar at D1/L1 and D2/L2 vertices in these animals. It was also reduced at both vertices in a similar manner in *nmy(ne1490ts)* embryos at restrictive temperature (25°C) and in *let-502(RNAi)* embryos (grey and green line respectively; Figure 8C). This accumulation was also significantly increased at D2/L2 in *pix-1(gk416)* and *pak-1(ok448)* when compared to *wt* (blue and red lines respectively; Figure 8C). If we postulate that AJM-1::GFP accumulates at the cell-cell junctions in response to an increased tension and/or pulling forces applied on the junctions, it suggests that NMY-2 and LET-502 increase the tension/pulling forces applied on both D1/L1 and D2/L2 vertices which is consistent with their expected function on myosin contraction (Piekny *et al.*, 2003 ; Gally *et al.*, 2009). These data also suggest that the function of PIX-1 and PAK-1 tend to decrease the tension applied on D2/L2 vertex and has no significant impact on the tension applied on D1/L1 vertex.

4.4.7 Cell autonomous antagonism between *let-502* and *pix-1/pak-1* controls the switch between Rac1- and RhoA-like morphogenetic programs

In order to assess whether the cell-to-cell heterogeneity observed in hypodermis during early elongation depends on a cell autonomous antagonism between the Rac1 and RhoA pathways, as shown for isogenic population of mesenchymal cells *in vitro* Sailem *et al.*, 2014, we assessed whether knockout of *pix-1* or *pak-1* may induce a switch of the morphogenetic program adopted by dorsal cells towards *let-502*. To do so, we measured the anisotropy of AJM-1::GFP at D1 and D2 junctions between dorsal cells in *pix-1(gk416); let-502(RNAi)* and in *pak-1(ok448); let-502(RNAi)*. This

analysis revealed that *let-502(RNAi)* significantly reduced AJM-1::GFP anisotropy at D2 when compared to *pix-1(gk416)* and *pak-1(ok4486)* embryos (t-test, *p*-value ≤ 0.046; Figure 9A). This suggests that *let-502* controls the remodelling of apical junctions between dorsal cells in the absence of *pix-1* or *pak-1*. The spreading rate and the antero-posterior distribution of the protrusions produced by dorsal cells in *let-502(RNAi); pix-1(gk416)* and *pix-1(gk416)* were, however, similar (Figure 6B and C), suggesting that *let-502* does not control the formation and polarity of protrusions produced by these cells in the absence of *pix-1*. Unfortunately, the level of filamentous actin detected by the VAB-10(ABD)::mCherry probe in *pak-1(ok4480); let-502(RNAi)* embryos was too low to assess the morphology and spreading of protrusions produced by dorsal cells in these animals.

We subsequently assessed whether the knock-down of *let-502* may switch lateral cells from a RhoA- to a Rac-1-like program. To do so, we measured AJM-1::GFP anisotropy at L1 and L2 junctions in *pix-1(gk416); let-502(RNAi)* and *pak-1(ok448); let-502(RNAi)*. This analysis revealed that *pak-1(ok448),* but not *pix-1(gk416),* significantly reduced AJM-1::GFP anisotropy at L2 junction of *let-502(RNAi)* embryos (Figure 9B), suggesting that *pak-1* has a significant function on the remodelling of the L2 apical junctions upon *let-502* knock-down.

To better understand the mechanisms underlying this switch between RhoA- and Rac1-like programs, we further characterized the structure of apical junctions in different genetic backgrounds through measurement of AJM-1::GFP cluster density (see Materials and methods; Figure 9B). It revealed that both L1 and L2 displayed a significant increase of AJM-1 cluster density in *let-502(RNAi)* when compared to *wt, pix-1(gk416)* and *pak-1(ok448)* (t-test *p*-values < 0.025; Figure 9C). This increase was maintained in *pak-1(ok448); let-502(RNAi)* and completely suppressed at both L1 and L2 junctions in *pix-1(gk416); let-502(RNAi)* embryos (Figure 9C). As identification of protein clusters at cell-cell junctions requiring high accumulation

levels of these proteins, this analysis could not be done for junctions between dorsal cells.

Together, these data suggest that lateral hypodermal cells switch from a RhoA-like program to a Rac1-like program involving *pix-1* and *pak-1* upon functional alteration of *let-502*. In these conditions, *pix-1* controls AJM-1 clusters density and *pak-1* controls the AJM-1 accumulation at the junctions between lateral cells.

These data suggest that the adoption of a RhoA-like program by lateral cells depends on the inhibition of *pix-1* and *pak-1* by *let-502*. *let-502* is expected to control early elongation mainly through activation of myosin contraction at the apical junctions of hypodermal cells (Piekny *et al.*, 2000). The function of *pix-1* and its homolog β-PIX were shown in both *C. elegans* and mammals to be regulated by mechanical stimuli (Zhang *et al.*, 2011 ; Plutoni *et al.*, 2016). We consequently assessed whether *pix-1* inhibition by *let-502* in lateral cells may be indirect and depend on the level of myosin contraction at the apical junctions between lateral cells. To test this possibility, we measured AJM-1 cluster density at L2 junctions in *nmy-2(ne1490ts)* embryos at permissive (18°C) and restrictive temperatures (25.5°C; Figure 9B and C). No significant difference of AJM-1::GFP cluster density was observed in these conditions when compared to *wt* animals, suggesting that LET-502 inhibits PIX-1 in lateral cells, independently from its function on NMY-2 contraction.

We also assessed whether the switch between morphogenetic programs controlling apical junction remodelling upon *let-502(RNAi)* is also associated to a change of protrusion morphology. The over-spread protrusion produced by H2 in *let-502(RNAi)* animals was inhibited in more than 50% (N=10) of *pix-1(gk416); let-502(RNAi)* embryos (Figure 7B and C). These data suggest that *pix-1* controls the morphology of protrusions produced by lateral cells upon *let-502(RNAi)*. The low penetrance of this inhibition by *pix-1(ok416)* also suggests that *pix-1* controls the morphology of these protrusions, in parallel with gene(s) that remain(s) to be identified. Unfortunately, the

protrusions produced by lateral cells could not be analyzed in *pak-1(ok4480); let-502(RNAi)* due to the low level of filamentous actin detected in these embryos.

4.5 Discussion

Antagonism between Rac1 and RhoA has been shown to control different morphogenetic processes during embryonic development, the activation of these GTPases being restricted to mutually exclusive subcellular compartments or sequential (Duan *et al.*, 2010 ; Chauhan *et al.*, 2011). We used here a novel imaging approach to characterize the function of the RhoA-like *rho-1/let-502* and the Rac1-like *pix-1/pak-1* pathways at a single cell level during early elongation in *C. elegans*. This study revealed that *pix-1* and *pak-1* are mainly involved in the remodelling of apical junctions between dorsal and ventral anterior cells while *let-502* controls the remodelling of apical junctions between lateral cells and between ventral posterior cells. This study also revealed that dorsal and lateral anterior cells produce basolateral protrusions in a polarized and convergent manner: dorsal cells producing flat lamellipodia-like protrusions towards the lateral cells and lateral cells producing deep amoeboid-like protrusions towards the dorsal cells. Intriguingly, this study also revealed that *pix-1/pak-1*-dependent protrusions produced by dorsal cells tend to reduce the tension building between dorsal and lateral cells during early elongation. Importantly, these data suggest that adoption by the cells of either a *pix-1/pak-1* (Rac1-like) or *let-502* (RhoA-like) program defines their morphology and behaviour during morphogenesis (Figure 10). Therefore, cell-autonomous antagonism between *pix-1/pak-1* and *let-502* defines cell-to-cell heterogeneity during epidermal morphogenesis, enabling cells to switch between programs when one of these genes gets genetically compromised (Figure 10B-C). *pix-1/pak-1* and *let-502* pathways, while being antagonistic at a single cell level, function in a synergistic manner when

considered at the organism level, presumably due to the cooperation of cells during elongation.

4.5.1 The remodelling of apical junctions use either LET-502 or PIX-1/PAK-1

The data presented in this study revealed that PIX-1 and PAK-1 control the remodelling of apical junctions between dorsal anterior cells, while LET-502 controls this remodelling between lateral cells. These observations are in agreement with previous studies showing that PIX-1 and PAK-1 control early elongation in parallel with LET-502 (Gally *et al.*, 2009 ; Martin *et al.*, 2014) and predominantly function at the anterior part of the embryo (Martin *et al.*, 2014). During *D. melanogaster* development, DPAK/PAK-1 was shown to control salivary gland lumen size through modulation of myosin-dependent endocytic processes (Pirraglia *et al.*, 2010). A similar function was also reported for ROCK/LET-502 during germ-band extension in this organism (Bertet *et al.*, 2004). Remodelling of apical junctions through the regulation of myosin-dependent endocytic processes by PIX-1/PAK-1 or LET-502 is an attractive hypothesis that needs to be tested during early elongation in *C. elegans*.

This study also revealed that while both PIX-1 and PAK-1 control the anisotropy of AJM-1::GFP at the apical junctions between dorsal cells, they tend to display distinct molecular functions at the apical junctions between lateral cells in the absence of LET-502. For instance, in these later conditions, PAK-1 controls AJM-1::GFP anisotropy at apical junctions while PIX-1 controls AJM-1::GFP cluster density. The fact that PIX-1 and PAK-1 may have common and independent function during morphogenesis has already been suggested (Martin *et al.*, 2014). We cannot however exclude the possibility that PIX-1 and PAK-1 may function redundantly with genes that remain to be identified in lateral cells.

4.5.2 Basolateral protrusions may reduce the tension building at cell-cell junctions during morphogenesis

Basolateral protrusions produced by epithelial cells during morphogenesis have been described as motor structures enabling directional cell movement (Heid *et al.*, 2001 ; Farooqui et Fenteany, 2005 ; Zallen, 2007). Such protrusions were shown to drive dorsal intercalation (Williams-Masson *et al.*, 1998 ; Walck-Shannon *et al.*, 2015) and ventral enclosure (Williams-Masson *et al.*, 1997) in *C. elegans*. The protrusions produced by dorsal and lateral cells during early elongation, identified here, are not associated to any notable relative displacement of these cells within the epithelium. Moreover, while the function of the amoeboid-like protrusions produced by lateral cells is unknown, *pix-1* and *pak-1*-dependent protrusions produced by the dorsal cells appear to reduce the tension applied on the vertex at the intersection of D2 and L2 junctions (Figure 8). Mechano-coupling between epithelial cells during morphogenesis and its involvement in the modulation of the cell protrusive activity have mostly been described during collective migration of epithelial cells (reviewed by (Mayor et Etienne-Manneville, 2016). Mechano-biology studies recently revealed that forces at the cell-cell junctions or cell-bead contact are counterbalanced by traction forces biased away from this interface (Liu *et al.*, 2010 ; Maruthamuthu *et al.*, 2011 ; Weber *et al.*, 2012). In the current system, D2 and L2 are remodelled by either PIX-1/PAK-1 or LET-502-dependent mechanisms aiming to shrink junctions in two opposite directions. We hypothesize that PIX-1/PAK-1-dependent protrusions generate traction forces at D2/L2 vertex in the opposite direction than forces produced by PIX-1/PAK-1 pathway controlling D2 shrinking. Forces produces by these protrusions may consequently reduce the tugging forces applied to this vertex (Figure 8B). Supporting the involvement of PIX-1 in this process, β-PIX/PIX-1 has been identified as a mechanotransducer in both mammals and *C. elegans* (Kuo *et al.*, 2011 ; Vicente-Manzanares *et al.*, 2011 ; Zhang *et al.*, 2011 ; Plutoni *et al.*, 2016). β-PIX, PAK1 complex and their partner Scribble have also been shown to shuffle

between apical junctions and focal adhesion complexes enabling polarized migration during wound-healing (Dow *et al.*, 2007). These data suggest that PIX-1 may have the required mechanosensing and mechanotransduction abilities to drive the formation of polarized protrusions in response to high tension/tugging forces sensed at the apical junctions. While attractive, this hypothesis implies the conservation of β-PIX/PIX-1 at focal adhesions during protrusion formation. It is, however, important to highlight the fact that integrins and consequently, focal adhesion complexes have not been involved yet in the formation of protrusions by hypodermal cells during epidermal morphogenesis in *C. elegans*.

4.5.3 Bistable behavior of RhoA-like and Rac1-like programs define cell-to-cell heterogeneity during epidermal morphogenesis

Double-negative feedback loops resulting from mutual inhibition can lead to bistability (Kholodenko, 2006). A bistable system, such as that involving the mutual inhibition between Rac1 and RhoA can flip between two biochemical processes and can promote different cellular phenotypes (Jilkine *et al.*, 2007 ; Symons et Segall, 2009 ; Tsyganov *et al.*, 2012). It also allows the cell to make a discrete decision when exposed to environmental fluctuation while ensuring robustness of the cellular behavior (Byrne, 2016). Bistability of Rac1/RhoA system allows the mutually exclusive activation of Rac1 and RhoA during cell migration and organogenesis (Jilkine *et al.*, 2007 ; Pertz, 2010 ; Guilluy *et al.*, 2011 ; Semplice *et al.*, 2012). It was also proposed to control morphological changes of isogenic populations of BG-2 *D. melanogaster* cells (Sailem *et al.*, 2014). Interestingly, in carcinoma cells, the mutual inhibition of Rac1 and RhoA controls the morphological switch enabling cells to migrate using either lamellae formation (Rac1 program) or amoeboid migration mode (RhoA program) (Ohta *et al.*, 2006 ; Saito *et al.*, 2012 ; Nakamura, 2013). Altogether, these studies are consistent with data reported here showing that cells produce either

lamellipodia-like protrusion in a PIX-1/PAK-1-dependent manner or produce amoeboid-like protrusions in a LET-502-dependent manner.

Several mechanisms involving regulators and effectors of RhoA and Rac1 have been involved in the mutual inhibition of these GTPases as reviewed by Guilluy *et al.* (Guilluy *et al.*, 2011). Data presented here suggest that PIX-1, PAK-1 and LET-502 control Rac1/RhoA bistability during embryonic elongation. In the absence of PIX-1 or PAK-1, LET-502 partially restores apical junction remodelling between dorsal cells. The partial compensation provided by LET-502 in these conditions suggests that PIX-1 and PAK-1 may only partially contribute to the inhibition of LET-502 function in dorsal cells. The RHO-1/LET-502 pathway being inhibited in these cells by the RHO-1-specific GTPase-activating protein (GAP) RGA-2 (Diogon *et al.*, 2007), these data suggest that PIX-1 and PAK-1 may either activate RGA-2 in a redundant manner with genes that remain to be identified or may inhibit RHO-1-specific GEFs as shown for PAK1/PAK-1 in several system (Alberts *et al.*, 2005 ; Rosenfeldt *et al.*, 2006). In this later case, RHO-1 specific GEFs may be activated in dorsal cells in the absence of PIX-1 and PAK-1 and may compete with RGA-2 leading to moderate RHO-1 activation (Figure 10 D). The current study also suggests that LET-502 inhibits PIX-1 and PAK-1 in the lateral cells during early elongation. ROCK/LET-502 and β-PIX/PIX-1 have already been involved in RhoA-dependent inactivation of Rac1 in mammalian cells; ROCK function, displacing β-PIX from focal adhesion complex during junction maturation (Kuo *et al.*, 2011 ; Vicente-Manzanares *et al.*, 2011). The limited ability of PAK-1 to fully restore apical remodelling between lateral cells in *let-502(RNAi)* animals, may be due to the lower ability of PAK-1 to phosphorylate myosin-light chain or to its inability to inhibit MEL-11 (Piekny *et al.*, 2003 ; Gally *et al.*, 2009 ; Martin *et al.*, 2014), both resulting to an expected reduced level of myosin contraction at apical junctions.

Taken together, these data suggest that epithelial cells can adopt either RhoA or Rac1 morphogenetic programs which are associated to morphological distinctive properties

while being fully polarized, cohesive and cooperative during morphogenesis. These are quite novel and provocative results that could explain the evolutionarily conserved cell-shape heterogeneity observed in animals and plants epithelia. This study also suggests that morphogenetic processes should be characterized at a single cell level, in order to assess whether cell-to-cell heterogeneity during epithelial morphogenesis is a specific characteristic of *C. elegans* hypodermis or an evolutionarily conserved characteristics of epithelial cell types.

4.6 Methods

4.6.1 Strains and Culture Methods

Control N2 (*wild type / wt*) and other animals were maintained using standard culture conditions at 20°C (Brenner, 1974). Worm strains carrying the following mutations and markers: *pix-1(gk416) X, pak-1(ok448) X, jcIs1 [ajm-1::GFP + unc-29(+) + rol-6(su1006)] IV* and *mcIs40 [lin-26p::ABDvab-10::mcherry + myo-2p::gfp]* and *unc-119(ed3)* were obtained from the *Caenorhabditis Genetic Center* (CGC). Mutant strains were backcrossed at least three times against *wt* animals prior to analysis. Strain carrying *let-502(sb118) I; jcIs1 [ajm-1::GFP + unc-29(+) + rol-6(su1006)] IV, nmy-2(ne1490ts);jcIs1 [ajm-1::GFP + unc-29(+) + rol-6(su1006)] IV* were provided by Dr Alisa Piekny (Concordia University, Montreal, Canada). *jcIs1 [ajm-1::GFP + unc-29(+) + rol-6(su1006)] IV*; *mcIs40 [lin-26p::ABDvab-10::mcherry + myo-2p::gfp]* was generated after crossing *mcIs40 [lin-26p::ABDvab-10::mcherry + myo-2p::gfp]* males with *jcIs1 [ajm-1::GFP + unc-29(+) + rol-6(su1006)] IV* hermaphrodites. *pix-1(gk416) X, jcIs1 [ajm-1::GFP + unc-29(+) + rol-6(su1006)] IV*; *mcIs40 [lin-26p::ABDvab-10::mcherry + myo-2p::gfp]* and *pak-1(ok448) X, jcIs1 [ajm-1::GFP + unc-29(+) + rol-6(su1006)] IV*; *mcIs40 [lin-26p::ABDvab-10::mcherry + myo-2p::gfp]* were generated after crossing *jcIs1 [ajm-1::GFP + unc-*

29(+) + rol-6(su1006)] IV; *mcIs40 [lin-26p::ABDvab-10::mcherry + myo-2p::gfp]* hermaphrodites with *pix-1(gk416) X* or *pak-1(ok448) X* males. *unc-119(ed3); jcIs1 [ajm-1::GFP + unc-29(+) + rol-6(su1006)] IV* was generated by crossing *unc-119(ed3)* hermaphrodites with *jcIs1 [ajm-1::GFP + unc-29(+) + rol-6(su1006)] IV* males.

4.6.2 Generation of Transgenic animals

unc-119(ed3); sajIs50 [lin-26p::KAEDE + unc-119^{R}] animals were generated by biolistic bombardment. Expression vector used to generate this transgene was generated using multisite gateway technology (Invitrogen). pCG150 destination vector (Addgene) was recombined with a pDONRP4P1R vector containing 5kb of the *lin-26* promoter *(lin-26p)* (Martin *et al.*, 2014), a pDONR201 containing the coding sequence for *KAEDE* protein amplified from Kaede-N1 (Addgene) and a pCM5.37 containing the *unc-54* 3'UTR (Addgene). This construct was used to generate transgenic animals by biolistic bombardment of *unc-119(ed3)* strain, using a PDS-1000/He system with the Hepta adaptor (Bio-Rad) as previously done (Martin *et al.*, 2014).Transgenic animals expressing AJM-1::GFP together with KAEDE were obtained through crossing *unc-119(ed3)*; *jcIs1 [ajm-1::GFP + unc-29(+) + rol-6(su1006)] IV* hermaphrodites with *unc-119(ed3); sajIs50 [lin-26p::KAEDE + unc-119^{R}]* males.

4.6.3 RNA interference treatment

pL4440 construct containing *let-502* coding sequence were retrieved from the Genome-wide library (Kamath et Ahringer, 2003) and confirmed by sequencing. HT115 bacteria transformed with pL4440 vectors were plated on LB ampicillin (30µg/ml) - tetracyclin (30µg/ml) and grown overnight at 37°C. The next day, isolated colonies of HT115 clones were picked and gown overnight in LB ampicillin

(30µg/ml). RNAi expression was induced by IPTG (30µg/ml) during 1 hour at 37°C. 700µl of bacterial culture were pelleted and resuspended in 300µl S-Basal- ampicillin (30µg/ml) - IPTG (30µg/ml) and put in a 24-well plate. 150-200 L1 worms synchronized through hypochlorite treatment were resuspended in 200µl S-Basal and incubated with 300µl of induced bacterias at 20°C for 48-60 hours before proceeding to microscopy analysis.

4.6.4 Measurement of cell-cell junction deformation

Images used to measure membrane deformation were captured using a Nikon A1R confocal microscope equipped with 60 X oil CFI NA 1.4 Plan Apochromat λ objective. 60 Z-planes (define the top and the bottom to record throughout the entire embryo) were acquired per embryo with a calibration of 0.12 µm/pixel and a Z-step of 0.4 µm. Z-stacked were captured at the beginning of the early elongation (t_0) and after 15 to 20 minutes making sure that the last recording was done before the beginning of late elongation - considered as the time-point when body wall muscles start to contracting. Deformation of cell-cell junction was measured using Vaa3D software (Peng, Ruan, Long, *et al.*, 2010). To do so, Z-stack acquisitions were resampled using a 0.3 factor in order to obtain cubic voxels (0.12 x 0.12 x 0.12 µm) enabling accurate measurement of cell-cell junctions using the 3D reconstruction of image stacks. Cell-cell junction lengths at t_0 (L_0) and after 15 to 20 min (L_{end}) were measured (in pixel) between each vertex identified in the 3D reconstruction. The deformation rate (*DR*) of a junction x in a mutant m was computed as follow: $DR_{x/m} = (L_{end}-L_0)/(t_{end}-t_0)$. With $DR_{x/wt}$ being the deformation rate of the junction x in wild-type embryos, we calculated the relative deformation rate (RDR) of junction x in the mutant m as follow: if both $DR_{x/wt}$ and $DR_{x/m}$ are positive or negative, $RDR_{x/m} = |\log(DR_{x/m} / DR_{x/wt})|$

if ($DR_{x/wt} > 0$ and $DR_{x/m} < 0$), or ($DR_{x/wt} < 0$ and $DR_{x/m} > 0$) : $RDR_{x/m} = |\log(|DR_{x/m} - DR_{x/wt}| / |DR_{x/wt}|)|$. RDR is assigned a negative value if junction x is shorter in m than in *wt* and a positive value otherwise.

4.6.5 Measurement of AJM-1::GFP Anisotropy

Acquisitions recorded for membrane deformation were also used to measure AJM-1::GFP anisotropy. ImageJ software was used to generate a Z-projection of 15-20 upper stacks. Fluorescence intensity plot profiles were drew for each cell-cell junction between vertices using the segmented line tool. The minimum (*Imin*) and maximum (*Imax*) of intensity were thus extracted from these profiles for each junction and the anisotropy (*A*) of AJM-1::GFP accumulated at this junction was computed as previously reported Engl *et al.*, 2014:

$$A = Imax \,/\, Imin$$

4.6.6 Measurement of protrusion surface, spreading and polarity

Image acquisitions to measure protrusions formation by hypodermal cells were done on *wt* and mutant animals expressing *jcIs1[ajm-1::GFP + unc-29(+) + rol-6(su1006)] IV*; *mcIs40[lin-26p::ABDvab-10::mcherry + myo-2p::gfp]* embryos using both Nikon A1R confocal and swept-field confocal microscopes with a 100X oil CFI NA 1.45 Plan Apochromat λ objective. The Nikon A1R confocal was used to photobleach F-actin binding probe in cells surrounding the cell of interest. Photobleaching used several stimulations at 100% power efficiency of 488nm and 561nm laser. F-actin binding probe and AJM-1::GFP were then recorded in unbleached cells using the swept-field confocal microscope by capturing 15 Z-planes with 0.400 µm Z-intervals every 40 seconds for 7 minutes (for protrusions produced by the lateral cells towards the dorsal cells) or for 20 minutes (for protrusions

produced by dorsal and ventral cells towards the lateral cells). The length of the protrusions formed by the dorsal cells was measured using ImageJ software, as well as the length of the cell-cell junction between D1/L1 and D2/L2 vertices. The spreading rate of the protrusions produced by dorsal cells was then calculated as the length of protrusions versus the length of the measured cell-cell junctions. Considering the peculiar morphology of the amoeboid-like protrusion produced by the lateral cells, we measured the surface covered by this protrusion on a Z-projection of the image stack as shown in Figure 7. The spreading rate of the protrusion produced by dorsal cells was measured for 24 time points per embryos for four different embryos. The surface of protrusions produced by lateral cells was measured for 9 time-points per embryo for five different embryos.

To measure the polarity/distribution of the protrusions produced by the dorsal cells, we divided the cell-cell junction located between de D1/L1 and the D2/L2 vertices in ten equal sections. We identified the presence of the protrusion at each section for 24 different time points for four different embryos. We subsequently computed the distribution as the percentage of positive events per measurement per section as indicated in Figure S5. Fisher equal test (computed using R statistical tools, Bioconductor) was used to assess how surprising it is to witness a reduction or an increase of the distribution of protrusions at a given section for a given mutant when compared to *wt* embryos.

4.7 Acknowledgments

Thanks to Dr Alisa Piekny (U. Concordia, Montréal, Canada) for sharing biological materials. Some of the strains were provided by the *Caenorhabditis* Genetics Center, which is funded by NIH Office of Research Infrastructure Programs (P40 OD010440).

4.8 Figures

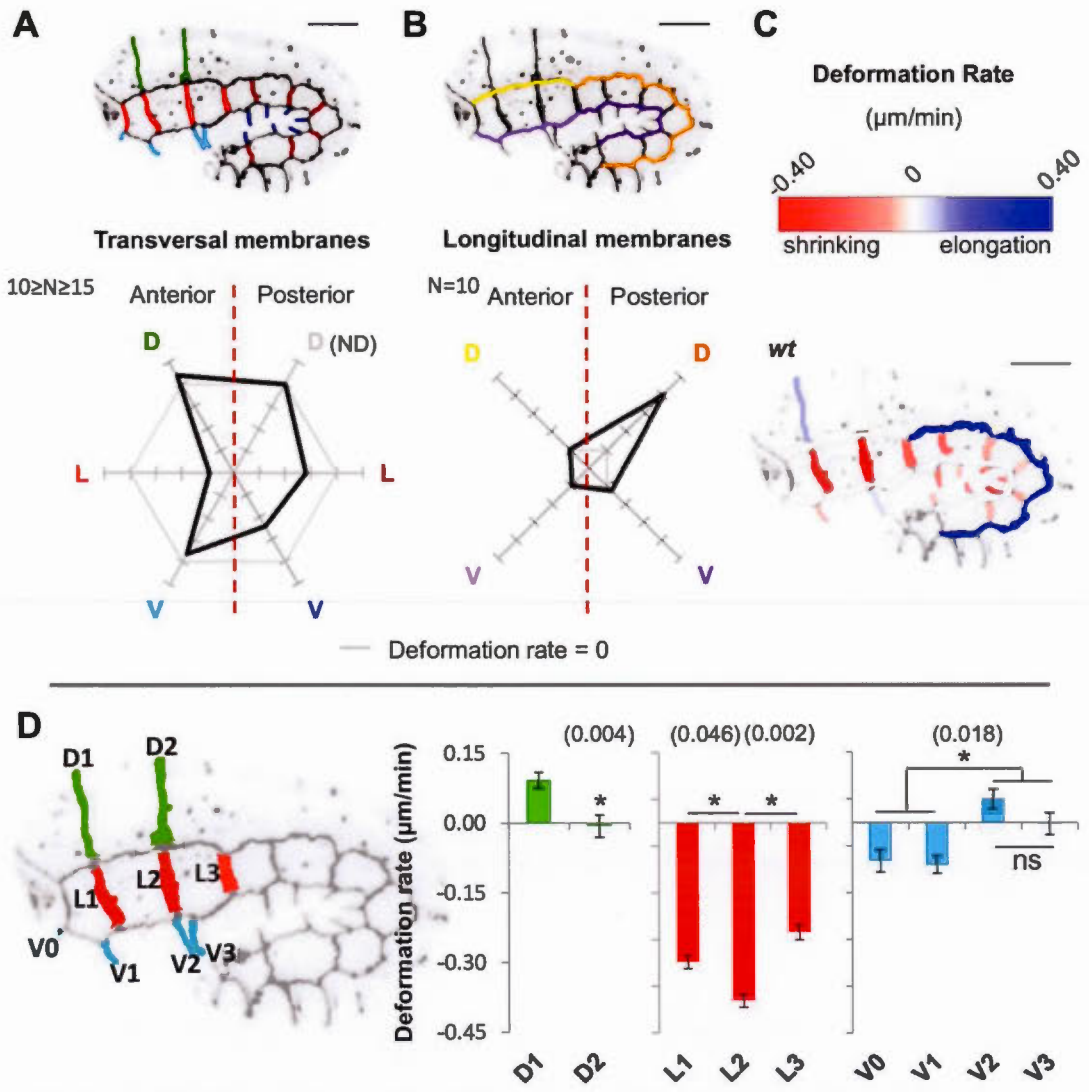

Figure 4.1 : Hypodermal cells follow different morphogenetic programs during early elongation.

Radar graph representing deformation of **(A)** transversal and **(B)** longitudinal cell-cell junctions identified in AJM-1::GFP and VAB-10(ABD)::mCherry expressing embryos. Groups of junctions are identified using color code (upper panel). Antero-posterior orientation of the embryo is indicated in the rose-graph (left to right). Cell-cell junctions between dorsal (D), lateral (L) and ventral (V) hypodermal cells are respectively located at the top, middle and bottom parts of the graph. The zero value

corresponding to junctions with invariant size is indicated by a grey line on rose graph. Positive and negative deformation rates (elongation or shrinking of the junctions) are represented towards the exterior and the interior of the graph respectively. N are the number of embryos analyzed. **(C)** Deformation rates (DR) of the junctions are indicated using artificial color gradient. White junction display constant length, red are shrinking junctions and blue are elongating junctions. **(D)** DR are indicated for junctions between dorsal (D1-2), lateral (L1-3) and ventral cells (V1-3). ND: not determined; ns: not significant; significant T-test *p*-values (*) are indicated within brackets.

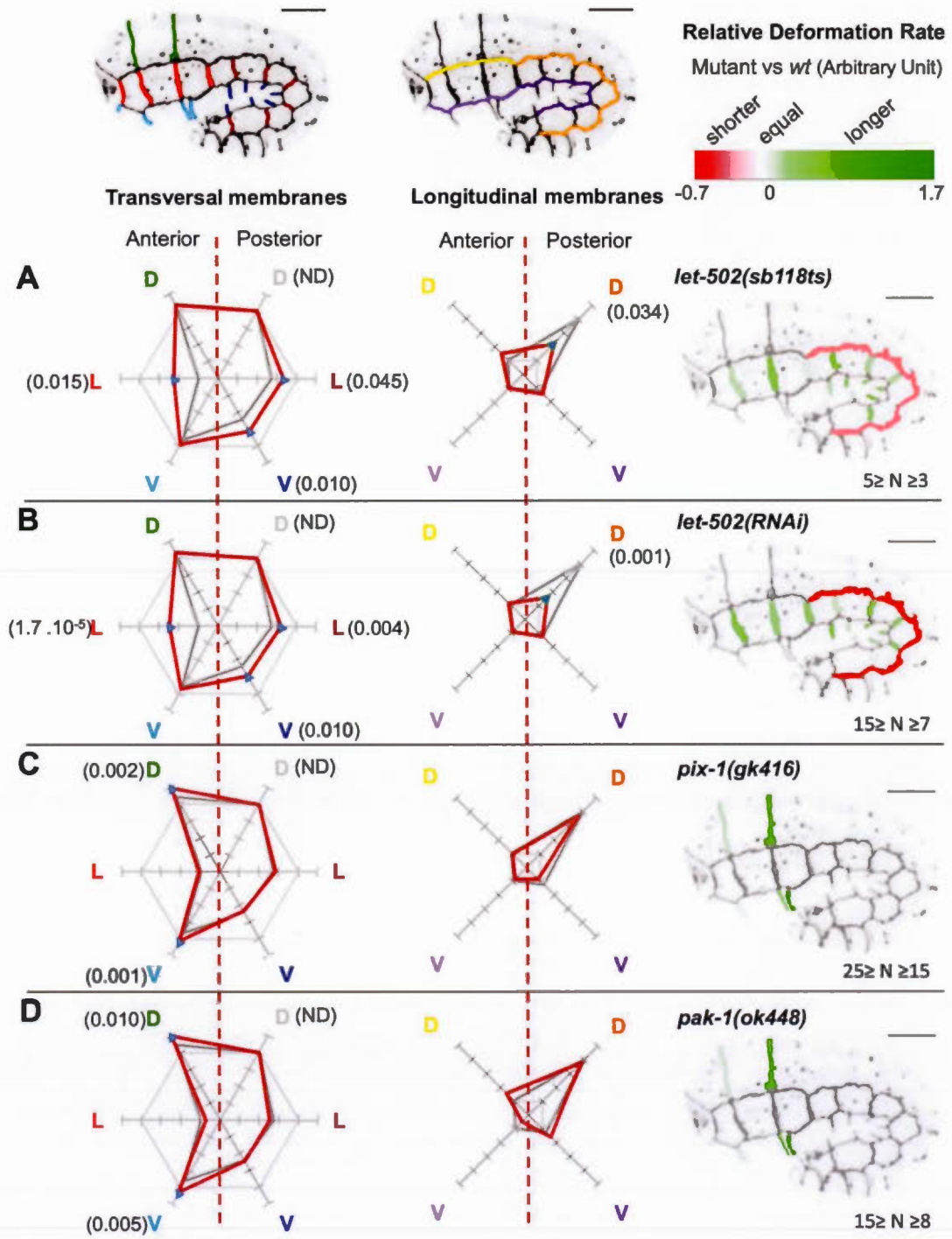
Relative Deformation Rate
Mutant vs wt (Arbitrary Unit)
shorter
equal
longer
-0.7
0
1.7
Transversal membranes
Longitudinal membranes
Anterior
Posterior
A
let-502(sb118ts)
D (ND)
(0.015)L
L (0.045)
V
V (0.010)
D
(0.034)
5≥ N ≥3
B
let-502(RNAi)
(1.7 .10-5)L
(0.001)
15≥ N ≥7
C
pix-1(gk416)
(0.002)D
(0.001)V
25≥ N ≥15
D
pak-1(ok448)
(0.010)D
(0.005)V
15≥ N ≥8

Figure 4.2 : *let-502* and *pix-1/pak-1* control the morphogenesis of different sets of hypodermal cells during early elongation.

Radar graph representing the deformation of cell-cell junctions in **(A)** *let-502(sb118ts)*, **(B)** *let-502(RNAi)*, **(C)** *pix-1(gk416)* and **(D)** *pak-1(ok448)* embryos expressing AJM-1::GFP and VAB-10(ABD)::mCherry. Average deformation rates (DR) of groups of transversal and longitudinal junctions are indicated on the left and in the middle respectively. Relative deformation rates (RDR) compared than *wt* are indicated for each individual junctions on the right. Junction located at the anterior part of the embryo are located at the left of the graph, junctions between dorsal (D) at the top, lateral (L) in the middle and ventral (V) at the bottom. The null DR is represented by thin grey line in the graphs. Positive DR (elongation) are indicated towards the exterior of the radar, and a negative values (shrinking) towards the center. DR for *wt* embryos are represented by a thick grey line. Blue triangles correspond to DR significantly different than observed for *wt* embryos. N corresponds to the number of analyzed embryo. ND: not determined; significant T-test *p*-values are indicated within brackets.

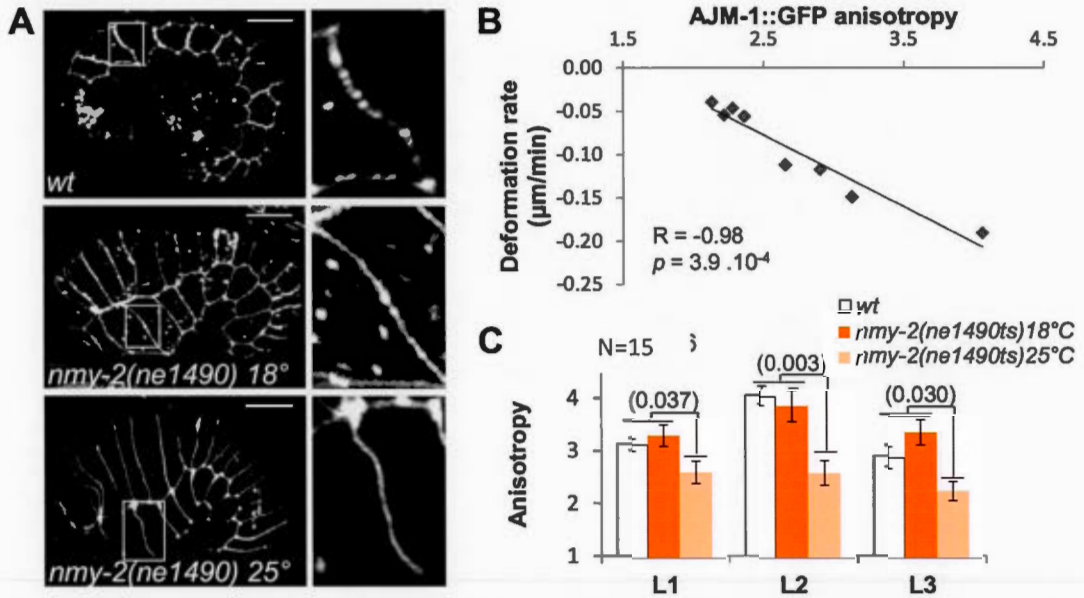

Figure 4.3 : AJM-1::GFP anisotropy is indicative of the level of myosin-dependent cell-cell junction remodelling.

(A) Z-projections of confocal images of AJM-1::GFP expressed in *wt* and *nmy-2(ne1490ts)* at 18°C or 25°C. Locations of the enlarged image (right panel) are indicated by a white box. Scale bar = 10µm. **(B)** Scatter plot expressing the average deformation rates (DR) of transversal junctions between lateral cells in µm/min with respect to the average AJM-1::GFP anisotropy measured for these junctions. The Spearman correlation test (R) is indicated as well as the corresponding *p-value*. **(C)** AJM-1::GFP anisotropy of lateral anterior L1, L2 and L3 junctions in *ajm-1::GFP; vab-10(ABD)::mCh (wt)* and in *nmy-2(ne1490ts); ajm-1::GFP* embryos at 18°C or 25°C. Significant T-test *p*-values are indicated within brackets.

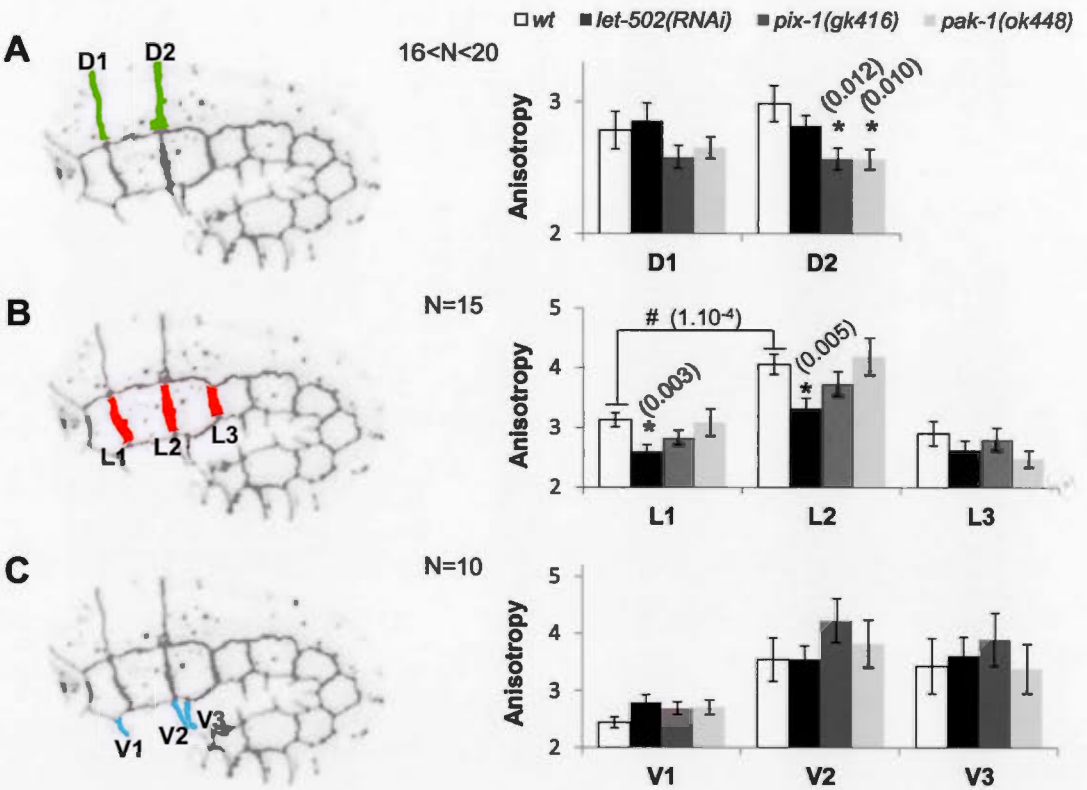

Figure 4.4 : *let-502* and *pix-1/pak-1* control the remodelling of the apical junctions of lateral and dorsal cells respectively.

Mean of AJM-1::GFP anisotropy measured for junction between **(A)** dorsal, **(B)** lateral and **(C)** ventral anterior cells in *wt*, *let-502(RNAi)*, *pix-1(gk416)* and *pak-1(ok448)* embryos expressing AJM-1::GFP and VAB-10(ABD)::mCherry. Error-bars indicate the standard error of the mean. N corresponds to the number of embryos analyzed. Significant T-test *p*-values are indicated within brackets. * indicate T-test *p*-value significantly different than *wt* and # T-test *p*-value significantly different between L1 and L2 junctions in *wt*.

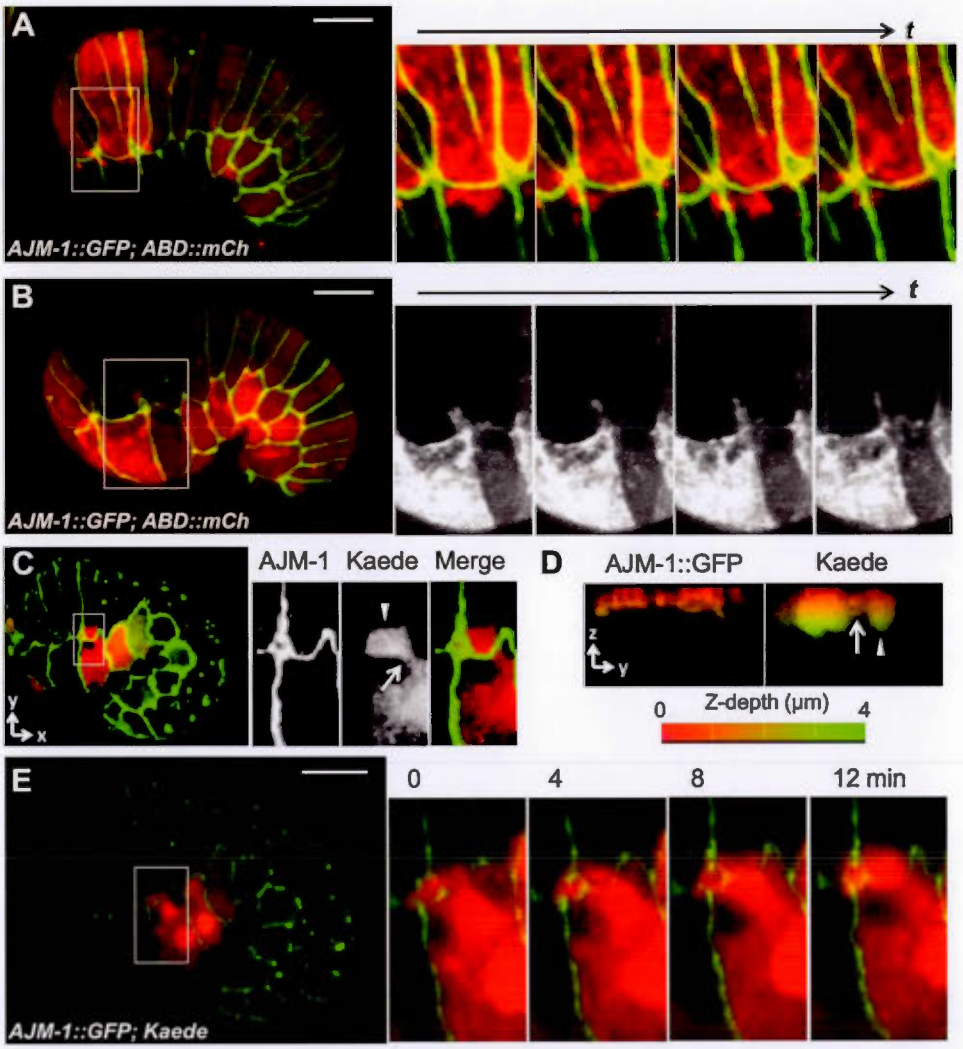

Figure 4.5 : Hypodermal cells produce convergent protrusions during early elongation.

(A) Lamellipodia-like and **(B)** amoeboid-like protrusions produced by dorsal and lateral cells respectively observed in AJM-1::GFP (green) and VAB-10(ABD)::mCherry (red) expressing embryos. Location of the enlarged images is indicated by a white box. They also correspond to time-lapse images with two-minutes intervals. **(C)** Z-projection of embryos expressing AJM-1::GFP (green) and Kaede (red) in hypodermal cells. Location of enlarged imaged are indicated by a white box. **(D)** 3-dimensional reconstruction of embryos expressing AJM-1::GFP (left) and Kaede (right) viewed from the ZY plan. The Z-depth is represented by artificial color from surface (0 µm, red) to 4 µm depth (green). Arrow indicates cell body and arrowhead indicates the head of the protrusion. **(E)** Time lapse recording of AJM-1::GFP (green) and Kaede (red).

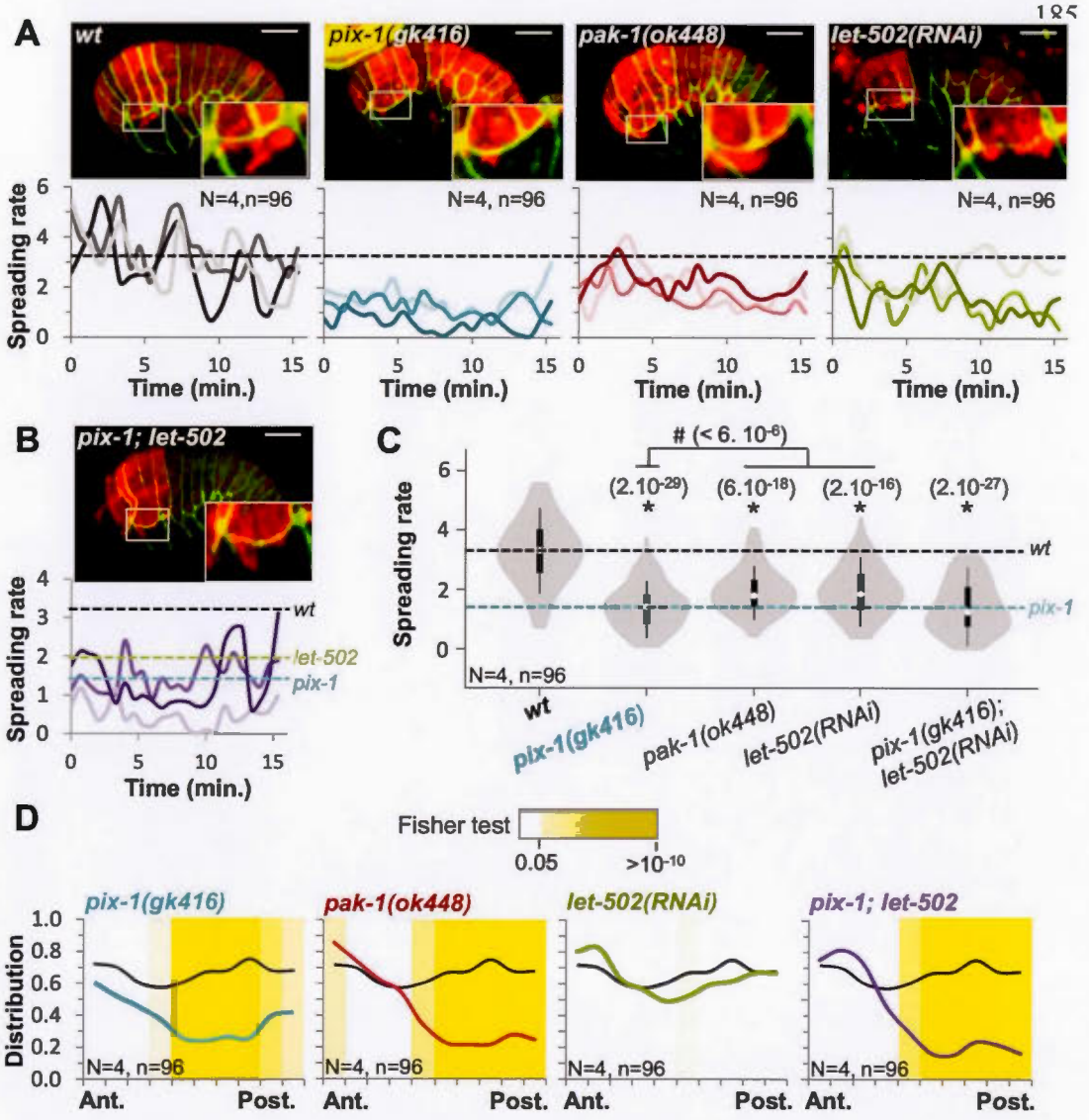

Figure 4.6 : *pix-1* and *pak-1* control the formation of protrusions by dorsal anterior cells.

Z-projections of confocal images and spreading rate of protrusion produced by dorsal cells are indicated over time (lower panel) for 3 representative **(A)** *wt, pix-1(gk416), pak-1(ok448)* and *let-502(RNAi)* and **(B)** *pix-1(gk416); let-502(RNAi)* embryos expressing AJM-1::GFP (green; upper panel) and VAB-10(ABD)::mCherry (red; upper panel). The dashed lines correspond to the mean of spreading rate for *wt* (black), *pix-1(gk416)* (blue) and *let-502(RNAi)* (green). **(C)** Violin plot representing the distribution and average spreading rates for N embryos and n total measurements. **(D)** Antero-posterior distribution of protrusions produced by dorsal cells. The black line corresponds to the distribution observed in *wt* embryos. T-test *p*-value significantly different than *wt* (*), *let-502(RNAi)* (#) are indicated within brackets.

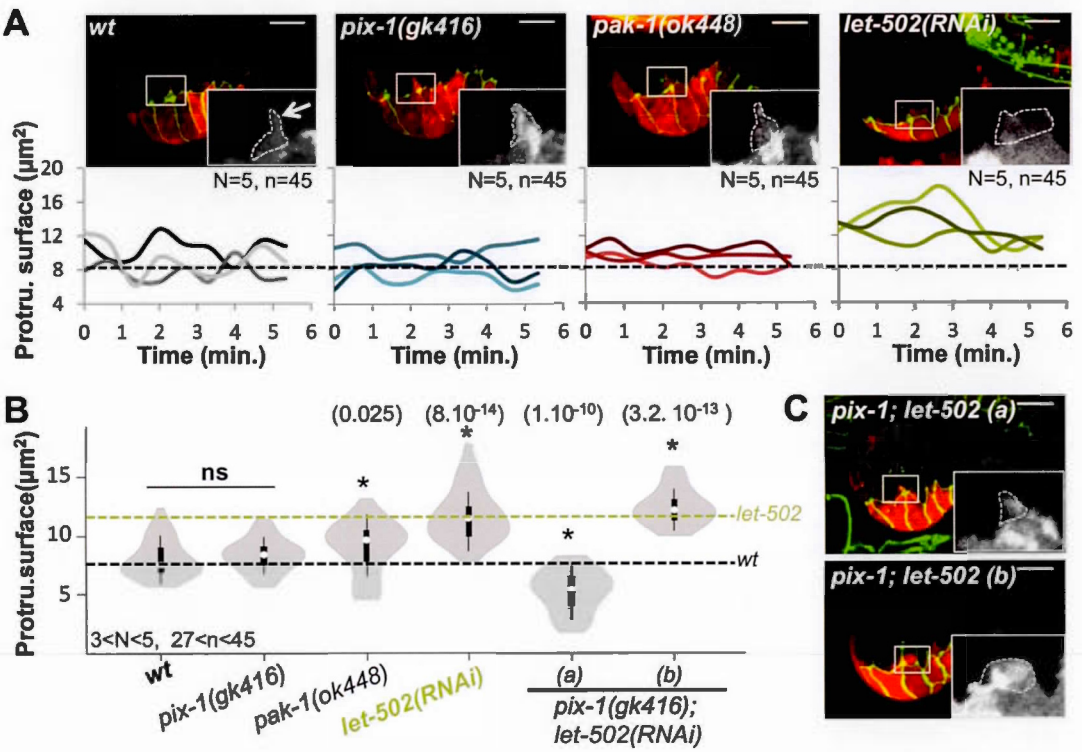

Figure 4.7 : *let-502* controls the formation of protrusions by lateral anterior cells.

(A) Z-projections of confocal images and protrusion surface over time (lower panel) are indicated for 3 representative *wt, pix-1(gk416), pak-1(ok448)* and *let-502(RNAi)* embryos expressing AJM-1::GFP (green; upper panel) and VAB-10(ABD)::mCherry (red; upper panel). The dashed lines correspond to the mean of spreading rate for *wt* (black; A and B) and *let-502(RNAi)* (green; B). **(B)** Violin plot representing the distribution and average of the protrusions surfaces for N analyzed embryos and n analyzed protrusions. **(C)** Z-projections of confocal images of population (a) and (b) of *pix-1(gk416); let-502(RNAi)* embryos. Significant T-test vs *wt, p*-values (*) are indicated within brackets.

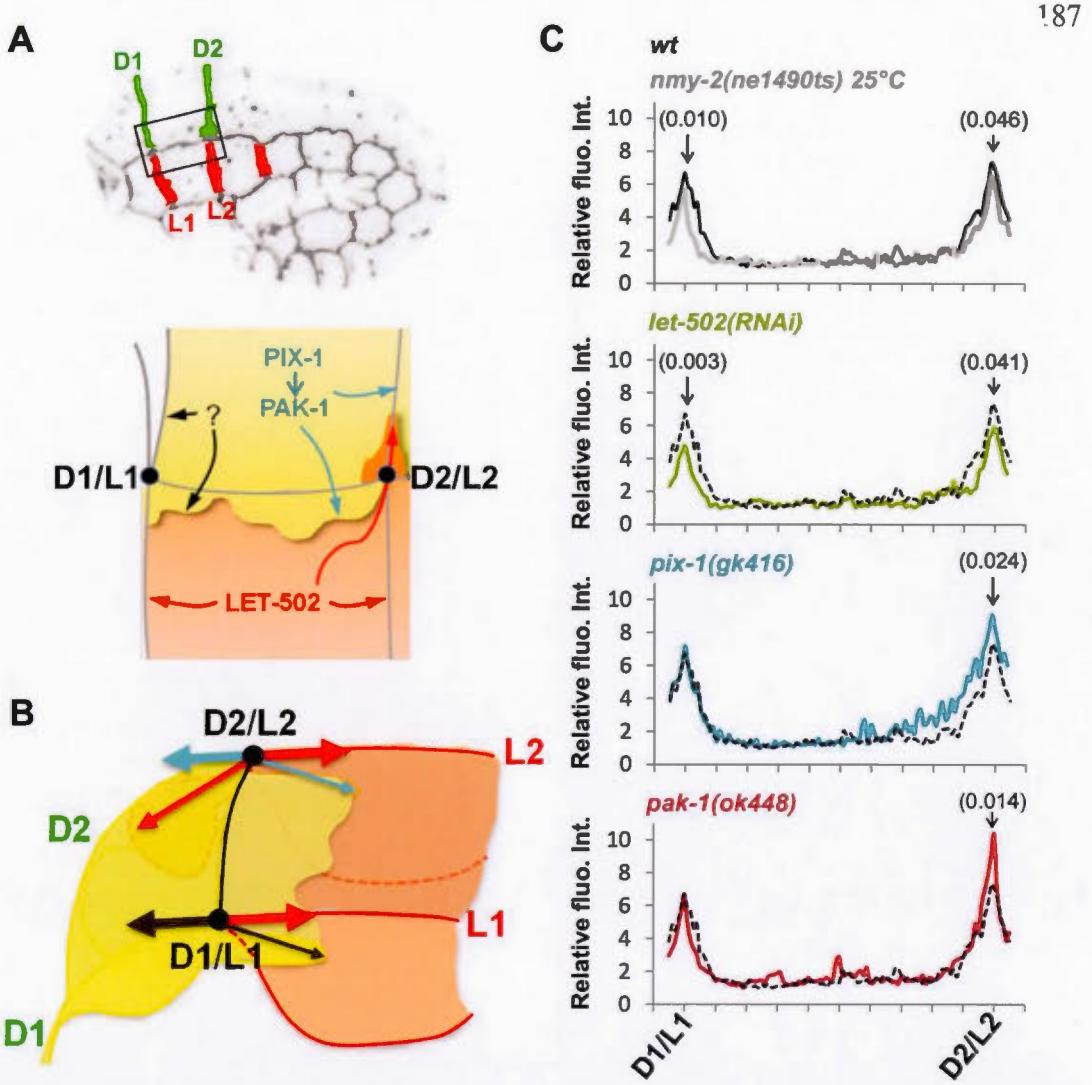

Figure 4.8 : AJM-1::GFP accumulation at D2/L2 vertice is reduced in *pix-1* and *pak-1* mutants.

(A) Schematic representation of lateral and dorsal anterior cells, identifying junctions between dorsal (D1-2) and lateral (L1-2) cells and also the function shown for *let-502*, *pix-1/pak-1* at apical junction and basolateral protrusions. D1/L1 and D2/L2 vertices are also indicated. **(B)** 3D-representation of lateral and dorsal cells showing vertices and longitudinal junction between H1 lateral cells and dorsal 1/2 cells. Arrows represent direction of forces produced by machineries remodeling apical junction and basolateral protrusions. **(C)** Intensity plots of AJM::GFP along the longitudinal junction between D1/L1 and D2/L2 vertices in *wt* (black line), *nmy-2(ne1490ts)* at restrictive temperature 25.5C, *let-502(RNAi)*, *pix-1(gk416)* and *pak-1(ok448)*. Sites of significant T-test vs *wt* are indicated by an arrow; *p*-values are indicated within brackets.

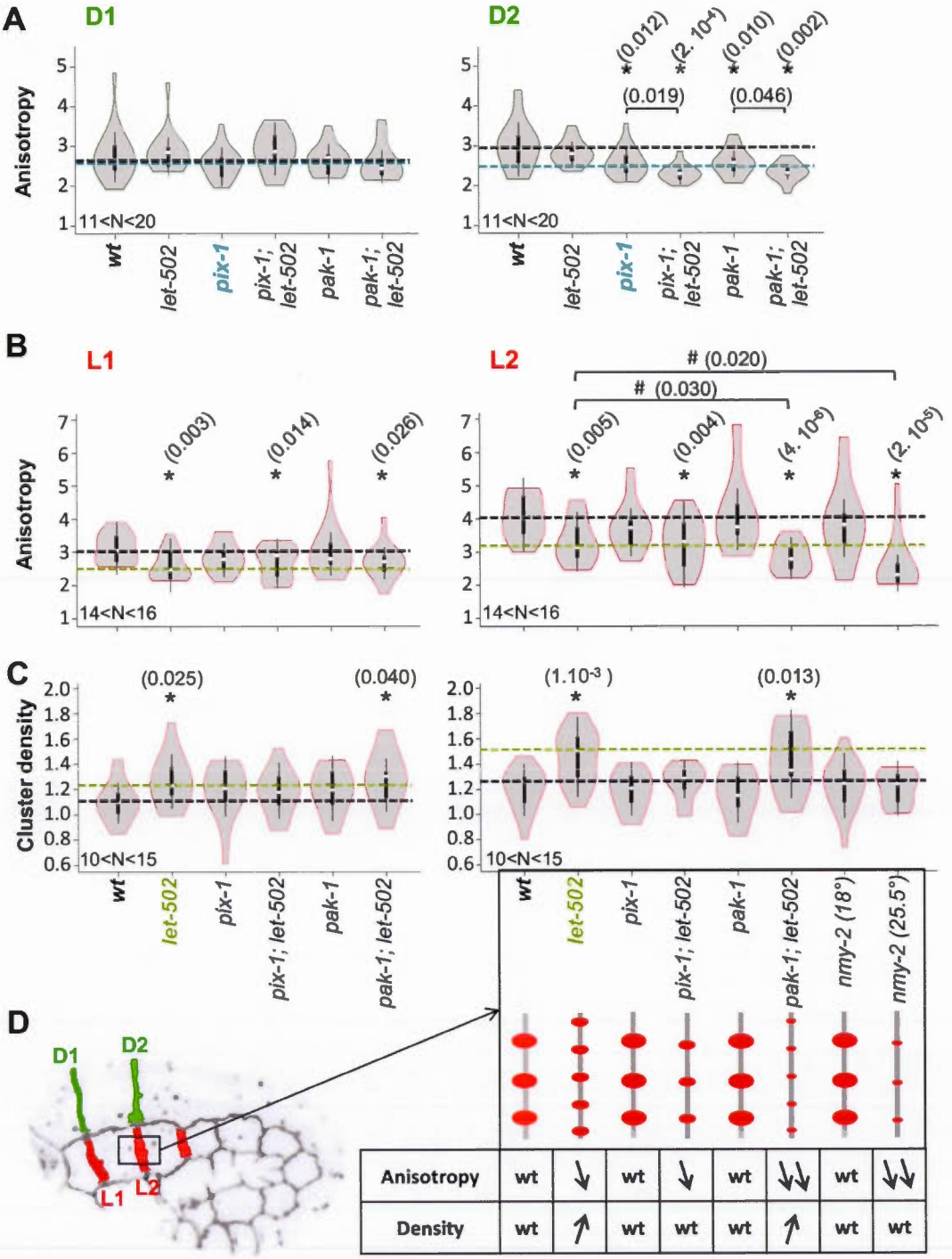
A
D1
D2
Anisotropy
11<N<20
wt
let-502
pix-1
pix-1; let-502
pak-1
pak-1; let-502
*(0.012)
*(2. 10-4)
*(0.010)
*(0.002)
(0.019)
(0.046)
B
L1
L2
14<N<16
*(0.003)
*(0.014)
*(0.026)
(0.020)
(0.030)
*(0.005)
*(0.004)
*(4. 10-6)
*(2. 10-5)
C
Cluster density
10<N<15
(0.025)
(0.040)
(1.10-3)
(0.013)
nmy-2 (18°)
nmy-2 (25.5°)
D
D1
D2
L1
L2
Anisotropy
Density

Figure 4.9 : PIX-1/PAK-1 and LET-502 are antagonistic in dorsal and lateral anterior cells.

Violin plot representing the distribution and mean of AJM-1::GFP anisotropy measured at **(A)** dorsal anterior D1 and D2 junctions and at **(B)** lateral anterior L1 and L2 junctions, and **(C)** the density of AJM-1::GFP clusters (number of cluster per micrometers) measured for the lateral anterior L1 and L2 junctions in *wt*, *let-502(RNAi)*, *pix-1(gk416)*, *pix-1(gk416);let-502(RNAi)*, *pak-1(gk416)* and *pak-1(gk416);let-502(RNAi)* embryos expressing AJM-1::GFP and VAB-10(ABD)::mCherry as well as *nmy-2(ne1490ts); ajm-1::GFP* at 18°C or 25°C. The dashed lines indicate the mean value for *wt* (black), *pix-1(gk416)* (blue) and *let-502(RNAi)* (green). **(D)** Schematic representation of cluster density and anisotropy for each strain. N: analyzed embryos. T-test *p*-value significantly different than *wt* (*) and *let-502(RNAi)* (#) are indicated within brackets.

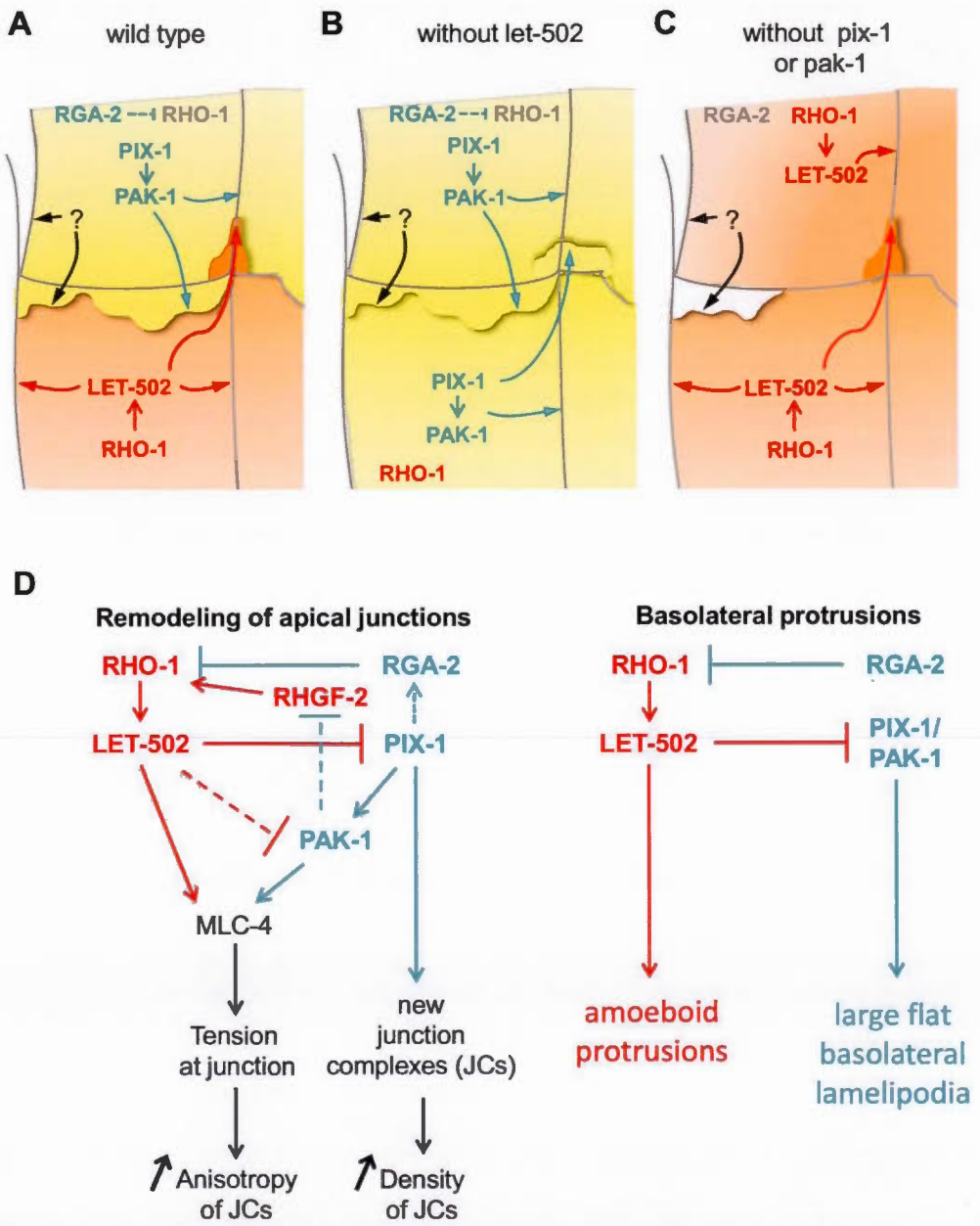

Figure 4.10 : Model for Rho/Rac-like antagonism during early elongation.

(A-C) Schematic representation of signalling pathways activated in dorsal and lateral cells in wild-type embryos **(A)**, or in *let-502* knock-down or mutant **(B)**, *pix-1* or *pak-1* mutants **(C)**. Cells following a Rac1-like morphogenetic program involving PIX-1 and PAK-1 are represented in yellow and those following a RhoA-like program involving RHO-1 and LET-502 are represented by orange. **(D)** Effect of the Rac1/RhoA antagonism on the remodelling of apical junction (left) and on basolateral protrusions (right).

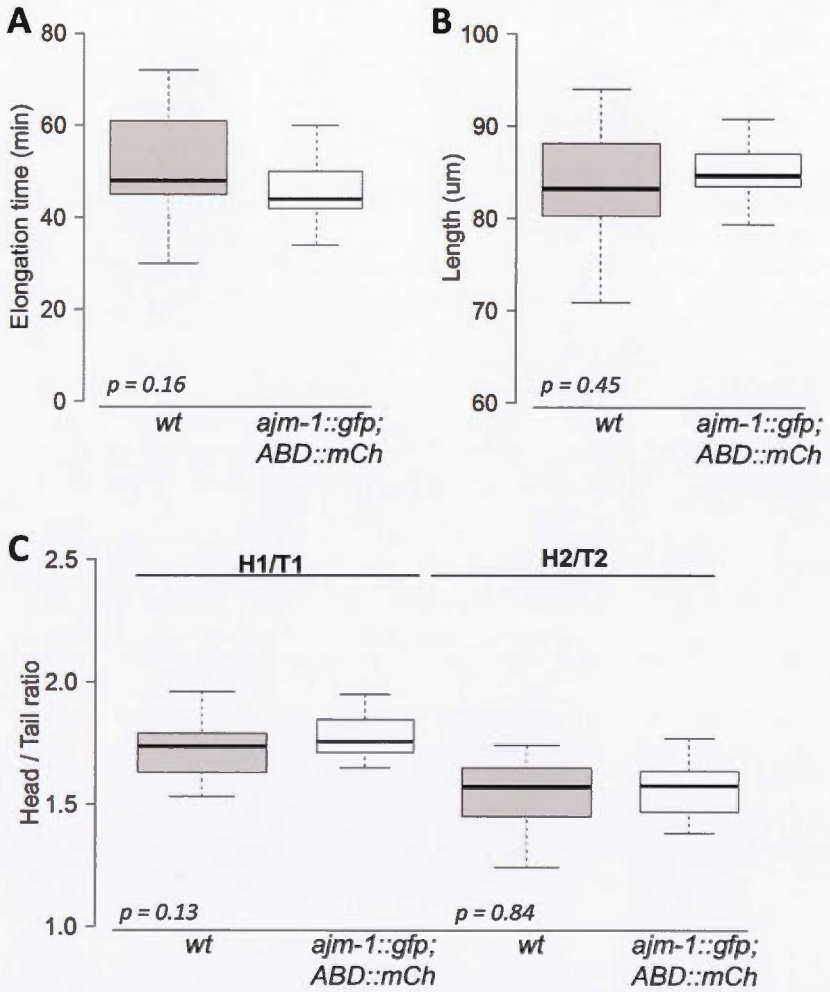

Supplementary Figure 4.1 : *ajm-1::GFP; vab-10(ABD)::mCherry* carrying embryos develop as *wild-type* (*wt*) animals.

(A-C) Box plot representing **(A)** the early elongation time, **(B)** the length of the embryos at the end of early elongation and **(C)** the head to tail width ratio at 1.2-fold (H1/T1) and at the end of early elongation (H2/T2) in *wt* and *ajm-1::GFP; abd::mCherry*. Box plots represent the min, max 25th, 50th (median) and 75th percentiles of the population. T-test *p-values* are indicated on the graph. This study revealed that transgenic animals expressing AJM-1::GFP and the filamentous actin binding probe VAB-10(ABD)::mCherry display similar elongation rate than *wt* embryos (A). The length of transgenic and *wt* embryos is also similar at the end of early elongation - being identified when body-wall muscles start contracting (B). Moreover, the morphology of these embryos is similar with similar head to tail width ratio at the beginning (H1/T1) and at the end (H2/T2) of early elongation. For details on the method used to generate these data refer to (Martin *et al.*, 2014 ; Martin, 2016).

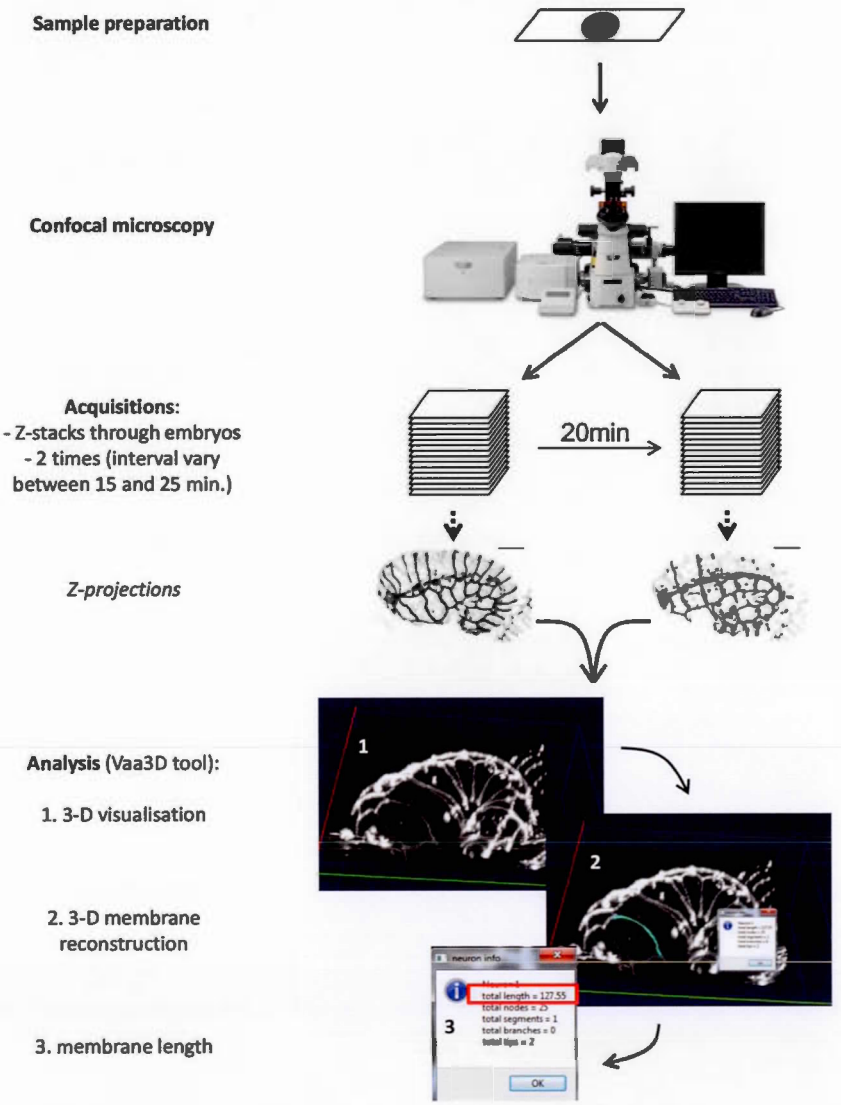

Supplementary Figure 4.2 : Step-by step method to quantify junction elongation rate.

Embryos were mounted on an agarose pad and observed using pin-point confocal microscope. Z-stacks covering the entire width of the embryos were recorder at the beginning of early elongation (comma stage) and after 15 to 20 minutes, being sure that the second measurement is made before body-wall muscle start contracting. Z-stacks were subsequently analyzed using the Vaa3D tools. This analysis included resampling of images and three-dimensional (3D) reconstruction. Vaa3D linear object identification and measurement tools in 3D were used to measure the length of cell-cell junction located between two identified vertices. As previously reported 3D measurement of cell-cell junction is more accurate than measurement of junction observed in Z-projections of Z-stacks (Kang *et al.*, 2015).

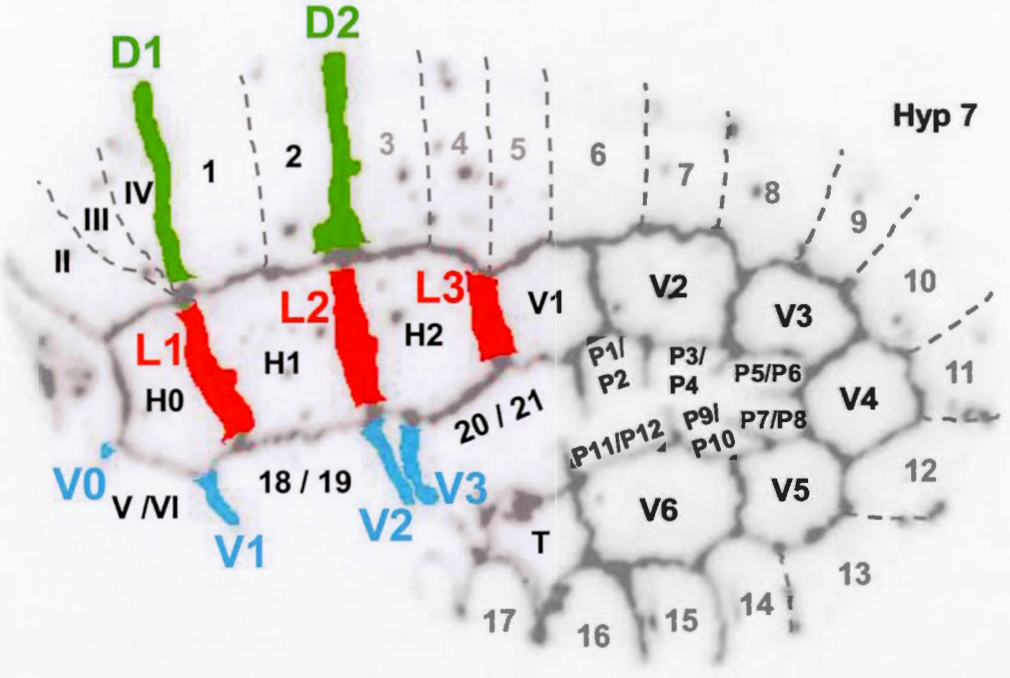

Hyp 7 = fusion of cells 3/17

Supplementary Figure 4.3 : Identification of hypodermal cells and their cell-cell junctions during early elongation.

Cell-cell junctions between dorsal, lateral and ventral anterior cells are indicated in green, red and blue respectively. Dashed lines represent junctions disappearing upon cells fusion.

A

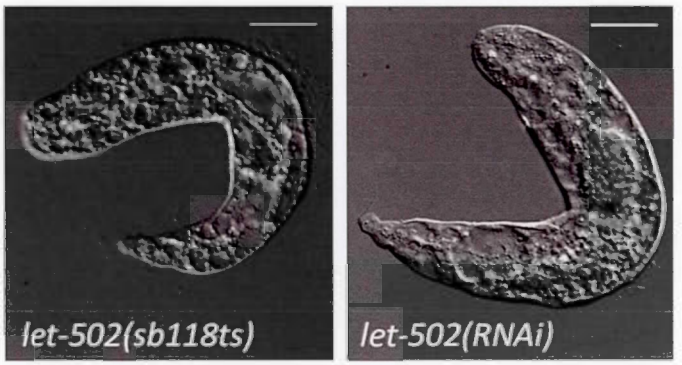

B

Genotype		Emb (%)	Lva (%)	n
let-502(sb118ts)	*25.5°C*	7.9	91.2	353
let-502(RNAi)		-	100	70

C

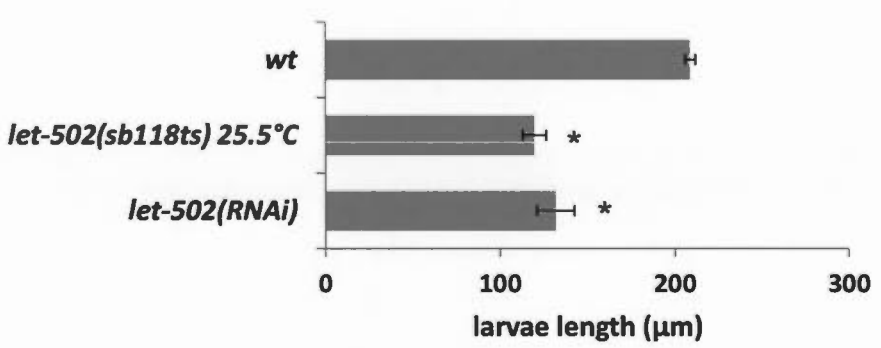

Supplementary Figure 4.4 : *let-502(RNAi)*-treated animals display similar defects than *let-502(sb118ts)* mutant grown at non-permissive temperature.

(A) Arrested larvae observed for *let-502(sb118ts)* mutants grown at 25.5°C and *let-502(RNAi)*-treated animals grown at 20°C upon DIC illumination **(B)** Percentage of embryonic lethality (Emb %) and larval arrest (Lva %) in *let-502(sb118ts)* and *let-502-(RNAi)*. **(C)** Bar graph representing length of larvae in *wt*, *let-502(sb118ts)* and *let-502-(RNAi)*. T-test *p-value* < 0.05.

Distribution of protrusion along the junction

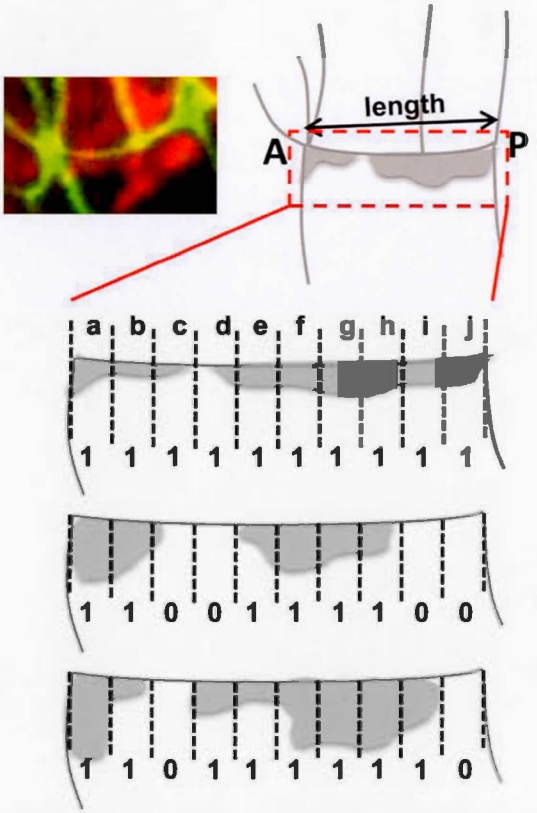

	a	b	c	d	e	f	g	h	i	j
Σ	3	3	1	2	3	3	3	3	2	1
N	3	3	3	3	3	3	3	3	3	3
%	100	100	33	66	100	100	100	100	66	33

Σ: sum of positive cases ("1")
N: sum of positive and negative cases ("1" and "0")
% (distribution): Σ/N

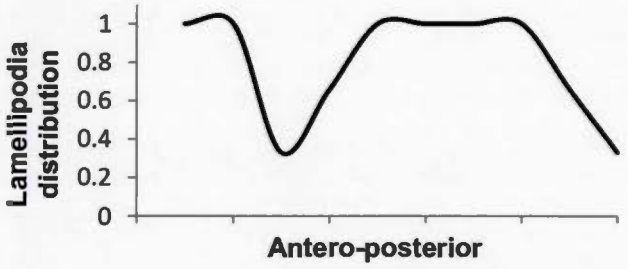

Supplementary Figure 4.5 : Method to quantify the distribution of protrusion along the junction between D1/L1 and D2/L2 vertices.

Briefly, the cell-cell junctions located between the D1/L1 and the D2/L2 vertices were divided in ten equal sections. The presence of the protrusion was identified for each section at 24 different time points for four different embryos. We subsequently computed the distribution as the percentage of positive events (Σ) per measurement per section (N), and plotted this distribution (bottom graph). A Fisher equal test (computed using R statistical tools, Bioconductor) was used to assess how surprising it is to witness a reduction or an increase of the distribution of protrusions at a given section for a given mutant when compared to *wt* embryos.

CHAPITRE V

DISCUSSION

5.1 L'élongation embryonnaire précoce, un modèle remanié

La morphogenèse est essentielle au développement des organismes multicellulaires. Ce mécanisme dépend d'évènements cellulaires variés tels que le changement de forme des cellules, l'adhésion et la migration cellulaire. Ici, nous étudions une étape précise de la morphogenèse de l'épiderme du *C. elegans*, l'élongation embryonnaire. Celle-ci transforme un embryon ovoïde en une larve vermiforme et est divisée en deux étapes, l'élongation précoce et tardive. Nous nous intéressons spécifiquement à la phase précoce de l'élongation. A l'entame de ce travail de thèse, le modèle est tel que l'élongation précoce est menée par la contraction du système actine-myosine au pôle apical des cellules latérales de l'hypoderme tandis que les cellules dorsales et ventrales se trouvent dans un état relâché (Priess et Hirsh, 1986 ; Chisholm et Hardin, 2005 ; Diogon *et al.*, 2007 ; Zhang *et al.*, 2010). Il est également admis que toutes les cellules d'un même groupe cellulaire (dorsal, latéral ou ventral) se comportent de façon similaire le long de l'axe antéro-postérieur. Il est aussi montré que la contraction de la myosine est régulée par la phosphorylation de MLC-4/MLC *via* trois kinases, LET-502/ROCK (effecteur de RHO-1/RHOA), MRCK-1/MRCK (effecteur de CDC-42), PAK-1/PAK1 (effecteur de CDC-42 et des RACs), et une phosphatase MEL-11/MYPT (Wissmann *et al.*, 1997 ; Wissmann *et al.*, 1999 ; Piekny *et al.*, 2000 ; Piekny *et al.*, 2003 ; Gally *et al.*, 2009). Ces acteurs s'organisent en deux voies parallèles : une voie MEL-11/LET-502 impliquant également MRCK-1/MRCK, et une voie PAK-1 qui est très peu décrite (Piekny *et al.*, 2000 ; Gally *et al.*, 2009).

Dans le chapitre II (Martin *et al.*, 2014), nous avons montré que la GEF spécifique de Rac1 et Cdc42 PIX-1/β-PIX contrôle l'élongation embryonnaire précoce dans la même voie que PAK-1, en parallèle de la voie MEL-11/LET-502. Spécifiquement, les études d'interaction génétique ont montré que *pix-1* agit à la fois dans la voie *pak-1* en parallèle d'un gène qui n'a pas encore été identifié, et également indépendamment de *pak-1* en amont de *mel-11* (Table 2.2). Par ailleurs, nous avons développé des méthodes permettant l'analyse de la morphologie des embryons afin de caractériser plus précisément les défauts d'élongation observables à ce stade. Nous avons ainsi mis en place la mesure de la largeur de la tête, de la queue et du ratio tête/queue des embryons, la longueur des embryons à la fin de l'élongation précoce, et la longueur des larves L1 ; et cela pour les animaux sauvages (*wild-type*) et mutants. Ces méthodes d'analyse font d'ailleurs l'objet d'un article de méthode retrouvé dans le chapitre III (Martin *et al.*, 2016). La mesure du ratio tête/queue a permis de mettre en évidence une différence significative entre les voies *pix-1/pak-1* et *mel-11/let-502* le long de l'axe antéro-postérieur de l'embryon (Figure 2.2). Nous montrons en effet que *pix-1* et *pak-1* régulent principalement la réduction de la largeur de la tête alors que *let-502* contrôle la réduction de la largeur de la tête et de la queue. Notre étude révèle également que PIX-1::GFP est retrouvée plus faiblement dans les cellules dorsales postérieures de l'hypoderme comparée aux autres cellules de l'hypoderme (Figure 2.5). Cela implique un débalancement antéro-postérieur et dorso-ventral dans l'accumulation de cette protéine, et probablement dans la régulation de l'élongation précoce. Nous montrons enfin que le niveau d'accumulation de PIX-1::GFP dans les cellules dorsales postérieures de l'hypoderme doit être finement régulé et maintenu faible pour permettre une vitesse d'élongation optimale dans les animaux sauvages. Une expression élevée de PIX-1::GFP dans ces cellules nuit en effet à la morphogenèse correcte de l'embryon (Figure 2.6). Cette étude suggère donc qu'au cours de l'élongation précoce, *let-502* régulerait les forces de contraction permettant la réduction de la circonférence de l'embryon de façon homogène le long de l'axe antéro-postérieur, alors que la voie *pix-1/pak-1*

contrôlerait principalement les forces appliquées sur la partie antérieure de l'embryon. De plus, cette étude suggère qu'il est nécessaire de faire une distinction entre la partie antérieure – la tête – et la partie postérieure – la queue – de l'embryon lorsque l'on considère les processus morphogéniques contrôlant l'élongation précoce. Ces résultats modifient donc le modèle moléculaire de l'élongation précoce considérant que toutes les cellules d'un même groupe cellulaire (dorsal, latéral ou ventral) se comportent de façon similaire le long de l'axe antéro-postérieur (Zhang *et al.*, 2010).

Afin de mieux caractériser le rôle de chacune des deux voies – *let-502* et *pix-1/pak-1* – contrôlant l'élongation précoce, nous avons mis au point une caractérisation des animaux sauvages et mutants à l'échelle cellulaire. Dans le chapitre IV, nous avons utilisé ces paramètres pour cartographier l'activité et la fonction de *let-502*, *pix-1* et *pak-1* au cours de l'élongation précoce (Martin *et al.*, soumis à JCB). Cette étude révèle que *pix-1* et *pak-1* sont impliqués dans le remodelage des jonctions apicales des cellules dorsales antérieures (Figure 4.2 et 4.4), confirmant ainsi le rôle de la voie *pix-1/pak-1* au niveau de la tête de l'embryon (Martin *et al.*, 2014). Cette étude modifie le précédent modèle qui suggérait que les filaments d'actine-myosine situés au pôle apical des cellules dorsales et ventrales de l'embryon étaient soumis à un niveau de contraction équivalent, plus faible que celui des cellules latérales (Gally *et al.*, 2009 ; Zhang *et al.*, 2010). Nous montrons que *let-502* contrôle le remodelage des jonctions apicales des cellules latérales tout au long de l'axe antéro-postérieur (Figure 4.2, 4.4), ce qui est en accord avec le rôle connu de *let-502* (Piekny *et al.*, 2000 ; Gally *et al.*, 2009 ; Martin *et al.*, 2014). Il est à noter que *let-502* contrôle aussi le remodelage des jonctions apicales des cellules ventrales postérieures (Figure 4.2) ; un rôle nouveau mais loin d'être surprenant compte tenu du repliement de l'embryon à ce niveau. Nous montrons également que les cellules dorsales et latérales antérieures de l'hypoderme produisent des protrusions basolatérales polarisées (Figure 4.5). En effet, les cellules dorsales émettent des protrusions de type lamellipode vers les

cellules latérales, et les cellules latérales produisent des protrusions de type amiboïde vers les cellules dorsales. Nous remarquons également que la formation et la distribution des lamellipodes issus des cellules dorsales sont dépendantes de la voie *pix-1/pak-1* (Figure 4.6), et que ces lamellipodes pourraient réduire la tension exercée à la jonction apicale entre les cellules dorsales et latérales (Figure 4.8). De plus, nous montrons que les protrusions de type amiboïde sont régulées, au moins en partie, par la voie *let-502* (Figure 4.7). Cette étude révèle donc que, pour contrôler le remodelage des jonctions apicales et la formation des protrusions basolatérales, les cellules peuvent adopter une voie de signalisation *pix-1/pak-1*, ce que nous nommons programme de type « Rac1 », ou alternativement, une voie de signalisation impliquant *let-502*, programme morphogénique que nous nommons « RhoA ». L'adoption d'un de ces programmes par la cellule définit son comportement et sa morphologie au cours de l'élongation (Figure 4.10). Enfin, nous montrons que la dominance cellulaire d'un programme, Rac1 ou RhoA, est contrôlée par l'antagonisme entre *pix-1/pak-1* et *let-502*. Un tel antagonisme entre un programme Rac1 et un programme RhoA est retrouvé dans divers processus morphogéniques (Simoes *et al.*, 2006 ; Parri et Chiarugi, 2010 ; Pertz, 2010 ; Chauhan *et al.*, 2011 ; Guilluy *et al.*, 2011). Par ailleurs, bien que ces deux voies soient antagonistes au niveau de chaque cellule, elles restent tout de même redondantes lorsque l'on considère l'élongation précoce au niveau de l'organisme (Martin *et al*, soumis à JCB). En effet, lorsque la voie principale est mutée – RhoA dans les latérales et Rac1 dans les dorsales –, la seconde s'active et est capable de prendre le relai. La voie PIX-1/PAK-1 semble cependant moins efficace que la voie RHO-1/LET-502 lorsqu'activée dans les cellules latérales, ce qui explique que des défauts sont observables en absence de LET-502 (Wissmann *et al.*, 1997 ; Piekny *et al.*, 2000 ; Gally *et al.*, 2009 ; Martin *et al.*, 2014). D'autre part, l'activation de LET-502 est seulement partielle dans les cellules dorsales en absence de PIX-1 ou PAK-1 (Figure 4.6 et 4.8), probablement due à la persistance de l'inhibition de RHO-1 par RGA-2 dans ces cellules (Diogon *et al.*, 2007).

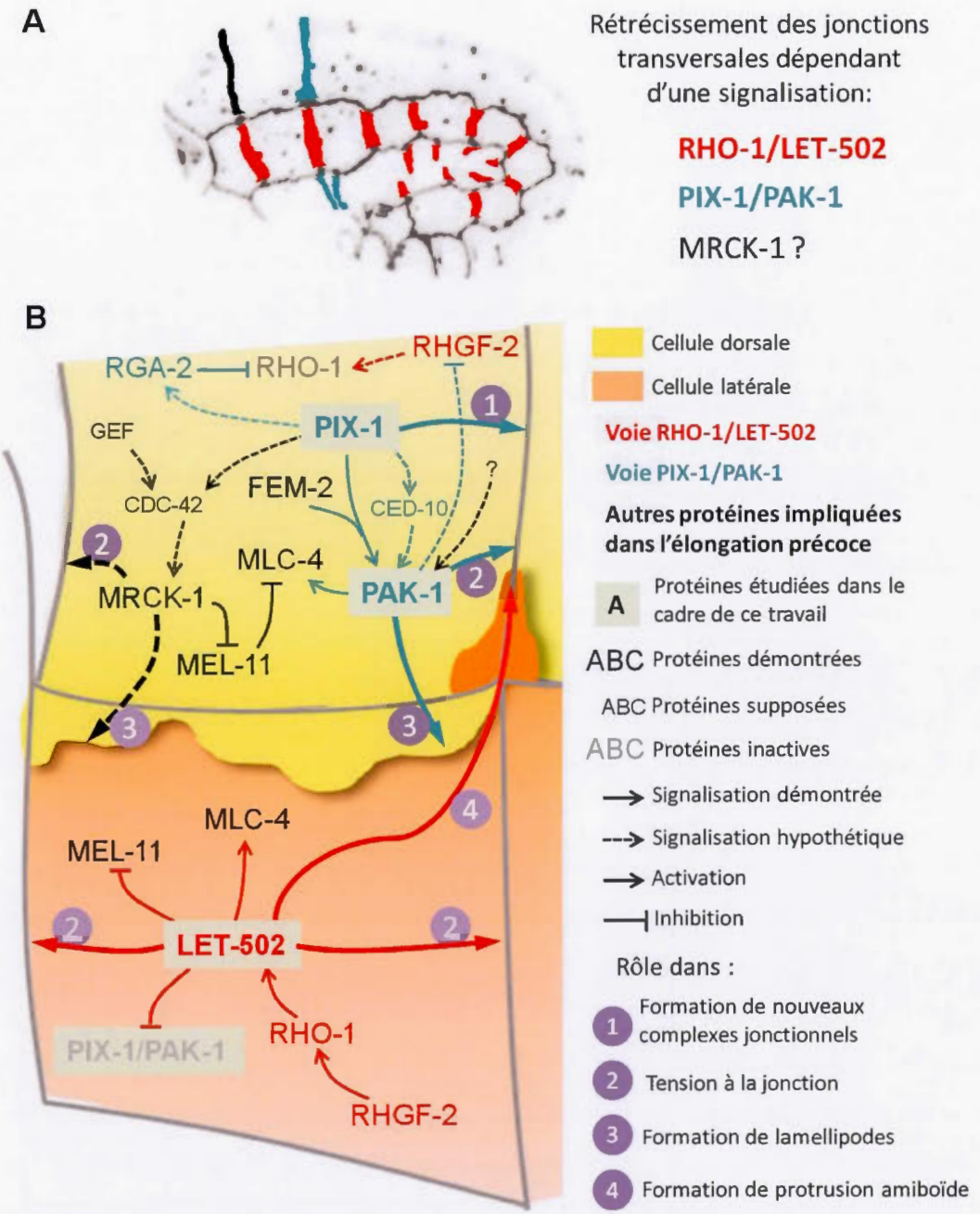

Figure 5.1 : L'élongation embryonnaire : un modèle revisité. (A) Répartition des voies de signalisation dont l'implication dans l'élongation précoce est démontrée (*rho-1/let-502* et *pix-1-pak-1*) ou supposée (*mrck-1*). Cette répartition tient compte de la mesure de rétrécissement des jonctions. (B) Modèle moléculaire de l'élongation embryonnaire précoce en fonction de ce qui a été démontré dans la littérature et dans notre travail (protéines et signalisation démontrées dans la légende), et de ce qui est discuté dans le présent chapitre (protéines supposées et signalisation hypothétique dans la légende).

Ce travail de thèse confirme une partie des hypothèses issues des études précédentes sur l'élongation embryonnaire précoce du *C. elegans*. En outre, il apporte des modifications majeures au modèle précédemment accepté, due principalement au développement de nouvelles méthodes permettant une analyse spatiale plus précise du site d'activation des voies de signalisation contrôlant l'élongation embryonnaire (Figure 5.1). Cette étude soulève de nouvelles questions sur les mécanismes moléculaires contrôlant cette étape de la morphogenèse. Nous allons explorer certaines d'entre elles dans les sections suivantes.

5.2 Le développement de nouvelles méthodes pour une caractérisation plus approfondie de l'élongation précoce et de la morphogenèse

Au commencement de ce travail, les seules méthodes utilisées pour caractériser les défauts de morphogenèse étaient la mesure du pourcentage de létalité embryonnaire (Emb) et des larves arrêtées au stade larvaire L1 (Lva), ainsi que la mesure de la longueur de ces larves comparée à celle des animaux sauvages (Wissmann *et al.*, 1997 ; Wissmann *et al.*, 1999 ; Piekny *et al.*, 2000 ; Diogon *et al.*, 2007 ; Gally *et al.*, 2009). Ces méthodes ne permettaient cependant pas une analyse spatiotemporelle des mécanismes de signalisation contrôlant la morphogenèse. Dans le but de mieux décrire l'élongation embryonnaire précoce, nous avons donc mis au point une série de méthodes permettant la caractérisation des évènements morphogéniques des animaux sauvages et mutants au niveau de la tête et de la queue de l'embryon (Martin *et al.*, 2014 ; Martin *et al.*, 2016), et au niveau de chaque cellule de l'hypoderme (Martin *et al.*, soumis à JCB). Les méthodes, permettant l'analyse de l'élongation embryonnaire, utilisées lors de notre étude publiée en 2014 dans PLoS ONE ont fait l'objet d'un article vidéo publié dans JoVE (Martin *et al.*, 2016). Les protocoles décris dans cet article permettent de mesurer le ratio tête/queue, la longueur des embryons à la fin de l'élongation précoce, et la mesure à grande échelle de la longueur des larves arrêtées en utilisant la cytométrie en flux. La caractérisation à l'échelle cellulaire est, elle,

basée sur : (i) la mesure de l'élongation et du rétrécissement des membranes de chacune des cellules de l'hypoderme en utilisant le programme Vaa3d. Ce programme a initialement été développé pour visualiser et mesurer les neurites dans des sections de tissus nerveux à partir de reconstructions tridimensionnelles des réseaux neuronaux (Peng, Ruan, Atasoy, *et al.*, 2010 ; Peng, Ruan, Long, *et al.*, 2010). Cette approche permet de mesurer la longueur des jonctions apicales entre les cellules de l'hypoderme au cours de l'élongation à partir d'une reconstruction tridimensionnelle des embryons. Ainsi que démontré pour un autre stade de développement, *via* l'utilisation d'une méthode analogue, cette approche est plus précise qu'une mesure des jonctions à partir d'une projection 2-dimensions qui sous-estime les différences réelles (Kang *et al.*, 2015). (ii) L'anisotropie des protéines jonctionnelles qui traduit la tension appliquée à la membrane apicale des cellules, comme précédemment montré dans un système mammifère (Engl *et al.*, 2014) et démontré dans notre système (Martin *et al.*, soumis à JCB). (iii) La densité de cluster de protéines jonctionnelles correspondant au nombre de cluster par micromètre de jonction, et dont la méthode est adaptée d'une autre étude effectuée dans notre laboratoire et à laquelle j'ai participé (Ouellette *et al.*, 2015 ; voir Annexe C) ; et (iv) la formation et la distribution des protrusions basolatérales, en mesurant la surface des protrusions *via* une méthode adaptée de Sheffield *et al.*, 2007 et Ouellette *et al.*, 2015. Ces différents paramètres feront prochainement l'objet d'un article de méthode décrivant étape par étape la marche à suivre pour l'acquisition et l'analyse des images. Ces méthodes de mesure d'anisotropie et de longueur de jonctions au niveau cellulaire au sein d'un tissu sont de plus en plus utilisées dans les études portant sur la morphogenèse, notamment chez la drosophile (Rauzi *et al.*, 2008 ; Rauzi *et al.*, 2010 ; Levayer et Lecuit, 2013 ; Sugimura et Ishihara, 2013 ; Kasza *et al.*, 2014 ; Collinet *et al.*, 2015).

Les résultats obtenus lors de nos études démontrent la nécessité de développer de nouvelles méthodes d'analyse permettant de décrire les mécanismes de signalisation

contrôlant la morphogenèse des épithéliums au niveau de chaque cellule, plutôt que de considérer les populations de cellules en culture ou au sein d'un même tissu comme un ensemble d'éléments se comportant de façon similaire. Bien que les analyses effectuées sur les processus de morphogenèse des épithéliums de la drosophile, particulièrement ceux impliqués dans l'extension de la bandelette germinative, utilisent des outils d'imagerie caractérisant le remodelage des jonctions (Rauzi *et al.*, 2008 ; Rauzi *et al.*, 2010 ; Levayer et Lecuit, 2013 ; Collinet *et al.*, 2015), une potentielle hétérogénéité du comportement des cellules dans ces systèmes n'a pas encore été abordée.

5.3 L'antagonisme Rho-Rac dans les cellules dorsales et latérales de l'hypoderme

Dans cette étude nous montrons que le programme Rac1, composé de PIX-1/β-PIX et PAK-1/PAK1, est antagoniste au programme RhoA, impliquant LET-502/ROCK, et que l'un ou l'autre de ces programmes est actif dans des sous-groupes cellulaires distincts.

Dans les cellules dorsales, nous montrons que LET-502 compense partiellement l'absence de PIX-1 et PAK-1. Cela suggère que PIX-1 et PAK-1 contribue, au moins en partie, à l'inhibition de la fonction de LET-502 dans ces cellules. Il a été montré que la voie RHO-1/LET-502 est inhibée par la GAP spécifique de RHO-1, RGA-2 (Diogon *et al.*, 2007). Il est donc possible que PIX-1 et PAK-1 activent RGA-2 en parallèle d'un gène qui reste à identifier. Comme décrit dans la discussion du chapitre IV, une autre possibilité permettant d'expliquer nos résultats est que la voie PIX-1/PAK-1 inhibe une GEF spécifique de RHO-1, comme déjà montré pour PAK1/PAK-1 dans d'autres modèles (Alberts *et al.*, 2005 ; Rosenfeldt *et al.*, 2006). Dans ce cas ci, en absence de PIX-1 ou PAK-1, cette GEF serait activée dans les cellules dorsales et entrerait en compétition avec RGA-2, provoquant une activation modéré de RHO-1 (Figure 5.1).

Dans les cellules latérales, nous montrons par contre que LET-502 inhibe l'activité de PIX-1 et PAK-1. Dans la discussion du chapitre IV, nous émettons l'hypothèse que LET-502 pourrait entrainer la relocalisation de PIX-1, et ainsi inhiber son activité tel que montré au niveau des adhésions focales de cellules mammifères en culture (Kuo *et al.*, 2011 ; Vicente-Manzanares *et al.*, 2011). Cependant, une voie alternative pourrait être envisagée. Nous savons que ROCK est capable d'inhiber l'activité de Rac1 *via* la régulation de FilGAP, une GAP spécifique de la GTPase Rac1 (Ohta *et al.*, 2006). De plus il a été montré que FilGAP contrôle les jonctions adhérentes dans des cellules MDCK (Nakahara *et al.*, 2015), supprime la formation des lamellipodes, et promeut la migration de type amiboïde (Ohta *et al.*, 2006 ; Saito *et al.*, 2012 ; Nakamura, 2013) ; trois propriétés en accord avec nos observations dans les cellules latérales. Le plus proche homologue de FilGAP retrouvé dans le génome du *C. elegans* est la GAP spécifique de CDC-42, PAC-1, qui possède des domaines similaires à ceux de FilGAP. Cette protéine se localise aux jonctions cellule-cellule au cours de la gastrulation et restreins la protéine de polarité PAR-6 aux membranes dépourvues de contact cellule-cellule au pourtour de l'embryon (Anderson *et al.*, 2008 ; Chan et Nance, 2013). Aucun lien entre PAC-1 et FilGAP n'a été fait à ce jour et il n'y a, de plus, aucune évidence permettant de penser que cette protéine puisse être régulée positivement par RHO-1.

5.4 Potentielle voie redondante avec *pix-1/pak-1* dans les cellules dorsales antérieures

Dans le chapitre IV, nous montrons que la voie *pix-1/pak-1* contrôle à la fois le remodelage des jonctions apicales et la formation des protrusions basolatérales de manière polarisée dans les cellules dorsales antérieures 1/2. En effet, en absence de *pix-1* ou *pak-1*, nous observons une réduction de l'anisotropie des protéines jonctionnelles à la jonction D2 (Figure 4.4), ainsi qu'une forte diminution de la formation et de la surface des lamellipodes à la jonction D2/L2 (Figure 4.6). Cependant, ces deux mécanismes restent inchangés à la partie antérieure de la cellule

résultant de la fusion des cellules dorsales antérieures 1/2 (jonction D1), suggérant qu'une autre voie de signalisation serait impliquée spécifiquement à cet endroit. De façon intéressante, MRCK-1/MRCK a été montré comme contrôlant la phosphorylation de la chaine légère de la myosine, MLC-4, en parallèle de LET-502 et PAK-1 au cours de l'élongation embryonnaire précoce (Gally *et al.*, 2009). De plus, MRCK joue un rôle dans la formation des protrusions et la migration cellulaire dans des fibroblastes et des cellules épithéliales mammifères en culture (Gomes *et al.*, 2005 ; Tan *et al.*, 2008). De manière spécifique, MRCK est impliquée dans la réorientation du centre organisateur des microtubules (MTOC) afin de polariser la migration cellulaire et de permettre l'assemblage du flux rétrograde d'actine dans les lamellipodes de cellules en culture (Gomes *et al.*, 2005 ; Tan *et al.*, 2008). En accord avec ces rôles connus sur la contraction apicale et dans la mise en place des lamellipodes polarisés, et avec le fait que MRCK-1 soit exprimée dans les cellules dorsales de l'hypoderme (Gally *et al.*, 2009), nous émettons l'hypothèse que *mrck-1* serait impliqué en parallèle de la voie *pix-1/pak-1* dans les cellules dorsales 1/2 au cours de l'élongation précoce. Dans ces cellules, MRCK-1 pourrait donc contrôler, de manière polarisée, à la fois la tension à la jonction D1 et la formation des lamellipodes à la jonction D1/L1 (Figure 5.1). Cette hypothèse peut facilement être testée en utilisant un traitement d'ARN interférence, tel que fait précédemment (Gally *et al.*, 2009), dans une souche exprimant le marqueur jonctionnel AJM-1::GFP et le marqueur d'actine ABD::mCherry.

Cette hypothèse n'est pas en total désaccord avec le modèle que nous avions proposé à la fin du chapitre II (Martin *et al.*, 2014). Nous émettions effectivement l'hypothèse qu'en plus de son rôle avec *pak-1*, *pix-1* peut agir en amont de *mel-11*. Dans le modèle de ce chapitre (Figure 2.7), nous proposions que PIX-1 active CDC-42 qui active lui-même son effecteur MRCK-1/MRCK, lequel inhibe la déphosphorylation des MLC par MEL-11. Autrement dit, *pix-1* agirait indirectement sur *mel-11 via mrck-1*. Si nous émettons l'hypothèse que PIX-1 agit effectivement sur MRCK-1, et

que MRCK-1 contrôle la tension et la formation des lamellipodes le long de la jonction D1/L1, alors PIX-1 devrait également contrôler la tension à la jonction D1 et la formation des lamellipodes le long de la jonction D1/L1. Les résultats du chapitre IV montrent que, bien que non significatifs en l'état actuel des choses, *pix-1(gk916)* a tendance à réduire l'anisotropie à la jonction D1 et la formation des lamellipodes à la jonction D1/L1. Ces résultats pourraient suggérer que PIX-1 agirait à la jonction D1 en parallèle d'un autre gène, ce qui expliquerait que les résultats obtenus pour cette jonction ne soient pas significatifs. Supportant cette hypothèse, l'étude du chapitre II suggérait que PIX-1 agisse en parallèle d'un autre gène, possiblement une GEF, en amont de PAK-1 (Martin *et al.*, 2014), et donc possiblement de MRCK-1. Ainsi, il devient donc aisé d'imaginer que MRCK-1 contrôlerait la tension à la jonction D1 et la formation des lamellipodes le long de la jonction D1/L1, et que PIX-1 jouerait un rôle dans l'activation de MRCK-1 *via* CDC-42, et en parallèle d'un gène qui reste à être identifié (Figure 5.1). Une telle ségrégation spatiale de deux voies impliquant PIX-1 – une dans la partie antérieure des cellules dorsales 1/2 impliquant CDC-42 et MRCK-1, et une dans la partie postérieure de ces cellules et impliquant CED-10 et PAK-1 – est intéressante et intrigante.

5.5 *pix-1/pak-1*, polarité planaire et mécano-transduction

Au cours de ce travail, nous avons montré que l'activité de la voie PIX-1/PAK-1 est hétérogène le long de l'axe antéro-postérieur et dorso-ventral de l'embryon (Martin *et al.*, 2014) et qu'au sein même des cellules dorsales antérieures, l'activité de PIX-1 et PAK-1 est polarisée le long de la jonction D2 (Martin *et al.*, soumis à JCB). Nous ignorons cependant ce qui régule spatialement cette activité.

Une des possibilités envisageables serait que PIX-1/PAK-1 soit régulée en aval d'une protéine régulant la polarité planaire. Nous savons que β-PIX/PIX-1 possède un domaine d'interaction avec la protéine Scribble/LET-413 (Audebert *et al.*, 2004). Par

ailleurs, il a été montré que Scrb1/Scribble, bien qu'identifiée comme une protéine de la polarité apico-basale et pour son rôle de suppresseur de tumeur chez la drosophile (Bilder *et al.*, 2000 ; Pagliarini et Xu, 2003), joue un rôle essentiel dans la polarité planaire chez les mammifères (Montcouquiol *et al.*, 2003 ; Murdoch *et al.*, 2003 ; Yates *et al.*, 2013). Cette protéine interagit aussi avec une autre protéine impliquée dans la polarité planaire, Vangl2, et qui possède également un orthologue chez le *C. elegans*, VANG-1. Il est donc possible que l'activité polarisée de PIX-1/PAK-1 soit régulée par LET-413 et VANG-1 au cours de l'élongation embryonnaire précoce. Cette hypothèse reste donc tester dans notre système.

Par ailleurs, il a été montré que β-PIX/PIX-1 agit comme un mécano-transducteur chez les mammifères et chez le *C. elegans* (Kuo *et al.*, 2011 ; Zhang *et al.*, 2011 ; Plutoni *et al.*, 2016). Il serait donc probable que l'activité de la voie PIX-1/PAK-1 soit soumise à une régulation mécanique, répondant ainsi à une augmentation de la tension au niveau des jonctions cellulaires (cellule-cellule dans notre cas). Supportant cette hypothèse, nous montrons que la voie *pix-1/pak-1* est en effet active aux endroits où la tension est supposément la plus élevée dans l'embryon au cours de l'élongation précoce, c'est-à-dire dans la tête de l'embryon où la contraction est forte (Martin *et al.*, 2014), et le long de la jonction D2/L2 qui représente la membrane qui réduit le plus rapidement au cours de l'élongation (Martin *et al.*, soumis à JCB).

Ces deux hypothèses mériteraient donc d'être testées afin de mieux comprendre la répartition spatiale de l'activité de la voie PIX-1/PAK-1.

5.6 Étudier le rôle des protrusions au cours de l'élongation précoce

Dans le travail du chapitre IV, nous montrons que les cellules dorsales et latérales antérieures de l'hypoderme produisent des protrusions basolatérales polarisées. Basée sur la mesure de l'anisotropie locale de AJM-1::GFP au niveau des vertex D1/L1 et D2/L2 (Figure 4.8), nous émettons l'hypothèse que ces protrusions réduisent la

tension exercée à la jonction apicale entre les cellules dorsale et latérale. Il pourrait donc être intéressant d'étudier le rôle de ces protrusions afin de confimer/infirmer cette hypothèse. Différentes méthodes sont envisageables.

La méthode la plus simple serait d'utiliser une souche mutante telle que *nmy-2(ne1490ts)* afin de réduire la tension, puis observer l'évolution des protrusions dans ce contexte. Cependant, si une réduction de la formation des protrusions est observée, comme cela est attendu, nous ne pourrons pas affirmer que celle-ci est due à une diminution de la tension apicale. En effet, nous ne pourrons pas exclure la possibilité que la myosine puisse être impliquée dans la formation des lamellipodes comme cela a déjà été observé dans les cellules endothéliales, les neurones et les cellules épithéliales de cancer du sein en culture (Kolega, 2006 ; Betapudi, 2010 ; Morimura *et al.*, 2011 ; Vicente-Manzanares *et al.*, 2011 ; Sayyad *et al.*, 2015). Il est donc nécessaire ici de découpler le rôle de la myosine au cours du remodelage des jonctions apicales et dans la formation des lamellipodes, en manipulant son activité avec une précision spatiale micrométrique. Une des techniques possibles pour réduire la tension ou la formation des lamellipodes à l'échelle cellulaire au sein d'un organisme en développement est l'utilisation de l'ablation laser (Rauzi *et al.*, 2008 ; Martin *et al.*, 2010). Cette technique est efficace et permet une réponse rapide avec une forte précision spatiale, mais est cependant irréversible. De plus, les équipements permettant d'effectuer une telle ablation tout en mesurant les protrusions et le remodelage des jonctions avec une résolution et une vitesse suffisante pour supporter notre étude sont rares, et actuellement non disponibles pour notre laboratoire. Une seconde possibilité serait d'utiliser des outils optogénétiques permettant de contrôler de façon spatio-temporelle la tension apicale ou la formation des lamellipodes. De nombreuses méthodes impliquant ce type d'outil ont été développées en culture cellulaire pour suractiver ou inhiber des protéines d'intérêt (Wu *et al.*, 2009 ; Bugaj *et al.*, 2013 ; Kato *et al.*, 2014 ; Lee *et al.*, 2014), mais la transition aux organismes vivants reste peu testée. Récemment, Guglielmi et ses collègues ont développé une

méthode optogénétique qui permet de moduler la contraction dans un tissu en cours de morphogenèse (Figure 5.2) (Guglielmi *et al.*, 2015). Ils ont montré que leur outil est capable de réduire localement la contractilité cellulaire et d'empêcher ainsi l'invagination du mésoderme au cours de l'embryogenèse de *D. melanogaster*. Il serait donc possible de transposer cette méthode chez le *C. elegans* afin de moduler le niveau de contraction dans les cellules latérales antérieures de l'hypoderme, et d'observer l'impact sur la formation des lamellipodes.

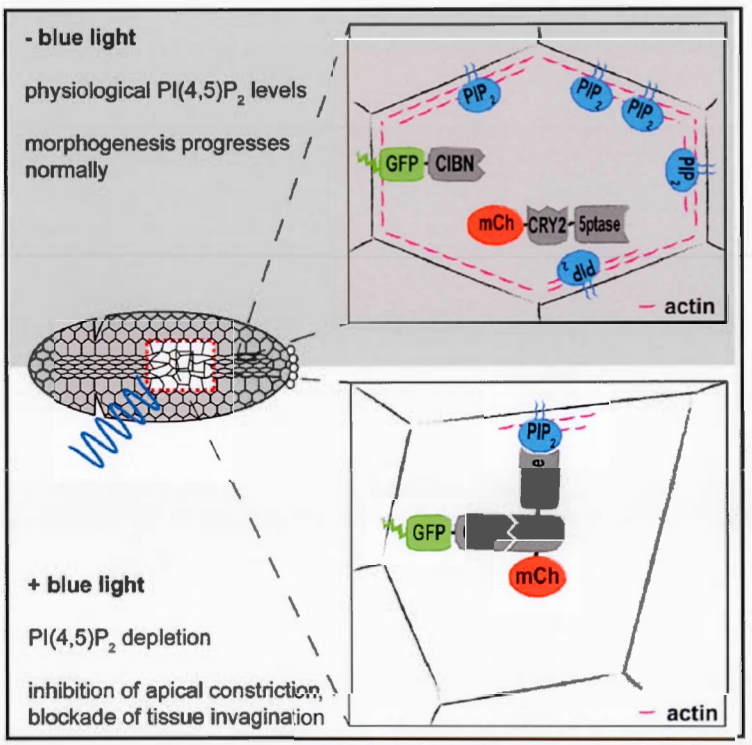

Figure 5.2 : Une méthode optogénétique pour moduler la contractilité cellulaire durant la morphogenèse tissulaire. Cette méthode est basée sur l'induction, par une lumière bleue, de l'interaction du domaine N-terminal de CIB1 (CIBN) avec le cryptochrome 2 (CRY2). CIBN est fusionnée avec l'eGFP et avec un motif CaaX permettant l'ancrage à la membrane plasmique. CRY2 est fusionnée au domaine catalytique de l'inositol polyphosphate 5-phosphatase OCRL (5-ptase) et à la mCherry. En absence de lumière bleue, la 5-ptase est cytosolique, et sous une illumination bleue, la 5-ptase est recrutée à la membrane où elle est capable de déphosphoryler le $PI(4,5)P_2$ en PI(4)P. Cela provoque une réduction de la concentration en $PI(4,5)P_2$ à la membrane plasmique, entrainant une dépolymérisation de l'actine corticale. Figure extraite de Guglielmi *et al.*, 2015.

5.7 L'hétérogénéité cellulaire au sein d'une population de cellules ou d'un tissu

Dans notre étude, nous montrons que des cellules de l'hypoderme peuvent adopter des programmes morphogéniques différents, entrainant une hétérogénéité cellulaire au sein du tissu. Nous nous demandons cependant quel est le rôle d'une telle hétérogénéité pour les processus de morphogenèse des épithéliums et comment est-ce que cette hétérogénéité s'établit au sein du tissu.

Depuis plusieurs années maintenant, l'hétérogénéité phénotypique est fréquemment observée dans des populations de cellules isogéniques en culture cellulaire (Stockholm *et al.*, 2007 ; Yin *et al.*, 2013 ; Sailem *et al.*, 2014), dans des populations génétiquement homogènes d'organismes unicellulaires, tels que les bactéries et les levures (Avery, 2005 ; Holland *et al.*, 2014 ; Sheik *et al.*, 2016), ou dans des tissus en morphogenèse (van de Wijngaert *et al.*, 1984 ; Edwards, 1985 ; Colic *et al.*, 1988 ; Kanno *et al.*, 2000 ; Gibson *et al.*, 2006 ; Liu *et al.*, 2012). Plusieurs études ont suggérées que cette hétérogénéité phénotypique/morphologique, retrouvée dans une population isogénique de cellules ou d'organisme, confère un avantage adaptatif et évolutif aux fluctuations de l'environnement (de Jong *et al.*, 2011 ; Yin *et al.*, 2013 ; Holland *et al.*, 2014). Par exemple, au sein d'une population génétiquement homogène de bactéries *Escherichia coli* exposée à une dose létale d'ampicilline, la majorité des bactéries meurent alors que certaines, même si c'est un phénomène rare, persistent et croissent lentement (Balaban *et al.*, 2004). Dans les tissus épithéliaux, l'hétérogénéité cellulaire a davantage été étudiée d'un point de vue morphologique. Les études portant sur la géométrie des formes cellulaires révèlent que seulement 40% des cellules épithéliales de l'aile de la drosophile sont hexagonales (Gibson *et al.*, 2006). De façon surprenante, ce pourcentage d'hexagones et la distribution des polygones au sein des épithéliums sont conservés entre les plantes et les animaux (Gibson et Gibson, 2009). Il a été montré que ROCK jouerait un rôle clé dans la maintenance de cette distribution (Kalaji *et al.*, 2012). La fonction de cette

hétérogénéité morphologique est cependant toujours énigmatique et les mécanismes permettant l'établissement d'une telle hétérogénéité restent obscurs.

Intéressons-nous maintenant à l'établissement de l'hétérogénéité au sein d'un tissu. Dans notre modèle d'étude, nous pourrions nous demander si un facteur de détermination, par exemple un facteur de transcription spécifique exprimé dans les cellules ectodermique à l'origine des cellules dorsales et ventrales de l'hypoderme, contrôlerait l'expression de RGA-2 dans ces cellules, et inhiberait de ce fait l'adoption par ces cellules d'un programme RhoA pour permettre l'adoption d'un programme Rac1. Chez le *C. elegans*, nous savons que les cellules suivent un lignage invariant et bien caractérisé (Sulston et Horvitz, 1977 ; Sulston *et al.*, 1983). La détermination et la différenciation des cellules de l'hypoderme dépendent de l'expression de ELT-1, un facteur de transcription de type GATA (Page *et al.*, 1997). L'existence de facteurs de transcription permettant aux cellules dorsales et ventrales d'adopter un programme de différenciation différent de celui adopté par les cellules latérales est à ce jour encore inconnu. D'autre part, l'analyse du lignage des cellules de l'hypoderme ne nous permet pas d'identifier de cellules à l'origine de toute la lignée des cellules dorsales, ventrales ou latérales. Cela suggère que le même processus de détermination et/ou différenciation permettant l'adoption d'un programme dorsal/ventral ou latéral, s'il existe, serait un mécanisme d'induction appliqué sur plusieurs cellules simultanément, ou non, au cours du développement.

Une seconde éventualité serait que l'induction permettant l'adoption d'un programme RhoA ou Rac1 par les cellules de l'hypoderme ait lieu au moment de la morphogenèse et non au cours de la différenciation de ces cellules. Nous savons que l'activation de la voie *rho-1/let-502* dans les cellules latérales induit la contraction de ces cellules, augmentant ainsi la tension. En réponse à cette augmentation de tension, les cellules dorsales pourraient adopter un comportement spécifique pour inhiber le programme RhoA et ainsi éviter que l'embryon ne rupture suite à une contraction trop élevée. Supportant cette hypothèse, il a été montré le mutant *rga-2* induit une

augmentation excessive de la tension appliquée aux jonctions entrainant une rupture au niveau de la tête des embryons (Diogon *et al.*, 2007). De plus, l'activité de RGA-2 est spécifique aux cellules ventrales et dorsales, même si RGA-2 est exprimée dans toutes les cellules de l'hypoderme au cours de l'élongation précoce (Diogon *et al.*, 2007). Ceci suggère que la fonction de RGA-2 n'est pas contrôlée au niveau transcriptionnel à ce stade, et donc que son expression n'induit pas le phénotype dorsal ou ventral comme suggéré par l'hypothèse déterministe. Cela suggère donc que RGA-2 serait activée dans les cellules dorsales et ventrales, à ce stade, en aval d'un stimulus qui reste à déterminer. Comme cela a déjà été montré pour d'autres régulateurs des GTPases, RGA-2 pourrait aussi être régulée soit par un domaine d'auto-inhibition, soit par phosphorylation, ou encore par sa localisation (Ahmed *et al.*, 1993 ; Mertens *et al.*, 2005 ; Tcherkezian *et al.*, 2005). L'hypothèse selon laquelle l'adoption des programmes Rac1 et RhoA par les cellules dorsales/ventrales et latérales respectivement ne serait pas issue de processus de détermination ayant lieu au cours de la différenciation de l'hypoderme, mais plutôt d'un mécanisme d'induction ayant lieu au cours de la morphogenèse de l'épiderme, semble ainsi la plus probable.

En conclusion, ce travail démontre que les voies *pix-1/pak-1* et *let-502* agissent de façon redondantes et synergiques à l'échelle de l'organisme, et antagonistes à l'échelle cellulaire, dans les cellules de l'hypoderme au cours de l'élongation précoce du *C. elegans*. Ce travail apporte des modifications majeures au modèle précédemment établi permettant d'expliquer la base moléculaire de l'élongation précoce. Cette étude démontre l'importance d'étudier les processus morphogéniques des épithéliums à l'échelle de la cellule plutôt que du tissu. Nous espérons, en toute modestie, que cette étude ouvrira la voie à des études similaires dans d'autres organismes. Cela permettra de savoir si une hétérogénéité cellulaire telle qu'observée

dans notre modèle est une étrangeté spécifique au nématode ou une particularité répandue lors de la morphogenèse des épithéliums.

ANNEXES

Annexe A : Article publié :

Martin, E., Harel, S., Nkengfac, B., Hamiche, K., Neault, M. et Jenna, S. (2014). *pix-1* controls early elongation in parallel with *mel-11* and *let-502* in *Caenorhabditis elegans*. *PLoS ONE* 9(4): e94684.

OPEN ACCESS Freely available online

PLOS | ONE

pix-1 Controls Early Elongation in Parallel with *mel-11* and *let-502* in *Caenorhabditis elegans*

Emmanuel Martin[◔], Sharon Harel[◔], Bernard Nkengfac, Karim Hamiche, Mathieu Neault, Sarah Jenna*

Department of Chemistry, Pharmaqam, Biomed, Université du Québec à Montréal (UQÀM), Montréal, Québec, Canada

Abstract

Cell shape changes are crucial for metazoan development. During *Caenorhabditis elegans* embryogenesis, epidermal cell shape changes transform ovoid embryos into vermiform larvae. This process is divided into two phases: early and late elongation. Early elongation involves the contraction of filamentous actin bundles by phosphorylated non-muscle myosin in a subset of epidermal (hypodermal) cells. The genes controlling early elongation are associated with two parallel pathways. The first one involves the *rho-1*/RHOA-specific effector *let-502*/Rho-kinase and *mel-11*/myosin phosphatase regulatory subunit. The second pathway involves the CDC42/RAC-specific effector *pak-1*. Late elongation is driven by mechanotransduction in ventral and dorsal hypodermal cells in response to body-wall muscle contractions, and involves the CDC42/RAC-specific Guanine-nucleotide Exchange Factor (GEF) *pix-1*, the GTPase *ced-10*/RAC and *pak-1*. In this study, *pix-1* is shown to control early elongation in parallel with *let-502/mel-11*, as previously shown for *pak-1*. We show that *pix-1*, *pak-1* and *let-502* control the rate of elongation, and the antero-posterior morphology of the embryos. In particular, *pix-1* and *pak-1* are shown to control head, but not tail width, while *let-502* controls both head and tail width. This suggests that *let-502* function is required throughout the antero-posterior axis of the embryo during early elongation, while *pix-1/pak-1* function may be mostly required in the anterior part of the embryo. Supporting this hypothesis we show that low *pix-1* expression level in the dorsal-posterior hypodermal cells is required to ensure high elongation rate during early elongation.

Citation: Martin E, Harel S, Nkengfac B, Hamiche K, Neault M, et al. (2014) *pix-1* Controls Early Elongation in Parallel with *mel-11* and *let-502* in *Caenorhabditis elegans*. PLoS ONE 9(4): e94684. doi:10.1371/journal.pone.0094684

Editor: Bob Goldstein, University of North Carolina at Chapel Hill, United States of America

Received December 16, 2013; **Accepted** March 17, 2014; **Published** April 14, 2014

Funding: This work was supported by grants from the Natural Sciences and Engineering Research Council (NSERC) of Canada and The Canada Foundation for Innovation. SJ is funded by the Canada Research Chair program. SH is funded by the NSERC and by the "Fonds de recherche en santé du Quebec" EM is funded by the FARE UQAM research fellowship. The funders had no role in study design, data collection and analysis, decision to publish, or preparation of the manuscript.

Competing Interests: The authors have declared that no competing interests exist.

* E-mail: jenna.sarah@uqam.ca

◔ These authors contributed equally to this work.

Introduction

In mammals, the CDC42/RAC-specific Guanine-nucleotide exchange factor (GEF) α/β-PIX and the CDC42/RAC-specific effector kinase PAKs were shown to control cell migration, cell polarity, cytoskeleton remodeling and focal adhesion complex assembly/disassembly dynamics [1]. Their involvement in the control of epithelium morphogenesis and migration of epithelial sheets has also been recently established in mammals [2], and in model organisms such as *Drosophila melanogaster* and *Caenorhabditis elegans* [3 5]. Study of epithelial morphogenesis in *C. elegans* appears as an excellent model to better understand the function of α/β-PIX and PAKs during complex morphogenic events in living organisms.

In the nematode *C. elegans*, embryonic elongation involves the extension of the embryo along its longitudinal axis and a reduction of its transverse diameter, resulting in a 4-fold increase in length. This morphogenetic event involves dramatic changes in the shape of the epidermal (hypodermal) cells. Elongation is divided into an early and a late phase. The early phase, from comma to 1.75-fold stage corresponding to embryos that are 1.75-fold in length compared to non-elongated embryos , occurs through contraction of filamentous actin bundles (FBs) in hypodermal cells [6]. The hypodermis is composed of ventral, lateral (seam cells) and dorsal cells, which are linked by adherens junctions [7]. Contraction of FBs during early elongation is thought to be high in the seam cells and low in dorsal and ventral hypodermal cells [6,8].

The late phase of elongation involves mechanotransduction signaling from the body-wall muscles to the dorsal and ventral hypodermal cells [4]. At the 1.5-fold stage of development, muscle cells form connections, called trans-epidermal attachment structures (TEAs), with the dorsal and ventral hypodermis [9]. As embryos develop to the 1.75-fold stage, the muscles become functional and start contracting, thus inducing chemical changes in the overlying hypodermal cells through mechanical tension applied on the TEAs [4].

The signal transduction pathways that regulate early and late elongation have been extensively investigated over the last 15 years. Interestingly, many genes controlling morphological changes of the hypodermis during elongation are effectors or regulators of Rho GTPases [3,4,10,11]. Rho GTPases are molecular switches controlling a wide-range of cellular functions involving cell shape changes, cell migration, cell proliferation and differentiation [12]. They cycle between an "ON" GTP-bound form and an "OFF" GDP-bound form. When bound to GTP, they interact with specific effectors. They are regulated by three families of proteins: Guanine nucleotide-Exchange Factors (GEFs);

GTPase-Activating Proteins (GAPs); and Guanine nucleotide-Dissociation Inhibitors (GDIs). To date, although three Rho GTPases (*rho-1*/RHOA, *ced-10*/RAC and *mig-2*/RHOG) have been implicated in pathways controlling elongation, only three of their regulators (GAPs and GEFs) have been shown to be involved in this process [4,10,11,13], suggesting that others remain to be identified.

In hypodermal cells, contraction of the FBs during early elongation depends on the regulation of myosin-light-chain (MLC-4/MLC) phosphorylation by three serine-threonine kinases, the RHO-1/RHOA-effector kinase LET-502/ROCK, the *C. elegans* ortholog of the CDC42-effector myotonic dystrophy kinase MRCK-1/MRCK and the CDC42/RAC-effector kinase PAK-1/PAK1. These kinases act antagonistically with the MEL-11/PP-1M and are organized in two parallel pathways: The *let-502/mel-11* pathway including *mrck-1* and a second pathway involving *pak-1* [3,8,10]. Downstream of these pathways, MLC-4/MLC phosphorylation leads to non-muscle myosin filament assembly and contractility, while its dephosphorylation is associated with relaxation.

LET-502/ROCK is an essential component of the *let-502/mel-11* pathway and an essential regulator of elongation [14]. It is activated downstream of the Rho GTPase RHO-1/RHOA [15], that may itself be activated by the GEF RHGF-2 [13] and inactivated by the GAP RGA-2 [11]. Inactivation of RHO-1 by RGA-2, occurs in ventral and dorsal hypodermal cells during early elongation leading to inactivation of LET-502/ROCK and reduction of FB contractions in these cells [11]. RHO-1/RHOA and LET-502/ROCK may then be activated in the lateral hypodermal cells where most of the FB contractions may occur during early elongation. Consistent with this model, expression of MLC-4/MLC in the lateral cells can rescue *mlc-4 loss-of-function*-associated elongation defects, while expression of MLC-4/MLC in ventral and dorsal cells cannot [3]. In seams cells, MEL-11/PP-1M may be inhibited by LET-502/ROCK and MRCK-1/MRCK presumably through phosphorylation [3,8].

The second pathway involves the CDC42/RAC-effector PAK-1, the PP2C phosphatase FEM-2/POPX2 and a RHO/RAC-specific GTP-nucleotide exchange factor (GEF) UNC-73/TRIO. The function of these two later proteins in the regulation of MLC-4 phosphorylation and/or PAK-1 function remains unknown [3,8,10,16].

To date, the genes controlling the *pak-1* pathway during early elongation remain unknown. Moreover, the biological significance of the functional redundancy of the *mel-11/let-502* and *pak-1* pathways is not clear. This redundancy is intriguing since it does not appear to add robustness to the elongation system: a single perturbation in any component of the *mel-11/let-502* pathway induces a high proportion of embryonic lethality [10]. This suggests that the *mel-11/let-502* and *pak-1* pathways have unique functions during elongation that remain to be identified.

The CDC42/RAC-specific GEF, PIX is a well-known activator of PAKs in several organisms [1]. In *C. elegans*, *pix-1* codes for a protein homologous to the mammalian β-PIX (Figure S1). It contains a Src-homology 3 (SH3); a GEF/dbl homology (DH); a GIT-binding (GBD), and a PDZ binding (ZB) domains (Figure S1). These conserved domains are shown in mammals to mediate β-PIX interaction with PAK1-3, the Rho GTPases CDC42 and RAC, the phosphatases POPX1/2, the ARFGAP GIT, the tumor suppressor Scribble and the postsynaptic density protein Shank [1]. In *C. elegans*, PIX-1 was shown to activate PAK-1 in a GTPase-independent manner in migrating distal tip cells (DTC) during gonad morphogenesis in larvae [17]. In this system, PAK-1 activation still appears to be at least partially dependent on CED-10/RAC [18]. PIX-1 was also shown to activate PAK-1 through the GTPase CED-10/RAC in hypodermal cells during late elongation of embryos [4].

In this study, we demonstrate that *pix-1* controls early elongation in parallel with *mel-11/let-502*. Our data suggest that *pix-1* is a novel component of the *pak-1* pathway while retaining some function during early elongation independent from *pak-1*. We show that the *pix-1/pak-1* pathway controls the antero-posterior morphology of the embryo during early elongation through regulating head width, while *let-502*/ROCK controls both the head and tail width. Our study proposes a novel model for early elongation where the *mel-11/let-502* and *pix-1/pak-1* pathways have redundant and complementary functions to shape the antero-posterior axis of the embryo.

Results

pix-1 and *pak-1* control early elongation

To investigate the role of *pix-1* during early elongation, we examined the phenotypes of *pix-1(gk416)* and *pix-1(ok982)* embryos. As controls, we characterized the elongation phenotypes of *pak-1(ok448)* and *let-502(sb118ts)* mutant embryos, which display early elongation defects [3,10]. *pix-1(gk416)* and *pak-1(ok448)* are null alleles [3,17]. *pix-1(ok982)* contains a 1002 bp deletion spanning exons 8 to 11 and may code for a protein that retains the N-terminal SH3 and RhoGEF/DH domains of PIX-1 (Figure S1). *let-502(sb118ts)* is a thermosensitive allele coding for the RHO-1/RHOA-effector kinase LET-502/ROCK. This allele shows no obvious phenotypes at 20°C, but displays strong elongation defects and L1-larval arrest characteristic of strong hypomorphic and null *let-502* alleles at 25.5°C [10] (Figure 1).

Phenotypic characterisation of animals carrying *pix-1(gk416)*, *pix-1(ok982)* and *pak-1(ok448)* alleles revealed low penetrance embryonic lethality (Emb) and early larval arrest (Lva) confirming previous findings (Table 1) [4]. Measurements of *pix-1(gk416)*, *pix-1(ok982)*, *pak-1(ok448)* and *let-502(sb118ts)* arrested larvae showed that they were significantly shorter than synchronized *wt* L1 larvae at 25.5°C (T-test, $p<0.01$) (Figure 1A and B). To better characterize the elongation defects associated with the *pix-1*, *pak-1* and *let-502* alleles, we measured the duration of early elongation using four-dimensional light microscopy. To do so, embryos were collected through dissection of hermaphrodites grown at 25.5°C, and embryonic development was imaged at 23 24°C. The duration of early elongation was measured from the 1.2-fold stage to the beginning of late elongation when body wall muscles started contracting (Figure 1C). Animals carrying *let-502(sb118ts)* (n = 10), *pix-1(gk416)* (n = 25) and *pak-1(ok448)* (n = 20) alleles developed significantly slower than *wt* animals (n = 17) during early elongation (Figure 1C). We also measured the length of the embryos at the end of early elongation (Figure 1D), and found that mutant embryos were significantly shorter than *wt* embryos (Figure 1D). These data demonstrate that the elongation rate of *pix-1*, *pak-1* and *let-502* mutant embryos is significantly reduced during early elongation, and provide the first evidence of a requirement for *pix-1* at this stage. They also confirm the involvement of *pak-1* during early elongation [3].

Interestingly, *pix-1* and *pak-1* arrested larvae had very similar morphologies and behavior. For example, they were thin and clear when compared to *let-502* arrested larvae (Figure 1A). Furthermore, they appeared to have different antero-posterior morphologies when compared to *wt* and *let-502* larvae. When the width of the head (H3, Figure 2A and B) and the width of the tail (T3, Figure 2A and B) were measured and combined as a head/tail width ratio (H3/T3, Figure 2B), *pix-1(gk416)*, *pix-1(ok982)* and *pak-*

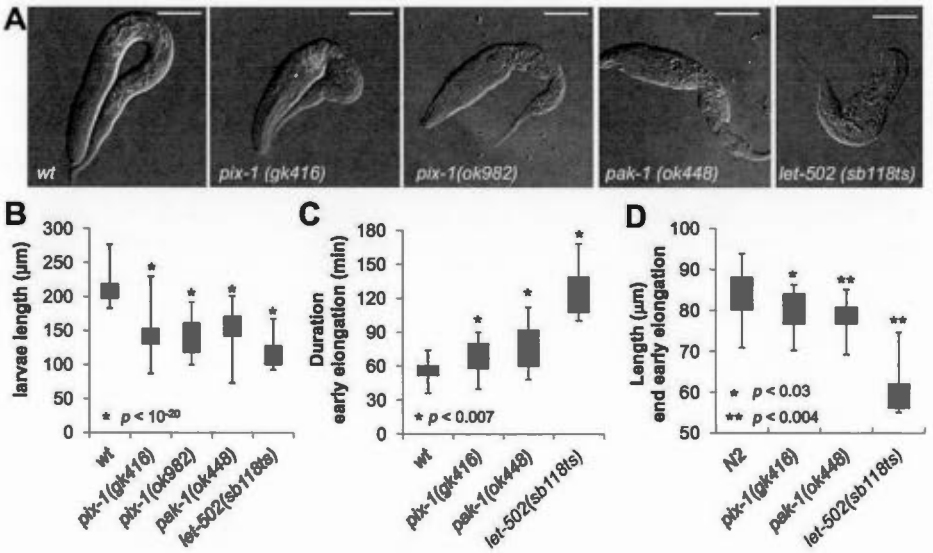

Figure 1. *pix-1* and *pak-1* control early elongation. A) Arrested larvae of *pix-1(gk416)*, *pix-1(ok982)*, *pak-1(ok448)* and *let-502(sb118ts)* mutants grown at 25.5°C. Bar = 25 µm. B) Box-plot representing the distribution of sizes of arrested larvae in mutant populations grown at 25.5°C. The box-plot represents the min, max, 25th, 50th (median) and 75th percentile of the population. Distribution of *wild-type* animals (*wt*) has been established using N2 L1 larvae synchronized by starvation after hypochlorite treatment. C) Box-plot representing the distribution of the duration in minutes of early elongation for *wt* and mutants embryos. Embryos are collected through dissection of hermaphrodites grown at 25.5°C. Embryonic development is recorded at 23–24°C. D) Box-plot representing the distribution of the length of embryos (in µm) at the end of early elongation. The same population of embryos was used to generate data presented in panel C and D. Student's T-test *p-values* are indicated.
doi:10.1371/journal.pone.0094684.g001

1(ok448) had significantly higher ratios than *wt* and *let-502* larvae (H3/T3, Figure 2B, data not shown). This indicates that *pix-1* and *pak-1* mutant arrested larvae present a morphological alteration characterized by an inflated anterior part of their body when compared to their posterior part. These mutants arrested larvae also had severe pharynx pumping defects and were completely paralyzed, although pumping in L3 escapers was similar to *wt* larvae (Figure S2). While these later phenotypes may be physiological consequences of primary developmental phenotypes, they support the fact that a similar array of phenotypes is observed in *pix-1* and *pak-1* mutant animals. These data support then the hypothesis that *pix-1* and *pak-1* could be part of the same developmental pathway. This also suggests that *pix-1* and *pak-1* control the relative width of the head vs. the tail of developing embryos, a process that does not seem to require *let-502*.

pix-1 and *pak-1* control the head to tail width of the embryos during early elongation

Since *pix-1* and *pak-1*are also involved in the control of late elongation, we investigated whether their function during early elongation is required to control the head to tail width of the animal. To do so, we measured the H/T ratio of *pix-1(gk416)*, *pak-1(ok448)* and *let-502(sb118ts)* embryos at the beginning, 1.2-fold stage (H1/T1, Figure 2A and B), and at the end of the early elongation (H2/T2, Figure 2A and B). These experiments were done using the same populations of embryos characterized previously (Figure 1C and D). While no change, or a reduced H/T ratio was observed in *pix-1*, *pak-1* and *let-502* mutants when compared to *wt* animals at the beginning of early elongation (H1/T1, Figure 2A), all three mutants showed a significantly higher H/T ratio than *wt* embryos at the end of early elongation (T-test *p-values*<0.006; H2/T2, Figure 2A). This shows that the inflated head vs tail morphology observed in *pix-1* and *pak-1* arrested larvae is also observed at the end of early elongation in *pix-1*, *pak-1*

Table 1. Embryonic lethality and arrest of non-elongated larvae in *pix-1 and pak-1* mutants.

	18°C			25.5°C		
allele	**Emb (%)**	**Lva (%)**	**n**	**Emb (%)**	**Lva (%)**	**n**
wt	0	0	709	0.5	0	2367
pix-1 (ok982)	6	7	1140	11	15	679
pix-1 (gk416)	1	6	713	2.14	8.5	1216
pix-1(gk416);sajEx1[pix-1p::pix-1::GFP; rol-6]	-	-	-	1.2	2.0	917
pak-1(ok448)	1	12	2502	3	25.6	264

doi:10.1371/journal.pone.0094684.t001

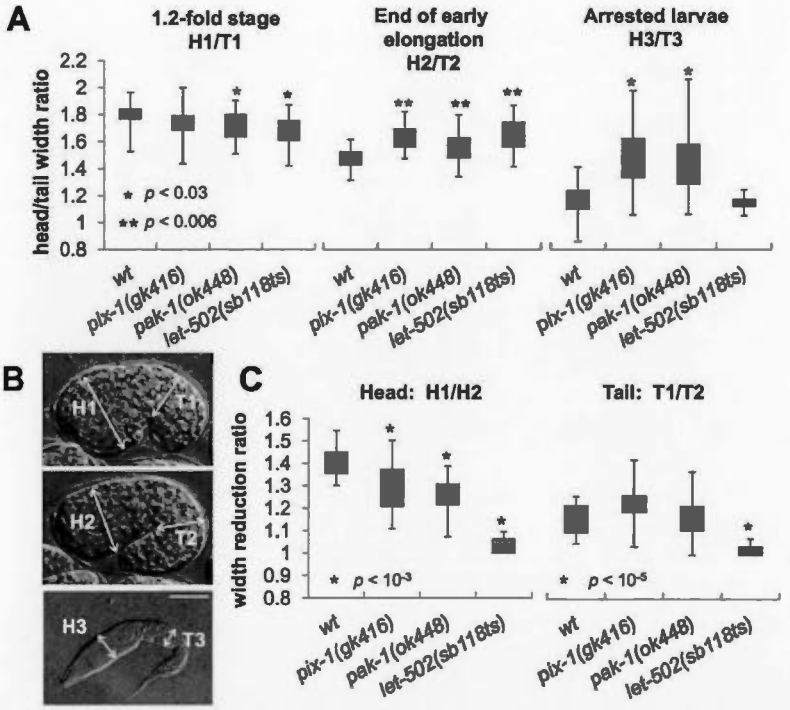

Figure 2. *pix-1, pak-1* and *let-502* control the head to tail width ratio of elongating embryos. Head (H) and tail (T) width are measured on 1.2-fold stage embryos (H1 and T1); at the end of early elongation (H2 and T2) and in arrested larvae (H3 and T3). In all panels of this figure animals were grown at 25.5°C. Embryos were collected through dissection of hermaphrodite grown at 25.5°C. Embryonic development is then recorded using 4-dimensional microscopy at 23–24°C. A) Distribution of ratio between the head and tail width of embryos at 1.2-fold stage (H1/T1; left panel), at the end of early elongation (H2/T2; middle panel) and of arrested larvae (H3/T3; right panel) in *wt*, *pix-1(gk416)*, *pak-1(ok448)* and *let-502(sb118ts)* mutants. B) Localisation of measured areas in embryos and larvae C) Distribution of the head (H1/H2) and tail (T1/T2) width reduction ratios during early elongation. The box-plots represent the min, max, 25th, 50th (median) and 75th percentiles of the populations. Student's T-test *p-values* are indicated
doi:10.1371/journal.pone.0094684.g002

and *let-502* mutant embryos, suggesting that *pix-1*, *pak-1* and *let-502* control the head to tail width of the embryos at that stage. We then measured the reduction of head (H) and tail (T) width during early elongation. To do so, we compared the width of the head and the width of the tail of the embryos at the beginning and the end of early elongation (H1/H2 and T1/T2 respectively; Figure 2C). In *wt* embryos the head and the tail appeared to be 1.4- and 1.16-fold wider at the beginning than at the end of early elongation (Figure 2C). This shows that the head width reduces more than the tail width during early elongation in *wt* animals. We found that the head width of the *pix-1* and *pak-1* mutant embryos reduced significantly less during early elongation than *wt* embryos (Figure 2C left panel). We also found that the tail width reduced similarly in *pix-1* and *pak-1* mutant embryos than in *wt* embryos. Interestingly, the degrees of head and tail width reduction in *let-502(sb118ts)* embryos were significantly lower than *wt* embryos and not significantly different than 1, suggesting that in *let-502* mutant animals neither the head, nor the tail width of the animal reduce during early elongation (Figure 2C).

Together, these data suggest that the higher reduction of the head versus the tail width of the embryo during early elongation requires *pix-1*, *pak-1* and *let-502* function. These three genes appear to be required for reduction of the head width of the embryo, while only *let-502* may be required for reduction of the tail width.

pix-1 and *pak-1* control early elongation in parallel with *mel-11/let-502* pathway

pak-1 was previously proposed to control early elongation in parallel with the *mel-11/let-502* pathway [3]. To assess whether *pix-1* also controls early elongation in parallel with the *mel-11/let-502* pathway, we tested whether *pix-1(gk416)* genetically interacts with *mel-11(it26)* and *let-502(sb118ts)* temperature sensitive mutants, as reported for *pak-1* [3]. At 18°C, 98% of *mel-11(it26)* mutant embryos rupture during elongation as previously described (Table 2, line 3) [10]. The penetrance of this phenotype is increased to 100% at 25.5°C. As previously shown, *mel-11(it26); pak-1(ok448)* double mutant embryos display phenotypes similar to *mel-11(it26)* at both 18°C and 25.5°C (Table 2 line 10) [3]. Interestingly, the *mel-11(it26)*-associated embryonic rupturing is completely suppressed by *pix-1(gk416)* at 18°C and 25.5°C (Table 2, line 4). A small fraction of *mel-11(it26); pix-1(gk416)* hatched larvae arrest at the L1 stage with characteristic *pix-1* phenotypes, and a penetrance similar to *pix-1(gk416)* at 18°C (Table 2, line 2 and 4). Surprisingly, at 25.5°C, 9.7% of *mel-11(it26); pix-1(gk416)* embryos arrest between 1.2- and 2-fold stages without rupturing and 40.3% of them display late elongation defects and stop developing without hatching (Table 2, line 4). These results show that *pix-1(gk416)* suppresses both the expressivity – the embryos arresting at 1.2–2 fold stages without rupturing – and the penetrance of *mel-11* early elongation defects at 25.5°C. Considering *mel-11(it26)* to be null at 25.5°C

Table 2. Genetic interactions of *pix-1* and *pak-1* with *mel-11* and *let-502* mutants.

		18°C			25.5°C		
	Genotype	early elongation arrest (%)	Lva (%)	n	early elongation arrest (%)	Lva (%)	n
1	*wt*	0	0	531	0	0	323
2	*pix-1(gk416)*	0	5	420	0	8,5*	1190
3	*mel-11(it26)*	98$	0	508	100$	0	65
4	*mel-11(it26); pix-1(gk416)*	0	3	100	9,7$$	40,3***	62
5	*let-502(sb118ts)*	0	0	645	7,9	91,2**	353
6	*let-502(sb118ts); pix-1(gk416)*	18,1	2,5	764	89	11**	373
7	*mel-11(it26); let-502(sb118ts)*	96	0	905	24	0	487
8	*mel-11(it26); let-502(sb118ts); pix-1(gk416)*	29,8	2,2	359	43,1	31*	297
9	*pak-1(ok448)*	0	12	1714	0	25,8*	256
10	*mel-11(it26); pak-1(ok448)*	98	0	763	100	0	931
11	*let-502(sb118ts); pak-1(ok448)*	1	90	2417	100	0	2003
12	*mel-11(it26); let-502(sb118ts); pak-1(ok448)*	100	0	1066	100	0	891

Early elongation arrest include embryos arresting between comma and 1.75-fold with or without rupturing.
* arrested larvae present a *pix-1(gk416)* specific morphology (Figure 1A).
** arrested larvae present a *let-502 (sb118ts)* specific morphology (Figure 1A).
*** late elongation arrest without hatching.
$all arrested embryos rupture.
$$0% rupture.
doi:10.1371/journal.pone.0094684.t002

[19], these data suggest that *pix-1* functions in parallel with *mel-11* during early elongation. The aggravation of *pix-1* associated late elongation defects in a *mel-11(it26)* background is somewhat intriguing and provides the first evidence suggesting an involvement of *mel-11* in late elongation, in parallel with *pix-1*.

We then assessed whether *pix-1(gk416)* and *pak-1(ok448)* interacts with *let-502(sb118ts)* at 25.5°C. As previously shown, few *let-502(sb118ts)* embryos arrest between the 1.2- and 2-fold stage at restrictive temperature and the vast majority of the animals hatch as non-elongated larvae (Table 2, line 5, Figure 1A) [10]. 89% and 100% of *let-502(sb118ts)* embryos arrest between 1.2- and 2-fold stages in *pix-1(gk416)* and *pak-1(ok448)* backgrounds, respectively at 25.5°C (Table 2, line 6 and 11). In addition, *let-502(sb118ts); pix-1(gk416)* hatched larvae arrested with more severe elongation defects than *let-502(sb118ts)* animals (Table 2, line 6; Figure 3A and C), while their head/tail width ratio is not significantly different than *wt* as observed for *let-502(sb118ts)* arrested larvae (Figure 3D). These results suggest that *pix-1* functions in parallel with *let-502* to control elongation, as previously shown for *pak-1* [3], and that the loss of *let-502* function suppress the higher H/T ratio observed in *pix-1* mutant arrested larvae when compared to *wt*. Interestingly, the aggravation of *let-502* defects by *pix-1(gk416)* appears to be weaker than that observed for *pak-1(ok448)*, suggesting that *pix-1* is redundant with a yet unidentified gene in parallel with *let-502*.

To assess if *pix-1* functions in parallel with the *let-502/mel-11* pathway, we generated *mel-11(it26); let-502(sb118ts); pix-1(gk416)* triple mutants. At 18°C, *mel-11(it26); let-502(sb118ts)* display similar elongation defects to *mel-11(it26)* single mutant embryos due to the thermosensitive nature of *let-502(sb118ts)* (e.g. *wt* phenotype at 18°C; Table 2, compare lines 3 and 7). At non-restrictive temperature, a reduced number of *mel-11(it26); let-502(sb118ts); pix-1(gk416)* animals arrest during early elongation when compared to *mel-11(it26); let-502(sb118ts)* (Table 2, compare lines 7 and 8). This is consistent with our data showing suppression of *mel-11(it26)* early elongation defects by *pix-1(gk416)* (Table 2 line 4). At 25.5°C, *mel-11(it26); let-502(sb118ts)* are viable and embryos display 24% early elongation arrest (Table 2 line 7). At restrictive temperature, elongation defects are aggravated in *mel-11(it26); let-502(sb118ts); pix-1(gk416)* triple mutants in comparison to *mel-11(it26); let-502(sb118ts)* double mutants (Table 2, compare lines 7 and 8): 43.1% embryos arrested during early elongation (compared to 24% in *mel-11(it26); let-502(sb118ts)*), and 31% of animals hatched as non-elongated larvae presenting *pix-1* mutant-associated morphology (compared to 0% in *mel-11(it26); let-502(sb118ts)*; Figure 3B and C). Interestingly, *mel-11(it26); let-502(sb118ts); pix-1(gk416)* arrested larvae present a H/T width ratio significantly higher than *wt* and similar to that observed in *pix-1(gk416)* arrested larvae (Figure 3D). This suggests that in *mel-11(it26)* background, loss of *let-502* function is not anymore able to suppress *pix-1*-induced H/T ratio defect.

As previously shown, 100% of *mel-11(it26); let-502(sb118ts); pak-1(ok448)* embryos failed to hatch and displayed early elongation arrest (Table 2, line 12) [3]. These results suggest that *pix-1* functions in parallel with the *let-502/mel-11* pathway during early elongation, as shown for *pak-1*. However, the increased phenotypic severity observed in *pak-1 vs. pix-1* mutants suggests that *pix-1* functions redundantly with a gene or a group of genes in parallel with *mel-11/let-502* during early elongation. The different relationship observed between *mel-11* and *pix-1* or *pak-1* mutants also suggests that *pix-1* and *pak-1* have independent functions during early elongation. Whether this is the case during late elongation, could not be ascertained from our data.

PIX-1::GFP is homogeneously distributed in the cytoplasm and at cell periphery of hypodermal cells

pix-1 was previously shown to be involved in mechanotransduction signaling in ventral and dorsal hypodermal cells upon muscle

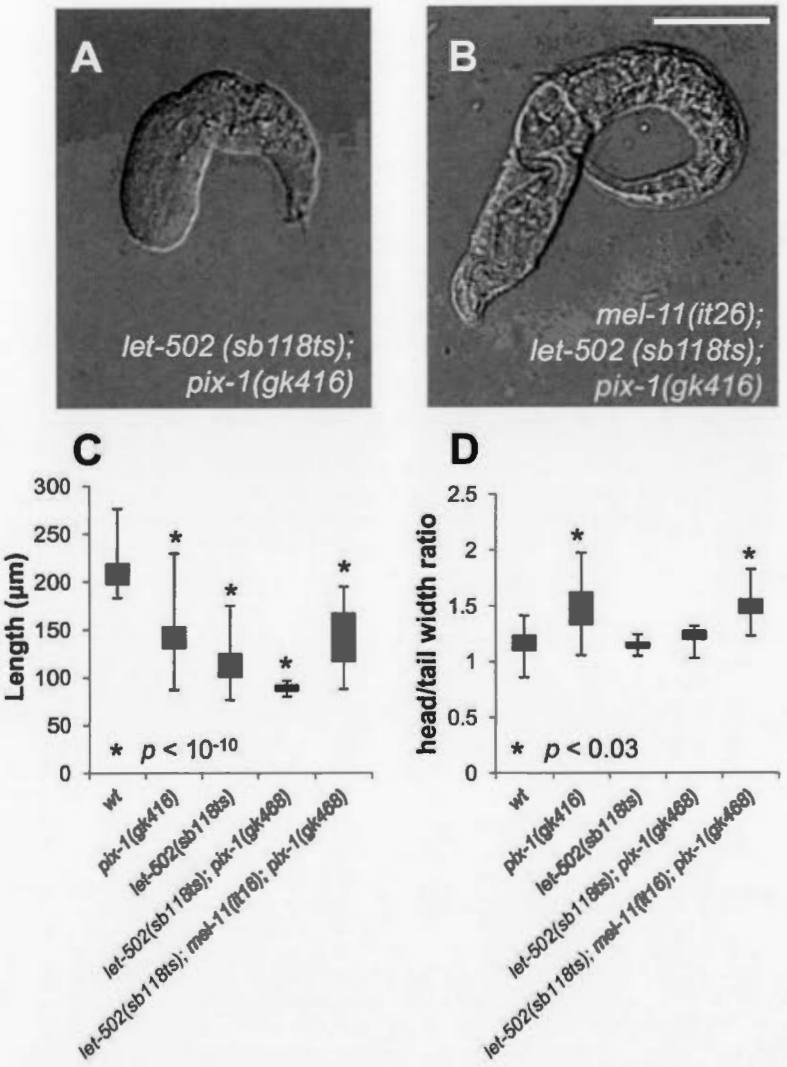

Figure 3. *pix-1(gk416)* controls early elongation in parallel with *mel-11/let-502*. A) Morphology of *let-502 (sb118ts); pix-1(gk416)* and B) *mel-11(it26); let-502 (sb118ts); pix-1(gk416)* arrested larvae grown at 25.5°C. C) Distribution of sizes of arrested larvae in mutants' populations, at 25.5°C. Distribution of wild-type animals (*wt*) has been established using N2 L1 larvae synchronized by starvation after hypochlorite treatment. D) Distribution of ratio between the head and tail width of arrested larvae in mutant populations. The box-plot represents the min, max, 25th, 50th (median) and 75th percentiles of the population. Student's T-test *p-values* are indicated.
doi:10.1371/journal.pone.0094684.g003

contraction during late elongation events [4]. The localisation of PIX-1 at the TEA in dorsal and ventral hypodermal cells supports this function [4]. Our data suggest that *pix-1* also controls early elongation events. These events are thought to be directed by the contraction of filamentous actin bundles (FBs) at the cell periphery and at the most apical part of the lateral hypodermal cells [3]. To better understand the function of PIX-1 during early elongation, we characterized its subcellular localization in hypodermal cells during early elongation. To do so, we examined the localisation of PIX-1::GFP expressed under the control of the *pix-1* endogenous promoter in *pix-1(gk416)* animals immuno-stained with MH27 antibodies (staining of hypodermal adherens junctions; Figure 4) or expressing the filamentous actin-binding probe VAB-10$_{ABD}$::m-Cherry in hypodermal cells (Figure S4). Confocal microscopy analysis revealed that during early elongation, PIX-1::GFP is expressed in the dorsal (Figure 4A-C, Figure S4A–F), lateral (Figure 4D–F) and ventral hypodermal cells (Figure 4G–I, Figure S4D–F). Throughout early elongation, PIX-1::GFP is located at the TEA in dorsal and ventral hypodermal cells, as previously reported (Figure 4 E, arrow-head) [4] and is also homogeneously distributed in the cytoplasm and at the cell periphery of all expressing cells (Figure 4, Figure S4). Interestingly, at the comma stage, PIX-1::GFP expression appears to be reduced in several posterior dorsal hypodermal cells (Figure 4 B, arrowhead). Concomitant with the fusion of these cells, around the 1.2-fold stage, the expression of PIX-1::GFP appears to be reduced in the fused cells (Figure 5A).

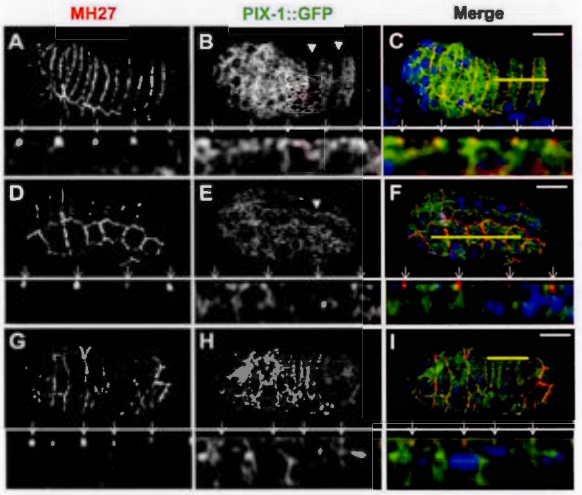

Figure 4. PIX-1 is homogeneously distributed in the cytoplasm and at the cell periphery of hypodermal cells. A–I) Immunostaining of *pix-1(gk416); sajEx1[pix-1p::pix-1::gfp]* expressing embryos with MH27 antibodies (A, D, G and red in merge panel C, F, I) and anti-GFP antibodies (B, E, H and green in merge panel C, F, I). Lower panel of each view correspond to orthogonal views of embryos Z-sectioning. Position of Z-sectioning is indicated in upper panel by a yellow line in dorsal (A–C) and lateral (D–F) and ventral (G–I) hypodermis. In orthogonal views, arrows point to adherens junctions which partially colocalize with PIX-1::GFP immunostaining. Arrowheads show the decrease in PIX::GFP expression every other cell in the dorsal-posterior hypodermis (at comma stage) in picture B (upper panel); Arrow-head indicates dorsal trans-epithelial attachment structures (TEA) in picture E (upper panel). Scale bars: 10 µm.
doi:10.1371/journal.pone.0094684.g004

High expression of *pix-1* in dorsal posterior hypodermis is detrimental for early elongation

Considering that *pix-1* controls reduction of the head but not the tail width of the embryos during early elongation, we were intrigued by the reduction of the expression of PIX-1::GFP in the dorsal-posterior hypodermal cells in the transgenic animals. We then quantified PIX-1::GFP expression in dorsal-anterior (DA), dorsal-posterior (DP), ventral-anterior (VA), ventral-posterior (VP), lateral-anterior (LA) and lateral-posterior (LP) hypodermal cells (Figure 5 A). This study revealed a significant lower ratio of DP/DA and DP/V expression when compared to LP/LA, VP/VA, DA/V and DA/L ratios, which were not significantly different than 1 (Figure 5 B). Similar data were obtained using two independent transgenic lines expressing translational fusions of PIX-1::GFP under the control of the *pix-1* endogenous promoter, one transgenic line carrying an extrachromosomal array (*pix-1(gk416);sajEx1*) and one stable transgenic line carrying an integrated array (*unc-119(ed3);pix-1(gk416);sajIs1* see Methods). We also found that all measured ratios were constant throughout early elongation (Figure S5).

We then assessed whether the *sajEx1[pix-1p::pix-1::GFP,rol-6]* transgene could rescue elongation defects in *pix-1(gk416)* animals. We found that the transgene significantly rescued the larval arrest phenotype (Lva) of *pix-1(gk416)* from 8.5% (N = 1216) to 2.0% (N = 917) (Table 1; T-test, *p-value* = 0.03). Using time-lapse microscopy, we also measured the elongation rate of wild-type (*wt*), *pix-1(gk416)* and *pix-1(gk416);sajEx1[pix-1p::pix-1::GFP, rol-6]* embryos and found that the transgene did not significantly rescue the elongation rate of mutant animals (Figure 6 B). This suggests that while the expression of PIX-1::GFP fusion protein is sufficient to support PIX-1 function during early elongation (rescuing Lva), it was not as efficient as the endogenous protein.

We then observed the elongation rate of embryos at the single animal level and attempted to see if there was any correlation between a given expression pattern of the transgene and the ability of the transgene to efficiently rescue the mutant elongation rate defect. We found that transgenic embryos with similar elongation rates to *wt* embryos (elongation≥288 nm/min, Figure 6D) had DP/DA and DP/V ratios of PIX-1::GFP intensity that were significantly lower than embryos that elongated slower (elongation<288 nm/min, *p-value*<0.01; Figure 6D). No significant difference was observed for the LP/LA, VP/VA DA/V and DA/L ratios between the two populations of embryos (Figure 6D). These data show that PIX-1::GFP expression was significantly reduced in dorsal-posterior cells when compared to dorsal-anterior and ventral cells in rescuing animals. Such reduction of PIX-1::GFP expression in dorsal-posterior cells was not observed in non-rescuing animals. Importantly, animals presenting a DP/DA ratio higher than 0.5, elongated almost 3 times slower than *wt* animals (Figure 6A). Overall, the speed of early elongation appeared to be negatively correlated to the DP/DA ratio of PIX-1::GFP expression (Spearman correlation coefficient R^2>0.427; *p-value*<0.002; Figure 6C), but not to any other PIX-1::GFP intensity ratio measured in hypodermal cells (Figure S6). Similar results were obtained using two independent *pixp::pix-1::GFP* expressing transgenic lines, one carrying an extrachromosomal array (*pix-1(gk416);sajEx1*), and a stable transgenic line carrying an integrated array (*unc-119(ed3);pix-1(gk416);sajIs1*). These data suggest that transgenic animals expressing PIX-1::GFP homogeneously in dorsal-anterior, lateral and ventral hypodermal cells, but two times less in dorsal-posterior cells, elongate at a *wt*-rate during early elongation. However, animals expressing the transgene in dorsal-posterior cells at a similar/higher level when compared to other cells elongated significantly slower.

PIX-1::GFP is expressed in cells other than the hypodermis, and we cannot exclude the possibility that differential expression of PIX-1::GFP in other cells may affect the rescuing ability of the transgene. To test this possibility, we generated transgenic animals expressing PIX-1::GFP under the control of the hypodermal specific promoter, *lin-26p*. This promoter is thought to drive the expression of coding sequences only in hypodermal cells and in a homogenous manner [3]. We confirmed this later assumption through measurements of the DP/DA fluorescence intensity ratios in *lin26p::vab-10(ABD)::GFP* and *lin-26p::vab-10(ABD)::mCherry* transgenic animals carrying integrated arrays expressing actin-binding fluorescent probes in all hypodermal cells under the control of *lin-26p* [3]. We showed that these ratio were not significantly different than 1 (Figure 5 C and D).

As observed with *pix-1p::pix-1::GFP* expressing animals, transgenic animals carrying an integrated array expressing PIX-1::GFP under the control of *lin-26p* segregated into two populations. The embryos of the first population displayed an elongation rate similar to *wt* (elongation rate≥288 nm/min, Figure S7) and had DP/DA and DP/L intensity ratios that were significantly lower than the second population of embryos that elongated slower (elongation rate<288 nm/min, Figure S7). As shown for transgenic animals expressing *pix-1p::pix-1::GFP*, all animals expressing PIX-1::GFP under the control of *lin-26p* express similar levels of the transgene in DA, L and V cells (Figure S7). These data support our hypothesis that a DP/DA PIX-1::GFP expression ratio higher than 0.5 may hinder early elongation.

To determine if the lower DP/DA, DP/L and DP/V intensity ratios observed in embryos with a *wt*-like elongation rate were due

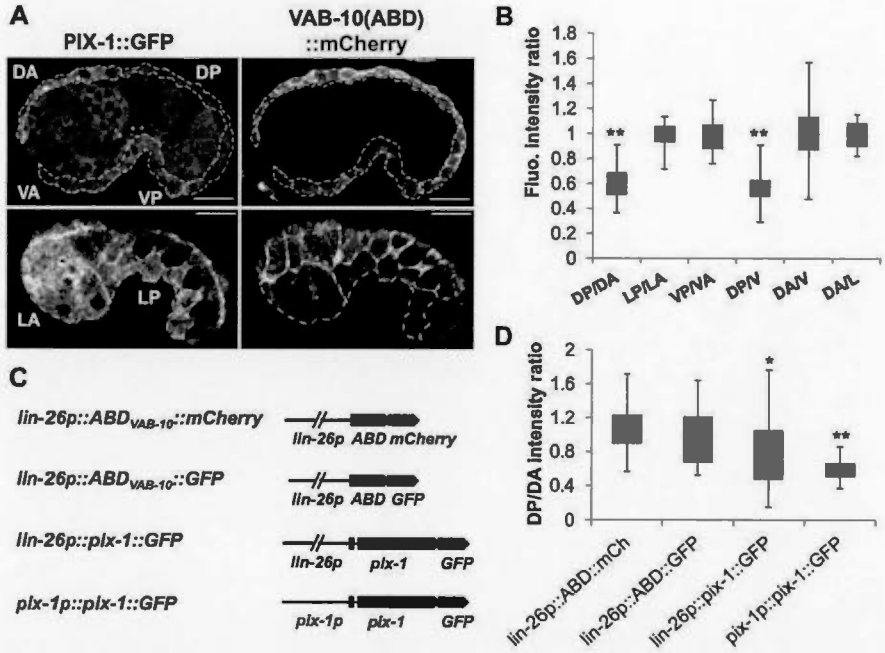

Figure 5. PIX-1::GFP is differentially expressed in hypodermal cells during elongation. A) Confocal lateral projections of *pix-1(gk416); sajEx1[pix-1p::pix-1::GFP]; mcIs40 [lin-26p::ABDvab-10::mcherry + myo-2p::gfp]* embryos. Dorsal-anterior (DA, upper panel), dorsal-posterior (DP, upper panel), ventral-anterior (VA, upper panel), ventral-posterior (VP, upper panel), lateral-anterior (LA, lower panel) and lateral-posterior (LP, lower panel) hypodermis are surrounded by dashed line and have been identified using *lin-26p::vab-10(ABD)::MCHERRY* hypodermal markers. B) Distributions of the dorsal-posterior/dorsal-anterior (DP/DA), lateral-posterior/lateral-anterior (LP/LA), ventral-posterior/ventral-anterior (VP/VA), dorsal-posterior/ventral (DP/V); dorsal-anterior/ventral (DA/V), dorsal-anterior/lateral (DA/L) rates of fluorescence intensity measured in *pix-1(gk416); sajEx1[pix-1p::pix-1::GFP; rol-6]; mcIs40 [lin-26p::ABDvab-10::mcherry + myo-2p::gfp]* embryos between comma and 1.75-fold stages (n = 26 embryos). Similar results were also obtained in *pix-1(gk416); sajIs1[pix-1p::pix-1::GFP; unc-119^{+}]; mcIs40 [lin-26p::ABDvab-10::mcherry + myo-2p::gfp]*. The box-plots represent the min, max, 25th, 50th (median) and 75th percentiles of the populations. ** T-test comparing ratios to 1 $p<0.01$. C) Schematic representation of *pix-1::GFP* and ABD_{VAB-10} (control) constructs used to measure the DP/DA intensity ratio reported in panel D. DP/DA of animals carrying *mcIs40* (*lin-26p::ABD::mCh* expressing), *mcIs50* (*lin-26p::ABD::GFP* expressing), *sajIs2* (*lin-26p::pix-1::GFP* expressing) or *sajEx1* (*pix-1p::pix-1::GFP* expressing). ratios** T-test comparing DP/DA ratios measured on *pix-1::GFP* expressing embryos to ratio measured in ABD_{VAB-10} expressing transgenics, $p<0.01$. The box-plots represent the min, max, 25th, 50th (median) and 75th percentiles of populations.
doi:10.1371/journal.pone.0094684.g005

to a reduced expression of PIX-1::GFP in DP cells or to an increased expression of PIX-1::GFP in DA, L and V cells, we measured the fluorescence intensity of PIX-1::GFP in DA and DP cells in *lin-26p::pix-1::GFP* expressing animals. We found that the PIX-1::GFP fluorescence intensity was not significantly different in the DA cells of embryos developing at a *wt*-rate when compared to those developing at slower rates (Figure 6 E). However, PIX-1::GFP fluorescence intensity appeared to be significantly lower in the DP hypodermal cells in the subpopulation of embryos that elongated faster. This phenomenon was observed in two independent stable transgenic lines. These data suggest that the DP/DA ratios in embryos that elongated at a *wt*-rate was not due to an increased expression of PIX-1::GFP in the DA cells, but to decreased PIX-1::GFP expression in the DP cells.

Altogether, these data suggest that homogenous expression of PIX-1::GFP in dorsal-anterior, lateral and ventral hypodermal cells, and decreased expression in dorsal-posterior cells significantly rescued the elongation defects observed in the *pix-1(gk416)* animals. They also suggest that expression of the transgene in dorsal-posterior cells above a threshold corresponding to half the expression in the other hypodermal cells decreases the efficiency of early elongation. This suggests that *pix-1* may be submitted to a tight control of its expression level in hypodermal cells, particularly to decrease its level in the dorsal-posterior cells.

Discussion

Embryonic elongation transforms the ovoid embryo into the long, thin vermiform nematode. This morphogenetic process occurs in two phases. The early elongation is driven by the contraction of Filamentous actin Bundles (FBs) in hypodermal cells. The late elongation is driven by a mechanotransduction pathway in the dorsal and ventral hypodermis resulting from contraction of the underlying muscle cells.

Two parallel pathways control early elongation. One pathway involves two kinases: the RHO-1/RHOA effector LET-502/ROCK and the ortholog of the CDC-42-effector human myotonic dystrophy kinase MRCK-1/MRCK [8,10]. Both kinases are thought to inhibit the function of MEL-11/PP-1M thus permitting phorphorylation of myosin-light chain (MLC-4/MLC) and contraction of FBs. The second pathway involves the CDC42/RAC-effector PAK-1, the PP2C phosphatase FEM-2/POPX2 and a RHO/RAC GTP nucleotide-exchange factor (GEF) UNC-73/TRIO. The function of these two later genes in the regulation of MLC-4/MLC phosphorylation and/or PAK-1 function remains unknown [3,8,10,16]. Downstream of the two parallel pathways LET-502/ROCK and PAK-1 are thought to phosphorylate MLC-4/MLC in the hypodermal cells and to control contraction of FBs. This contraction is assumed to be high in the lateral and

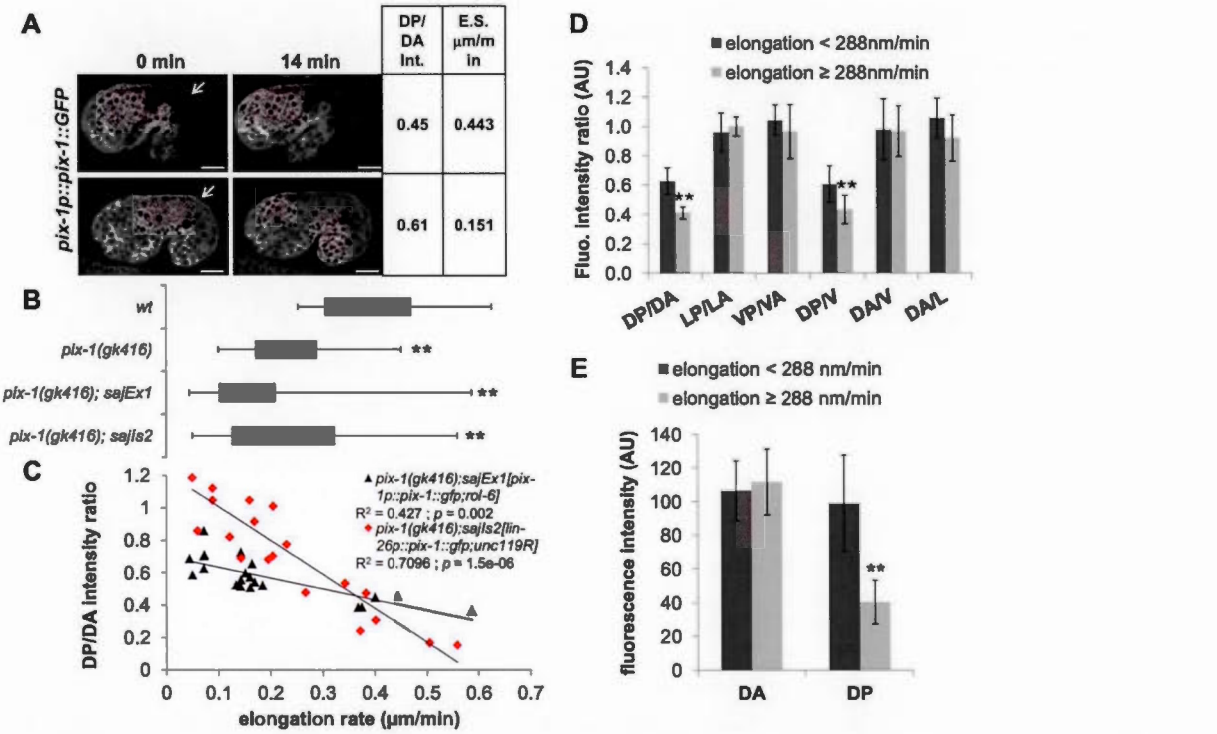

Figure 6. High expression of PIX-1::GFP in dorsal posterior hypodermis is detrimental for elongation rate of embryos. A) Confocal projections of *pix-1(gk416); sajEx1[pix-1p::pix-1::GFP, rol-6]* at t = 0 min and t = 14 min. The DP/DA fluorescence intensity ratio and elongation rate (in µm/min) are indicated. Arrows indicate the dorsal-posterior hypodermis. Scale bar: 10 µm. B) Distribution of elongation rate in µm/min of *wild-type (wt), pix-1(gk416),* and *pix-1(gk416)* animals carrying *sajEx1[pix-1p::pix-1::GFP, rol-6]* or *sajIs2[lin-26p::pix-1::GFP, unc-119^R]* during early elongation. Elongation rate was measured from 4-dimensional recording of embryonic development between comma and the end of early elongation upon DIC illumination. Box-plots represent the min, max, 25th, 50th (median) and 75th percentile of the populations. ** T-test $p<0.01$ vs *wt*. C) Scatter plot representing the relationship between the dorsal-posterior/dorsal-anterior (DP/DA) intensity ratio of PIX-1::GFP and the elongation rate in µm/min during early elongation of *pix-1(gk416)* embryos carrying *sajEx1[pix-1p::pix-1::GFP, rol-6]* or *sajIs2[lin-26p::pix-1::GFP, unc-119^R]* (n = 20 for each line). The spearman correlation (R2) between the elongation rate and the DP/DA ratio are indicated, as well as the *p-values* rejecting the null hypothesis being that the two values are not significantly correlated. Similar results were obtained for *pix-1(gk416)* animals carrying *sajIs1* and *sajIs3* (see methods). D) DP/DA, lateral-posterior/lateral-anterior (LP/LA), ventral-posterior/ventral-anterior (VP/VA), dorsal-posterior/ventral (DP/V), dorsal-anterior/ventral (DA/V) and dorsal-anterior/lateral (DA/L) fluorescence intensity ratio measured for *pix-1(gk416); sajEx1[pix-1p::pix-1::GFP, rol-6]* embryos elongating at a *wt*-rate (elongation≥288nm/min) or elongating slower (elongation<288nm/min) during early elongation. Bar correspond to the mean and error bars to the standard deviation. ** T-test p-value<0.01. E) PIX-1::GFP fluorescence intensity (AU) was measured in DA and DP hypodermal cells of embryos elongating at a *wt*-rate (elongation≥288nm/min) or elongating slower (elongation<288nm/min) during early elongation (see methods). ** T-test p-value<0.01.

doi:10.1371/journal.pone.0094684.g006

low in the ventral and dorsal hypodermal cells during early elongation [11].

In this study, we show that the CDC42/RAC-GEF *pix-1* controls early elongation in parallel with the *mel-11/let-502* pathway. Our data suggest that *pix-1* controls this process as part of the *pak-1* pathway in parallel with a gene (or a group of genes) that remains to be identified. *pix-1* may also function independently from *pak-1*. Our data suggest that PIX-1/PAK-1 and LET-502/ROCK have different function along the antero-posterior axis of the embryo during early elongation: PIX-1, PAK-1 and LET-502/ROCK appear to control the constriction of the head while only LET-502/ROCK controls the constriction of the tail of the elongating embryo. Our study also revealed that PIX-1::GFP fusion protein is homogeneously distributed in the cytoplasm and at the cell periphery of hypodermis during early elongation. We showed that this fusion protein rescues the reduced elongation rate observed *pix-1(gk416)* in a subset of transgenic animals expressing the transgene homogenously in dorsal-anterior, lateral and ventral cells and at a lower level in dorsal-posterior cells. Our results also suggest that PIX-1 expression above a certain threshold in dorsal-posterior hypodermal cells is detrimental for early elongation.

pix-1 functions with unidentified genes in parallel with *mel-11/let-502*

Both *pix-1* and *pak-1* mutants have similar elongation phenotypes and both aggravate the elongation defects observed in *mel-11; let-502* double mutant suggesting that these two genes control together a subset of developmental mechanisms in parallel with *mel-11; let-502* during early elongation. However, *pix-1* mutant aggravates elongation defects associated with *mel-11; let-502* to a lesser extent than the *pak-1* mutant. This suggests that *pix-1* functions with other genes that act in parallel with *mel-11/let-502* pathway (Figure 7).

In both mammals and *C. elegans* βPIX/PIX-1 was shown to activate PAK-1 kinase activity in a GTPase-dependent (canonical) or GTPase-independent (non-canonical) manner [4,17,18]. M.

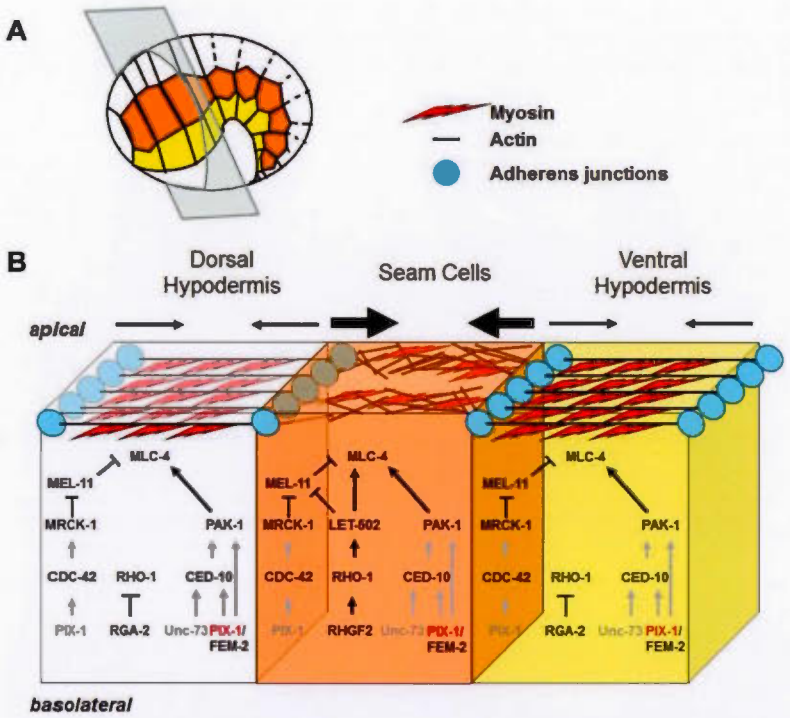

Figure 7. Model for signaling pathways controlling embryonic elongation. A) Schematic representation of an embryo during early elongation. Anterior is at the left and dorsal side on the top. Dorsal (white), lateral (orange) and ventral (yellow) hypodermal cells are represented. The blue plan indicates the location of the transversal sectioning of the hypodermal cells represented in panel B. B) Signaling pathways in the dorsal (white), lateral (orange) and ventral (yellow) hypodermis in the anterior part of the embryo during early elongation. In this model PIX-1 is expressed at similar level in all hypodermal cells of the anterior part of the embryo. While homogenous expression of PIX-1::GFP in these cells rescues elongation defects of *pix-1(gk416)*, we cannot exclude the possibility that *pix-1* may be required only in a subset of these cells. In PIX-1-expressing cells, PAK-1 is activated in a GTPase-dependant (through activation of CED-10 by PIX-1 and/or UNC-73) or in a GTPase-independent manner (by PIX-1 directly). LET-502 is activated only in seam cells through activation of RHO-1 by RHGF-2. PIX-1 may also activate MRCK-1 through CDC-42 upstream of MEL-11. Following this model, the contraction pressure applied on the actin cytoskeleton is similar in ventral and dorsal hypodermis and higher in seams cells. Arrows represent relative contraction forces within each cell.
doi:10.1371/journal.pone.0094684.g007

Labouesse's laboratory (IGBMC, Illkirch, France) showed using GTPase pull-down assays that the level of activation of the Rho GTPase CED-10/RAC was significantly lower in *pix-1(gk416)* than in *wt* embryos, suggesting that PIX-1 regulates CED-10/RAC activity during embryonic development [4]. We can then hypothesize, that PIX-1 may activate PAK-1 in a canonical manner through CED-10/RAC during early elongation as shown during late elongation [4]. Supporting this hypothesis, CED-10/RAC was located at both cell junctions and at the TEA within hypodermal cells in elongating embryos [4,20]. However, we cannot exclude the possibility that PIX-1 may also activate PAK-1 during early elongation in a GTPase-independant/non-canonical manner as shown during gonad morphogenesis [17,18]. Interestingly, the RHO/RAC specific GEF *unc-73*/TRIO was also shown to control early elongation in parallel to *mel-11/let-502* [10]. The allele used in that study, *rh40*, consists of a missense mutation that eliminates its exchange activity towards CED-10/RAC, RAC-2/RAC and MIG-2/RHOG without affecting its activity towards RHO-1/RHOA [15,21]. A UNC-73/TRIO - CED-10/RAC - PAK-1 pathway would then be an excellent candidate pathway controlling early elongation in parallel with a non-canonical PIX-1 – PAK-1 or a canonical PIX-1 - CED-10/RAC - PAK-1 pathway (Figure 7). Careful study will be required to test these hypotheses and to better understand the molecular mechanisms involving PIX-1 and controlling the activity of PAK-1 during early elongation.

pix-1 may control early elongation in a *pak-1*-dependent manner

While *pix-1* and *pak-1* may be part of the same pathway in parallel with *mel-11/let-502*, *mel-11(it26)*-inducing embryo rupturing is suppressed by *pix-1(gk416)* but not by *pak-1(ok448)* (Table 2). This intriguing genetic interaction between *pix-1* and *mel-11*/PP-1M during elongation is similar to that observed between *fem-2*/POPX2 and *mel-11*/PP-1M, another gene shown to be part of the *pak-1* pathway [16].

It was shown that the *fem-2* null allele induces weak larval arrest with non-elongated larvae similar to that observed in *pix-1* and *pak-1* mutants [10]. The *fem-2* mutant can also aggravate *mel-11*; *let-502* double mutants and suppress the *mel-11* rupturing phenotype. [10,16]. This suggests that *pix-1*, and *fem-2*/POPX2 function together to control early elongation in parallel with *mel-11/let-502*. Interestingly, the PP2C-like serine/threonine phosphatases, POPX2/Protein Phosphatase 1F, the closest homolog of FEM-2 in mammals, was shown to interact with β-Pix (ortholog of PIX-1) and to dephosphorylate and inactivate PAK1 (ortholog of PAK-1) kinase activity in mammalian cells [22]. It was suggested that the β-PIX - POPX2 complex controls the

activation/inactivation turnover of PAK1 in mammalian cells [22,23]. Considering that these proteins are highly conserved between *C. elegans* and mammals, we hypothesize that PIX-1, FEM-2/POPX2 and PAK-1 may have functional relationships similar to their homologs in mammals. Following this hypothesis, PIX-1 and FEM-2/POPX2 may control the activation/inactivation turnover dynamics of PAK-1 during early elongation. Considering that *pix-1* and *fem-2* mutant have similar interactions with *mel-11* and *let-502* during early elongation, this hypothesis suggests that a reduced or a sustained activation of PAK-1 alters similarly early elongation process. While this hypothesis would explain the genetic data obtained with *pix-1*, *fem-2* and *pak-1* mutants during elongation, it still remains to be confirmed through a careful analysis of a possible relationship existing between PAK-1 activation/inactivation dynamics and the regulation of myosin contraction in *C. elegans* hypodermal cells during early elongation.

pix-1 may control early elongation in a *pak-1*-independent manner

Considering the molecular analysis of *mel-11(it26)* allele [19], we cannot exclude the possibility that this allele may not be completely null even at 25.5°C. We can then hypothesize that *pix-1* may function together with *pak-1* in parallel with *mel-11* and may also function upstream of *mel-11* independently of *pak-1*. This would constitute an alternative explanation for the suppression of *mel-11(it26)*-inducing rupturing by *pix-1* but not by *pak-1* allele. Interestingly, the kinase MRCK-1/MRCK, whose mammalian ortholog, is an effector of CDC-42 [24] was shown to control early elongation upstream of *mel-11* [3]. CDC-42 being expressed in hypodermal cells during early elongation [20], and being also a potential target of PIX-1 GEF activity, we can hypothesize that PIX-1 may activate MRCK-1 through CDC-42 upstream of MEL-11 and may also activate PAK-1 in parallel with *mel-11/let-502* (Figure 7).

The *pix-1/pak-1* pathway mainly controls the constriction of the head of the embryos during early elongation

Observation of the head to tail morphology of the elongating embryo showed that the anterior part of the embryo at 1.2-fold stage is much wider than the posterior part. This suggests that contraction forces applied on the anterior part of the embryo is higher than in the posterior part at that stage. We showed that the mechanism leading to a faster reduction of the head width during early elongation is dependent on *pix-1*, *pak-1* and *let-502*/ROCK and that reduction of the tail width is dependent on *let-502*/ROCK but neither on *pix-1* nor on *pak-1*. This suggests that contraction forces controlled by *let-502*/ROCK are required for the embryo morphogenesis along the antero-posterior axis, while those controlled by the *pix-1/pak-1* pathway may mostly be required in the anterior part of the embryo. This also suggests that either the *pix-1/pak-1* pathway induces contractions mostly in the anterior part of the embryo, or this pathway is redundant with another pathway (in addition to *let-502/mel-11*) specifically involved in the control of contractions in the posterior part of the embryo.

Interestingly, we found that animal expressing PIX-1::GFP at a reduced level in the dorsal posterior cells present an elongation rate similar to *wt*. Higher expression of PIX-1::GFP in the dorsal-posterior cells is also shown to be detrimental for the elongation rate of embryos during early elongation. This suggests that the function of *pix-1* is required at a low level in the dorsal-posterior hypodermal cells to ensure optimal elongation rate. This supports the hypothesis that the *pix-1/pak-1* pathway may induce more contractions in the anterior part of the embryo than in the posterior part. However, this hypothesis will have to be tested through careful measurement of contraction forces induced by the *let-502/mel-11* and *pix-1/pak-1* pathways in individual sets of hypodermal cells during early elongation.

We also showed that loss of *let-502* function suppresses the increased head/tail width ratio observed in *pix-1* arrested larvae when compared to *wt* and that this suppression occurs only in embryos expressing an active *mel-11* (Figure 3D). These data support our observations that *let-502; pix-1* arrested larvae display *let-502* morphology, while *let-502; mel-11; pix-1* larvae display *pix-1* morphology (Table 2). To explain these results, we may hypothesize that loss of *let-502* may induce a severe reduction of contraction forces in hypodermal cells due to the activation of *mel-11*. This activated *mel-11* may then strongly suppress the contraction forces induced by the *pix-1/pak-1* pathway and consequently the difference of contraction forces applied on the head and tail during early elongation. According to this hypothesis, in absence of both *let-502* and *mel-11*, deletion of *pix-1* function is associated with the arrest of larvae displaying a similar increase of H/T width ratio than observed in single *pix-1(gk416)* mutants. These data confirm that MEL-11 function antagonizes both contraction forces induced by LET-502 and those induced by the PIX-1/PAK-1 pathway (Figure 7) [3,14].

In summary, our study demonstrates a function for *pix-1* during early elongation within the *pix-1/pak-1* pathway in parallel with *mel-11/let-502*. At that stage, *let-502* may drive the contraction forces leading the reduction of the embryo circumference along the antero-posterior axis, while the *pix-1/pak-1* pathway may mainly control the contraction forces applied on the anterior part of the embryo.

Methods

Strains and Culture Methods

Control N2 and other animals were maintained in standard conditions at 20°C [23]. Worm strains carrying the following mutations and markers: *pix-1(gk416) X, pix-1(ok982) X, pak-1(ok448) X, mcIs40 [lin-26p::ABDvab-10::mcherry + myo-2p::gfp]* and *mcIs50 [lin-26p::ABDvab-10::gfp + myo-2p::gfp]*, were obtained from the *Caenorhabditis Genetic Center* (CGC). Mutant strains were backcrossed at least 3 times against wild-type (*wt*) animals prior to analysis. Strains carrying *let-502(sb118) I, mel-11(it26) unc-4(e120)/mnC1 II* and *mel-11(it26) unc-4(e120) II; let-502(sb118) I*, were kindly provided by Dr Paul Mains (University of Calgary, Calgary, Canada). *mel-11(it26) unc-4(e120) II; let-502(sb118) I* were maintained at 25.5°C. *mel-11(it26) unc-4(e120) II; let-502(sb118) I; pix-1(gk416) X* and *mel-11(it26) unc-4(e120) II; let-502(sb118) I; pak-1(ok448) X* were generated after crossing *mel-11(it26) unc-4(e120) II; let-502(sb118) I* hermaphrodites with *pix-1(gk416) X* or *pak-1(ok448) X* males. Genotyping of F2 progeny was done through isolation of Unc F2 (*mel-11(it26) unc-4 (e120) II homozygotes)* at 15°C. Mutations in *pix-1* and *pak-1* genes were identified using Polymerase chain Reaction (PCR) and *let-502(sb118) I* homozygotes were identified through scoring of embryonic lethality (Emb) and larval arrest (Lva) phenotypes of populations grown at 18°C and 25.5°C.

Generation of Transgenic animals

pix(gk416); sajEx1[pix-1p::pix-1::GFP;rol-6(su1006)] animals were generated by injection. Translational PIX-1::GFP fusion construct (*pix-1p::pix-1::gfp*) was obtained from Dr Chen HJ's laboratory (University of California Davis, Davis, California, USA) [17] and

injected at 15 ng/µl with pRF4 (containing *rol-6(su1006)* at 50 ng/µl) in *pix(gk416)* animals. Rol transgenic animals were isolated and expression of PIX-1::GFP was assessed by fluorescent microscopy. *unc-119(ed3); pix-1(gk416); sajIs1[pix-1p::pix-1::gfp; unc-119^{R}]* was generated using biolistic bombardment. To do so, constructs were generated through amplification of the *pix-1* promoter (1.6 kb upstream of the initiation codon), amplification using reverse-transcription and PCR using thermoscript II (life technologies) kit of *pix-1* cDNA (from the ATG the codon in 5′of the endogenous stop codon, including the intron between exon 1 and 2). Both DNA fragments were inserted using gateway recombination in pDONRP4P1R and pDONR201 respectively and recombined together in pMB14. This construct was integrated by biolistic bombardment in *unc-119(ed3); pix-1(gk416)* strain, using a PDS-1000/He system with the Hepta adaptor (Bio-Rad) as previously reported [24]. *unc-119(ed3); pix-1(gk416); sajIs2[lin-26p::pix-1::GFP]* and *unc-119(ed3); pix-1(gk416); sajIs3[lin-26p::pix-1::GFP]* were independent, stable transgenic lines generated also using biolostic bombardment. It contains 5kb of the *lin-26* promoter *(lin-26p)*, the *pix-1* coding sequence including the intron between exon 1 and 2, and the GFP coding sequence in pMB14 vector. This construct was also integrated by biolistic bombardment in *unc-119(ed3); pix-1(gk416)* strain, using a PDS-1000/He system with the Hepta adaptor (Bio-Rad).

Transgenic animals expressing PIX-1::GFP together VAB-10(ABD)::mCherry were obtained through crossing *pix(gk416); sajEx1, unc-119(ed3); pix-1(gk416); sajIs1, unc-119(ed3); pix-1(gk416); sajIs2* and *unc-119(ed3); pix-1(gk416); sajIs3* hermaphrodites with *mcIs40[lin-26p::ABDvab-10::mcherry+myo-2p::gfp]* males. Stable lines expressing GFP, mCherry transgenes and carrying *pix-1(gk416)* allele were isolated from the F2 progeny.

Phenotyping mutant animals and 4-dimensional microscopy

To score Emb and Lva phenotypes, worms were synchronized by hypochlorite treatment. After synchronisation 10 20 worms were deposited on NGM agar with OP50 as a source of food Worms were allowed to lay eggs at 18°C or 25.5°C for 4 to 5 hours and were washed off the plate with M9 medium. After 24 and 48 hours dead eggs and arrested L1 larvae were counted and observed at high magnification. The stage of embryonic arrest was confirmed in mutant animals using four-dimension microscopy. Embryos dissected from adult hermaphrodites were mounted on 3% agarose pads in M9 buffer and coverslips were sealed with drawing gum (pébéo). Elongation was recorded using 4-dimensional microscopy (3D and time), which recorded a Z-stack every 2 minutes during 10 hours at 23 24°C using a Leica DM5500 microscope equipped with a 63X oil immersion objective upon differential interference contrast illumination (DIC). Images were captured using the Leica LAS AF imaging software. These recording were used to measure the duration of early elongation for at least 20 eggs from 1.2- to the end of early elongation identified as the moment when body-wall muscles start contracting, the length of the embryos at the end of early elongation, the width of the head (measured at equidistance from the tip of the nose to the pharynx-intestinal valve), the width of the tail (measured at equidistance from the pharynx-intestinal valve to the distal extremity of hyp10) at 1.2-fold and at the end of early elongation in the different mutant animals. These measurements were done using Leica LAS AF6000 imaging analysis tools. The reproducibility of these measurements was tested as detailed in the supplementary Figure 3. Length and head/tail width measurements were also done on mutant arrested larvae and wild-type (*wt*) L1 arrested by starvation after hypochlorite treatment. The head/tail ratio was calculated as the ratio of the head width with the tail width in µm per animal. The head (and tail) width reduction ratio was calculated as the ratio of the head width (or tail width) at 1.2-fold stage over the head width (or tail width) at the end of early elongation. Statistical significance was calculated using unpaired Student's T-test.

Immunostaining of embryos

For indirect immunofluorescence, embryos were fixed using 3% paraformaldehyde at room temperature for 10 minutes. Following washes with PBS (137 mM NaCl, 2.7 mM KCl, 4.3 mM Na_2HPO_4, 1.47 mM KH_2PO_4 Adjust to a final pH of 7.4.), embryos were incubated 10 minutes in cold methanol, and extensively washed with PBS. Fixed embryos were incubated overnight at 4°C with appropriate dilutions of primary antibodies in culture media (4X eggs salt, 0.5% Hepes 1M, 5% goat serum). Mouse anti-MH-27 antibodies (The Developmental Studies Hybridoma Bank, University of Iowa) were used at 1:10 dilution, rabbit anti-GFP antibodies were used at 1:500 (Invitrogen). After three washes with culture media (4X egg salt, 0.5% HEPES 1M, goat serum 5%), embryos were incubated at room temperature for 1 h with 1:200 dilution of either anti-mouse IgG conjugated to TRITC or anti-rabbit IgG conjugated to FITC (Jackson ImmunoResearch) in 1X-PBS. Embryos were washed three times with culture media and incubated with 100 ng/ml of DAPI for 1 minute at room temperature, washed with water, resuspended in 40 µl of Mowiol (sigma Aldrich) and mounted on slides.

Confocal fluorescence microscopy

The expression pattern of PIX-1::GFP in living animals was observed using a Nikon A1R confocal microscope with 100X oil CFI NA 1.45 Plan Apochromat λ objective. All images were captured with a pinhole size of 59.1 µm, with a calibration of 0.12 µm/pixel (radial resolution of 0.20 µm) and a Z-step of 0.15 µm. Images were captures using NIS-element software (Nikon). Deconvolution was done using Autoquant 3X, 3D deconvolution software. Orthogonal views, and fluorescence quantifications were generated using ImageJ software. For fluorescence quantification, individual Z-steps were extracted from Z-stacks recording of elongating embryos. DP, DA, LP, LA, VP, VA hypodermal cells were selected using ImageJ 'polygon selections' tool. Nuclei of cells in these areas were also selected using the same tool. The Raw intensities of selected areas were measured using area and gray value function. Raw Intensities of nuclei were subtracted to raw intensities of selected hypodermal sections. The pixel mean value was then calculated dividing this adjusted raw intensity by the area size selected excluding also size of nuclei. Intensity ratios and raw intensities were calculated and used using the resulting value. Comparison of raw intensities between different animals was done on image captured within a week, to limit the impact of laser fluctuation. This fluctuation was controlled through comparison of intensities obtained for the same sample at different days. Fluorescence intensity was compared on images captured using the same laser power and adjusted photomultiplier tube (PMT). Statistical significance of quantification was assessed using the unpaired student T-test. Spearman correlation coefficients and statistical tests for significance of correlation between two quantitative variables were calculated using spearman cor.test function in R (Bioconductor).

Supporting Information

Figure S1 Schematic representation of human (Hs) and *C. elegans* (Ce) PIX and PAKs. Modular structure has been

identified using the SMART tool (www.smart.org) or by alignment of consensus sequence using CLUSTALW. Binding-domains for protein partners reported in the literature are indicated. Proteins coded by *C. elegans* mutant alleles are indicated. * indicate the location of translation arrest. CH: calponin homology domain; SH3: src homology domain; DH: dbl homology domain; PH: Pleckstrin homology domain; PR: Proline Rich sequence, GBD: GIT-binding domain, CC: coil-coiled domain, ZB: PDZ binding domain, PBD: GTPase binding domain; Ser/Thr kinase: serine threonine kinase domain.
(TIF)

Figure S2 *pix-1(ok982)* and *pak-1(ok448)* arrested larvae present severe pharynx pumping defects. 48 hours after egg-laying, pharynx pumping rates were counted on arrested L1 animals and escaper L3 animals moving freely on a bacterial lawn. At least 10 animals per genotype were examined during 15-sec periods. N = 3. ** T-test p (mutant/N2)<0.001
(TIF)

Figure S3 Establishment of embryo width measurement as a robust metrics to characterize embryonic elongation. A) We tested the robustness and reproducibility of head width measurement of embryos. To do so, head width was measured five times on a given population of *wt* embryos at 1.2-fold stage (n = 12 embryos). Means and standard deviation were calculated and Brown-Forsythe test (using R statistical package) was used to test for homogeneity of variances among the five different groups of measurement. This test revealed no significant variance difference amongst the measurements (F-test p-value>0.5). B) The repeatability and batch effect of our measurements were assessed through measurement of the head width of *wt* embryos at 1.2-fold stage from 4D-recording done at three different days (n = 12 embryos). Means and standard deviation were calculated and Brown-Forsythe test was used to test for homogeneity of variances among the three different groups of measurements. This test revealed no significant variance difference amongst the measurements (F-test *p-value*>0.5). Similar results were obtained for tail width measurements and for measurement done at different stages of early elongation (data not shown). These data indicate that the significant differences observed between genotypes using head-width, tail-width and head/tail width ratio measurements are not due to measurement variability and batch effect.
(TIF)

Figure S4 PIX-1 is homogeneously distributed in the cytoplasm and at the cell periphery of hypodermal cells during early elongation. Confocal microscopy analysis of *pix-1(gk416)* embryos carrying *sajEx1[pix-1p::pix-1::gfp; rol-6]; mcIs40[lin-26p::ABDvab-10::mCherry + myo-2p::gfp]*. *PIX-1::GFP* is observed in B and E (green in C, F) and *VAB-10$_{ABD}$::mCherry* in A and D (red in C, F). Embryos are oriented anterior to the left and dorsal up. Enlarged views (lower panels) show areas indicated by white rectangles in upper panels. Apical and basolateral membrane are indicated by arrow and arrowhead, respectively (L, lower panel). Scale bars upper panels: 10 µm; lower panels 5 µm.
(TIF)

Figure S5 PIX-1::GFP intensity ratio are constant throughout early elongation. Dorsal-posterior/dorsal-anterior (DP/DA), lateral-posterior/lateral-anterior (LP/LA), ventral-posterior/ventral-anterior (VP/VA), dorsal-posterior/ventral (DP/V), dorsal-anterior/ventral (DA/V) and dorsal-anterior/lateral (DA/L) fluorescence intensity ratio were measured as detailed in methods and in Figure 5 in *pix-1(gk416); unc-119; sajIs2[lin-26p::pix-1::GFP,unc-119^{R}]* embryos during early elongation. Bar correspond to the mean and error bars to the standard deviation. * T-test<0.05
(TIF)

Figure S6 Only DP/DA ratio inversely correlates with the elongation rate of the embryos during early elongation. Scatter plot representing the relationship between the lateral-posterior/lateral-anterior (LP/LA), ventral-posterior/ventral-anterior (VP/VA), dorsal-posterior/dorsal-anterior (DP/DA) and dorsal-anterior/ventral (DA/V) intensity ratio of PIX-1::GFP and the elongation rate in µm/min during early elongation of *pix-1(gk416); sajEx1[pix-1p::pix-1::GFP, rol-6]* embryos (n = 20). The spearman correlation (R2) between the elongation rate and the PIX-1::GFP intensity ratio are indicated, as well as the *p-values* rejecting the null hypothesis being that the two values are not significantly correlated. Similar results were obtained from two independent transgenic lines.
(TIF)

Figure S7 High expression of PIX-1::GFP in dorsal-posterior hypodermis is detrimental for elongation rate of embryos. Dorsal-posterior/dorsal-anterior (DP/DA), lateral/ventral (L/V), dorsal-anterior/lateral (DA/L) and dorsal-posterior/lateral (DP/L) fluorescence intensity ratio were measured as detailed in methods and in Figure 5 in *pix-1(gk416); unc-119; sajIs2[lin-26p::pix-1::GFP;unc-119^{R}]* embryos elongating at a *wt*-rate (elongation≥288 nm/min) or elongating slower (elongation<288 nm/min) during early elongation. Bar correspond to the mean and error bars to the standard deviation. ** T-test p-value<0.01.
(TIF)

Acknowledgments

Thanks to Dr Paul Mains (University of Calgary, Calgary, Canada), to Dr Michel Labouesse (IGBMC, Illkirch, France) for sharing biological material. Thanks to Alexander Parker (university of Montreal, Montréal, Canada) for technical support for generation of transgenic animals by injection. Thanks to Dr Alisa Pickny (U. Concordia, Montréal, Canada) for discussions and helpful comments on the manuscript. Thanks to Claire Jacquelin, and Maria Corrimaya (UQAM, Montréal, Canada) for technical support. Some of the strains were provided by the *Caenorhabditis* Genetics Center, which is funded by NUH Office of Research Infrastructure Programs (P40 OD010440).

Author Contributions

Conceived and designed the experiments: EM SH SJ. Performed the experiments: EM SH BN MN. Analyzed the data: EM SH SJ. Contributed reagents/materials/analysis tools: EM SH MN BN KH. Wrote the paper: SJ EM SH.

References

1. Priess JR, Hirsh DI (1986) *Caenorhabditis elegans* morphogenesis: the role of the cytoskeleton in elongation of the embryo. Dev Biol 117: 156 173.
2. Keller R (2006) Mechanisms of elongation in embryogenesis. Development 133: 2291 2302.
3. Pickny AJ, Johnson JL, Cham GD, Mains PE (2003) The *Caenorhabditis elegans* nonmuscle myosin genes *nmy-1* and *nmy-2* function as redundant components of the *let-502*/Rho-binding kinase and *mel-11*/myosin phosphatase pathway during embryonic morphogenesis. Development 130: 5695 5704.

4. Zhang H, Landmann F, Zahreddine H, Rodriguez D, Koch M, et al. (2011) A tension-induced mechanotransduction pathway promotes epithelial morphogenesis. Nature 471: 99 103.
5. Ding M, Woo WM, Chisholm AD (2004) The cytoskeleton and epidermal morphogenesis in *C. elegans*. Exp Cell Res 301: 84 90.
6. Piekny AJ, Wissmann A, Mains PE (2000) Embryonic morphogenesis in *Caenorhabditis elegans* integrates the activity of LET-502 Rho-binding kinase, MEL-11 myosin phosphatase, DAF-2 insulin receptor and FEM-2 PP2c phosphatase. Genetics 156: 1671 1689.
7. Diogon M, Wissler F, Quintin S, Nagamatsu Y, Sookhareea S, et al. (2007) The RhoGAP RGA-2 and LET-502/ROCK achieve a balance of actomyosin-dependent forces in *C. elegans* epidermis to control morphogenesis. Development 134: 2469 2479.
8. Gally C, Wissler F, Zahreddine H, Quintin S, Landmann F, et al. (2009) Myosin II regulation during *C. elegans* embryonic elongation: LET-502/ROCK, MRCK-1 and PAK-1, three kinases with different roles. Development 136: 3109 3119.
9. Takai Y, Sasaki T, Matozaki T (2001) Small GTP-binding proteins. Physiol Rev 81: 153 208.
10. Lin L, Tran T, Hu S, Cramer T, Komuniecki R, et al. (2012) RHGF-2 is an essential Rho-1 specific RhoGEF that binds to the multi-PDZ domain scaffold protein MPZ-1 in *Caenorhabditis elegans*. PLoS One 7: e31499.
11. Spencer AG, Orita S, Malone CJ, Han M (2001) A RHO GTPase-mediated pathway is required during P cell migration in *Caenorhabditis elegans*. Proc Natl Acad Sci U S A 98: 13132 13137.
12. Vanneste CA, Pruyne D, Mains PE (2013) The role of the formin gene *fhod-1* in *C. elegans* embryonic morphogenesis. Worm 2:3, e25040
13. Lundquist EA, Reddien PW, Hartwieg E, Horvitz HR, Bargmann CI (2001) Three *C. elegans* Rac proteins and several alternative Rac regulators control axon guidance, cell migration and apoptotic cell phagocytosis. Development 128: 4475 4488.
14. Lucanic M, Cheng HJ (2008) A RAC/CDC-42-independent GIT/PIX/PAK signaling pathway mediates cell migration in *C. elegans*. PLoS Genet 4: e1000269.
15. Piekny AJ, Wissmann A, Mains PE (2000) Embryonic morphogenesis in *Caenorhabditis elegans* integrates the activity of LET-502 Rho-binding kinase, MEL-11 myosin phosphatase, DAF-2 insulin receptor and FEM-2 PP2c phosphatase. Genetics 156: 1671 1689.
16. Peters EC, Gossett AJ, Goldstein B, Der CJ, Reiner DJ (2013) Redundant canonical and noncanonical *Caenorhabditis elegans* p21-activated kinase signaling governs distal tip cell migrations. G3 (Bethesda) 3: 181 195.
17. Chen W, Chen S, Yap SF, Lim L (1996) The *Caenorhabditis elegans* p21-activated kinase (CePAK) colocalizes with CeRac1 and CDC42Ce at hypodermal cell boundaries during embryo elongation. J Biol Chem 271: 26362 26368.
18. Steven R, Kubiseski TJ, Zheng H, Kulkarni S, Mancillas J, et al. (1998) UNC-73 activates the Rac GTPase and is required for cell and growth cone migrations in *C. elegans*. Cell 92: 785 795.
19. Koh CG, Tan EJ, Manser E, Lim L (2002) The p21-activated kinase PAK is negatively regulated by POPX1 and POPX2, a pair of serine/threonine phosphatases of the PP2C family. Curr Biol 12: 317 321.
20. Huang R, Lian JP, Robinson D, Badwey JA (1998) Neutrophils stimulated with a variety of chemoattractants exhibit rapid activation of p21-activated kinases (Paks): separate signals are required for activation and inactivation of paks. Mol Cell Biol 18: 7130 7138.
21. Wissmann A, Ingles J, Mains PE (1999) The *Caenorhabditis elegans mel-11* myosin phosphatase regulatory subunit affects tissue contraction in the somatic gonad and the embryonic epidermis and genetically interacts with the Rac signaling pathway. Dev Biol 209: 111 127.
22. Wilkinson S, Paterson HF, Marshall CJ (2005) Cdc42-MRCK and Rho-ROCK signalling cooperate in myosin phosphorylation and cell invasion. Nat Cell Biol 7: 255 261.
23. Brenner S (1974) The genetics of *Caenorhabditis elegans*. Genetics 77: 71 94.
24. Berezikov E, Bargmann CI, Plasterk RH (2004) Homologous gene targeting in *Caenorhabditis elegans* by biolistic transformation. Nucleic Acids Res 32: e40.

Annexe 2 : Article publié :

Martin, E., Rocheleau-Leclair, O. et Jenna, S. (2016).Novel metric to characterize embryonic elongation of the nematode *Caenorhabditis elegans. J. Vis. Exp.* (109), e53712.

jove Journal of Visualized Experiments www.jove.com

Video Article

Novel Metrics to Characterize Embryonic Elongation of the Nematode *Caenorhabditis elegans*

Emmanuel Martin[1], Olivier Rocheleau-Leclair[1], Sarah Jenna[1]

[1]Department of Chemistry, Pharmaqam, Université du Québec à Montréal

Correspondence to: Sarah Jenna at jenna.sarah@uqam.ca

URL: http://www.jove.com/video/53712
DOI: doi:10.3791/53712

Keywords: Neuroscience, Issue 109, morphogenesis, *Caeanorhabditis elegans*, elongation, 4-D microscopy, flow cytometry, embryonic development

Date Published: 3/28/2016

Citation: Martin, E., Rocheleau-Leclair, O., Jenna, S. Novel Metrics to Characterize Embryonic Elongation of the Nematode *Caenorhabditis elegans*. *J. Vis. Exp.* (109), e53712, doi:10.3791/53712 (2016).

Abstract

Dissecting the signaling pathways that control the alteration of morphogenic processes during embryonic development requires robust and sensitive metrics. Embryonic elongation of the nematode *Caenorhabditis elegans* is a late developmental stage consisting of the elongation of the embryo along its longitudinal axis. This developmental stage is controlled by intercellular communication between hypodermal cells and underlying body-wall muscles. These signaling mechanisms control the morphology of hypodermal cells by remodeling the cytoskeleton and the cell-cell junctions. Measurement of embryonic lethality and developmental arrest at larval stages as well as alteration of cytoskeleton and cell-cell adhesion structures in hypodermal and muscle cells are classical phenotypes that have been used for more than 25 years to dissect these signaling pathways. Recent studies required the development of novel metrics specifically targeting either early or late elongation and characterizing morphogenic defects along the antero-posterior axis of the embryo. Here, we provide detailed protocols enabling the accurate measurement of the length and the width of the elongating embryos as well as the length of synchronized larvae. These methods constitute useful tools to identify genes controlling elongation, to assess whether these genes control both early and late phases of this stage and are required evenly along the antero-posterior axis of the embryo.

Video Link

The video component of this article can be found at http://www.jove.com/video/53712/

Introduction

For nearly 50 years the nematode *Caenorhabditis elegans* established itself as a powerful model to study important questions in development, neurobiology, evolution, host-pathogen interactions, *etc.*[1] The strength of this model in the study of development lies in: its short life cycle of 3 days; the ease with which these animals can be genetically altered; its transparency that enables the observation of cell displacement and morphology in living animals and its development that is mostly extra-uterine. The developmental stages of the nematode involve embryogenesis and four larval stages (L1 to L4), followed by adulthood. During embryonic development, epidermal morphogenesis drew considerable attention for its ability to enable a better understanding of how epithelial cells migrate as a group, how they reorganize their junctions and modify their individual morphology as well as their relative positioning within a functional epithelium. Epidermal morphogenesis is divided into four stages: dorsal intercalation consisting in the reorganization of dorsal epidermal cells, referred to as the hypodermis; ventral enclosure, consisting in migration of ventral hypodermal cells towards the ventral midline thus encasing the embryo in an epithelial cell monolayer; early and late elongation transforming the bean-shaped embryo into vermiform larvae. Following morphogenesis, embryo hatch and L1 larvae start feeding using available bacteria in their immediate environment.

Embryonic elongation is therefore a late phase of the embryonic development. It consists of the extension of the embryo along its longitudinal axis and a reduction of its transverse diameter. This involves a dramatic modification of the shape of the hypodermal cells. Elongation is divided into an early and a late phase. The early phase starts at the comma stage and ends when body-wall muscles start contracting at 1.75-fold stage in *wild-type* (*wt*) embryos — corresponding to embryos that are 1.75-fold in length compared to non-elongated embryos. Morphogenic processes occurring at that stage are mainly driven by contraction of filamentous actin bundles (FBs) located at the apical pole of hypodermal cells that drive their elongation along the antero-posterior axis of the embryo[2]. Contraction of FBs is control by phosphorylation of myosin-light chains by three kinases LET-502/ROCK, MRCK-1 and PAK-1 [5]. The late phase of the elongation, starts when body-wall muscles become functional and start contracting. It involves mechanotransduction signaling from the body-wall muscles to the dorsal and ventral hypodermal cells and ends when animals hatch[3].

Elongation defects are generally characterized by the percentage of animals dying as embryos (Embryonic lethality; Emb) and those arresting their development as L1 larvae (Larval arrest phenotype; Lva) and being significantly shorter than *wt*. Identification of the stage of developmental arrest requires microscopic observation of dead embryos and arrested Larvae[3-6].

It was recently shown that several genes, such as the Cdc42/Rac regulator and effector *pix-1* and *pak-1*, control morphogenic processes during both early and late elongation[3,7]. We also recently showed that morphogenic processes differ along the antero-posterior axis of the embryos during early elongation[3,7]. These findings motivated the development of novel metrics specifically targeting early or late elongation stages and other metrics enabling the characterization of the morphology of embryos along their antero-posterior axis during early elongation.

These novel methods consist in measuring the length of embryos at the beginning and at the end of early elongation as well as the width of their heads and tails.[7] Two protocols were also developed to measure the length of newly hatched larvae, synchronized at L1 stage[7].

The eggshells of the embryos protect them against alkaline hypochlorite treatment while larvae, adults and bacteria present in the culture media are dissolved by the treatment. This treatment is then used to purify embryos from a non-synchronized population containing a majority of well-fed adults[8]. Food restriction is used to synchronize newly hatched larvae. Measuring the length of these larvae is then used to detect elongation defects. This measurement is preferred over the measurement of arrested larvae on culture plates because larvae that hatch from non-fully elongated embryos can recover to "normal length" when feeding but will maintain their reduced size when arrested in the absence of food.

Here, we present detailed protocols enabling the measurement of the length of elongating embryos as well as the width of their head and tail using time-lapse DIC microscopy and image analysis (Protocol 1). We also provide detailed protocols to measure the length of synchronized larvae using image analysis (Protocol 2) and Flow-Cytometry (Protocol 3).

Protocol

1. Characterization of Early Elongation Defects in *WT* and Mutant Animals

1. **Mounting Embryos for Normarski DIC Microscopy**
    1. Prepare the following culture media and material:
        1. M9 Buffer, dissolve 12.8 g/L $Na_2HPO_4 \cdot 7H_2O$, 3 g/L KH_2PO_4, 5 g/L NaCl, 0.25 g/L $MgSO_4 \cdot 7H_2O$ in distilled water and autoclave to sterilize.
        2. NGM plates, dissolve 3 g/L NaCl, 16 g/L agar, 2.5 g/L bactopeptone in ddH_2O. Autoclave and add 1 mM $MgSO_4$, 1 mM $CaCl_2$, 1 mM phosphate buffer and 5 µg/ml cholesterol. Pour 6 ml of NGM per 60 mm dishes. Allow the medium to solidify for 24 hr at room temperature. Add a few drops of a saturated culture of *E. coli* OP50 bacteria grown in Luria broth (LB). Let the bacteria grow for 48 hr and store the plates at 4 °C.
        3. To generate the worm pick, mount a 0.01" diameter platinum wire on a short Pasteur pipette. Fasten the platinum wire to the extremity of the glass pipet by heating this extremity with a benzene burner. Flatten the extremity of the wire to generate a sort of shovel.
    2. Grow the worm strain on 60 mm NGM plates with OP50 at 20 °C.
       NOTE: Thermosensitive alleles may require growing the animals at non-permissive temperatures at up to 25.5 °C. Plates should contain many young adults and still plenty of food in order to pursue the protocols.
    3. Place a microscope slide between two spacer slides covered by two layers of masking tape (**Figure 1A**).
    4. Prepare a 3% agarose solution (weight/volume) in M9 buffer by dissolving 0.6 g of agarose powder in 20 ml M9 buffer by heating in the microwave during 30 sec. Allow the solution to cool down for 5 min.
       NOTE: The agarose solution can be used for a few days after melting in a microwave. It can also be aliquoted and stored at 4 °C for weeks.
    5. Place a drop of hot 3% agarose solution on the glass slide located between the two spacer-slides. Avoid forming bubbles.
    6. Rapidly cover the agarose with another slide as shown in **Figure 1B** and press down gently. The top slide will flatten the agarose drop and generate a pad with the thickness of two layers of masking tape.
    7. Allow the agarose to solidify for at least 1 min at room temperature or until the embryos are ready to be transferred to the pad.
    8. Using a worm pick, transfer 20 to 30 well fed young adults from the NGM-plate into a micro-centrifuge tube containing 400 µl of M9 buffer.
    9. Allow the worms to sediment by gravity for approximately 5 min and remove the supernatant using a micropipette. This step aims to remove the maximum of bacteria picked with the nematodes.
    10. Add 200 µl of M9 buffer to each tube.
    11. Using a Pasteur pipette, transfer the content of the tube (buffer and nematodes) to a watch glass.
    12. Use one or two 25G 5/8" needles to cut the animals at the mid-body section (between the spermatheca and the vulva).
        NOTE: A scalpel blade can also be used as an alternative to needle(s). Do this on swimming nematodes and may require some practice. The idea is to use needles as scissors or as a knife depending how many needles are used. Once the animals are cut open, hermaphrodites release their embryos into the buffer.
    13. Concentrate embryos at the center of the watch glass through generation of a circular vortex within the liquid.
    14. Remove most of the M9 from the watch glass using a micropipette. Leave approximately 30 µl of M9 with the embryos.
    15. Remove the slide covering the agarose pad (**Figure 1B**) by sliding it off the pad.
    16. Cut the pad with a razor blade in order to be able to completely cover it with a coverslip (**Figure 1C**).
    17. Using a Pasteur pipette, transfer all the embryos (and worm debris) onto the agarose pad.
    18. Group the embryos at the center of the pad using an eyelash glued at the extremity of a tip used for 200 µl micropipettes.
    19. Slowly place a coverslip on the pad avoiding bubble formation and seal it.
        NOTE: Several sealers can be used. We use drawing gum found in art and craft stores (usually used as masking gum for aquarelle painting). This gum is used because it is hydrophilic and solidifies reasonably fast and is not toxic for the worms. Slides can also be sealed with nail polish or VALAP (mixture made of Vaseline, Lanolin and Parafin wax).
    20. Allow the drawing gum dry for approximately 15 min.
2. **Recording Early Elongation using Four-dimensional Normarski DIC Microscopy**

NOTE: The objective of this step is to record early elongation from comma to the beginning of late elongation — defined as the moment when the body-wall muscles start contracting. We also aim to record more than one embryo at the time. Eight hours of recording are usually required to record early elongation for a group of non-synchronized embryos.

1. Place the mounted-slide on the stage of a microscope. Ensure that the microscope is equipped with 10X and 60X objectives as well as DIC lenses, prism, camera and capture software enabling time-lapse microscopy and generation of Z-stacks (automated Z-platform).
   NOTE: ensure that the temperature is constant between 20 and 23 °C in the microscopy room. A heating-cooling chamber may be required on the microscope stage, especially when using thermosensitive mutants.
2. Identify a group of embryos at pre-morphogenesis stages using the 10X objective.
3. Once located, slide off the 10X objective and add a drop of oil immersion on the slide.
4. Using the 60X objective, identify the top and the bottom of embryos to setup the Z-stack imaging parameters.
   NOTE: Do not hesitate to set the Z-stack larger than the thickness of the embryos. Set the distance between two adjacent planes as 0.8 µm. This will enable to cover the total depth of the embryos in 35 to 50 Z-plans.
   NOTE: If the microscope contains an automated xy platform, embryos located at different locations of the pad could be recorded simultaneously. To do so, record xy coordinates of each location on the pad you wish to analyze during the course of the experiment. Make sure to select the xy when setting the recording parameter and follow the rest of the protocol as indicated. Thin Z-sectioning of the embryo during recording is not necessarily required for the measurements detailed in this protocol. Recording embryonic development of *wt* and mutant animals with the maximum resolution is however a good practice in order to build a library of recordings able to support additional analyses.
5. Set up the time-lapse with 2 min intervals between two acquisitions lasting 8 hr.
   NOTE: The exposure time will depend on the light intensity set for the microscope. Cell movement during early elongation is very slow; exposure-time could be approximately one frame per second or less. If the embryos are at early morphogenesis stages (dorsal intercalation, ventral enclosure), early elongation would be recorded within 1 hr. Make sure light shutter is closed between each acquisition.
6. Run the acquisition and save it.

3. **Measurement of Early Elongation Defects using Image Analysis**
   1. Open Fiji-ImageJ software (v1.48o – http://fiji.sc/Fiji).
   2. In the menu select Analyze/Set Measurements, select Perimeter. For each embryo, adjust the Z-scale bar to focus on the pharynx of the embryo as shown in **Figure 2A**. This will ensure that you focus on the center of the embryo.
   3. To measure the length of the embryo, adjust the time scale bar to have the embryo of interest at the start of the early elongation (comma stage; **Figure 2A**). Note the time ("Time-beginning").
   4. Choose the segmented line tool. Draw a segmented line from the tip of the mouth of the embryo up to the tip of its tail following the midline of the embryo (**Figure 2A**). Using the menu tab Analyze/Measure, obtain the length of the drawn line ("Length beginning").
   5. Repeat this measurement for the same embryo at the end of early elongation (moment when muscles start contracting). Note the time ("Time-end") and measure the length of the embryo ("Length-end") as detailed above (**Figure 2B**).
   6. Calculate the duration (D) of early elongation and the length increase (L) during this stage as follows:
      D = "Time-end"-"Time-beginning"
      L = "Length-end" -"Length-beginning"
   7. To measure the head width, adjust the time scale bar to have an embryo at the stage of interest (1.2-fold stage or end of early elongation). Choose the straight-line tool. Draw the transversal (dorso-ventral axis) midline of the head. This section is the thickest part of the embryo (**Figure 2C**). Using the menu Analyze/Measure, obtain the length of the line corresponding to the head width.
   8. At the same time point, repeat this step by drawing the transversal midline of the tail (Mid-line between the intestinal valve and the tip of the tail; **Figure 2C**) and measure it to obtain the tail width.
      NOTE: Use this measurement to compare embryos at the same stage across different phenotypes. To ensure the reproducibility of this measurement, make sure to find a location located around the mid-line of the tail of the animal that can easily be recognized from one animal to another.
   9. To calculate the head to tail width ratio, divide the head width by the tail width.

2. Characterization of Late Elongation Defects Using Image Analysis

1. **Synchronization of L1 Larvae using Alkaline Hypochlorite Treatment**
   1. From a non-starved 60 mm plate containing many gravid adults, collect all worms in a micro-centrifuge tube by washing the nematodes off the plate with 1 ml of M9 buffer using a Pasteur pipette.
   2. Sediment nematodes at 3,500 x g for 3 min at room-temperature and remove the supernatant using a micropipette without disturbing the worm pellet.
   3. Add 1 ml of hypochlorite solution to each tube (0.4 M hypochlorite, 0.5 M NaOH) and shake for 3 min.
      NOTE: Alkaline hypochlorite solution should be freshly prepared and embryos in this solution should be agitated gently but continuously to optimize dissolution of the adults and oxygenation of the embryos. After 3 min agitation, most adults should release their eggs into the solution.
   4. Spin at 3,500 x g for 3 min at room-temperature and quickly remove the supernatant using a micropipette without disturbing the pellet.
   5. Wash four times with 1 ml of M9 buffer followed by centrifugation at 3,500 x g for 3 min.
   6. After the fourth wash, remove the supernatant and resuspend eggs in 700 µl of M9 buffer without pipetting up the eggs (as the eggs would stick to the plastic of the tip).
   7. Tape the tube on a 3-mm orbital shaker placed in an incubator at the appropriate growth temperature and shake at 600 rpm overnight.

2. **Length Measurement of Synchronized Larvae**

1. Centrifuge arrested L1 larvae at 3,500 x g for 3 min at room-temperature and remove the supernatant. Resuspend the larvae in 100 µl of M9 buffer and transfer them onto an agarose pad using a Pasteur pipette (agarose pads should be prepared as described at section 1.1.2 to 1.1.8). Place a coverslip on the pad.
   NOTE: The pad does not need to be sealed with gum for this experiment that involves short acquisition.
2. Use a 10X objective and phase contrast illumination to measure the length of the larvae if a high resolution camera is used. Increase the intensity of the light to be able to capture images within a few milliseconds and consequently obtain a clear picture of the larvae (**Figure 2D**).
   NOTE: While the swimming trashes of larvae are reduced by the agarose pad, they are still moving. Therefore, fast recording is essential to obtain a clear image.
3. Open Fiji-ImageJ and repeat step 1.3.1. To measure the length of larvae, choose the segmented line tool. Draw a segmented line from the tip of the head up to the tip of the tail following the midline of the larvae (**Figure 2D**, right panel).
4. Using the menu Analyze/Measure, obtain the length of the drawn line corresponding to the length of the larvae in micrometer.

3. Characterization of Late Elongation Defects Using Flow Cytometry

1. **Synchronize Larvae**
   1. Purify embryos using the alkaline hypochlorite treatment as described in section 2.1 from full 100 mm plates of well-fed young adults and let the embryo hatch and the L1 arrest in M9 buffer for 16 to 24 hr at 20 or 25.5 °C depending on the strain analyzed.
      NOTE: One full plate of well-fed adults per strain is sufficient for the analysis described below.

2. **Calibration of the Worm Sorter**
   NOTE: The flow cytometer used here is a large particle flow cytometer (hereafter referred to as the worm sorter). The worm sorter includes a 670 nm red diode laser, which is located in front of an extinction detector. The worm sorter also contains a multi-line argon laser for fluorescent excitation. The standard instruments have three photomultiplier tubes (PMT) fluorescence detectors used to detect fluorescence emissions in the green, yellow, and red regions of the spectrum. In the protocol described here, TOF will be used to measure the size of the larvae, the red channel will be used to identify dead worms that will be stained with Propidium Iodide (PI). GP (General Purpose) High Fluorescence Control Particles used to calibrate the instrument and as an internal control in our experiment display high fluorescence in green, yellow and red. They will be the only objects in the sample analyzed with high emission detected in the green channel and will subsequently be identified based on this characteristic.
   NOTE: Living animals are identified based on the absence of fluorescence in the Green and Red channel as well as on the TOF. Autofluorescent emission from the gut of the larvae is not detectable at L1 stage.
   1. Switch on the laser block, the computer, the compressor and the worm sorter instrument. Press the START button on the opened worm sorter software as indicated in the instruction manual of the instrument.
   2. Observe the argon laser control pop-up window. Select RUN mode and wait as the laser powers reach 10 ± 1 mW. Select DONE on the laser control window.
   3. Set the sheath and the sample pressures to 5.10 ± 0.02 and 5.51 ± 0.01 respectively. Allow the pressure to equilibrate for at least 15 min and click the PRESSURE OK check box.
      NOTE: The flow rate depends on the sheath and the sample pressures.
   4. Make sure to eliminate all bubbles present in the flow channel tubules between the sample cup and the analyzing chamber. To do so, click ACQUIRE and gently flick the tubule until no bubble are acquired (as seen in the acquisition window).
   5. Setup of all parameters for fluorescent and TOF measurement and detection as follows:
      1. Set the scales for TOF, Ext, Green, Yellow and Red to 256. Set gain as described in **Table 1**. Set PMT Control at 700 for Green and Yellow and to 900 for Red.
         NOTE: Two excitation filters are available (488 nm and 514 nm) and can be used to excite either Green fluorescent protein (GFP) or Yellow fluorescent protein (YFP) or any fluorochromes excited at these wavelengths with the multiline argon laser. Appropriate filters need to be inserted in the filter chamber of the equipment. We used the 488 nm filter for the following experiment.
   6. To calibrate the worm sorter, select "run control particles" in tool menu. Put 20 ml of 1x GP (General Purpose) High Fluorescence Control Particles in the cup (these particles are fluorescent particles of precise size, sold by the cytometry manufacturer to calibrate their instrument).
   7. Click on ACQUIRE button to begin sheath and sample flow.
      NOTE: Expect a mean related to the control particle distribution of 21 ± 6 and a coefficient of variation around that mean (C.V.) ≤11. If the C.V. is >11 and the mean is >27 try to clean the tubules by clicking several times on the clean button or by flicking the flow channel.

3. **Acquisition of Animal TOF**
   NOTE: Light scatters when an object passes in the flow cell between the laser source and the extinction detector. The time it takes for the light to be scattered by the flying object (time of flight, TOF) is used to measure the axial length of the object. The extent of light masked by the object (extinction, EXT) is used as a measure of its opacity/optical density.
   1. Place 10 µl of synchronized wild-type (*wt*) L1 in a watch glass and estimate the percentage of dead-eggs using a dissecting microscope.
      NOTE: Synchronized L1 displaying high Emb (higher than 20%) in *wt* should not be used for further analysis.
   2. Transfer synchronized L1 from the microcentrifuge (approximately 700 µl of M9 containing L1) to a 15 ml conical tube. Add propidium iodide (PI) at a final concentration of 10 µg/ml (dilution 1/100th from a 1 mg/ml stock solution) and incubate for 30 min at room temperature.
      NOTE: Dead eggs and larvae will be stained using PI and detected as highly fluorescent objects using the red channel.
   3. Add 10 ml of M9 buffer to dilute stained populations. Take 5 ml of the diluted populations and dilute them four times by adding 15 ml of M9. Place this dilution in the sample cup.
   4. Run the sample flow by clicking ACQUIRE and observe the flow rate.

Measurement of the length of the embryos, as well as the width of their head and tail was done on *wt* and mutant embryos carrying null or thermosensitive strong loss-of function alleles for genes controlling early elongation: *pix-1(gk416)*; *pak-1(ok448)* and *let-502(sb118ts)*[7]. We measured the head/tail (H/T) width ratio of *wt* and mutant embryos at the beginning (1.2-fold stage) and at the end of the early elongation at non-permissive temperatures (**Figure 4C** left and right panel respectively). While at the beginning of early elongation there was no change- or a reduced H/T ratio was observed in *pix-1*, *pak-1* and *let-502* mutants when compared to *wt* animals (1.2-fold stage, **Figure 2C**, left panel), at the end of early elongation all three mutants showed a significantly higher H/T ratio than *wt* embryos (*t*-test *p*-values < 0.006; **Figure 4C**; right panel). This demonstrated that *pix-1*, *pak-1* and *let-502* mutant embryos display abnormal antero-posterior morphology at the end of early elongation. Further analysis comparing head width and tail width between 1.2-fold stage and the end of early elongation, using the same measurement parameters revealed that the head width is less reduced in *pix-1*, *pak-1* and *let-502* mutants while the tail width reduces significantly less in *let-502* mutants only [7]. This revealed that *let-502* controls morphogenic processes similarly along the antero-posterior axis of the embryo, while *pix-1* and *pak-1* control morphogenic processes occurring mainly at the anterior part of the embryo[7]. The length difference between the embryos at the end versus the beginning of early elongation (**Figure 4D**) was also measured. We found that early elongation was significantly reduced in *pix-1*, *pak-1* and *let-502* mutants when compared to *wt* suggesting that alteration of the anterior morphogenesis in *pix-1* and *pak-1* mutants alone is sufficient to significantly reduce the elongation of the embryo.

Protocol 2 and 3 were used to assess the length of arrested larvae in *wt* and mutant backgrounds. The length of these larvae was assessed using both image analysis (Protocol 2)[7] and flow-cytometry (Protocol 3; unpublished data). Measurements of larvae length using image analysis results in absolute measurements of animals' length in micrometers in a robust and highly reproducible manner (**Figure 5A**). This analysis revealed that synchronized mutant larvae display significantly reduced length when compared to *wt* (**Figure 5A**)[7]. Measurement of these larvae using the flow-cytometry based protocol (Protocol 3) gave comparable results (**Figure 5B**). However, it should be noted that the large number of larvae measured using the latter approach significantly increased the statistical robustness of genotype comparison (*t*-test *p*-values $<10^{-24}$). Based on these findings, the flow-cytometry approach may be a better choice over image analysis in order to characterize mutant animals displaying very subtle elongation defects.

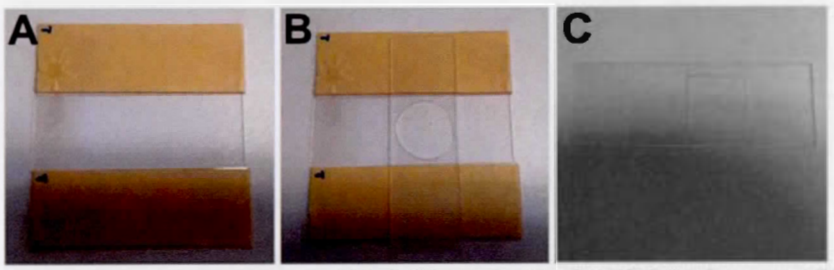

Figure 1. Preparation of an Agarose Pad. A, Microscope slide placed between two spacer-slides covered by two layers of masking tape. **B,** The agarose pad is covered with another slide supported by the two spacer-slides. **C,** The final shape and size of the agarose pad after cutting with a razor blade to fit the coverslip. Please click here to view a larger version of this figure.

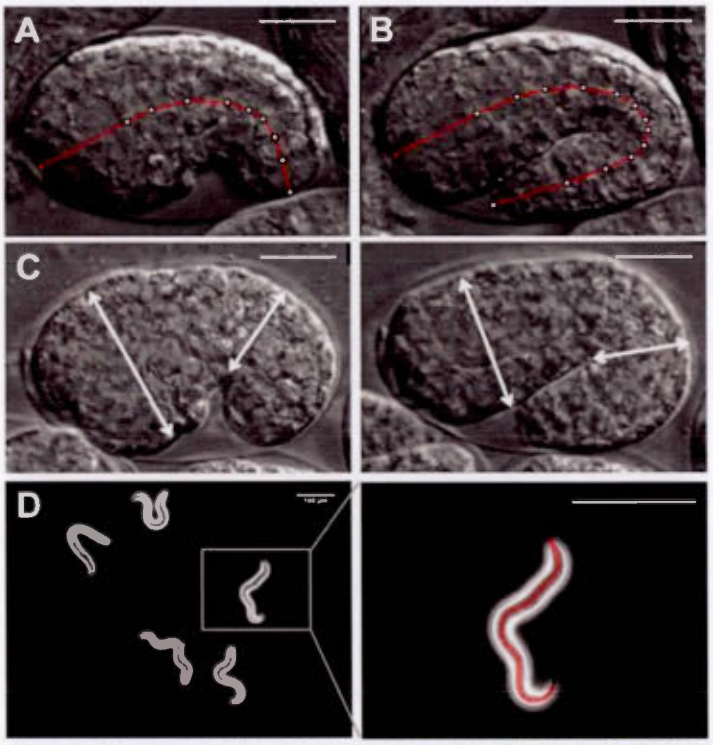

Figure 2. Measurement of Early and Late Elongation Defects. A - B, Measurement of the length of an embryo at comma stage (A) and at the end of early elongation (B). The red line, used to measure the embryos was drawn using the segmented line tool of ImageJ. **C,** Head and tail width are measured in embryos at 1.2-fold stage (left) and at the end of early elongation (right). Arrows represent the localization of measured areas (modified from Martin *et al.*, 2014). Scale bar: 20 µm. **D,** Length of Larvae is measured for synchronized L1-larvae. Right panel is an enlarged view of the captured image (left). The red line was drawn using the segmented line tool of ImageJ. It is used to measure the length of the larva. Scale bar: 100 µm. Please click here to view a larger version of this figure.

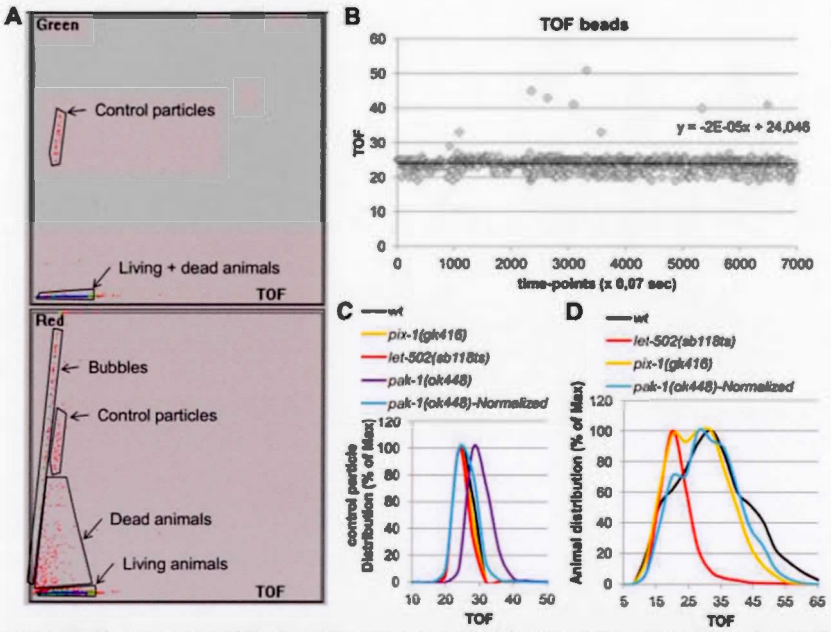

Figure 3. Measurement of the Length of Synchronized Larvae Using Flow-cytometry. A, Gating and sorting window of COPAS Biosort showing Green and Red emission of control particles, bubbles, dead and living animals with respect to their Time-Of-Flight (TOF). **B,** TOF of control particles at different time points for a representative experiment. The slope of the linear function of TOF versus time is around 10^{-5}, indicating that TOF of control particles is constant over time throughout the experiment. **C,** Distribution of control particle TOFs expressed as a percentage of maximal value of distributions. Non-normalized and normalized control particle distributions are represented for *pak-1(ok448)*. Other distributions are not normalized. **D,** distribution of TOFs for living animals expressed as a percentage of the maximal value of the distributions. TOFs are not normalized on control particles except for *pak-1(ok448)* as indicated. Please click here to view a larger version of this figure.

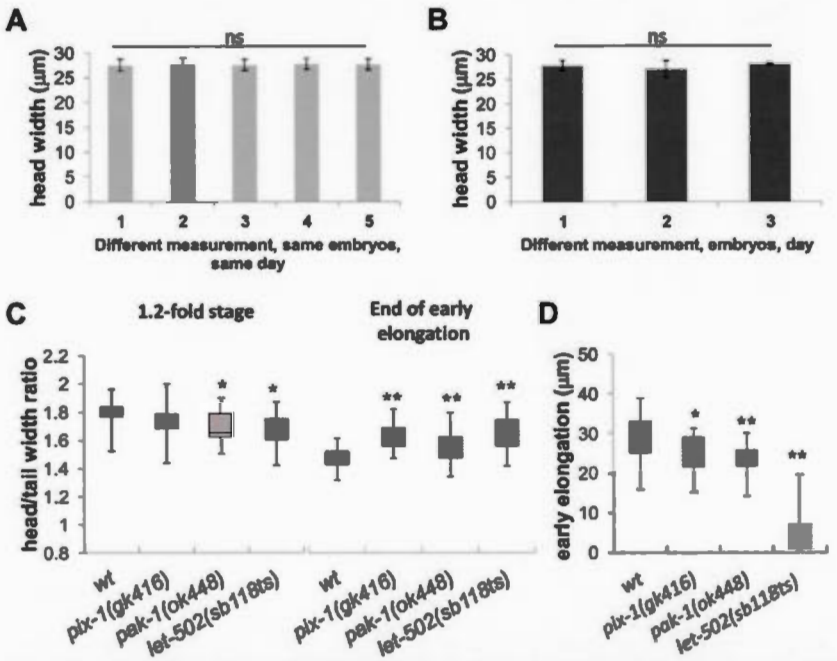

Figure 4. *Pix-1, Pak-1* and *Let-502* Mutants Present Early Elongation Defects. A - B, Reproducibility and robustness assessment of head width measurements. **A,** Five independent measurements of the head width for *wt* embryos at 1.2-fold stage (n = 12 embryos). Means and standard deviations (error bars) are indicated. Non significant (ns) differences between measurements were computed using the Brown-Forsythe test (using R statistical package) (F-test *p-value* > 0.5). **B,** Head width measurement for *wt* embryos at three different days (n = 12 embryos). Means and standard deviations are indicated as well; there was no significant difference in variance across the measurements (ns; Brown-Forsythe F-test *p*-value > 0.5). **C,** Distributions of head/tail width ratio at 1.2-fold stage (left panel), at the end of early elongation (right panel) in *wt*, *pix-1(gk416)*, *pak-1(ok448)* and *let-502(sb118ts)* mutants at 23 - 24 °C. Note that mothers of *let-502ts* embryos used for this study were grown at 25.5 °C. **D,** Distribution of the elongation in *wt*, *pix-1(gk416)*, *pak-1(ok448)* and *let-502(sb118ts)* mutants between comma stage and the start of late elongation. The box-plots represent the min, max, 25th, 50th (median) and 75th percentiles of the populations. * *t*-test *p*-value < 0.05, ** *t*-test *p*-value < 0.006 (modified from Martin *et al.*, 2014). Please click here to view a larger version of this figure.

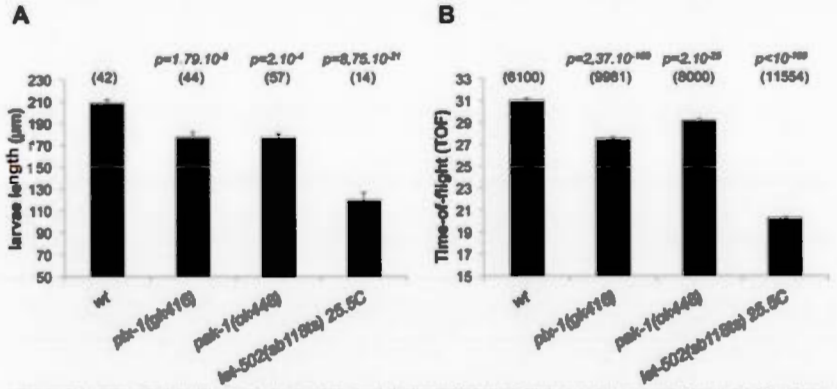

Figure 5. *Pix-1(gk416), Pak-1(ok448)* and *Let-502(sb118ts)* Larvae Present Length Defects. A, Length of larvae measured in *wt*, *pix-1(gk416)*, *pak-1(ok448)* and *let-502(sb118ts)* animals measured using image analysis (Protocol 2). **B,** Relative larvae length measured using flow-cytometer (Protocol 3). Numbers in brackets correspond to the number of animals used for the measurements. Means of lengths and standard error of the mean (SEM; error bars) are represented. Student's *t*-test *p*-values are indicated (p). Please click here to view a larger version of this figure.

Discussion

This protocol describes novel metrics to characterize early and late phases of embryonic elongation.

In section 1, the critical step is the potential presence of bacteria on the pad. The embryos are hermetically enclosed between the pad and the coverslip during image acquisition. Sealing the slide is required to avoid desiccation of the animals during acquisition that lasts more than two hours. To our knowledge, none of the sealers used to mount agarose pads between slide and coverslip are air-permeable. Consequently, when a

large amount of bacteria (or embryos) is present on the pad, they may be deprived of oxygen after a few hours leading to their premature death. Having three-fold embryos — corresponding to embryos that are 3-fold in length compared to non-elongated embryos — recorded along with the embryos of interest will be a good indicator of potential hypoxic conditions, since those embryos will stop moving in their eggshells in the absence of oxygen. No morphological measurements should be done on hypoxic conditions or on dead embryos.

Another critical step when using time-lapse imaging is temperature at which development of the embryo occurs. Thermosensitive mutants are currently used in *C. elegans*. The biological effect of temperature shift may be immediate or delayed depending on the half-life of the protein and the nature of the mutation its carries. Consequently, the temperature at which the embryo is exposed should be constant over time and should be controlled by appropriate ventilation of the microscopy room or a heating-cooling chamber on the microscope stage.

Section 2 is dependent on larvae synchronization using alkaline hypochlorite treatment. Under certain circumstances, this treatment may lead to embryonic lethality (Emb). Emb above 20% in *wt* population suggests an elevated toxicity during hypochlorite treatment that may negatively impact morphogenesis. Synchronized L1 displaying high Emb in *wt* background should not be used for further analysis. This restriction also applies to protocol 3.

We do not recommend the use of anesthetic drugs to immobilize larvae. Levamisol in particular, immobilizes the nematode through induction of muscle tetany that tends to shrink the larvae introducing experimental bias. If exposure time is not quick enough as a result of the limitations of the microscope, we recommend reducing the motility of larvae by increasing the concentration of the agarose in the pad and reducing the amount of liquid between the pad and the coverslip. Care should be taken however, not to desiccate the larvae, since desiccation will reduce their size.

In section 3, measurement of the length of larvae used comparison of flow rates between analyzed samples. To do so, the distribution of control particles needs to be compared. If the distributions fully overlay, the TOF (time-of-flight) values obtained for corresponding samples can be compared, if not, these values need to be normalized. Normalization of sample-TOF over control particles-TOF (as detailed in 3.4.5.1) has been used successfully as shown for *pak-1(ok448)* (**Figure 3C** and **Figure 5B**). Relative length of *pak-1(ok448)* vs *wt* was found to be similar in at least 3 independent experiments with or without normalization (data not shown). However, we recommend, confirming the results obtained with normalization with those obtained without it, especially when comparing larvae with small size differences. It should be noted that measurement of the larvae length using flow-cytometry provides a length relative to a control sample, in this case, *wt* larvae rather than an absolute length in micrometer as for image analysis. This implies that measurements from independent experiments cannot be combined unless computing size ratio over *wt*.

The buffer used for dilution in the sample cup will have an impact on the flow rate. We observed that the sheath buffer recommended by the manufacturer contains detergent that increases the amount of bubbles generated during acquisition. Using M9 buffer, which does not contain detergent, significantly reduced the formation of bubbles but was less efficient in avoiding the plugging of eggs in the tubules of the sorter, which affects the flow rate of samples. Egg plugging is easily detected during the acquisition by a marked decrease of the observable TOF of control particles for a few seconds followed by an elevated TOF- also for a few seconds. Egg plugging may also lead to the obstruction of the channel and the complete arrest of the particle flow (less that 5 objects per second). If this should occur, click on the CLEAN button until flow rate is restored. Any measurements occurring during these events should be excluded from the data analysis. Sheath buffer may be recommended for experiments involving strains characterized by high rates of dead eggs.

The sample and sheath pressure (set at the step 3.2.3), may change (slightly) over time and should be adjusted manually throughout the experiment in order to ensure a very constant flow rate. Reduction or increase of the low rate will be observable when analyzing the results and plotting the TOFs of control particles over time (**Figure 3C**). Reduction of the flow rate will result in the increase of the average TOFs of particles over time, while an increase of the flow rate will result in the opposite. Alteration of the flow rate will negatively impact the sensitivity of the method in detecting small size differences between populations of larvae.

Methods aiming to identify genes controlling elongation and requiring time-lapse microscopy recording are generally highly time-consuming and tedious when phenotyping several genotypes. The flow-cytometer-based approach, while requiring equipment not available to all laboratories, is less time-consuming and consequently more efficient when several strains need to be characterized. This method is also more statistically robust compared to measurements using image analysis (assessed by the student's *t*-test comparing mutant and *wt* TOF distributions; **Figure 5A and B**). This method may then be highly suitable for strains expressing elongation defects with low expressivity/penetrance.

Several methods using flow-cytometry have been developed in the past to measure fitness of nematodes[9-12]. These methods use animals dispensed in a 96-well plates and the Reflex module of the worm sorter[1]. The Reflex module enables direct analysis of nematode population dispensed within 96-well plates. Consequently, these methods are able to characterize hundreds of conditions per day and constitute a robust manner in which to measure the fitness of a non-synchronized population. They are however, not well suited to identify small size differences between synchronized L1. Measurement of small differences between L1 larvae requires the measurement across a large number of animals, which is incompatible with the use of 96-well plates and of the Reflex module that may efficiently characterize 100 objects at the most per well. The method described here is designed for this purpose at the expense of the throughput, which is significantly reduced. It enables the characterization of 3 to 4 conditions per hour once the instrument is calibrated, which is a marked improvement over using image analysis in protocol 2.

Measurement of head and tail width ratio is the first method that was developed to characterize morphogenic processes occurring unevenly along the antero-posterior axis of the embryo[7]. When applied to genes shown to control early elongation, these methods will clarify the spatial distribution of signaling pathways controlling morphogenesis at that stage. Measurement of the length of arrested larvae using either image analysis or flow cytometry in combination with measurement of the length of the embryos at the end of early elongation will enable the identification of genes controlling either early or late elongation or both with high sensitivity and precision. These procedures may then contribute significantly to future understanding of the spatial and temporal regulation of signaling pathways controlling embryonic elongation in *C. elegans*. Furthermore, these approaches can also be adapted to study signaling pathways controlling body length such as the insulin and TGF-beta pathways[13,14] and chronic exposure to environmental contaminants[15,16]. These measurements can be done at different larval stages or in adults

using minor variations of Protocols 2 and 3. Measuring size differences in L1 is more challenging with the worm sorter than larger objects such as L3, L4 larvae or adults. Protocol 3 can then easily be adapted to do these measurements.

Disclosures

The authors declare that they have no competing financial interests.

Acknowledgements

This work was supported by grants from the Natural Sciences and Engineering Research Council (NSERC) of Canada and The Canada Foundation for Innovation. Thanks to Dr Paul Mains (University of Calgary, Calgary, Canada) for *let-502(sb118ts)* strain. Some of the strains were provided by the *Caenorhabditis* Genetics Center, which is funded by NIH Office of Research Infrastructure Programs (P40 OD010440).

References

1. Corsi, A. K., Wightman, B., & Chalfie, M. A Transparent Window into Biology: A Primer on Caenorhabditis elegans. *Genetics.* **200**, 387-407 (2015).
2. Priess, J. R., & Hirsh, D. I. Caenorhabditis elegans morphogenesis: the role of the cytoskeleton in elongation of the embryo. *Developmental biology.* **117**, 156-173 (1986).
3. Zhang, H. *et al.* A tension-induced mechanotransduction pathway promotes epithelial morphogenesis. *Nature.* **471**, 99-103 (2011).
4. Diogon, M. *et al.* The RhoGAP RGA-2 and LET-502/ROCK achieve a balance of actomyosin-dependent forces in C. elegans epidermis to control morphogenesis. *Development.* **134**, 2469-2479 (2007).
5. Gally, C. *et al.* Myosin II regulation during C. elegans embryonic elongation: LET-502/ROCK, MRCK-1 and PAK-1, three kinases with different roles. *Development.* **136**, 3109-3119, (2009).
6. Piekny, A. J., Wissmann, A., & Mains, P. E. Embryonic morphogenesis in Caenorhabditis elegans integrates the activity of LET-502 Rho-binding kinase, MEL-11 myosin phosphatase, DAF-2 insulin receptor and FEM-2 PP2c phosphatase. *Genetics.* **156**, 1671-1689 (2000).
7. Martin, E. *et al.* pix-1 controls early elongation in parallel with mel-11 and let-502 in Caenorhabditis elegans. *PloS one.* **9**, e94684 (2014).
8. Sulston, J., & Hodgkin, J. in *Methods.* (ed W. B. Wood) 587-606 (1988).
9. Andersen, E. C. *et al.* A Powerful New Quantitative Genetics Platform, Combining Caenorhabditis elegans High-Throughput Fitness Assays with a Large Collection of Recombinant Strains. *G3 (Bethesda).* **5**, 911-920 (2015).
10. Boulier, E. L., & Jenna, S. Genetic dissection of Caenorhabditis elegans embryogenesis using RNA interference and flow cytometry. *Methods Mol Biol.* **550**, 181-194 (2009).
11. Verster, A. J., Ramani, A. K., McKay, S. J., & Fraser, A. G. Comparative RNAi screens in C. elegans and C. briggsae reveal the impact of developmental system drift on gene function. *PLoS genetics.* **10**, e1004077 (2014).
12. Ramani, A. K. *et al.* The majority of animal genes are required for wild-type fitness. *Cell.* **148**, 792-802 (2012).
13. So, S., Miyahara, K., & Ohshima, Y. Control of body size in C. elegans dependent on food and insulin/IGF-1 signal. *Genes to cells : devoted to molecular & cellular mechanisms.* **16**, 639-651 (2011).
14. Dineen, A., & Gaudet, J. TGF-beta signaling can act from multiple tissues to regulate C. elegans body size. *BMC developmental biology.* **14**, 43 (2014).
15. Tan, L., Wang, S., Wang, Y., He, M., & Liu, D. Bisphenol A exposure accelerated the aging process in the nematode Caenorhabditis elegans. *Toxicology letters.* **235**, 75-83 (2015).
16. Yu, Z., Yin, D., & Deng, H. The combinational effects between sulfonamides and metals on nematode Caenorhabditis elegans. *Ecotoxicology and environmental safety.* **111**, 66-71 (2015).

Annexe 3 : Autre contribution :

Ouellette, M.-H., **Martin, E.**, Lacoste-Carron, G., Hamiche, K. et Jenna, S. (2015). Spatial control of active CDC-42 during collective migration of hypodermal cells in *Caenorhabditis elegans*. *JMCB* online.

Journal of Molecular Cell Biology Advance Access published December 18, 2015

doi:10.1093/jmcb/mjv062 *Journal of Molecular Cell Biology* (2015), 0(0), 1–15 | 1

Article

Spatial control of active CDC-42 during collective migration of hypodermal cells in *Caenorhabditis elegans*

Marie-Hélène Ouellette, Emmanuel Martin, Germain Lacoste-Caron, Karim Hamiche, and Sarah Jenna*

Department of Chemistry, Pharmaqam, Biomed, Université du Québec à Montréal, Montréal, Québec, Canada
*Correspondence to: Sarah Jenna, E-mail: jenna.sarah@uqam.ca

Collective epithelial cell migration requires the maintenance of cell–cell junctions while enabling the generation of actin-rich protrusions at the leading edge of migrating cells. Ventral enclosure of *Caenorhabditis elegans* embryos depends on the collective migration of anterior-positioned leading hypodermal cells towards the ventral midline where they form new junctions with their contralateral neighbours. In this study, we characterized the zygotic function of RGA-7/SPV-1, a CDC-42/Cdc42 and RHO-1/RhoA-specific Rho GTPase-activating protein, which controls the formation of actin-rich protrusions at the leading edge of leading hypodermal cells and the formation of new junctions between contralateral cells. We show that RGA-7 controls these processes in an antagonistic manner with the CDC-42's effector WSP-1/N-WASP and the CDC-42-binding proteins TOCA-1/2/TOCA1. RGA-7 is recruited to spatially distinct locations at junctions between adjacent leading cells, where it promotes the accumulation of clusters of activated CDC-42. It also inhibits the spreading of these clusters towards the leading edge of the junctions and regulates their accumulation and distribution at new junctions formed between contralateral leading cells. Our study suggests that RGA-7 controls collective migration and junction formation between epithelial cells by spatially restricting active CDC-42 within cell–cell junctions.

Keywords: *Caenorhabditis elegans*, Cdc42, Rho GAP, collective migration, ventral enclosure, epithelial, morphogenesis

Introduction

Collective migration of epithelial cells is characterized by maintaining cell–cell adhesion whilst creating an antero-posterior polarity essential for directional migration (Khursheed and Bashyam, 2014). It plays an important role in organ morphogenesis, tissue regeneration, and tumour dissemination (Friedl and Gilmour, 2009). Collective migration is also required for dorsal and ventral enclosure in *Drosophila melanogaster* (Bastock and Strutt, 2007) and *Caenorhabditis elegans*, respectively (Chisholm and Hardin, 2005).

The late phase of *C. elegans* embryonic development includes epidermal morphogenic events that enable the embryo to acquire its final tubular shape (Chisholm and Hardin, 2005). One of these events, termed ventral enclosure, involves the migration of ventral hypodermal cells towards the ventral midline to cover the embryo in an epidermal layer. This event occurs in two phases. In the first phase, the anterior ventral hypodermal cells, referred to as the leading cells, migrate towards the ventral midline using large actin-rich protrusions, where they form junctions with their contralateral neighbours (Chisholm and Hardin, 2005). Afterwards, the posterior ventral hypodermal cells, called the pocket cells, migrate towards the ventral midline using a contraction-dependent, purse-string mechanism, which is still poorly described (Williams-Masson et al., 1997). These migratory mechanisms are supported by signals from underlying neuroblasts (Chisholm and Hardin, 2005).

During ventral enclosure, Rho GTPases control hypodermal cell migration in a cell-autonomous manner. Rho GTPases are molecular switches controlling a wide range of cellular functions including shape changes and cell migration (Takai et al., 2001). They cycle between an 'ON' GTP-bound form, during which they interact with specific effectors, and an 'OFF' GDP-bound form. They are regulated by guanine nucleotide exchange factors (GEFs) and GTPase-activating proteins (GAPs). The Rho GTPase CED-10/Rac1 regulates early migration of leading and pocket cells during ventral enclosure through the activation of effectors, including GEX-1/WVE-1/Scar and the ARP2/3 complex, to promote remodelling of the actin cytoskeleton (Lundquist et al., 2001; Withee et al., 2004). An additional pathway involving another potential effector of CED-10, the ENA/VASP UNC-34, was shown to specifically control the protrusive activity of leading cells in parallel with the CDC-42's effector WSP-1/N-WASP/WASp (Withee et al., 2004; Sheffield et al., 2007). In mammals, regulation of actin cytoskeleton

Received February 24, 2015. Revised July 27, 2015. Accepted August 12, 2015.

remodelling and membrane trafficking by N-WASP/WASp and Cdc42 has been shown to depend on the F-BAR proteins TOCA1/FBP17 (Pichot et al., 2010). While CDC-42 has not been directly studied in *C. elegans* ventral enclosure, the two redundant homologues of TOCA1, TOCA-1 and TOCA-2, were shown to control endocytosis of junctional proteins at that stage together with WSP-1 (Giuliani et al., 2009). Another Rho GTPase, RHO-1/RhoA, and its effector LET-502/ROCK may also control myosin-dependent contraction events during ventral enclosure (Fotopoulos et al., 2013).

Coordinating the different Rho GTPases and generating spatially distinct active zones at the leading edge of migrating fibroblasts is required for the generation of actin-rich protrusions (Pertz, 2010). Spatially controlling the activity of the different Rho GTPases at cell–cell junctions is also important for the transmission of forces from the leading cells to those that follow (Friedl et al., 2014) and for the maintenance of cell–cell junction integrity (Hidalgo-Carcedo et al., 2011). Antagonism between Cdc42 and RhoA at cell–cell junctions reduces actomyosin contractility between collectively migrating cells, which enables a better coordination of their movement (Hidalgo-Carcedo et al., 2011). In collectively migrating MDCK cells, active RhoA is found at the front of the leading cell(s), while active Cdc42 is restricted to more posterior/back locations (Reffay et al., 2014). Similarly, spatially distinct concentric zones of active RhoA and Cdc42 form in *Xenopus* oocytes during wound healing (Benink and Bement, 2005). This suggests that the spatial restriction of active Rho GTPases is evolutionary conserved and important for collective migration.

Signalling mechanisms spatially controlling active Cdc42 have been described in the yeast *Saccharomyces cerevisiae* (Park and Bi, 2007). The clustering of active Cdc42 at the bud site involves exocytic mechanisms targeting Cdc42 from intracellular compartments to the plasma membrane. It also involves feed-forward loops in which active Cdc42 controls exocytic mechanisms promoting its own accumulation and activation by GEFs at forming clusters (Harris and Tepass, 2010). The spatial restriction of active Cdc42 also involves actin-dependent endocytosis, and the recruitment of Rho GAPs to the bud site (Park and Bi, 2007; Wu and Lew, 2013). These studies highlight the interdependence of the spatial regulation of active Cdc42 and membrane trafficking, and the critical role for Cdc42-specific GAPs and GEFs in these processes in yeast.

In the epithelia of multicellular organisms, the mechanisms controlling the spatial distribution of active Cdc42 are less well understood. Membrane trafficking was however shown to spatially control the targeting of active Cdc42 at the leading edge of migrating primary rat astrocytes (Osmani et al., 2010). The function of Cdc42 in regulating actin-dependent endocytosis together with the F-BAR protein TOCA1/FBP17 and N-WASP/WSP-1 and endocytic recycling events at cell junctions is also well established in multicellular organisms (Leibfried et al., 2008; Giuliani et al., 2009; Bu et al., 2010; Harris and Tepass, 2010). Whether regulation of membrane trafficking by Cdc42 contributes to the spatial regulation of its active zone at the junctions between epithelial cells is, to date, unknown. Feed-forward loops involving N-WASP/WASp and Cdc-42-specific GEFs (Hussain et al., 2001; Kovacs et al., 2011; Humphries et al., 2014), as well as feedback mechanisms involving recruitment of Rho GAPs to prevent excessive activation of Cdc42 at cell–cell junctions were also described in the epithelia of multicellular organisms (Elbediwy et al., 2012). However, whether these mechanisms spatially control active Cdc42 at cell junctions and collective migration of epithelial cells is still unknown.

In this study, we characterized the function of the Rho GTPase-activating protein 7 (*rga-7*) during *C. elegans* ventral enclosure. This gene, called also *spv-1* (Spermatheca variant 1), encodes a protein containing a RhoGAP domain, an F-BAR domain that interacts with curved membranes, and a C1 domain that may interact with diacylglycerol (DAG) (Tan and Zaidel-Bar, 2015). RGA-7/SPV-1 was previously shown to regulate the activity of RHO-1/RhoA in the spermatheca during expulsion of embryos towards the uterus, and has three close human homologues: GMIP, ARHGAP29/PARG1, and HMHA1 (Tan and Zaidel-Bar, 2015). We show here that RGA-7 displays GAP activity towards CDC-42 in addition to RHO-1/RhoA. RGA-7 is required for migration of leading cells towards the ventral midline and regulation of the dynamics of junction formation between contralateral leading cells. We also show that RGA-7 functions in parallel with LET-502/ROCK and antagonistically with WSP-1/N-WASP and TOCA-1/2/TOCA1/FBP17. RGA-7 regulates the accumulation and distribution of active CDC-42 clusters at the junctions between adjacent leading cells and between contralateral leading cells. Our data suggest that spatial regulation of active CDC-42 at the cell–cell junctions by RGA-7 plays an important role in the ability of leading cells to migrate collectively towards the ventral midline and also regulates junction expansion between contralateral cells.

Results

RGA-7 is expressed in the hypodermis and controls ventral enclosure in a cell-autonomous manner

To gain a better understanding of the regulation of Rho GTPases during ventral enclosure, we searched for available strains carrying mutations in genes encoding for Rho GTPase regulators and displaying ventral enclosure defects. We obtained a strain carrying a 577-bp deletion within *rga-7* from the *C. elegans* genetic center (CGC), which was previously described as a loss-of-function mutation (Tan and Zaidel-Bar, 2015) (Supplementary Figure S1A). We observed that *rga-7(ok1498)* hermaphrodites laid 27.9% $\pm$ 3.5% SEM dead embryos ($n = 227$; Figure 1A). Imaging *rga-7(ok1498)* embryonic development revealed that 62.9% (34 out of 54) of embryos displayed morphogenic problems during late embryogenesis: 9.3% (5 out of 54) of the embryos arrested their development during ventral enclosure (Figure 1B, D and Supplementary Video S1); 11.1% (6 out of 54) arrested during elongation (arrow; Figure 1B, E and Supplementary Video S2); and 37% (20 out of 54) displayed slow ventral enclosure—defined as ventral enclosure that lasted for >1 h at 25°C but hatched and developed into adults (Figure 1B). A small proportion of embryos arrested before morphogenesis (7.4%; 4 out of 54; Figure 1B) and 3.7% (2 out of 54) displayed spherical eggshells and died at various stages of embryonic development (eggshells defects; Figure 1B). Finally, 31.5% (17 out of 54) developed normally into adults and did not display any of the above phenotypes.

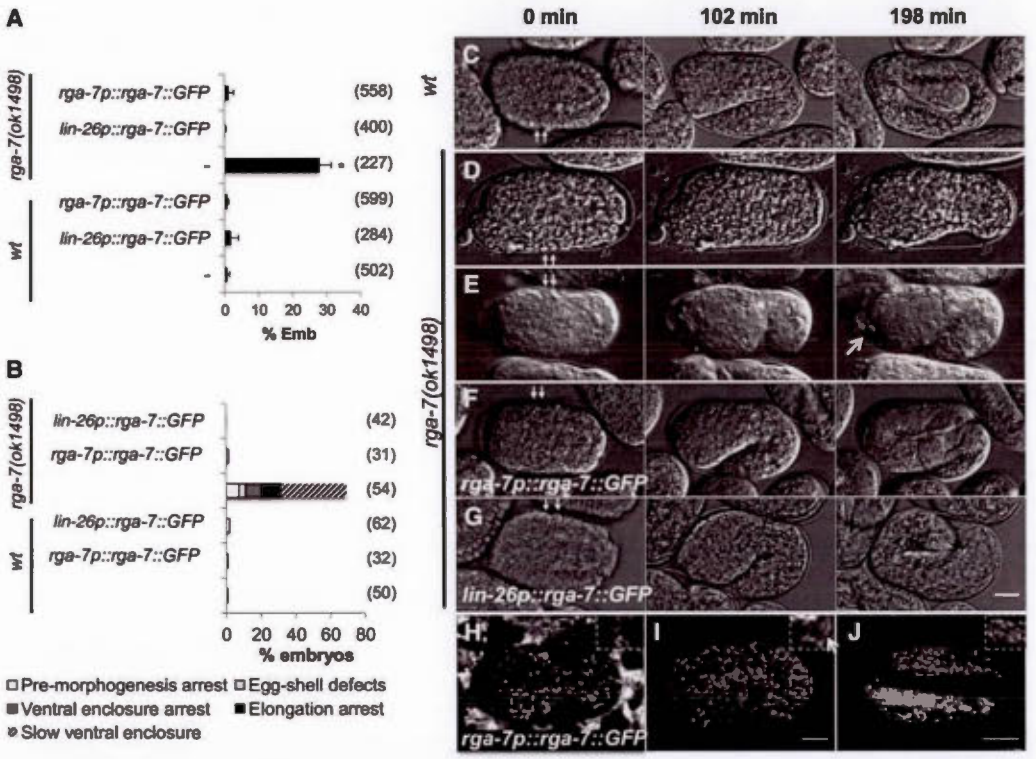

Figure 1 *rga-7* controls ventral enclosure. (**A**) Percentage of embryonic lethality (Emb) is measured for each indicated genotype. (**B**) Percentage of embryonic defects is indicated for each genotype. (**C**–**G**) Embryonic development progress for *wt* (**C**), *rga-7(ok1498)* (**D** and **E**), *rga-7(ok1498);saIIs22[rga-7p::rga-7::GFP]* (**F**), and *rga-7(ok1498);saIIs20[lin-26p::rga-7::GFP]* (**G**). Time = 0 min corresponds to the time when leading cells start to be observable ventrally (arrows). Expression pattern of RGA-7::GFP in *saIIs22[rga-7p::rga-7::GFP]* animals during ventral enclosure (**H**); early elongation (**I**) and late elongation (**J**). Arrow in **I** indicates tubular structures enriched in RGA-7::GFP. Scale bar, 10 μm.

We crossed *rga-7(ok1498)* hermaphrodites with wild-type (*wt*) males and found that the ventral enclosure defects observed in *rga-7* mutant embryos are due to zygotic requirements for the gene (see Supplementary data and Figure S1B). We also tested whether *rga-7* loss-of-function was responsible for the embryonic lethality (Emb) phenotype observed in *ok1498*-carrying animals using rescue experiments. To do so, we characterized the molecular structure and expression of *rga-7* in embryos (see Supplementary data and Figure S1A, C, and D). This revealed that *rga-7* codes for three transcripts with the two larger ones, *rga-7l* and *rga-7m*, detected in embryos (see Supplementary data and Figure S1A, C, and D). We then generated transgenic animals carrying *saIIs22[rga-7p::rga-7::GFP; unc-119R]*, driving the expression of a fusion protein between RGA-7 and the green fluorescent protein (GFP) under the control of the *rga-7p* endogenous promoter (Supplementary Figure S2A, see Materials and methods). RGA-7::GFP was detectable in several cells of the embryo during ventral enclosure where it accumulated as perinuclear punctate structures (Figure 1H). RGA-7::GFP was more tubular during early elongation (arrow; Figure 1I). During late elongation, it was mainly expressed in the dorsal and ventral hypodermal cells where it organized itself into stripes reminiscent of filamentous actin bundles (Chisholm and Hardin, 2005) (Figure 1J). RGA-7::GFP was also expressed in a wide range of cells in larvae and adults including the hypodermis, head and tail neurons, and spermatheca (Supplementary Figure S2B–D, respectively). Embryos expressing *saIIs22* did not present any significant Emb or significant delay during ventral enclosure compared with wild-type (*wt*) embryos (Figure 1A and B). When expressed in *rga-7(ok1498)* hermaphrodites, this transgene fully rescued *rga-7(ok1498)*-associated Emb and ventral enclosure defects (Figure 1A, B, and F). Our results suggest that the mutation in *rga-7(ok1498)* is responsible for the ventral enclosure defects observed in the mutant strain and that *saIIs22* expresses functional RGA-7 protein.

Ventral enclosure defects arise in embryos carrying mutations in genes required either in the hypodermis for their migration or in the underlying neuroblasts (Chisholm and Hardin, 2005). To assess whether *rga-7* is required in the hypodermis during ventral enclosure, we generated transgenic animals expressing RGA-7::GFP under the control of the hypodermal-specific promoter *lin-26p* (*saIIs20[lin-26p::rga-7::GFP; unc-119R]*; Supplementary Figure S2A). *rga-7 (ok1498)* mutant embryos expressing this transgene did not display any Emb phenotypes or ventral enclosure defects (Figure 1A, B, G and Supplementary Video S3), suggesting that the function of *rga-7* is required in the hypodermal cells during ventral enclosure.

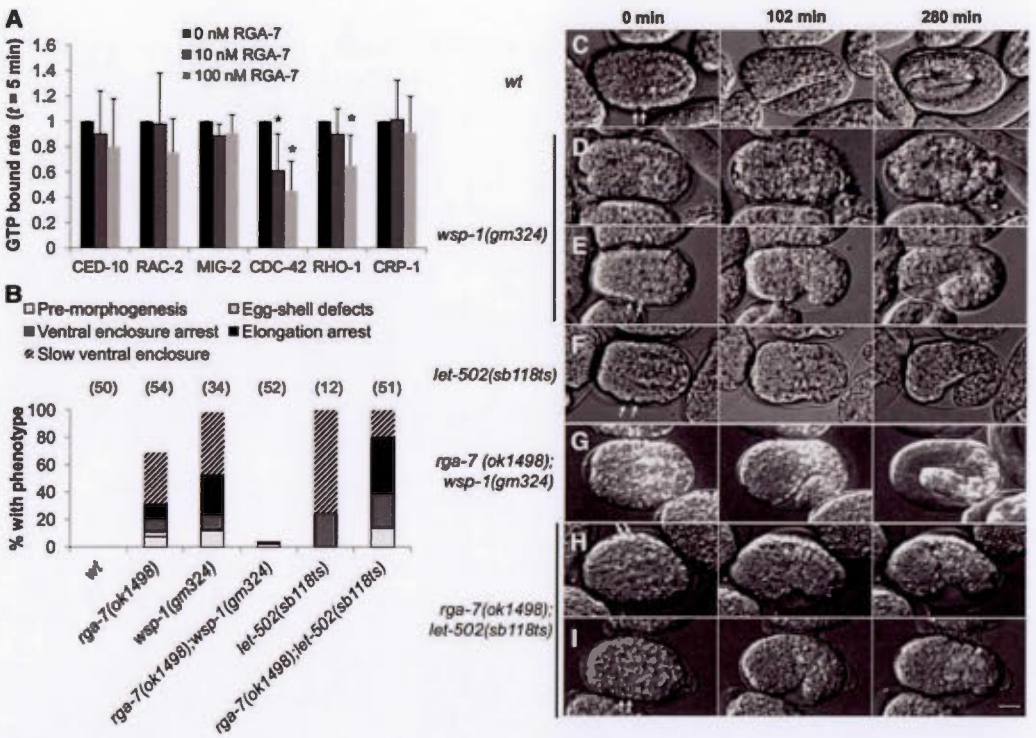

Figure 2 RGA-7 is a GAP for CDC-42 and RHO-1 and controls ventral enclosure in an antagonistic manner with WSP-1 and in parallel with LET-502. (**A**) The rate of GTP remaining bound on recombinant GTPases after 5 min incubation in the presence of 10 or 100 nM of recombinant GAP domain of RGA-7 compared with control (0 nM RGA-7) is indicated. (**B**) Percentages of embryonic defects for indicated genotypes. Phenotypes indicated by different shades of grey are associated to embryonic lethality. (**C–I**) Embryonic development progress from time = 0 min corresponding to the time when leading cells start to be observable ventrally (arrows) for *wt* (**C**), *wsp-1(gm324)* (**D** and **E**), *let-502(sb118ts)* at 25.5°C (**F**), *rga-7(ok1498);wsp-1(gm324)* (**G**), and *rga-7(ok1498);let-502(sb118ts)* at 25.5°C (**H, I**). Scale bar, 10 μm. *t-test *P*-value < 0.05.

RGA-7 is a GAP for CDC-42 and RHO-1 and controls ventral enclosure in an antagonistic manner with WSP-1/N-WASP/WASp and in parallel with LET-502/ROCK

RGA-7 contains a RhoGAP domain that may play an important role during ventral enclosure. To assess the specificity of RGA-7 GAP activity, we tested the ability of the recombinant RhoGAP domain of RGA-7 to catalyse the GTPase activity of the six Rho GTPases identified in the *C. elegans* genome (Figure 2A; see Materials and methods). We found that the RGA-7 GAP domain had significant GAP activity towards CDC-42 and, to a lesser extent (~10× less), towards RHO-1/RhoA, but it did not have any significant GAP activity towards the other GTPases tested (Figure 2A). We then assessed whether RGA-7 regulates CDC-42 and/or RHO-1 during ventral enclosure. Maternal disruption of *cdc-42* and *rho-1* causes defects during early embryogenesis because they are required for cell polarity and/or cytokinesis (Kumfer et al., 2010). Therefore, we assessed the requirement of RGA-7 function during ventral enclosure by monitoring genetic interactions between *rga-7(ok1498)* and mutants of CDC-42 and RHO-1-specific effectors shown to control ventral enclosure: WSP-1/N-WASP/WASp and LET-502/ROCK (Sawa et al., 2003; Sawa and Takenawa, 2006; Fotopoulos et al., 2013). *wsp-1(gm324)* and *let-502(sb118ts)* alleles have been described as null and/or strong loss-of-function alleles at 20°C and 25.5°C, respectively (Withee et al., 2004; Lin et al., 2012). Embryos carrying *wsp-1 (gm324)* displayed slow ventral enclosure, ventral enclosure arrest, and arrest during early elongation with internal cells extruding from the embryos as observed by DIC microscopy (Figure 2B, D–F and Supplementary Video S4). As expected, in light of the known functions of *let-502* during early embryogenesis, ventral enclosure, and elongation (Piekny et al., 2000; Fotopoulos et al., 2013), 25% of embryos carrying *let-502(sb118ts)* and grown at 25.5°C arrested their development during ventral enclosure, and 70.6% (9 out of 12) displayed slow ventral enclosure defects and were arrested as non-elongated larvae (Figure 2B; Supplementary Video S5). Interestingly, *rga-7(ok1498); wsp-1(gm324)* developed normally with no visible ventral enclosure defects (Figure 2B, G and Supplementary Video S6). On the other hand, our results show that *let-502(sb118ts)* is synergistic with *rga-7(ok1498);* double-mutant embryos at 25.5°C were 80.4% Emb ($n = 51$), with 25.5% of embryos arresting at an early stage of ventral enclosure, 41.2% arresting during early elongation with internal cells extruding from the embryos (Figure 2B, H, I and Supplementary Video S7), and 13.7% dying at pre-morphogenic stages (Figure 2B). These data suggest that *rga-7* functions antagonistically with *wsp-1* and in parallel with

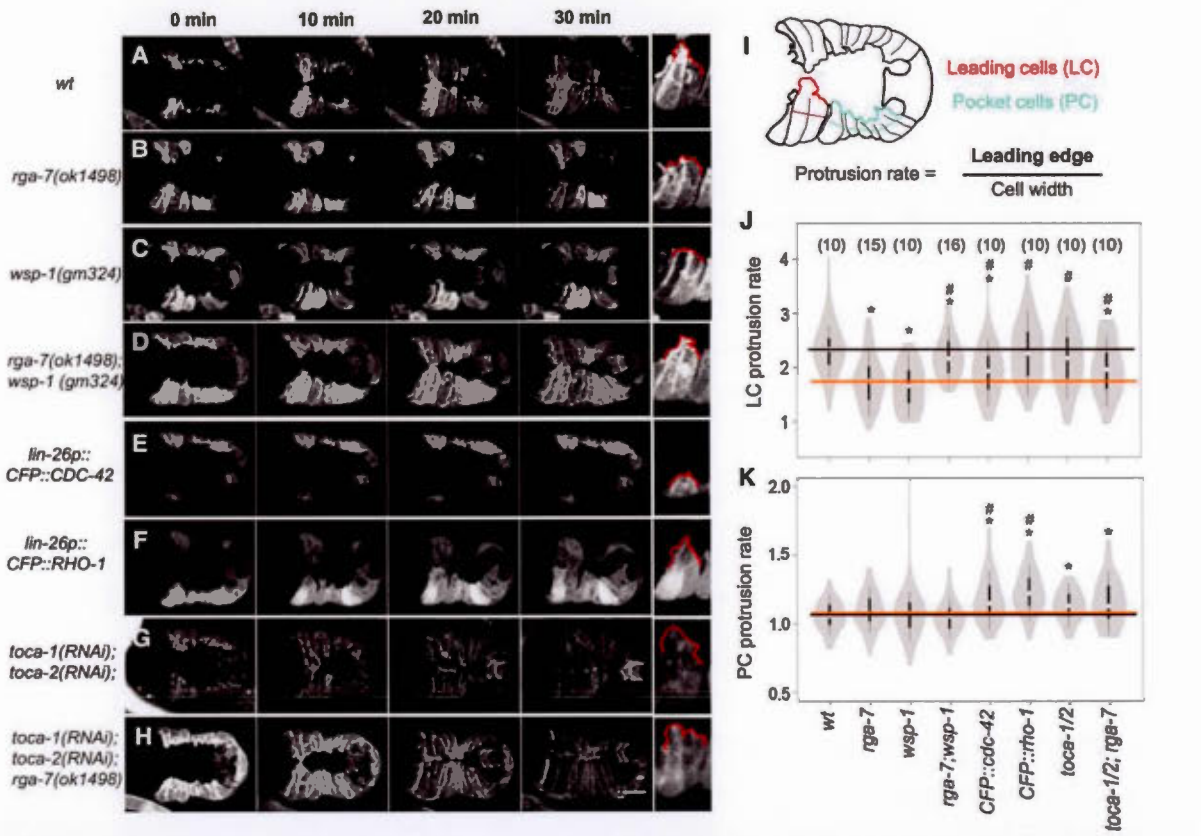

Figure 3 *rga-7* controls the protrusive activity of leading cells during ventral enclosure. Time-lapse confocal microscopy of ventral enclosure in *wt* (A), and indicated genotypes (B–H). Except *lin-26p::CFP::CDC-42* (E) and *lin-26p::CFP::RHO-1* (F), all strains expressed a *lin-26p::VAB-10(ABD)::GFP* transgene. The protrusion measured to calculate the protrusion rate is indicated by a thick line in the right panel of each time course. Scale bar, 10 μm. (I) Schematic representation of an embryo indicating measured protrusions (thick line) and cell width (thin lines) for leading cells and pocket cells (J, K). Violin plots represent the distribution of protrusion rate for leading cells (LC; J) and pocket cells (PC; K) for animals of indicated genotypes. Lines indicate average protrusion rate for *wt* and *rga-7(ok1498)* embryos. Number of quantified embryos is indicated for each genotype. *t-test *P*-value < 0.001 vs. *wt*, #t-test *P*-value < 0.02 vs. *rga-7(ok1498)*.

let-502 during ventral enclosure. These data also support the hypothesis that *rga-7* may function in the *cdc-42/wsp-1* pathway and in parallel with *rho-1/let-502* during ventral enclosure. The fact that *rga-7* and *wsp-1* mutants display similar ventral enclosure defects and mutually rescue each other is intriguing.

N-WASP/WASp was shown in several systems to be involved in feed-forward loops promoting Cdc42 activation by GEFs (Hussain et al., 2001; Kovacs et al., 2011; Humphries et al., 2014). In light of this, we hypothesize that during ventral enclosure, WSP-1 and RGA-7 control CDC-42 activation and inactivation, respectively. Following this hypothesis, the balance of CDC-42 cycling and consequently its function may be restored in the *rga-7;wsp-1* double mutant, although it would be reduced compared with *wt*.

RGA-7 controls the formation of actin-rich protrusions at the leading edge of leading cells

To gain a better understanding of the cellular function of *rga-7*, we assessed whether it controls the formation of actin-rich protrusions at the leading edge of leading cells during ventral enclosure, as demonstrated for *wsp-1* (Sawa et al., 2003). To do so, we expressed the filamentous actin-binding probe *lin-26p::VAB-10(ABD)::GFP* in hypodermal cells of *wt* (Supplementary Video S8) or mutant animals (Supplementary Videos S9 and S10) and measured the size of protrusions in leading (LCs; anterior – Figure 3I) and pocket cells (PCs; posterior – Figure 3I) as previously described (Sheffield et al., 2007). Briefly, the length of the protrusions formed by the LCs (red thick line; Figure 3A–I) was measured, as well as the width of these cells (Figure 3I). The protrusion rate of leading cells was then calculated as the length of protrusions vs. the width of these cells. Similar measurements were made for the pocket cells. Both *wsp-1(gm324)* and *rga-7(ok1498)* embryos displayed a significant reduction in the LC protrusion rate compared with *wt* embryos (*t*-test *P*-values = 10^{-11} and 10^{-14}, respectively; compare Figure 3A with B and C; Figure 3J), but did not display any change in their PC protrusion rates (Figure 3K). *rga-7(ok1498); wsp-1(gm324)* double-mutant embryos displayed a significantly

increased protrusion rate for the LCs compared with *rga-7(ok1498)* and *wsp-1(gm324)* animals (*t*-test *P*-values = 10^{-8} and 10^{-12}, respectively; Figure 3J), though still significantly lower compared with *wt* embryos (*t*-test *P*-value = 0.002; Figure 3J). In addition, while *rga-7(ok1498); wsp-1(gm324)* embryos enclosed faster than single mutants (compare Figure 3D with B and C), they were still delayed when compared with *wt* embryos (compare Figure 3D with A). These data suggest that *rga-7* and *wsp-1* control the formation of actin-rich protrusions in the LCs in an antagonistic manner. In addition, the loss of both *rga-7* and *wsp-1* functions only partially restored the ability of the LCs to form actin-rich protrusions and to migrate towards the ventral midline.

Since RGA-7 may negatively regulate CDC-42 activity during ventral enclosure, and WSP-1 activity may depend on active CDC-42 and/or promote its activation, we propose that the misregulation of CDC-42 activity should cause ventral enclosure defects similar to those seen in *rga-7(ok1498)* and *wsp-1(gm324)* embryos. Overexpressing CFP::CDC-42 in hypodermal cells using the *lin-26p* promoter triggered a significant reduction in the protrusion rate of LCs (*t*-test *P*-value = 10^{-6}; Figure 3J), while causing a significant increase in the PC protrusion rate when compared with *wt* embryos (*t*-test *P*-value = 10^{-6}; Figure 3K). Moreover, CFP::CDC-42-expressing embryos had delayed ventral enclosure compared with *wt* embryos (compare Figure 3E and A), and 72.2% of them (13 out of 15 embryos) failed to complete ventral enclosure. Interestingly, overexpression of CFP::RHO-1 in hypodermal cells did not significantly alter the LC protrusion rate (Figure 3F and J), but significantly increased the PC protrusion rate (*t*-test *P*-value = 10^{-11}; Figure 3K). Moreover, the LCs of the CFP::RHO-1 embryos migrated in a similar manner as the LCs of *wt* embryos, while the PCs were delayed (compare Figure 3F and A). Supporting the predominant role of CDC-42 regulation over that of RHO-1 during LC migration, the average intensity of overexpressed CFP::RHO-1 was ~1.67-fold as high as CFP::CDC-42 (Supplementary Figure S3A). These data suggest that misregulation of CDC-42, but not of RHO-1, may be responsible for the reduced protrusion rate of LCs in *rga-7(ok1498)* embryos.

The F-BAR proteins TOCA1/FBP17 and their orthologs in *C. elegans*, TOCA-1 and TOCA-2, control actin cytoskeleton remodelling and membrane trafficking together with WSP-1/N-WASP/WASp and CDC-42 (Pichot et al., 2010). We then assessed whether *rga-7* antagonizes *toca-1/2* functions during ventral enclosure, similar to *wsp-1*. To do so, we submitted *rga-7(ok1498)* and *wt* animals expressing VAB-10(ABD)::GFP to RNAi against *toca-1* and *toca-2* and measured the protrusion rate of LCs and PCs during ventral enclosure. *toca-1/2(RNAi)* embryos did not display any change in their LC protrusion rate relative to *wt* embryos (Figure 3J), but the protrusion rate of PCs was significantly higher (*t*-test *P*-value = 0.0009; Figure 3K). However, the protrusion rate of LCs was significantly increased in *rga-7(ok1498); toca-1/toca-2(RNAi)* compared with *rga-7(ok1498)* animals (*t*-test *P*-value = 0.006; Figure 3J). These data suggest that *rga-7* controls the formation of actin-rich protrusions in the leading cells in an antagonistic manner with *wsp-1* and *toca-1/2*, possibly by regulating CDC-42 activity. In addition, in the absence of both *rga-7* and *wsp-1/toca-1/2*, a parallel pathway drives the formation of actin-rich protrusions in LCs, which is slightly less efficient than the *rga-7/wsp-1* pathway(s).

RGA-7::GFP is recruited to cell–cell junctions

To better understand the molecular function of RGA-7 in leading cells during ventral enclosure, we assessed its subcellular location in these cells. To do so, we used embryos expressing RGA-7::GFP and the actin-binding probe VAB-10(ABD)::mCherry under the control of the hypodermal promoter *lin-26p* (Figure 4). As observed in transgenic animals expressing RGA-7::GFP under the control of its own promoter (Figure 1H), the fusion protein was found mainly at punctate and tubular structures within the cytosol of ventral hypodermal cells during ventral enclosure (Figure 4). It was also excluded from the actin-rich protrusions observed at the leading edges of both leading and pocket cells (orange line; Figure 4A and B). We measured RGA-7::GFP intensity along the junction located between adjacent leading cells (dashed arrow; Figure 4C), and identified two subdomains: the distal junction located within 4 μm from the edge of the junction (light blue line; Figure 4A) and the proximal junction located between 4 and 7 μm from this edge (dark blue line; Figure 4A). RGA-7::GFP was excluded from distal junctions (Figure 4C) and was found to form clusters with variable intensities along the proximal junction (Figure 4C). During the later stages of ventral enclosure, we measured the levels of RGA-7::GFP at new junctions that form and expand between contralateral neighbouring cells (red line; Figure 4A). RGA-7::GFP was excluded from expanding junctions immediately after collision of contralateral cells (Figure 4D and F) and was found to form clusters with variable intensities along the junction in fully enclosed embryos (Figure 4E and G). These data suggest that RGA-7::GFP is recruited to proximal junctions between adjacent leading cells and at a late stage of junction formation between contralateral cells.

RGA-7 promotes the accumulation of active CDC-42 to proximal junctions between adjacent leading cells

In light of the subcellular localization of RGA-7::GFP at proximal junctions and the known function of WSP-1 in actin cytoskeleton remodelling, we measured the accumulation of F-actin along the junctions between adjacent leading cells. We found that *rga-7*, *wsp-1*, and *toca-1/2* control the accumulation of F-actin at the distal junctions (see Supplementary data and Figure S4). These data also reveal that the parallel pathway driving the formation of actin-rich protrusions in LCs in *rga-7(ok1498);wsp-1* and *rga-7(ok1498); toca-1/2(RNAi)* double-mutants does not drive F-actin accumulation at distal junctions as efficiently as *rga-7/wsp-1/toca-1/2* pathway(s) (see Supplementary data and Figure S4).

We then determined whether RGA-7 controls the activation levels of CDC-42 at proximal and distal junctions. To do this, we first assessed the distribution of hypodermally expressed CFP::CDC-42 at junctions between adjacent LCs (Figure 5A and B; arrow head indicates distance = 0 μm). We observed that CFP::CDC-42 accumulates at proximal junctions rather than distal junctions (Figure 5B and C). We then expressed a probe in hypodermal cells that contains the Cdc42/Rac interactive binding (CRIB) domain of WSP-1 fused

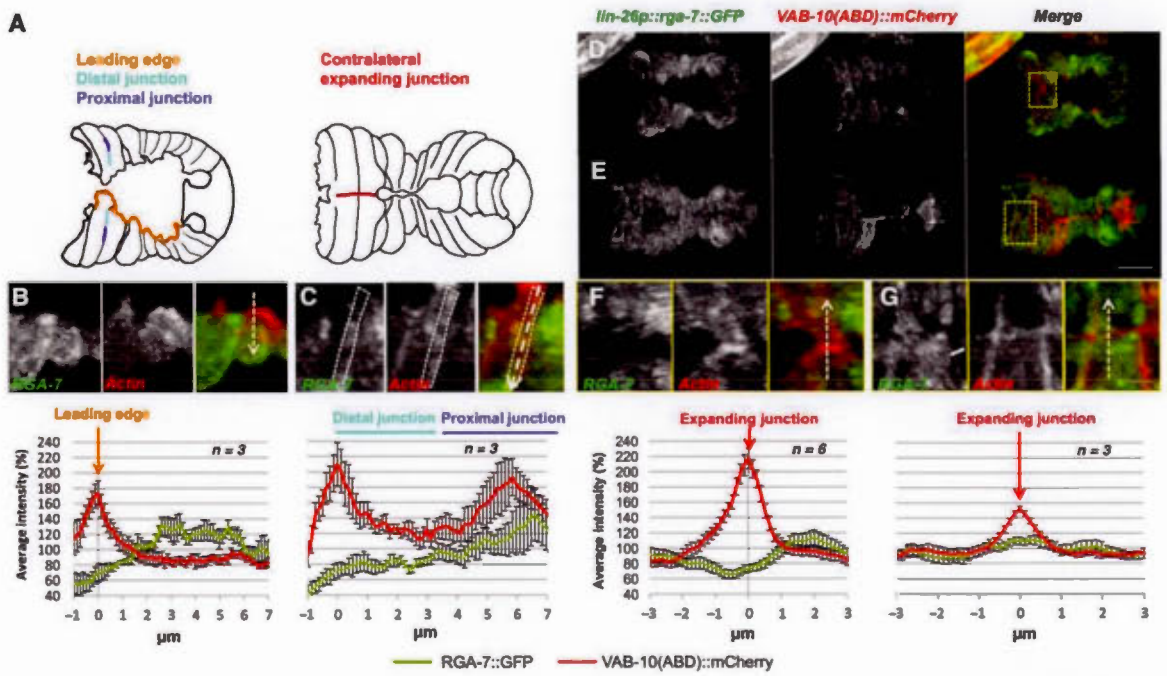

Figure 4 RGA-7::GFP is located at intracellular compartments and recruited to cell–cell junctions. (**A**) Schematic representation of embryos during ventral enclosure. The leading edge, distal junctions, and proximal junctions between adjacent cells (left panel) as well as expanding junctions between contralateral cells (right panel) are indicated. (**B**–**G**) Z-projection confocal images for *saIs20[lin-26p::rga-7::GFP]; mcIs40[lin-26p::VAB-10(ABD)::mCherry + myo-2p::GFP]* embryos during ventral enclosure. RGA-7::GFP (left panel) and F-actin-binding probe (middle panel) are shown at leading edge of pocket cells (**B**), distal and proximal junctions between adjacent leading cells (**C**), embryo and expanding junctions between colliding contralateral leading cells (**D** and **F**), fully enclosed embryo and fully expanded junctions between contralateral cells (**F** and **G**). Plain arrow in **G** represents RGA-7::GFP at intracellular tubular structures. Scale bar, 10 µm (**D** and **E**) and 2 µm (**B**, **C**, **F**, and **G**). Dashed arrows indicate the line-scans used to generate the intensity plots associated to each panel (**B**, **C**, **F**, and **G**). *n* = number of embryos submitted to this analysis; 3–10 measurements were done per embryo.

with mCherry, which was previously shown to specifically detect the active form of CDC-42 (Kumfer et al., 2010). We expressed this probe together with VAB-10(ABD)::GFP in *wt* and *rga-7(ok1498)* animals. WSP-1(CRIB)::mCherry accumulated at junctions between adjacent LCs and PCs (Figure 5D). Interestingly, this probe was enriched at the proximal junctions between adjacent LCs (arrow; Figure 5D and E) and was significantly reduced in *rga-7(ok1498)* embryos (one-way ANOVA; genotype effect, distance between 4 and 6 µm ; *P*-value = 10^{-14}; Figure 5D and E). These data suggest that RGA-7 is required for the accumulation of active CDC-42 at proximal junctions between adjacent leading cells.

The accumulation of CDC-42 at subdomains of the plasma membrane is regulated by CDC-42-specific GAPs and GEFs (Park and Bi, 2007; Harris and Tepass, 2010). Although counter-intuitive, since loss-of-function of a CDC-42-specific GAP would be expected to lead to an accumulation of active CDC-42, our data, using both CFP::CDC-42- and WSP-1(CRIB)::mCherry-expressing animals, are consistent with a role for RGA-7 in regulating the localization of CDC-42 at cell–cell junctions. Unfortunately, we were unable to create transgenic lines expressing CFP::CDC-42 in *rga-7(ok1498)* likely as a result of synthetic lethality. These data suggest that RGA-7 controls the accumulation of active CDC-42 at proximal junctions, presumably by regulating the targeting of CDC-42 at this specific location.

RGA-7, WSP-1, and TOCA-1/2 control junction expansion between contralateral cells

In the initial phase of epithelial cell–cell junction formation, Rac1 and Cdc42 are activated and control the expansion of the junctional surface through N-WASP/WAVE2/Arp2/3-mediated actin polymerization (Citi et al., 2014). They also promote directed targeting of membrane vesicles to cell junctions and the accumulation of junctional proteins (Citi et al., 2014). Considering the genetic interaction of *rga-7* and *wsp-1* during ventral enclosure (Figures 2 and 3) and the recruitment of RGA-7::GFP to expanding junctions between contralateral cells upon enclosure (Figure 3A, F, and G), we determined the function of *rga-7*, *wsp-1*, and *toca-1/2* during the expansion of these junctions.

We monitored the accumulation of filamentous actin (F-actin) at expanding junctions between contralateral leading cells (red line, Figure 4A) in embryos expressing the actin-binding probe VAB-10(ABD)::mCherry together with the junctional marker AJM-1::GFP (Figure 6A). F-actin began accumulating at the site of collision between contralateral leading cells before AJM-1::GFP

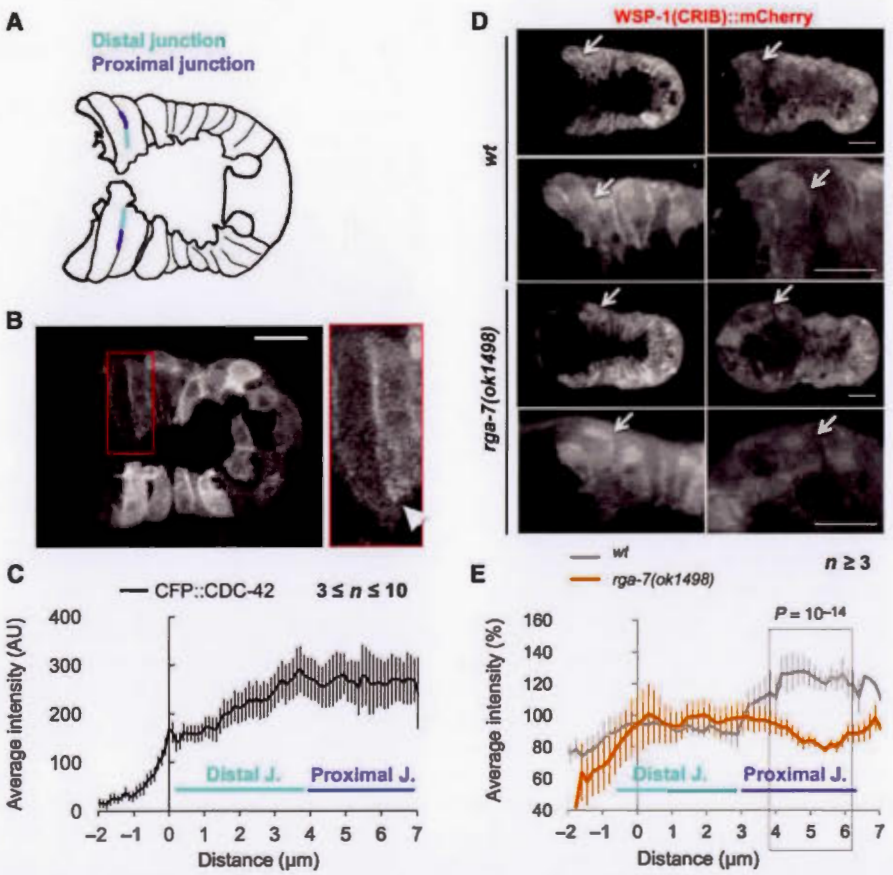

Figure 5 *rga-7* controls the accumulation of activated CDC-42 at the proximal junctions between adjacent leading cells. **(A)** Schematic representation of embryos indicating the location of the distal and proximal junctions between adjacent leading cells. **(B)** Transgenic embryo expressing CFP::CDC-42 in the hypodermis. Arrowhead indicates the reference point of intensity plots (distance = 0 µm in **C**). **(C)** Intensity plot showing the accumulation of CFP::CDC-42 along the distal and proximal junctions between adjacent leading cells. **(D)** Spatial distribution of activated CDC-42-binding probe (*WSP-1(CRIB)::mCherry* respectively) in *wt* and *rga-7(ok1498)* embryos during ventral enclosure (left panel) and in fully enclosed embryo (right panel). Scale bar, 10 µm. Arrows indicate the proximal junctions between adjacent leading cells. **(E)** Quantification of *WSP-1(CRIB)::mCherry* accumulation along the junctions between adjacent leading cells in *wt* and *rga-7(ok1498)* animals (distance = 0 is located at the leading edge of the distal junction). Student's *t*-test *P*-values are indicated. *n* = number of embryos quantified.

(time = 0 min; Figure 6A). AJM-1::GFP started to accumulate at the expanding junctions between 6 and 8 min post-collision (Figure 6A). By following F-actin, we measured changes in the length of the expanding junctions over time in *wt* and mutant embryos expressing the actin-binding probe VAB-10(ABD)::GFP (arrows; Figure 6A). The arrows in Figure 6A indicate the extremities of the line-scans used to perform these measurements. We also used these values to calculate the expansion rate of mutants vs. *wt* embryos (Figure 6C; empty cells indicate an expansion rate not significantly different than 1; two-way ANOVA without interaction; genotype effect *P*-value > 0.05). This analysis revealed that in *wsp-1(gm324)* embryos, junction expansion was significantly reduced between 2 and 6 min after collision compared with *wt* embryos (Figure 6B and C; one-way ANOVA; *P*-value = 0.006) and accelerated between 8 and 16 min (Figure 6B and C; one-way ANOVA; *P*-value = 0.0004). From 8 min after collision, junctions expanded 1.5 to 1.7-fold faster in *rga-7(ok1498)* mutants and 1.3 to 1.6-fold faster in *toca-1/2(RNAi)* than in *wt* embryos (one-way ANOVA; *P*-value = 1.92×10^{-8} and 5.7×10^{-8}, respectively; Figure 6A–C). *rga-7(ok1498); wsp-1(gm423)* and *rga-7(ok1498);toca-1/2(RNAi)* embryos displayed expansion rates similar to *wt* embryos (Figure 6B and C).

These data suggest that *wsp-1* promotes junction expansion at an early stage of junction formation (up to 8 min after cell collision) as shown in mammals (Citi et al., 2014), and subsequently displays an anti-expansion function together with *rga-7* and *toca-1/2*. In addition, *rga-7* antagonizes *wsp-1* and *toca-1* anti-expansion functions.

We also measured F-actin accumulation during junction expansion between contralateral LCs in *wt* and mutant animals (see Supplementary data and Figure S5A). This analysis reveal that (i) *rga-7*, *wsp-1*, and *toca-1/2* control the accumulation of F-actin at

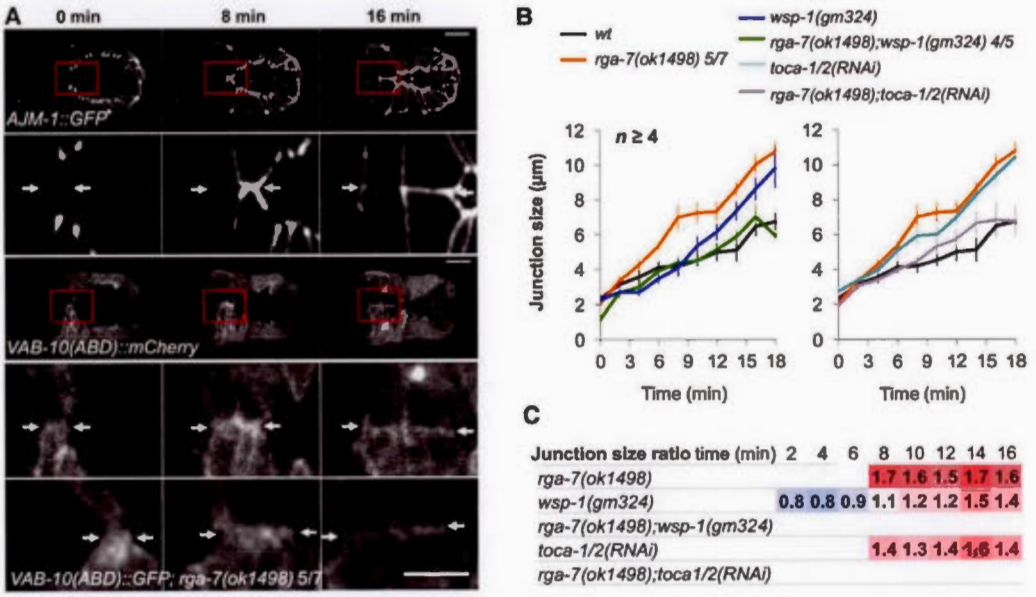

Figure 6 *rga-7*, *wsp-1*, and *toca-1/2* regulate the expansion of the junctions between contralateral leading cells. (**A**) Time-lapse confocal images showing the junction expansion from collision between contralateral leading cells (0 min), in *wt* animals expressing *AJM-1::GFP; VAB-10(ABD)::mCherry* as well as *wt* and *rga-7(ok1498)* animals expressing *VAB-10(ABD)::GFP* probes. Arrows indicate the edge of expanding junctions. (**B**) Average size of junctions between contralateral leading cells for *wt* and mutant animals expressing *VAB-10(ABD)::GFP* probe at indicated times after collision (time = 0 min). Error bars indicate SEM. (**C**) This table contains ratio of junction size for mutants vs. *wt* for each time point (see Materials and methods). Ratio higher than 1 or lower than 1 indicate that cell–cell junctions expand significantly faster or slower, respectively in mutant than in *wt*. White cells indicate that the size of the junctions of mutant and *wt* are not significantly different.

these junctions in a synergistic manner; and (ii) F-actin accumulation is regulated differently by *rga-7*, *wsp-1*, and *toca-1/2* at distal junctions between adjacent LCs and at expanding junctions between contralateral cells.

RGA-7 controls the accumulation and distribution of active CDC-42 at cell junctions

Given that RGA-7 promotes the accumulation of active CDC-42 at proximal junctions between adjacent leading cells (Figure 5D), we measured this accumulation at expanding junctions between contralateral leading cells (red line; Figure 4A) in *wt* and *rga-7(ok1498)* embryos. To do so, we measured the accumulation of the WSP-1(CRIB)::mCherry probe across the expanding junctions identified with the VAB-10(ABD)::GFP marker (dashed yellow line; Figure 7A). This analysis revealed that WSP-1 (CRIB)::mCherry accumulated significantly less at expanding junctions in *rga-7(ok1498)* embryos than in *wt* (Figure 7B; *t*-test *P*-value = 0.005). This suggests that RGA-7 promotes the accumulation of active CDC-42 at expanding junctions between contralateral leading cells.

We then assessed the distribution of RGA-7::GFP fusion protein at a late stage of junction expansion (>8 min after collision). This analysis revealed that RGA-7::GFP was centrally positioned within the expanding junctions (Figure 7C)—RGA-7::GFP was excluded from the domains of the junctions located on average 1.94 µm ± 0.323 SEM from the anterior and the posterior extremities of the expanding junctions (measured on 6.26 to 9.8 µm-wide expanding junctions; $n = 6$ embryos; Figure 7C).

Our study reveals that F-actin, RGA-7::GFP, and active CDC-42 form clusters of variable intensities along cell–cell junctions (Figures 4C, G and 7A, C). We then investigated the distribution of these clusters at cell–cell junctions in *wt* and *rga-7* mutant animals (see Materials and methods). Measurement of the average distance between RGA-7::GFP and F-actin clusters (A-G; Figure 7E) revealed that this distance was significantly lower than the distance observed between F-actin clusters (A-A; Figure 7E; *t*-test *P*-value < 0.00018) and between RGA-7::GFP clusters (G-G; Figure 7E; *t*-test *P*-value < 6.9×10^{-5}) at expanding, distal, and proximal junctions (Figure 7D and E). This suggests that RGA-7::GFP accumulates close to F-actin clusters at cell–cell junctions.

Similarly, analysis of the distribution of WSP-1(CRIB)::mCherry clusters revealed that they were also distributed in close proximity to F-actin clusters in *wt* animals (A-C; Figure 7F; *t*-test between A-C and C-C *P*-value < 0.003). Moreover, the average distance between WSP-1(CRIB)::mCherry and F-actin clusters did not significantly vary between *wt* and *rga-7(ok1498)* mutant animals (Figure 7G; *t*-test *P*-value > 0.05). This suggests that active CDC-42 accumulates close to F-actin clusters and that *rga-7* function is not required to ensure this relative positioning.

Interestingly, while the average density of WSP-1(CRIB):: mCherry (defined as the number of clusters per micrometer of junction, clusters/µm; Figure 7H) was similar at all junctions in *wt*

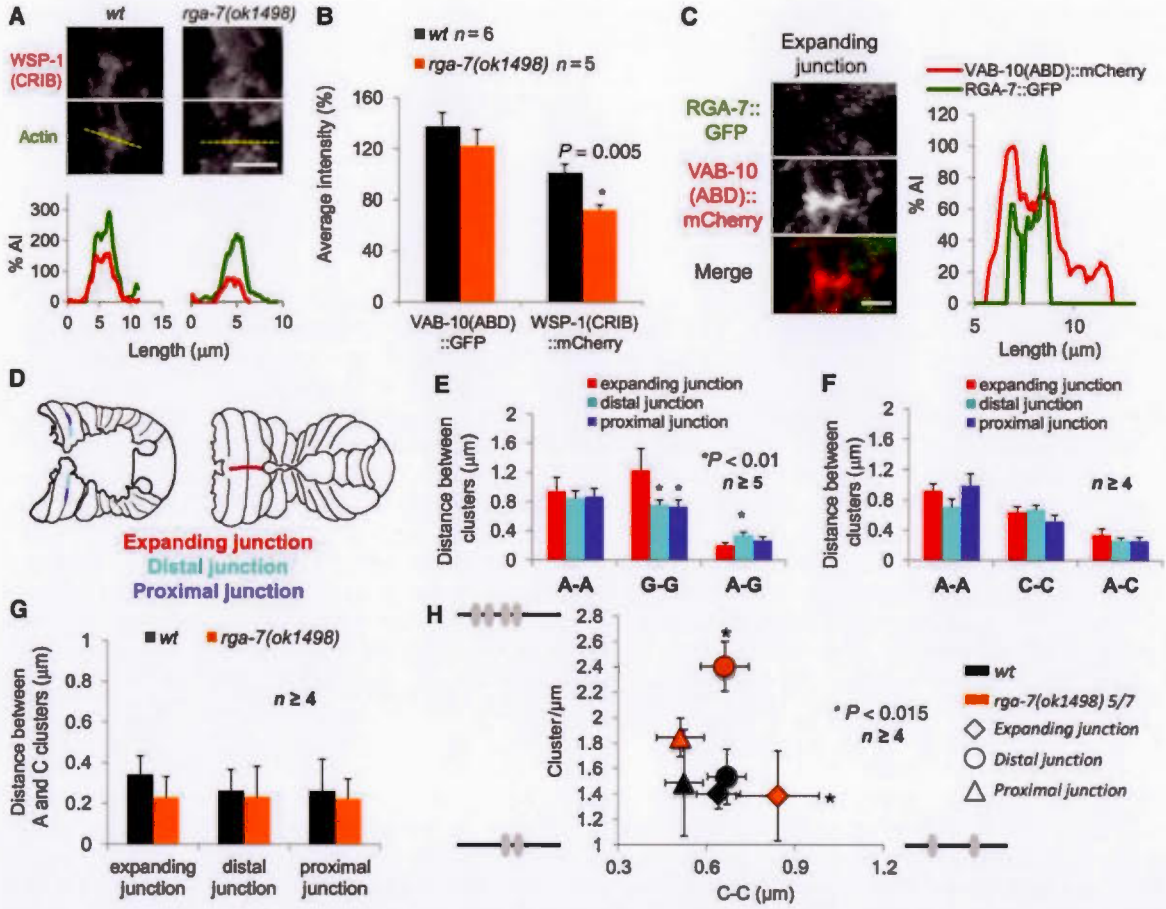

Figure 7 *RGA-7* regulates the distribution of activated CDC-42 clusters at cell–cell junctions. (**A**) Localization of *WSP-1(CRIB)::mCherry* and *VAB-10(ABD)::GFP* (Actin) probes in *wt* and *rga-7(ok1498)*. Dashed yellow lines indicate the line-scans used to generate the intensity plots (bottom panel). Scale bar, 5 μm. (**B**) Average intensity of *WSP-1(CRIB)::mCherry* and *VAB-10(ABD)::GFP* probes at expanding junctions are indicated. Student's *t*-test *P*-values are indicated. *n* = number of embryos analysed. (**C**) Distribution of RGA-7::GFP (upper panel) and actin (with probe VAB-10(ABD)::mCherry; middle panel) at expanding junctions. Graph on the right panel shows the distribution of the probes along the expanding junctions. Scale bar, 2 μm. (**D**) Schematic representation of embryos during early and late phases of ventral enclosure. The distal and proximal junctions between adjacent leading cells (left panel) as well as expanding junctions between contralateral leading cells (right panel) are indicated. (**E** and **F**) Distance between actin clusters (A-A), RGA-7::GFP clusters (G-G), activated CDC-42 clusters (C-C) and between filamentous actin (F-actin) and RGA-7 (A-G) or F-actin and activated CDC-42 (A-C) at expanding, distal, and proximal junctions. (**G**) Distance between F-actin clusters and activated CDC-42 clusters at expanding, distal, and proximal junctions in *wt* and *rga-7(ok1498)* animals. (**H**) Scatter plot representing the density (number of clusters per μm) and the distance between clusters of activated CDC-42 (C-C) in *wt* and *rga-7(ok1498)* embryos for expanding, distal, and proximal junctions. *t*-test *P*-values are indicated. *n* = number of embryos quantified. Error bars represent SEM.

animals, this density was significantly higher at distal junctions in *rga-7(ok1498)* animals (Figure 7H; *t*-test *P*-value = 0.012). This suggests that RGA-7 inhibits the formation/maintenance of active CDC-42 clusters at distal junctions between adjacent LCs. In addition, the average distance between WSP-1(CRIB)::mCherry clusters was significantly higher at the expanding junctions in *rga-7(ok1498)* mutants compared with *wt* (C-C; *t*-test *P*-value = 0.004; Figure 7H). This suggests that *rga-7* is required to maintain the relative distribution of active CDC-42 clusters at the expanding junctions.

All together, these data suggest that both RGA-7 and active CDC-42 are targeted to the vicinity of F-actin clusters at the proximal, distal, and expanding junctions. The distribution of these proteins relative to F-actin clusters may not specifically involve RGA-7 function. However, RGA-7 may negatively regulate the spreading of active CDC-42 clusters through inhibiting the generation/maintenance of these clusters at distal junctions between adjacent leading cells and maintaining the relative distance between clusters at new junctions expanding between contralateral cells. We hypothesize that RGA-7 functions in restricting active CDC-42 to specific

domains within both the junctions between leading cells undergoing collective migration, as well as newly formed and expanding junctions.

Discussion

Here, we show that *rga-7* gene codes for a RhoGAP with a GAP activity that is specific to CDC-42 and RHO-1/RhoA. We also propose that RGA-7 controls the spatial distribution of active CDC-42 at the junctions between leading cells during their collective migration towards the ventral midline and at the junctions forming and expanding between contralateral leading cells.

In this function, RGA-7 is required in hypodermal cells, in parallel with the RHO-1's effector LET-502/ROCK. More specifically, RGA-7 controls the formation of actin-rich protrusions at the front of migrating leading cells in a manner that is antagonistic with the CDC-42's effector WSP-1/N-WASP and the CDC-42-interacting proteins TOCA-1/2/Toca1/FBP17. It also functions in parallel with a pathway that is only functional in the absence of the combination of RGA-7 and WSP-1 or RGA-7 and TOCA-1/2 (Figure 8A). RGA-7, WSP-1, and TOCA-1/2 modulate the accumulation of F-actin at the junctions between adjacent leading cells during their migration—an accumulation inefficiently promoted by the parallel pathway identified above (Figure 8A). Importantly, our study reveals that RGA-7 is recruited to proximal junctions between adjacent leading cells where it promotes the accumulation of active CDC-42. It also inhibits the accumulation of activated CDC-42 at distal junctions located closer to the leading edge of migrating cells (Figure 8A).

The characterization of the functional roles of RGA-7, WSP-1, and TOCA-1/2 during the formation of new junctions between contralateral leading cells reveals that: (i) WSP-1 promotes the expansion of these junctions at an early stage of the junction formation independently of TOCA-1/2 or RGA-7 (<8 min after collision; Figure 8B); (ii) when junctional proteins start to accumulate at the junctions (≥8 min after collision; Figure 8B), the functions of RGA-7, WSP-1, and TOCA-1/2 tend to reduce the rate of expansion of the junctions in an antagonistic manner and in parallel with a pathway that remains to be identified. At this specific stage, RGA-7 promotes the accumulation of active CDC-42 clusters at the junctions and negatively regulates their spreading during the expansion process.

RGA-7 was recently shown to regulate embryo expulsion from spermatheca through the regulation of RHO-1/RhoA activity (Tan and Zaidel-Bar, 2015). This function is supported by the alleviating/epistatic interaction observed between *rga-7(ok1498)* and *let-502* hypomorphic allele in this system (Tan and Zaidel-Bar, 2015). We showed that *rga-7* controls ventral enclosure synergistically with *let-502* and antagonistically with *wsp-1* and *toca-1/2*, suggesting that RGA-7 regulates the GTPase activity of CDC-42 in the hypodermis during ventral enclosure. This hypothesis is also supported by the observation that overexpression of CDC-42 but not RHO-1 displays similar migratory defects of leading cells as *rga-7* loss-of-function.

Most RhoGAPs present GAP specificity towards several GTPases (Jenna and Lamarche-Vane, 2003). They usually display a more stringent specificity *in vivo* than *in vitro* (Jenna and Lamarche-vane, 2003), demonstrating a clear preference for a particular GTPase. However, few RhoGAPs display a specific GAP activity towards several GTPases *in vivo*. For instance, Rga4 controls cell polarity and morphogenesis of *Schizosaccharomyces pombe* through regulation of Cdc42 GTPase activity and cell integrity and cell separation through regulation of Rho2 (Cansado et al., 2010). Recent data, including ours, suggest that RGA-7 regulates the GTPase activity of RHO-1 in spermatheca during embryos expulsion to the uterus (Tan and Zaidel-Bar, 2015) and CDC-42 during ventral enclosure. Interestingly, RGA-7 exhibits almost 10-times more GAP activity towards CDC-42 than RHO-1 *in vitro*, and is more expressed in the spermatheca of adults than in the hypodermis of embryos during ventral enclosure (Supplementary Figure S2D). This suggests that RGA-7 GAP specificity may be, at least partially, regulated by its expression level. While genetic interaction with *let-502* in the two systems suggests that *rga-7* may exhibit GAP specificity predominantly towards either RHO-1 or CDC-42, the possibility that RGA-7 may regulate the GTPase activity of both CDC-42 and RHO-1 in both systems in a spatially restricted manner cannot be excluded.

As detailed in the introduction, restriction of the Cdc42 activation zone depends on exocytosis, endocytosis, feed-forward loops promoting Cdc42 accumulation and activation, as well as recruitment of RhoGAPs to limit the spatial expansion of activated Cdc42 clusters in yeast (Park and Bi, 2007; Harris and Tepass, 2010). Interestingly, Cdc42 together with the F-BAR protein TOCA1/TOCA-1 and N-WASP/WSP-1 were shown to control actin-dependent endocytosis of junctional proteins in several systems including *C. elegans* (Giuliani et al., 2009). N-WASP was also shown to participate in feed-forward mechanisms promoting Cdc42 activation during endocytosis (Hussain et al., 2001; Humphries et al., 2014).

The efficient cycling of Cdc42 between its active (GTP-bound) and inactive (GDP-bond) forms is essential for Cdc42 biological function across multiple systems (Fidyk et al., 2006). This is supported by experiments with mutants that either block Cdc42 activation (guanine-nucleotide exchange activity) or inactivate it (GTP hydrolysis activity) but still display similar phenotype(s) (Fidyk et al., 2006). An appealing hypothesis that explains RGA-7 antagonism with both WSP-1 and TOCA-1/2 during ventral enclosure is that the CDC-42-specific GAP activity of RGA-7 may antagonize WSP-1 and TOCA-1/2 function during endocytosis at cell junctions as well as WSP-1 potential feed-forward function on CDC-42 activation through GEFs. This later hypothesis is strongly supported by the observation that *rga-7;wsp-1* embryos complete ventral enclosure significantly more efficiently than single mutants but not quite as efficiently as *wt* embryos. Inhibition of CDC-42-dependent endocytosis at proximal and expanding cell junctions by RGA-7 may lead to the accumulation of CDC-42 at the junctions and explain the observed reduction of the accumulation of active CDC-42 at these junctions in *rga-7* mutants.

Studies using drugs disrupting actin structures in budding yeast revealed that once Cdc42 clustering at the bud site is established, exocytic delivery of Cdc42 is required to counteract the dispersal of Cdc42 clusters at the plasma membrane mediated by actin-dependent endocytosis (Park and Bi, 2007). Inhibition of endocytosis by RGA-7 may then reduce the dispersal of

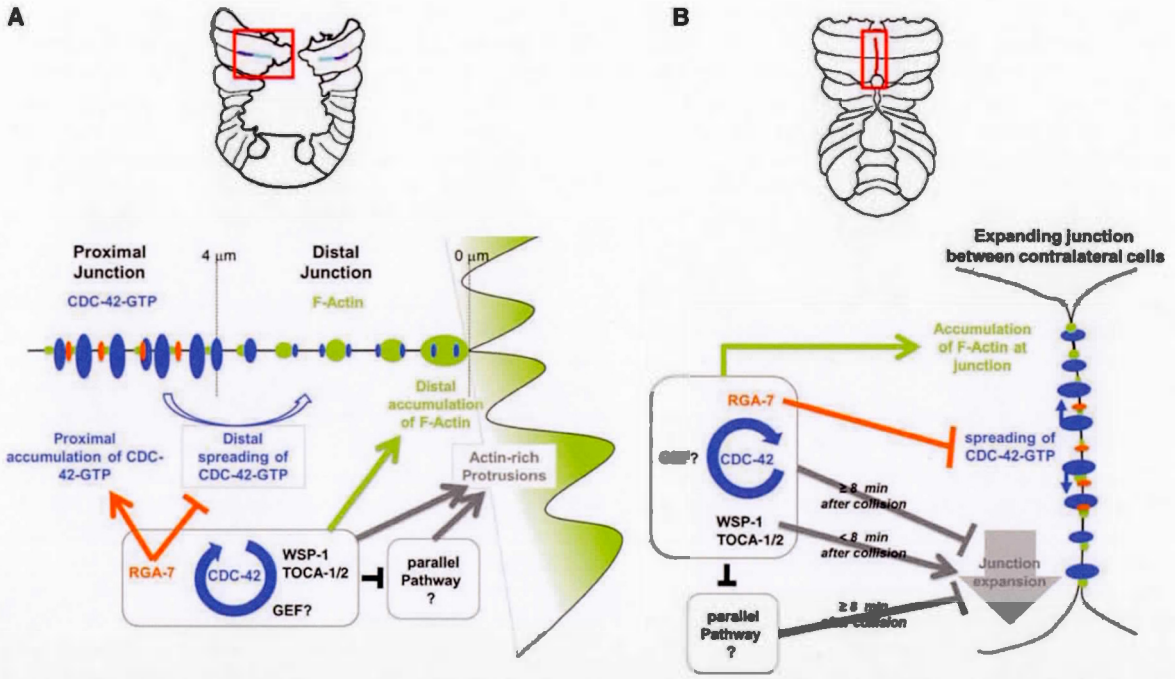

Figure 8 RGA-7 spatially controls active CDC-42 at cell–cell junctions during collective migration and expansion of newly formed junctions. **(A)** During early phase of ventral enclosure, RGA-7 is recruited to the proximal junctions between adjacent leading cells. It promotes the accumulation of active CDC-42 clusters at proximal junctions and inhibits their spreading towards the distal junctions. RGA-7 controls the formation of actin-rich protrusions at the leading edge of leading cells in an antagonistic manner with WSP-1 and TOCA-1/2 and in parallel of a pathway that remains to be identified. The function of RGA-7, WSP-1, and TOCA-1/2 is essential for the accumulation of F-actin at the distal junctions between adjacent leading cells. **(B)** Once leading cells meet at the ventral midline, the junctions between contralateral cells accumulate F-actin, and the expansion is promoted by WSP-1. Eight minutes after collision, junctional proteins start to accumulate at the expanding junctions, and RGA-7, WSP-1, and TOCA-1/2 tend to reduce the expansion rate of these junctions. At that specific stage, RGA-7 promotes the accumulation of activated CDC-42 at the expanding junctions and inhibits the dispersion of the clusters they form.

active CDC-42 clusters within junctions. This hypothesis also accounts for the increased spreading of these clusters from proximal to distal junctions between adjacent leading cells and within expanding junctions between contralateral cells in *rga-7(ok1498)* mutants.

Given the RGA-7::GFP accumulation at punctate and tubular endomembranes and its recruitment to proximal junctions, we cannot exclude that RGA-7 may regulate exocytic and/or endocytic recycling processes. Negative regulation of both CDC-42-dependent exocytosis and endocytosis by RGA-7 is also an attractive hypothesis that may explain the accumulation of activated CDC-42 clusters at distal junctions observed in *rga-7(ok1498)* embryos. Dissection of mechanisms that regulate CDC-42-dependent endocytosis and exocytosis/endocytic recycling at the junctions between hypodermal cells during ventral enclosure will be required to confirm these hypotheses.

During cell migration, coordination of Rho GTPases involves spatial segregation of active RhoA and Cdc42 as shown in migrating fibroblasts (Machacek et al., 2009) and during wound healing in *Xenopus* oocytes (Benink and Bement, 2005). This distribution of active RhoA at the distal/front of leading cells of collectively migrating cell groups and of Cdc42 at a proximal/back location compared with RhoA may be evolutionary conserved (Benink and Bement, 2005; Reffay et al., 2014). In this context, the function of RGA-7s in spatially controlling active CDC-42 accumulation at proximal junctions may contribute to the spatial segregation of active RHO-1/RhoA and CDC-42/Cdc42 at cell junctions between leading cells and to their ability to drive collective migration towards the ventral midline.

In conclusion, we show that the CDC-42 and RHO-1-specific GAP, RGA-7, controls the accumulation and distribution of the active CDC-42 at restricted sites of the junctions between leading cells migrating collectively and during the expansion of new junctions forming between contralateral cells. We show that RGA-7 functions antagonistically with WSP-1/N-WASP and TOCA-1/2, two proteins controlling actin- and CDC-42-dependent endocytosis. Our data suggest that spatial restriction of CDC-42 active zone by RGA-7 is critical for collective migration of hypodermal cells and important in regulating the dynamics of cell–cell junction formation and expansion.

Materials and methods

Strains and culture methods

Nematodes were maintained under standard conditions at 20°C (Brenner, 1974). Worm strains carrying the following mutations

and markers were obtained from the *Caenorhabditis* Genetic Center (CGC): *rga-7(ok1498) II, wsp-1(gm324) IV, mcIs40[lin-26p::VAB-10(ABD)::mCherry + myo-2p::GFP], mcIs50 [lin-26p::VAB-10(ABD)::GFP + myo-2p::GFP],* and jcIs1{ajm-1::GFP, pRF4[rol-6 (su1006)]}. The strain carrying *let-502(sb118ts) I* was kindly provided by Dr Paul Mains (University of Calgary, Calgary, Canada). Mutant strains were backcrossed at least 4 times against wild-type (*wt*) animals prior to analysis.

Generation of transgenic animals

All transgenic animals were generated through biolistic bombardment of *unc-119(ed3)* animals, using a PDS-1000/He system with the Hepta adaptor (Bio-Rad) as previously reported (Berezikov et al., 2004). At least three independent lines were isolated and characterized per construct. *sajIs22[rga-7p::rga-7::GFP; unc-119^R]* was generated through recombination of pDONRP4P1R-*rga-7p*, containing 5 kb of the genomic sequence upstream of RGA-7 initiation codon, with pDONR201-*rga-7* and pMB14. pDONR201-*rga-7* contains genomic sequence from RGA-7 initiation codon in exon 1 up to exon 8 fused to cDNA sequence up to the stop codon of the gene located at exon 20. Similarly, *sajIs20[lin-26p::rga-7::GFP; unc-119^R] was* generated through the recombination of pDONRP4P1R-*lin-26p* containing 5 kb of the *lin-26* promoter (Martin et al., 2014), pDONR201-*rga-7*, and pMB14. *sajIs29[lin-26p::CFP::rho-1::3′UTR; unc-119^R]* and *sajIs30[lin-26p::CFP::cdc42::3′UTR; unc-119^R]* were obtained through recombination of pDONRP4P1R-*lin-26p*, pDONR201-CFP-*rho-1* or pDONR201-CFP-*cdc-42*, pCM5.37 containing the *unc54* 3′UTR (Addgene), and pCG150 destination vector (Addgene). *wsp-1* CRIB domain (cDNA coding for 78 amino-acids from position 230 to 308 of WSP-1) was cloned in pDONR201 and recombined together with pDONRP4P1R-*lin-26p* in pULSRG1 (containing attB4-ccdB-attB2 followed by mCherry-pie-1 3′UTR; kindly provided by Dr Ian Hope, Univ. Leeds, UK). The resulting vector was used to generate *sajIs31[lin-26p::wsp-1(CRIB)::mCherry; unc-119^R]* transgenic animals. See Supplementary Methods for details.

Isolation of strains carrying several mutant alleles and transgenes

rga-7(ok1498) II; wsp-1(gm324) IV was generated by crossing *wsp-1(gm324) IV* hermaphrodites with *rga-7(ok1498) II* males. Mutant animals expressing *lin-26p::VAB-10(ABD)::GFP* were obtained by crossing mutant hermaphrodites with *mcIs50 [lin-26p::VAB-10(ABD)::GFP + myo-2p::GFP]* males. Double-mutant homozygotes and animals carrying two copies of transgenes were isolated from the F2 progenies as animals segregating only fluorescent progeny and mutant alleles in genomic DNA were identified using PCR. *let-502(sb118ts) I* was maintained at 20°C, and *rga-7(ok1498) II; let-502(sb118ts) I* was generated by crossing *let-502(sb118ts) I* hermaphrodites with *rga-7(ok1498) II* males. *let-502(sb118ts) I* homozygotes were identified through scoring of embryonic lethality (Emb) and larval arrest (Lva) phenotypes at 18°C and 25.5°C and identification of thermosensitive behaviour of isolated populations. pL4440 constructs containing *toca-1* and *toca-2* sequences were retrieved from the genome-wide RNA interference (RNAi) library (Kamath et al., 2003) and confirmed by sequencing. RNAi treatment was done using feeding protocol as detailed in Supplementary Methods.

Phenotyping mutant animals and 4-dimensional microscopy

Emb phenotype was scored after isolation of 10–12 worms on NGM agar with OP50 as a source of food. Worms were allowed to lay eggs at 20°C for 5–6 h and were removed from the plate, and laid embryos were counted. After 24 h, dead embryos were counted to assess Emb. The stage of embryonic arrest was confirmed in mutant animals using time-lapse DIC microscopy as previously described (Martin et al., 2014). Embryos dissected from adult hermaphrodites were mounted on 3% agarose pads in M9 buffer, and coverslips were sealed with drawing gum (Pébéo). Elongation was recorded using 4-dimensional microscopy (3D and time), which recorded a Z-stack every 2 min during 10 h at room temperature or 25.5°C using a Leica DM5500 microscope equipped with a 63× oil immersion objective upon differential interference contrast illumination (DIC). Images were captured using Leica LAS AF imaging software. These recordings were used to assess morphological defects during embryonic development. Slow ventral enclosure was identified for embryos completing their ventral enclosure in >1 h from the time leading cells could be observed migrating at the embryo periphery.

In vitro GAP activity assay

To assess the specificity of RGA-7 GAP activity, we expressed a His6-tagged RGA-7 GAP domain as a recombinant protein in bacteria using pTRcHis gateway converted vector as previously reported (Jenna et al., 2005). We purified the recombinant protein and measured its ability to catalyse the hydrolysis of GTP by the six recombinant Rho GTPases identified in the *C. elegans* genome, the Racs CED-10 and RAC-2, the RhoG MIG-2, the Cdc42 CDC-42, the RhoA RHO-1, and the atypical Rho GTPase CRP-1, which were expressed as recombinant Glutathione S Transferase (GST)-fusion proteins. To do so, we used a filtration assay as previously described (Jenna et al., 2005). We measured the amount of GTP-γ32P remaining bound to the GTPase after 5 min incubation at 25°C in the absence (control condition) or presence of 10 or 100 nM of GAP and computed the ratio of GTP-remaining bound on the GTPase over the control condition at each concentration of GAP.

Confocal fluorescence microscopy

The expression pattern of RGA-7::GFP and its subcellular localization in living animals was observed using a Nikon A1R confocal microscope using 100× oil CFI NA 1.45 Plan Apochromat λ objective. All images were captured using NIS-Elements software (Nikon) with a pinhole size of 85.6 μm, a calibration of 0.10 μm/pixel (radial resolution of 0.20 μm), and a Z-step of 0.200 μm. Deconvolution was done using Autoquant3X, 3D deconvolution software. Orthogonal views were generated using ImageJ software. Dynamic time-lapses were achieved by using 60× oil CFI NA 1.4 Plan Apochromat λ objective on Nikon A1R confocal microscope. Imaging of CFP::CDC-42 and CFP::RHO-1 were respectively done on *sajIs29*- and *sajIs30*-carrying embryos by capturing 19–21 Z-planes of 0.400 μm each every 2 min during 40 min. Acquisitions for ruffle ratios were obtained on embryos of other transgenic animals described in the Results by capturing 21 Z-planes of 0.400 μm each every 62 sec (no delay) during 1 h. Acquisition on *unc-119(ed3);sajIs31[lin-26p::wsp-1(CRIB)::*

mCherry];mcIs50[lin-26p::VAB-10(ABD)::GFP + myo-2p::GFP] and *rga-7(ok1498);unc-119(ed3); sajIs31[lin-26p::wsp-1(CRIB)::mCherry]; mcIs50[lin-26p::VAB-10(ABD)::GFP + myo-2p::GFP]* were done using a swept-field confocal microscope with a 100× oil CFI NA 1.45 Plan Apochromat λ objective. Image and statistical analysis were done as detailed in Supplementary Methods.

Supplementary material

Supplementary material is available at *Journal of Molecular Cell Biology* online.

Acknowledgements

The authors thank Drs Paul Mains (University of Calgary, Calgary, Canada) and Ian Hope (Leeds University, UK) for providing material and Drs Marc Lussier (UQAM, Montréal, Canada) and Alisa Piekny (Concordia University) for helpful discussions and comments on the manuscript. Some of the strains were provided by the *Caenorhabditis* Genetics Center, which is funded by NIH Office of Research Infrastructure Programs (P40 OD010440).

Funding

This work was supported by grants from the Natural Sciences and Engineering Research Council (NSERC) of Canada and the Canada Foundation for Innovation. S.J. is funded by Canada Research Chair program. M.-H.O. and E.M. are funded by the FARE UQAM research fellowship.

Conflict of interest: none declared.

References

Bastock, R., and Strutt, D. (2007). The planar polarity pathway promotes coordinated cell migration during Drosophila oogenesis. Development *134*, 3055–3064.

Benink, H.A., and Bement, W.M. (2005). Concentric zones of active RhoA and Cdc42 around single cell wounds. J. Cell Biol. *168*, 429–439.

Berezikov, E., Bargmann, C.I., and Plasterk, R.H. (2004). Homologous gene targeting in Caenorhabditis elegans by biolistic transformation. Nucleic Acids Res. *32*, e40.

Brenner, S. (1974). The genetics of Caenorhabditis elegans. Genetics *77*, 71–94.

Bu, W., Lim, K.B., Yu, Y.H., et al. (2010). Cdc42 interaction with N-WASP and Toca-1 regulates membrane tubulation, vesicle formation and vesicle motility: implications for endocytosis. PLoS One *5*, e12153.

Cansado, J., Soto, T., Gacto, M., et al. (2010). Rga4, a Rho-GAP from fission yeast: finding specificity within promiscuity. Commun. Integr. Biol. *3*, 436–439.

Chisholm, A.D., and Hardin, J. (2005). Epidermal morphogenesis. WormBook, 1–22.

Citi, S., Guerrera, D., Spadaro, D., et al. (2014). Epithelial junctions and Rho family GTPases: the zonular signalosome. Small GTPases *5*, 1–15.

Elbediwy, A., Zihni, C., Terry, S.J., et al. (2012). Epithelial junction formation requires confinement of Cdc42 activity by a novel SH3BP1 complex. J. Cell Biol. *198*, 677–693.

Fidyk, N., Wang, J.B., and Cerione, R.A. (2006). Influencing cellular transformation by modulating the rates of GTP hydrolysis by Cdc42. Biochemistry *45*, 7750–7762.

Fotopoulos, N., Wernike, D., Chen, Y., et al. (2013). Caenorhabditis elegans anillin (ani-1) regulates neuroblast cytokinesis and epidermal morphogenesis during embryonic development. Dev. Biol. *383*, 61–74.

Friedl, P., and Gilmour, D. (2009). Collective cell migration in morphogenesis, regeneration and cancer. Nat. Rev. Mol. Cell Biol. *10*, 445–457.

Friedl, P., Wolf, K., and Zegers, M.M. (2014). Rho-directed forces in collective migration. Nat. Cell Biol. *16*, 208–210.

Giuliani, C., Troglio, F., Bai, Z., et al. (2009). Requirements for F-BAR proteins TOCA-1 and TOCA-2 in actin dynamics and membrane trafficking during Caenorhabditis elegans oocyte growth and embryonic epidermal morphogenesis. PLoS Genet. *5*, e1000675.

Harris, K.P., and Tepass, U. (2010). Cdc42 and vesicle trafficking in polarized cells. Traffic *11*, 1272–1279.

Hidalgo-Carcedo, C., Hooper, S., Chaudhry, S.I., et al. (2011). Collective cell migration requires suppression of actomyosin at cell-cell contacts mediated by DDR1 and the cell polarity regulators Par3 and Par6. Nat. Cell Biol. *13*, 49–58.

Humphries, A.C., Donnelly, S.K., and Way, M. (2014). Cdc42 and the Rho GEF intersectin-1 collaborate with Nck to promote N-WASP-dependent actin polymerisation. J. Cell Sci. *127*, 673–685.

Hussain, N.K., Jenna, S., Glogauer, M., et al. (2001). Endocytic protein intersectin-l regulates actin assembly via Cdc42 and N-WASP. Nat. Cell Biol. *3*, 927–932.

Jenna, S., and Lamarche-Vane, N. (2003). The superfamily of Rho GTPase-activating-proteins. In: Symons, M. (ed). Rho GTPases. New York: Kluwer Academic, 68–95.

Jenna, S., Caruso, M.E., Emadali, A., et al. (2005). Regulation of membrane trafficking by a novel Cdc42-related protein in Caenorhabditis elegans epithelial cells. Mol. Biol. Cell *16*, 1629–1639.

Kamath, R.S., Fraser, A.G., Dong, Y., et al. (2003). Systematic functional analysis of the Caenorhabditis elegans genome using RNAi. Nature *421*, 231–237.

Khursheed, M., and Bashyam, M.D. (2014). Apico-basal polarity complex and cancer. J. Biosci. *39*, 145–155.

Kovacs, E.M., Verma, S., Thomas, S.G., et al. (2011). Tuba and N-WASP function cooperatively to position the central lumen during epithelial cyst morphogenesis. Cell Adh. Migr. *5*, 344–350.

Kumfer, K.T., Cook, S.J., Squirrell, J.M., et al. (2010). CGEF-1 and CHIN-1 regulate CDC-42 activity during asymmetric division in the Caenorhabditis elegans embryo. Mol. Biol. Cell *21*, 266–277.

Leibfried, A., Fricke, R., Morgan, M.J., et al. (2008). Drosophila Cip4 and WASp define a branch of the Cdc42-Par6-aPKC pathway regulating E-cadherin endocytosis. Curr. Biol. *18*, 1639–1648.

Lin, L., Tran, T., Hu, S., et al. (2012). RHGF-2 is an essential Rho-1 specific RhoGEF that binds to the multi-PDZ domain scaffold protein MPZ-1 in Caenorhabditis elegans. PLoS One *7*, e31499.

Lundquist, E.A., Reddien, P.W., Hartwieg, E., et al. (2001). Three C. elegans Rac proteins and several alternative Rac regulators control axon guidance, cell migration and apoptotic cell phagocytosis. Development *128*, 4475–4488.

Machacek, M., Hodgson, L., Welch, C., et al. (2009). Coordination of Rho GTPase activities during cell protrusion. Nature *461*, 99–103.

Martin, E., Harel, S., Nkengfac, B., et al. (2014). pix-1 controls early elongation in parallel with mel-11 and let-502 in Caenorhabditis elegans. PLoS One *9*, e94684.

Osmani, N., Peglion, F., Chavrier, P., et al. (2010). Cdc42 localization and cell polarity depend on membrane traffic. J. Cell Biol. *191*, 1261–1269.

Park, H.-O., and Bi, E. (2007). Central roles of small GTPases in the development of cell polarity in yeast and beyond. Microbiol. Mol. Biol. Rev. *71*, 48–96.

Pertz, O. (2010). Spatio-temporal Rho GTPase signaling—where are we now? J. Cell Sci. *123*, 1841–1850.

Pichot, C.S., Arvanitis, C., Hartig, S.M., et al. (2010). Cdc42-interacting protein 4 promotes breast cancer cell invasion and formation of invadopodia through activation of N-WASp. Cancer Res. *70*, 8347–8356.

Piekny, A.J., Wissmann, A., and Mains, P.E. (2000). Embryonic morphogenesis in Caenorhabditis elegans integrates the activity of LET-502 Rho-binding kinase, MEL-11 myosin phosphatase, DAF-2 insulin receptor and FEM-2 PP2c phosphatase. Genetics *156*, 1671–1689.

Reffay, M., Parrini, M.C., Cochet-Escartin, O., et al. (2014). Interplay of RhoA and mechanical forces in collective cell migration driven by leader cells. Nat. Cell Biol. *16*, 217–223.

Sawa, M., and Takenawa, T. (2006). Caenorhabditis elegans WASP-interacting protein homologue WIP-1 is involved in morphogenesis through maintenance of WSP-1 protein levels. Biochem. Biophys. Res. Commun. *340*, 709–717.

Sawa, M., Suetsugu, S., Sugimoto, A., et al. (2003). Essential role of the C. elegans Arp2/3 complex in cell migration during ventral enclosure. J. Cell Sci. *116*, 1505–1518.

Sheffield, M., Loveless, T., Hardin, J., et al. (2007). C. elegans enabled exhibits novel interactions with N-WASP, Abl, and cell-cell junctions. Curr. Biol. *17*, 1791–1796.

Takai, Y., Sasaki, T., and Matozaki, T. (2001). Small GTP-binding proteins. Physiol. Rev. *81*, 153–208.

Tan, Pei Y., and Zaidel-Bar, R. (2015). Transient membrane localization of SPV-1 drives cyclical actomyosin contractions in the C. elegans spermatheca. Curr. Biol. *25*, 141–151.

Williams-Masson, E.M., Malik, A.N., and Hardin, J. (1997). An actin-mediated two-step mechanism is required for ventral enclosure of the C. elegans hypodermis. Development *124*, 2889–2901.

Withee, J., Galligan, B., Hawkins, N., et al. (2004). Caenorhabditis elegans WASP and Ena/VASP proteins play compensatory roles in morphogenesis and neuronal cell migration. Genetics *167*, 1165–1176.

Wu, C.-F., and Lew, D.J. (2013). Beyond symmetry breaking: competition and negative feedback in GTPase regulation. Trends Cell Biol. *23*, 476–483.

REFERENCES

Abe, K. et M. Takeichi (2008). EPLIN mediates linkage of the cadherin catenin complex to F-actin and stabilizes the circumferential actin belt. *Proc Natl Acad Sci U S A* 105(1): 13-19.

Aghazadeh, B., W. E. Lowry, X. Y. Huang et M. K. Rosen (2000). Structural basis for relief of autoinhibition of the Dbl homology domain of proto-oncogene Vav by tyrosine phosphorylation. *Cell* 102(5): 625-633.

Ahmed, S., J. Lee, R. Kozma, A. Best, C. Monfries et L. Lim (1993). A novel functional target for tumor-promoting phorbol esters and lysophosphatidic acid. The p21rac-GTPase activating protein n-chimaerin. *J Biol Chem* 268(15): 10709-10712.

Akhtar, N. et N. A. Hotchin (2001). RAC1 regulates adherens junctions through endocytosis of E-cadherin. *Mol Biol Cell* 12(4): 847-862.

Alberts, A. S., H. Qin, H. S. Carr et J. A. Frost (2005). PAK1 negatively regulates the activity of the Rho exchange factor NET1. *J Biol Chem* 280(13): 12152-12161.

Alexandrova, A. Y., K. Arnold, S. Schaub, J. M. Vasiliev, J. J. Meister, A. D. Bershadsky et A. B. Verkhovsky (2008). Comparative dynamics of retrograde actin flow and focal adhesions: formation of nascent adhesions triggers transition from fast to slow flow. *PLoS One* 3(9): e3234.

Amann, K. J. et T. D. Pollard (2001). The Arp2/3 complex nucleates actin filament branches from the sides of pre-existing filaments. *Nat Cell Biol* 3(3): 306-310.

Amano, M., M. Ito, K. Kimura, Y. Fukata, K. Chihara, T. Nakano, Y. Matsuura et K. Kaibuchi (1996). Phosphorylation and activation of myosin by Rho-associated kinase (Rho-kinase). *J Biol Chem* 271(34): 20246-20249.

Andersen, E. C., T. C. Shimko, J. R. Crissman, R. Ghosh, J. S. Bloom, H. S. Seidel, J. P. Gerke et L. Kruglyak (2015). A Powerful New Quantitative Genetics Platform, Combining *Caenorhabditis elegans* High-Throughput Fitness Assays with a Large Collection of Recombinant Strains. *G3 (Bethesda)* 5(5): 911-920.

Anderson, D. C., J. S. Gill, R. M. Cinalli et J. Nance (2008). Polarization of the C. elegans embryo by RhoGAP-mediated exclusion of PAR-6 from cell contacts. *Science* 320(5884): 1771-1774.

Ando, R., H. Hama, M. Yamamoto-Hino, H. Mizuno et A. Miyawaki (2002). An optical marker based on the UV-induced green-to-red photoconversion of a fluorescent protein. *Proc Natl Acad Sci U S A* 99(20): 12651-12656.

Audebert, S., C. Navarro, C. Nourry, S. Chasserot-Golaz, P. Lecine, Y. Bellaiche, J. L. Dupont, R. T. Premont, C. Sempere, J. M. Strub, A. Van Dorsselaer, N. Vitale et J. P. Borg (2004). Mammalian Scribble forms a tight complex with the betaPIX exchange factor. *Curr Biol* 14(11): 987-995.

Avery, S. V. (2005). Cell individuality: the bistability of competence development. *Trends Microbiol* 13(10): 459-462.

Bagrodia, S., S. J. Taylor, K. A. Jordon, L. Van Aelst et R. A. Cerione (1998). A novel regulator of p21-activated kinases. *J Biol Chem* 273(37): 23633-23636.

Balaban, N. Q., J. Merrin, R. Chait, L. Kowalik et S. Leibler (2004). Bacterial persistence as a phenotypic switch. *Science* 305(5690): 1622-1625.

Balklava, Z., S. Pant, H. Fares et B. D. Grant (2007). Genome-wide analysis identifies a general requirement for polarity proteins in endocytic traffic. *Nat Cell Biol* 9(9): 1066-1073.

Ballestrem, C., N. Erez, J. Kirchner, Z. Kam, A. Bershadsky et B. Geiger (2006). Molecular mapping of tyrosine-phosphorylated proteins in focal adhesions using fluorescence resonance energy transfer. *J Cell Sci* 119(Pt 5): 866-875.

Barac, A., J. Basile, J. Vazquez-Prado, Y. Gao, Y. Zheng et J. S. Gutkind (2004). Direct interaction of p21-activated kinase 4 with PDZ-RhoGEF, a G protein-linked Rho guanine exchange factor. *J Biol Chem* 279(7): 6182-6189.

Baum, B. et M. Georgiou (2011). Dynamics of adherens junctions in epithelial establishment, maintenance, and remodeling. *J Cell Biol* 192(6): 907-917.

Baum, B. et N. Perrimon (2001). Spatial control of the actin cytoskeleton in *Drosophila* epithelial cells. *Nat Cell Biol* 3(10): 883-890.

Beningo, K. A., M. Dembo, I. Kaverina, J. V. Small et Y. L. Wang (2001). Nascent focal adhesions are responsible for the generation of strong propulsive forces in migrating fibroblasts. *J Cell Biol* 153(4): 881-888.

Berezikov, E., C. I. Bargmann et R. H. Plasterk (2004). Homologous gene targeting in *Caenorhabditis elegans* by biolistic transformation. *Nucleic Acids Res* 32(4): e40.

Bertet, C., L. Sulak et T. Lecuit (2004). Myosin-dependent junction remodelling controls planar cell intercalation and axis elongation. *Nature* 429(6992): 667-671.

Betapudi, V. (2010). Myosin II motor proteins with different functions determine the fate of lamellipodia extension during cell spreading. *PLoS One* 5(1): e8560.

Bilder, D., M. Li et N. Perrimon (2000). Cooperative regulation of cell polarity and growth by *Drosophila* tumor suppressors. *Science* 289(5476): 113-116.

Bilder, D. et N. Perrimon (2000). Localization of apical epithelial determinants by the basolateral PDZ protein Scribble. *Nature* 403(6770): 676-680.

Bhowmick, N.A., M. Ghiassi, A. Bakin, M. Aakre, C.A. Lundquist, M.E. Engel, C.L. Arteaga et H.L. Moses (2001) Transforming growth factor-beta1 mediates epithelial to mesenchymal transdifferentiation through a RhoA-dependent mechanism. *Mol Biol Cell*, (1): 27-36.

Blankenship, J. T., S. T. Backovic, J. S. Sanny, O. Weitz et J. A. Zallen (2006). Multicellular rosette formation links planar cell polarity to tissue morphogenesis. *Dev Cell* 11(4): 459-470.

Bokoch, G. M. (2003). Biology of the p21-activated kinases. *Annu Rev Biochem* 72: 743-781.

Bolis, A., S. Corbetta, A. Cioce et I. de Curtis (2003). Differential distribution of Rac1 and Rac3 GTPases in the developing mouse brain: implications for a role of Rac3 in Purkinje cell differentiation. *Eur J Neurosci* 18(9): 2417-2424.

Borges, R. M., M. L. Lamers, F. L. Forti, M. F. Santos et C. Y. Yan (2011). Rho signaling pathway and apical constriction in the early lens placode. *Genesis* 49(5): 368-379.

Bosher, J. M., B. S. Hahn, R. Legouis, S. Sookhareea, R. M. Weimer, A. Gansmuller, A. D. Chisholm, A. M. Rose, J. L. Bessereau et M. Labouesse (2003). The *Caenorhabditis elegans* vab-10 spectraplakin isoforms protect the epidermis against internal and external forces. *J Cell Biol* 161(4): 757-768.

Boulier, E. L. et S. Jenna (2009). Genetic dissection of Caenorhabditis elegans embryogenesis using RNA interference and flow cytometry. *Methods Mol Biol* 550: 181-194.

Brenner, S. (1974). The genetics of *Caenorhabditis elegans*. *Genetics* 77(1): 71-94.

Bugaj, L. J., A. T. Choksi, C. K. Mesuda, R. S. Kane et D. V. Schaffer (2013). Optogenetic protein clustering and signaling activation in mammalian cells. *Nat Methods* 10(3): 249-252.

Burnette, D. T., S. Manley, P. Sengupta, R. Sougrat, M. W. Davidson, B. Kachar et J. Lippincott-Schwartz (2011). A role for actin arcs in the leading-edge advance of migrating cells. *Nat Cell Biol* 13(4): 371-381.

Burridge, K., K. Fath, T. Kelly, G. Nuckolls et C. Turner (1988). Focal adhesions: transmembrane junctions between the extracellular matrix and the cytoskeleton. *Annu Rev Cell Biol* 4: 487-525.

Bustelo, X. R., V. Sauzeau et I. M. Berenjeno (2007). GTP-binding proteins of the Rho/Rac family: regulation, effectors and functions in vivo. *Bioessays* 29(4): 356-370.

Bustos, R. I., M. A. Forget, J. E. Settleman et S. H. Hansen (2008). Coordination of Rho and Rac GTPase function via p190B RhoGAP. *Curr Biol* 18(20): 1606-1611.

Byrne, K. M., N. Monsefi, J. C. Dawson, A. Degasperi, J. C. Bukowski-Wills, N. Volinsky, M. Dobrzynski, M. R. Birtwistle, M. A. Tsyganov, A. Kiyatkin, K. Kida, A. J. Finch, N. O. Carragher, W. Kolch, L. K. Nguyen, A. von Kriegsheim et B. N. Kholodenko (2016). Bistability in the Rac1, PAK, and RhoA Signaling Network Drives Actin Cytoskeleton Dynamics and Cell Motility Switches. *Cell Syst* 2(1): 38-48.

Carr, H. S., Y. Zuo, W. Oh et J. A. Frost (2013). Regulation of focal adhesion kinase activation, breast cancer cell motility, and amoeboid invasion by the RhoA guanine nucleotide exchange factor Net1. *Mol Cell Biol* 33(14): 2773-2786.

Casey, P. J. et M. C. Seabra (1996). Protein prenyltransferases. *J Biol Chem* 271(10): 5289-5292.

Chan, B. G., S. K. Rocheleau, R. B. Smit et P. E. Mains (2015). The Rho guanine exchange factor RHGF-2 acts through the Rho-binding kinase LET-502 to mediate embryonic elongation in C. elegans. *Dev Biol* 405(2): 250-259.

Chan, E. et J. Nance (2013). Mechanisms of CDC-42 activation during contact-induced cell polarization. *J Cell Sci* 126(Pt 7): 1692-1702.

Chang, F., C. A. Lemmon, D. Park et L. H. Romer (2007). FAK potentiates Rac1 activation and localization to matrix adhesion sites: a role for betaPIX. *Mol Biol Cell* 18(1): 253-264.

Charras, G. et E. Paluch (2008). Blebs lead the way: how to migrate without lamellipodia. *Nat Rev Mol Cell Biol* 9(9): 730-736.

Chauhan, B., T. Plageman, M. Lou et R. Lang (2015). Epithelial morphogenesis: the mouse eye as a model system. *Curr Top Dev Biol* 111: 375-399.

Chauhan, B. K., M. Lou, Y. Zheng et R. A. Lang (2011). Balanced Rac1 and RhoA activities regulate cell shape and drive invagination morphogenesis in epithelia. *Proc Natl Acad Sci U S A* 108(45): 18289-18294.

Chen, W., S. Chen, S. F. Yap et L. Lim (1996). The *Caenorhabditis elegans* p21-activated kinase (CePAK) colocalizes with CeRac1 and CDC42Ce at hypodermal cell boundaries during embryo elongation. *J Biol Chem* 271(42): 26362-26368.

Chen, X. et I. G. Macara (2005). Par-3 controls tight junction assembly through the Rac exchange factor Tiam1. *Nat Cell Biol* 7(3): 262-269.

Chin-Sang, I. D. et A. D. Chisholm (2000). Form of the worm: genetics of epidermal morphogenesis in *C. elegans*. *Trends Genet* 16(12): 544-551.

Chisholm, A. D. et J. Hardin (2005). Epidermal morphogenesis. *WormBook*: 1-22.

Cho, H.J., J. Yoo (2007). Rho activation is required for transforming growth factor-beta-induced epithelial-mesenchymal transition in lens epithelial cells. *Cell Biol Int* 31(10):1225-1230

Choi, C. K., M. Vicente-Manzanares, J. Zareno, L. A. Whitmore, A. Mogilner et A. R. Horwitz (2008). Actin and alpha-actinin orchestrate the assembly and maturation of nascent adhesions in a myosin II motor-independent manner. *Nat Cell Biol* 10(9): 1039-1050.

Ciarletta, P., M. Ben Amar et M. Labouesse (2009). Continuum model of epithelial morphogenesis during *Caenorhabditis elegans* embryonic elongation. *Philos Trans A Math Phys Eng Sci* 367(1902): 3379-3400.

Citi, S., D. Guerrera, D. Spadaro et J. Shah (2014). Epithelial junctions and Rho family GTPases: the zonular signalosome. *Small GTPases* 5(4): 1-15.

Colic, M., D. Matanovic, L. Hegedis et A. Dujic (1988). Heterogeneity of rat thymic epithelium defined by monoclonal anti-keratin antibodies. *Thymus* 12(2): 123-130.

Collinet, C., M. Rauzi, P. F. Lenne et T. Lecuit (2015). Local and tissue-scale forces drive oriented junction growth during tissue extension. *Nat Cell Biol* 17(10): 1247-1258.

Corsi, A. K., B. Wightman et M. Chalfie (2015). A Transparent Window into Biology: A Primer on *Caenorhabditis elegans*. *Genetics* 200(2): 387-407.

Costa, M., W. Raich, C. Agbunag, B. Leung, J. Hardin et J. R. Priess (1998). A putative catenin-cadherin system mediates morphogenesis of the *Caenorhabditis elegans* embryo. *J Cell Biol* 141(1): 297-308.

Cox, E. A. et J. Hardin (2004). Sticky worms: adhesion complexes in *C. elegans*. *J Cell Sci* 117(Pt 10): 1885-1897.

Cramer, L. P., M. Siebert et T. J. Mitchison (1997). Identification of novel graded polarity actin filament bundles in locomoting heart fibroblasts: implications for the generation of motile force. *J Cell Biol* 136(6): 1287-1305.

D'Amico, G., S. D. Robinson, M. Germain, L. E. Reynolds, G. J. Thomas, G. Elia, G. Saunders, M. Fruttiger, V. Tybulewicz, G. Mavria et K. M. Hodivala-Dilke (2010). Endothelial-Rac1 is not required for tumor angiogenesis unless alphavbeta3-integrin is absent. *PLoS One* 5(3): e9766.

Daniels, R. H., F. T. Zenke et G. M. Bokoch (1999). alphaPix stimulates p21-activated kinase activity through exchange factor-dependent and -independent mechanisms. *J Biol Chem* 274(10): 6047-6050.

de Jong, I. G., P. Haccou et O. P. Kuipers (2011). Bet hedging or not? A guide to proper classification of microbial survival strategies. *Bioessays* 33(3): 215-223.

Delorme-Walker, V. D., J. R. Peterson, J. Chernoff, C. M. Waterman, G. Danuser, C. DerMardirossian et G. M. Bokoch (2011). Pak1 regulates focal adhesion strength, myosin IIA distribution, and actin dynamics to optimize cell migration. *J Cell Biol* 193(7): 1289-1303.

Delorme, V., M. Machacek, C. DerMardirossian, K. L. Anderson, T. Wittmann, D. Hanein, C. Waterman-Storer, G. Danuser et G. M. Bokoch (2007). Cofilin activity downstream of Pak1 regulates cell protrusion efficiency by organizing lamellipodium and lamella actin networks. *Dev Cell* 13(5): 646-662.

Deng, W. M. et M. Bownes (1998). Patterning and morphogenesis of the follicle cell epithelium during *Drosophila* oogenesis. *Int J Dev Biol* 42(4): 541-552.

Dent, P., L. K. MacDougall, C. MacKintosh, D. G. Campbell et P. Cohen (1992). A myofibrillar protein phosphatase from rabbit skeletal muscle contains the beta isoform of protein phosphatase-1 complexed to a regulatory subunit which greatly enhances the dephosphorylation of myosin. *Eur J Biochem* 210(3): 1037-1044.

Didsbury, J., R. F. Weber, G. M. Bokoch, T. Evans et R. Snyderman (1989). rac, a novel ras-related family of proteins that are botulinum toxin substrates. *J Biol Chem* 264(28): 16378-16382.

Dineen, A. et J. Gaudet (2014). TGF-beta signaling can act from multiple tissues to regulate *C. elegans* body size. *BMC Dev Biol* 14: 43.

Ding, M., W. M. Woo et A. D. Chisholm (2004). The cytoskeleton and epidermal morphogenesis in C. elegans. *Exp Cell Res* 301(1): 84-90.

Diogon, M., F. Wissler, S. Quintin, Y. Nagamatsu, S. Sookhareea, F. Landmann, H. Hutter, N. Vitale et M. Labouesse (2007). The RhoGAP RGA-2 and LET-502/ROCK achieve a balance of actomyosin-dependent forces in *C. elegans* epidermis to control morphogenesis. *Development* 134(13): 2469-2479.

Dobens, L. L. et L. A. Raftery (2000). Integration of epithelial patterning and morphogenesis in *Drosophila* ovarian follicle cells. *Dev Dyn* 218(1): 80-93.

Dong, J. M., T. Leung, E. Manser et L. Lim (2002). Cdc42 antagonizes inductive action of cAMP on cell shape, via effects of the myotonic dystrophy kinase-related Cdc42-binding kinase (MRCK) on myosin light chain phosphorylation. *Eur J Cell Biol* 81(4): 231-242.

Dow, L. E., J. S. Kauffman, J. Caddy, K. Zarbalis, A. S. Peterson, S. M. Jane, S. M. Russell et P. O. Humbert (2007). The tumour-suppressor Scribble dictates cell polarity during directed epithelial migration: regulation of Rho GTPase recruitment to the leading edge. *Oncogene* 26(16): 2272-2282.

Drees, F., S. Pokutta, S. Yamada, W. J. Nelson et W. I. Weis (2005). Alpha-catenin is a molecular switch that binds E-cadherin-beta-catenin and regulates actin-filament assembly. *Cell* 123(5): 903-915.

Duan, L., G. Chen, S. Virmani, G. Ying, S. M. Raja, B. M. Chung, M. A. Rainey, M. Dimri, C. F. Ortega-Cava, X. Zhao, R. J. Clubb, C. Tu, A. L. Reddi, M. Naramura, V. Band et H. Band (2010). Distinct roles for Rho versus Rac/Cdc42 GTPases downstream of Vav2 in regulating mammary epithelial acinar architecture. *J Biol Chem* 285(2): 1555-1568.

Dyer, J. O., R. S. Demarco et E. A. Lundquist (2010). Distinct roles of Rac GTPases and the UNC-73/Trio and PIX-1 Rac GTP exchange factors in neuroblast protrusion and migration in *C. elegans*. *Small GTPases* 1(1): 44-61.

Edwards, P. A. (1985). Heterogeneous expression of cell-surface antigens in normal epithelia and their tumours, revealed by monoclonal antibodies. *Br J Cancer* 51(2): 149-160.

Ehrlich, J. S., M. D. Hansen et W. J. Nelson (2002). Spatio-temporal regulation of Rac1 localization and lamellipodia dynamics during epithelial cell-cell adhesion. *Dev Cell* 3(2): 259-270.

Engl, W., B. Arasi, L. L. Yap, J. P. Thiery et V. Viasnoff (2014). Actin dynamics modulate mechanosensitive immobilization of E-cadherin at adherens junctions. *Nat Cell Biol* 16(6): 587-594.

Etienne-Manneville, S. et Hall, A. (2002). Rho GTPases in cell biology. *Nature* 420: 629-635

Etienne-Manneville, S. (2004). Cdc42--the centre of polarity. *J Cell Sci* 117(Pt 8): 1291-1300.

Ewald, A. J., A. Brenot, M. Duong, B. S. Chan et Z. Werb (2008). Collective epithelial migration and cell rearrangements drive mammary branching morphogenesis. *Dev Cell* 14(4): 570-581.

Farooqui, R. et G. Fenteany (2005). Multiple rows of cells behind an epithelial wound edge extend cryptic lamellipodia to collectively drive cell-sheet movement. *J Cell Sci* 118(Pt 1): 51-63.

Feng, Q., D. Baird, X. Peng, J. Wang, T. Ly, J. L. Guan et R. A. Cerione (2006). Cool-1 functions as an essential regulatory node for EGF receptor- and Src-mediated cell growth. *Nat Cell Biol* 8(9): 945-956.

Feng, Q., D. Baird, S. Yoo, M. Antonyak et R. A. Cerione (2010). Phosphorylation of the cool-1/beta-Pix protein serves as a regulatory signal for the migration and invasive activity of Src-transformed cells. *J Biol Chem* 285(24): 18806-18816.

Firestein, B. L. et C. Rongo (2001). DLG-1 is a MAGUK similar to SAP97 and is required for adherens junction formation. *Mol Biol Cell* 12(11): 3465-3475.

Flanders, J. A., Q. Feng, S. Bagrodia, M. T. Laux, A. Singavarapu et R. A. Cerione (2003). The Cbl proteins are binding partners for the Cool/Pix family of p21-activated kinase-binding proteins. *FEBS Lett* 550(1-3): 119-123.

Francis, G. R. et R. H. Waterston (1985). Muscle organization in *Caenorhabditis elegans*: localization of proteins implicated in thin filament attachment and I-band organization. *J Cell Biol* 101(4): 1532-1549.

Francis, R. et R. H. Waterston (1991). Muscle cell attachment in *Caenorhabditis elegans*. *J Cell Biol* 114(3): 465-479.

Frank, S. R., J. H. Bell, M. Frodin et S. H. Hansen (2012). A betaPIX-PAK2 complex confers protection against Scrib-dependent and cadherin-mediated apoptosis. *Curr Biol* 22(19): 1747-1754.

Frank, S. R. et S. H. Hansen (2008). The PIX-GIT complex: a G protein signaling cassette in control of cell shape. *Semin Cell Dev Biol* 19(3): 234-244.

Fricke, R., C. Gohl, E. Dharmalingam, A. Grevelhorster, B. Zahedi, N. Harden, M. Kessels, B. Qualmann et S. Bogdan (2009). *Drosophila* Cip4/Toca-1 integrates

membrane trafficking and actin dynamics through WASP and SCAR/WAVE. *Curr Biol* 19(17): 1429-1437.

Friedl, P. et K. Wolf (2003). Tumour-cell invasion and migration: diversity and escape mechanisms. *Nat Rev Cancer* 3(5): 362-374.

Fristrom, D. (1988). The cellular basis of epithelial morphogenesis. A review. *Tissue Cell* 20(5): 645-690.

Galletta, B. J., D. Y. Chuang et J. A. Cooper (2008). Distinct roles for Arp2/3 regulators in actin assembly and endocytosis. *PLoS Biol* 6(1): e1.

Gally, C., F. Wissler, H. Zahreddine, S. Quintin, F. Landmann et M. Labouesse (2009). Myosin II regulation during C. elegans embryonic elongation: LET-502/ROCK, MRCK-1 and PAK-1, three kinases with different roles. *Development* 136(18): 3109-3119.

Gatti, A., Z. Huang, P. T. Tuazon et J. A. Traugh (1999). Multisite autophosphorylation of p21-activated protein kinase gamma-PAK as a function of activation. *J Biol Chem* 274(12): 8022-8028.

Gavard, J. et J. S. Gutkind (2006). VEGF controls endothelial-cell permeability by promoting the beta-arrestin-dependent endocytosis of VE-cadherin. *Nat Cell Biol* 8(11): 1223-1234.

Georgiou, M. et B. Baum (2010). Polarity proteins and Rho GTPases cooperate to spatially organise epithelial actin-based protrusions. *J Cell Sci* 123(Pt 7): 1089-1098.

Georgiou, M., E. Marinari, J. Burden et B. Baum (2008). Cdc42, Par6, and aPKC regulate Arp2/3-mediated endocytosis to control local adherens junction stability. *Curr Biol* 18(21): 1631-1638.

Gibson, M. C., A. B. Patel, R. Nagpal et N. Perrimon (2006). The emergence of geometric order in proliferating metazoan epithelia. *Nature* 442(7106): 1038-1041.

Gibson, W. T. et M. C. Gibson (2009). Cell topology, geometry, and morphogenesis in proliferating epithelia. *Curr Top Dev Biol* 89: 87-114.

Giepmans, B.N., S.C. van Ijzendoorn (2009). Epithelial cell-cell junctions and plasma membrane domains. *Biochim Biophys Acta* 1788, (4):820-831.

Goicoechea, S. M., S. Awadia et R. Garcia-Mata (2014). I'm coming to GEF you: Regulation of RhoGEFs during cell migration. *Cell Adh Migr* 8(6): 535-549.

Gomes, E. R., S. Jani et G. G. Gundersen (2005). Nuclear movement regulated by Cdc42, MRCK, myosin, and actin flow establishes MTOC polarization in migrating cells. *Cell* 121(3): 451-463.

Guglielmi, G., J. D. Barry, W. Huber et S. De Renzis (2015). An Optogenetic Method to Modulate Cell Contractility during Tissue Morphogenesis. *Dev Cell* 35(5): 646-660.

Guilluy, C., R. Garcia-Mata et K. Burridge (2011). Rho protein crosstalk: another social network? *Trends Cell Biol* 21(12): 718-726.

Gumbiner, B. M. (2000). Regulation of cadherin adhesive activity. *J Cell Biol* 148(3): 399-404.

Guo, W. H. et Y. L. Wang (2007). Retrograde fluxes of focal adhesion proteins in response to cell migration and mechanical signals. *Mol Biol Cell* 18(11): 4519-4527.

Hammer, A., P. Oladimeji, L. E. De Las Casas et M. Diakonova (2015). Phosphorylation of tyrosine 285 of PAK1 facilitates betaPIX/GIT1 binding and adhesion turnover. *FASEB J* 29(3): 943-959.

Harden, N., M. Ricos, Y. M. Ong, W. Chia et L. Lim (1999). Participation of small GTPases in dorsal closure of the *Drosophila* embryo: distinct roles for Rho subfamily proteins in epithelial morphogenesis. *J Cell Sci* 112 (Pt 3): 273-284.

Harris, K. P. et U. Tepass (2008). Cdc42 and Par proteins stabilize dynamic adherens junctions in the *Drosophila* neuroectoderm through regulation of apical endocytosis. *J Cell Biol* 183(6): 1129-1143.

Havrylenko, S., P. Noguera, M. Abou-Ghali, J. Manzi, F. Faqir, A. Lamora, C. Guerin, L. Blanchoin et J. Plastino (2015). WAVE binds Ena/VASP for enhanced Arp2/3 complex-based actin assembly. *Mol Biol Cell* 26(1): 55-65.

Heasman, S. J. et A. J. Ridley (2008). Mammalian Rho GTPases: new insights into their functions from in vivo studies. *Nat Rev Mol Cell Biol* 9(9): 690-701.

Heid, P. J., W. B. Raich, R. Smith, W. A. Mohler, K. Simokat, S. B. Gendreau, J. H. Rothman et J. Hardin (2001). The zinc finger protein DIE-1 is required for late events during epithelial cell rearrangement in *C. elegans*. *Dev Biol* 236(1): 165-180.

Hetherington, S., C. Gally, J. A. Fritz, J. Polanowska, J. Reboul, Y. Schwab, H. Zahreddine, C. Behm et M. Labouesse (2011). PAT-12, a potential anti-nematode target, is a new spectraplakin partner essential for *Caenorhabditis elegans* hemidesmosome integrity and embryonic morphogenesis. *Dev Biol* 350(2): 267-278.

Hofmann, C., M. Shepelev et J. Chernoff (2004). The genetics of Pak. *J Cell Sci* 117(Pt 19): 4343-4354.

Holland, S. L., T. Reader, P. S. Dyer et S. V. Avery (2014). Phenotypic heterogeneity is a selected trait in natural yeast populations subject to environmental stress. *Environ Microbiol* 16(6): 1729-1740.

Hresko, M. C., L. A. Schriefer, P. Shrimankar et R. H. Waterston (1999). Myotactin, a novel hypodermal protein involved in muscle-cell adhesion in Caenorhabditis elegans. *J Cell Biol* 146(3): 659-672.

Huang, R., J. P. Lian, D. Robinson et J. A. Badwey (1998). Neutrophils stimulated with a variety of chemoattractants exhibit rapid activation of p21-activated kinases (Paks): separate signals are required for activation and inactivation of paks. *Mol Cell Biol* 18(12): 7130-7138.

Hunter, M. P. et M. M. Zegers (2010). Pak1 regulates branching morphogenesis in 3D MDCK cell culture by a PIX and beta1-integrin-dependent mechanism. *Am J Physiol Cell Physiol* 299(1): C21-32.

Iino, Y. et M. Yamamoto (1998). Expression pattern of the *C. elegans* P21-activated protein kinase, CePAK. *Biochem Biophys Res Commun* 245(1): 177-184.

Itoh, M., S. Tsukita, Y. Yamazaki et H. Sugimoto (2012). Rho GTP exchange factor ARHGEF11 regulates the integrity of epithelial junctions by connecting ZO-1 and RhoA-myosin II signaling. *Proc Natl Acad Sci U S A* 109(25): 9905-9910.

Izumi, G., T. Sakisaka, T. Baba, S. Tanaka, K. Morimoto et Y. Takai (2004). Endocytosis of E-cadherin regulated by Rac and Cdc42 small G proteins through IQGAP1 and actin filaments. *J Cell Biol* 166(2): 237-248.

Jacinto, A., W. Wood, T. Balayo, M. Turmaine, A. Martinez-Arias et P. Martin (2000). Dynamic actin-based epithelial adhesion and cell matching during *Drosophila* dorsal closure. *Curr Biol* 10(22): 1420-1426.

Jacinto, A., S. Woolner et P. Martin (2002). Dynamic analysis of dorsal closure in *Drosophila*: from genetics to cell biology. *Dev Cell* 3(1): 9-19.

Jayo, A., M. Parsons et J. C. Adams (2012). A novel Rho-dependent pathway that drives interaction of fascin-1 with p-Lin-11/Isl-1/Mec-3 kinase (LIMK) 1/2 to promote fascin-1/actin binding and filopodia stability. *BMC Biol* 10: 72.

Jefferson, J. J., C. L. Leung et R. K. Liem (2004). Plakins: goliaths that link cell junctions and the cytoskeleton. *Nat Rev Mol Cell Biol* 5(7): 542-553.

Jilkine, A., A. F. Maree et L. Edelstein-Keshet (2007). Mathematical model for spatial segregation of the Rho-family GTPases based on inhibitory crosstalk. *Bull Math Biol* 69(6): 1943-1978.

Joberty, G., C. Petersen, L. Gao et I. G. Macara (2000). The cell-polarity protein Par6 links Par3 and atypical protein kinase C to Cdc42. *Nat Cell Biol* 2(8): 531-539.

Jockusch, B. M., P. Bubeck, K. Giehl, M. Kroemker, J. Moschner, M. Rothkegel, M. Rudiger, K. Schluter, G. Stanke et J. Winkler (1995). The molecular architecture of focal adhesions. *Annu Rev Cell Dev Biol* 11: 379-416.

Kalaji, R., A. P. Wheeler, J. C. Erasmus, S. Y. Lee, R. G. Endres, L. P. Cramer et V. M. Braga (2012). ROCK1 and ROCK2 regulate epithelial polarisation and geometric cell shape. *Biol Cell* 104(8): 435-451.

Kamath, R. S. et J. Ahringer (2003). Genome-wide RNAi screening in *Caenorhabditis elegans*. *Methods* 30(4): 313-321.

Kamioka, Y., S. Fukuhara, H. Sawa, K. Nagashima, M. Masuda, M. Matsuda et N. Mochizuki (2004). A novel dynamin-associating molecule, formin-binding protein 17, induces tubular membrane invaginations and participates in endocytosis. *J Biol Chem* 279(38): 40091-40099.

Kang, S., C. Y. Lee, M. Goncalves, A. D. Chisholm et P. C. Cosman (2015). Tracking epithelial cell junctions in *C. elegans* embryogenesis with active contours guided by SIFT flow. *IEEE Trans Biomed Eng* 62(4): 1020-1033.

Kanno, N., G. LeSage, S. Glaser, D. Alvaro et G. Alpini (2000). Functional heterogeneity of the intrahepatic biliary epithelium. *Hepatology* 31(3): 555-561.

Kasza, K. E., D. L. Farrell et J. A. Zallen (2014). Spatiotemporal control of epithelial remodeling by regulated myosin phosphorylation. *Proc Natl Acad Sci U S A* 111(32): 11732-11737.

Kato, T., K. Kawai, Y. Egami, Y. Kakehi et N. Araki (2014). Rac1-dependent lamellipodial motility in prostate cancer PC-3 cells revealed by optogenetic control of Rac1 activity. *PLoS One* 9(5): e97749.

Katsube, T., M. Takahisa, R. Ueda, N. Hashimoto, M. Kobayashi et S. Togashi (1998). Cortactin associates with the cell-cell junction protein ZO-1 in both *Drosophila* and mouse. *J Biol Chem* 273(45): 29672-29677.

Kawasaki, Y., R. Sato et T. Akiyama (2003). Mutated APC and Asef are involved in the migration of colorectal tumour cells. *Nat Cell Biol* 5(3): 211-215.

Keller, R. (2006a). Mechanisms of elongation in embryogenesis. *Development* 133(12): 2291-2302.

Keller, R. (2006b). Mechanisms of elongation in embryogenesis. *Development* 133(12): 2291-2302.

Kennedy, L. M., S. C. Pham et A. Grishok (2013). Nonautonomous regulation of neuronal migration by insulin signaling, DAF-16/FOXO, and PAK-1. *Cell Rep* 4(5): 996-1009.

Kholodenko, B. N. (2006). Cell-signalling dynamics in time and space. *Nat Rev Mol Cell Biol* 7(3): 165-176.

Kim, S., S. H. Lee et D. Park (2001). Leucine zipper-mediated homodimerization of the p21-activated kinase-interacting factor, beta Pix. Implication for a role in cytoskeletal reorganization. *J Biol Chem* 276(14): 10581-10584.

Kimble, J. et D. Hirsh (1979). The postembryonic cell lineages of the hermaphrodite and male gonads in *Caenorhabditis elegans*. *Dev Biol* 70(2): 396-417.

Kimura, K., M. Ito, M. Amano, K. Chihara, Y. Fukata, M. Nakafuku, B. Yamamori, J. Feng, T. Nakano, K. Okawa, A. Iwamatsu et K. Kaibuchi (1996). Regulation of myosin phosphatase by Rho and Rho-associated kinase (Rho-kinase). *Science* 273(5272): 245-248.

Kirchner, J., Z. Kam, G. Tzur, A. D. Bershadsky et B. Geiger (2003). Live-cell monitoring of tyrosine phosphorylation in focal adhesions following microtubule disruption. *J Cell Sci* 116(Pt 6): 975-986.

Kobielak, A., H. A. Pasolli et E. Fuchs (2004). Mammalian formin-1 participates in adherens junctions and polymerization of linear actin cables. *Nat Cell Biol* 6(1): 21-30.

Koh, C. G., E. J. Tan, E. Manser et L. Lim (2002). The p21-activated kinase PAK is negatively regulated by POPX1 and POPX2, a pair of serine/threonine phosphatases of the PP2C family. *Curr Biol* 12(4): 317-321.

Kolahi, K. S., P. F. White, D. M. Shreter, A. K. Classen, D. Bilder et M. R. Mofrad (2009). Quantitative analysis of epithelial morphogenesis in *Drosophila* oogenesis: New insights based on morphometric analysis and mechanical modeling. *Dev Biol* 331(2): 129-139.

Kolega, J. (2006). The role of myosin II motor activity in distributing myosin asymmetrically and coupling protrusive activity to cell translocation. *Mol Biol Cell* 17(10): 4435-4445.

Kondo, T. et S. Hayashi (2015). Mechanisms of cell height changes that mediate epithelial invagination. *Dev Growth Differ* 57(4): 313-323.

Kovacs, E. M., M. Goodwin, R. G. Ali, A. D. Paterson et A. S. Yap (2002). Cadherin-directed actin assembly: E-cadherin physically associates with the Arp2/3 complex to direct actin assembly in nascent adhesive contacts. *Curr Biol* 12(5): 379-382.

Kuo, J. C., X. Han, C. T. Hsiao, J. R. Yates, 3rd et C. M. Waterman (2011). Analysis of the myosin-II-responsive focal adhesion proteome reveals a role for beta-Pix in negative regulation of focal adhesion maturation. *Nat Cell Biol* 13(4): 383-393.

Kurokawa, K. et M. Matsuda (2005). Localized RhoA activation as a requirement for the induction of membrane ruffling. *Mol Biol Cell* 16(9): 4294-4303.

Lahuna, O., M. Quellari, C. Achard, S. Nola, G. Meduri, C. Navarro, N. Vitale, J. P. Borg et M. Misrahi (2005). Thyrotropin receptor trafficking relies on the hScrib-betaPIX-GIT1-ARF6 pathway. *EMBO J* 24(7): 1364-1374.

Lambert, M., D. Choquet et R. M. Mege (2002). Dynamics of ligand-induced, Rac1-dependent anchoring of cadherins to the actin cytoskeleton. *J Cell Biol* 157(3): 469-479.

Lammermann, T. et M. Sixt (2009). Mechanical modes of 'amoeboid' cell migration. *Curr Opin Cell Biol* 21(5): 636-644.

le Duc, Q., Q. Shi, I. Blonk, A. Sonnenberg, N. Wang, D. Leckband et J. de Rooij (2010). Vinculin potentiates E-cadherin mechanosensing and is recruited to actin-anchored sites within adherens junctions in a myosin II-dependent manner. *J Cell Biol* 189(7): 1107-1115.

Lechner, M. S. et G. R. Dressler (1997). The molecular basis of embryonic kidney development. *Mech Dev* 62(2): 105-120.

Lecuit, T. et A. S. Yap (2015). E-cadherin junctions as active mechanical integrators in tissue dynamics. *Nat Cell Biol* 17(5): 533-539.

Lee, S., H. Park, T. Kyung, N. Y. Kim, S. Kim, J. Kim et W. D. Heo (2014). Reversible protein inactivation by optogenetic trapping in cells. *Nat Methods* 11(6): 633-636.

Legouis, R., A. Gansmuller, S. Sookhareea, J. M. Bosher, D. L. Baillie et M. Labouesse (2000). LET-413 is a basolateral protein required for the assembly of adherens junctions in *Caenorhabditis elegans*. *Nat Cell Biol* 2(7): 415-422.

Lei, M., W. Lu, W. Meng, M. C. Parrini, M. J. Eck, B. J. Mayer et S. C. Harrison (2000). Structure of PAK1 in an autoinhibited conformation reveals a multistage activation switch. *Cell* 102(3): 387-397.

Leibfried, A., R. Fricke, M. J. Morgan, S. Bogdan et Y. Bellaiche (2008). Drosophila Cip4 and WASp define a branch of the Cdc42-Par6-aPKC pathway regulating E-cadherin endocytosis. *Curr Biol* 18(21): 1639-1648.

Leptin, M. et B. Grunewald (1990). Cell shape changes during gastrulation in *Drosophila*. *Development* 110(1): 73-84.

Leung, T., X. Q. Chen, I. Tan, E. Manser et L. Lim (1998). Myotonic dystrophy kinase-related Cdc42-binding kinase acts as a Cdc42 effector in promoting cytoskeletal reorganization. *Mol Cell Biol* 18(1): 130-140.

Levayer, R. et T. Lecuit (2013). Oscillation and polarity of E-cadherin asymmetries control actomyosin flow patterns during morphogenesis. *Dev Cell* 26(2): 162-175.

Levayer, R., A. Pelissier-Monier et T. Lecuit (2011). Spatial regulation of Dia and Myosin-II by RhoGEF2 controls initiation of E-cadherin endocytosis during epithelial morphogenesis. *Nat Cell Biol* 13(5): 529-540.

Lewis, F. T. (1928). The correlation between cell division and the shapes and sizes of prismatic cells in the epidermis of cucumis. *Anat. Rec.* 38(3): 341–376.

Lin, L., T. Tran, S. Hu, T. Cramer, R. Komuniecki et R. M. Steven (2012). RHGF-2 is an essential Rho-1 specific RhoGEF that binds to the multi-PDZ domain scaffold protein MPZ-1 in *Caenorhabditis elegans*. *PLoS One* 7(2): e31499.

Liu, F., L. Jia, A. M. Thompson-Baine, J. M. Puglise, M. B. Ter Beest et M. M. Zegers (2010). Cadherins and Pak1 control contact inhibition of proliferation by Pak1-betaPIX-GIT complex-dependent regulation of cell-matrix signaling. *Mol Cell Biol* 30(8): 1971-1983.

Liu, J. S., J. T. Farlow, A. K. Paulson, M. A. Labarge et Z. J. Gartner (2012). Programmed cell-to-cell variability in Ras activity triggers emergent behaviors during mammary epithelial morphogenesis. *Cell Rep* 2(5): 1461-1470.

Lohia, M., Y. Qin et I. G. Macara (2012). The Scribble polarity protein stabilizes E-cadherin/p120-catenin binding and blocks retrieval of E-cadherin to the Golgi. *PLoS One* 7(11): e51130.

Loo, T. H., Y. W. Ng, L. Lim et E. Manser (2004). GIT1 activates p21-activated kinase through a mechanism independent of p21 binding. *Mol Cell Biol* 24(9): 3849-3859.

Lu, W., S. Katz, R. Gupta et B. J. Mayer (1997). Activation of Pak by membrane localization mediated by an SH3 domain from the adaptor protein Nck. *Curr Biol* 7(2): 85-94.

Lucanic, M. et H. J. Cheng (2008). A RAC/CDC-42-independent GIT/PIX/PAK signaling pathway mediates cell migration in *C. elegans*. *PLoS Genet* 4(11): e1000269.

Lucanic, M., M. Kiley, N. Ashcroft, N. L'Etoile et H. J. Cheng (2006). The *Caenorhabditis elegans* P21-activated kinases are differentially required for UNC-6/netrin-mediated commissural motor axon guidance. *Development* 133(22): 4549-4559.

Lynch, H. E., S. M. Crews, B. Rosenthal, E. Kim, R. Gish, K. Echiverri et M. S. Hutson (2013). Cellular mechanics of germ band retraction in *Drosophila*. *Dev Biol* 384(2): 205-213.

Machacek, M., L. Hodgson, C. Welch, H. Elliott, O. Pertz, P. Nalbant, A. Abell, G. L. Johnson, K. M. Hahn et G. Danuser (2009). Coordination of Rho GTPase activities during cell protrusion. *Nature* 461(7260): 99-103.

Mana-Capelli, S., M. Paramasivam, S. Dutta et D. McCollum (2014). Angiomotins link F-actin architecture to Hippo pathway signaling. *Mol Biol Cell* 25(10): 1676-1685.

Manabe, R., M. Kovalenko, D. J. Webb et A. R. Horwitz (2002). GIT1 functions in a motile, multi-molecular signaling complex that regulates protrusive activity and cell migration. *J Cell Sci* 115(Pt 7): 1497-1510.

Manjon, C., E. Sanchez-Herrero et M. Suzanne (2007). Sharp boundaries of Dpp signalling trigger local cell death required for *Drosophila* leg morphogenesis. *Nat Cell Biol* 9(1): 57-63.

Manser, E., T. Leung, H. Salihuddin, Z. S. Zhao et L. Lim (1994). A brain serine/threonine protein kinase activated by Cdc42 and Rac1. *Nature* 367(6458): 40-46.

Manser, E., T. H. Loo, C. G. Koh, Z. S. Zhao, X. Q. Chen, L. Tan, I. Tan, T. Leung et L. Lim (1998). PAK kinases are directly coupled to the PIX family of nucleotide exchange factors. *Mol Cell* 1(2): 183-192.

Martin, A. C., M. Gelbart, R. Fernandez-Gonzalez, M. Kaschube et E. F. Wieschaus (2010). Integration of contractile forces during tissue invagination. *J Cell Biol* 188(5): 735-749.

Martin, A. C. et B. Goldstein (2014). Apical constriction: themes and variations on a cellular mechanism driving morphogenesis. *Development* 141(10): 1987-1998.

Martin, A. C., M. Kaschube et E. F. Wieschaus (2009). Pulsed contractions of an actin-myosin network drive apical constriction. *Nature* 457(7228): 495-499.

Martin, E., S. Harel, B. Nkengfac, K. Hamiche, M. Neault et S. Jenna (2014). pix-1 controls early elongation in parallel with mel-11 and let-502 in *Caenorhabditis elegans*. *PLoS One* 9(4): e94684.

Martin, E., O. Rocheleau-Leclair et S. Jenna (2016). Novel Metrics to Characterize Embryonic Elongation of the Nematode *Caenorhabditis elegans*. *J Vis Exp*(109).

Martin, E., Rocheleau-Leclair, O., Jenna, S. (2016). Novel Metrics to Characterize Embryonic Elongation of the Nematode *Caenorhabditis elegans*. *J. Vis. Exp.*(109): e53712.

Maruthamuthu, V., B. Sabass, U. S. Schwarz et M. L. Gardel (2011). Cell-ECM traction force modulates endogenous tension at cell-cell contacts. *Proc Natl Acad Sci U S A* 108(12): 4708-4713.

Mayor, R. et S. Etienne-Manneville (2016). The front and rear of collective cell migration. *Nat Rev Mol Cell Biol* 17(2): 97-109.

Meng, W. et M. Takeichi (2009). Adherens junction: molecular architecture and regulation. *Cold Spring Harb Perspect Biol* 1(6): a002899.

Merrifield, C. J., B. Qualmann, M. M. Kessels et W. Almers (2004). Neural Wiskott Aldrich Syndrome Protein (N-WASP) and the Arp2/3 complex are recruited to sites of clathrin-mediated endocytosis in cultured fibroblasts. *Eur J Cell Biol* 83(1): 13-18.

Mertens, A. E., T. P. Rygiel, C. Olivo, R. van der Kammen et J. G. Collard (2005). The Rac activator Tiam1 controls tight junction biogenesis in keratinocytes through binding to and activation of the Par polarity complex. *J Cell Biol* 170(7): 1029-1037.

Miki, H., T. Sasaki, Y. Takai et T. Takenawa (1998). Induction of filopodium formation by a WASP-related actin-depolymerizing protein N-WASP. *Nature* 391(6662): 93-96.

Monier, B., M. Gettings, G. Gay, T. Mangeat, S. Schott, A. Guarner et M. Suzanne (2015). Apico-basal forces exerted by apoptotic cells drive epithelium folding. *Nature* 518(7538): 245-248.

Monier, B. et M. Suzanne (2015). The Morphogenetic Role of Apoptosis. *Curr Top Dev Biol* 114: 335-362.

Montcouquiol, M., R. A. Rachel, P. J. Lanford, N. G. Copeland, N. A. Jenkins et M. W. Kelley (2003). Identification of Vangl2 and Scrb1 as planar polarity genes in mammals. *Nature* 423(6936): 173-177.

Moorhead, G., D. Johnson, N. Morrice et P. Cohen (1998). The major myosin phosphatase in skeletal muscle is a complex between the beta-isoform of protein phosphatase 1 and the MYPT2 gene product. *FEBS Lett* 438(3): 141-144.

Mori, C., N. Nakamura, S. Kimura, H. Irie, T. Takigawa et K. Shiota (1995). Programmed cell death in the interdigital tissue of the fetal mouse limb is apoptosis with DNA fragmentation. *Anat Rec* 242(1): 103-110.

Morimura, S., K. Suzuki et K. Takahashi (2011). Nonmuscle myosin IIA is required for lamellipodia formation through binding to WAVE2 and phosphatidylinositol 3,4,5-triphosphate. *Biochem Biophys Res Commun* 404(3): 834-840.

Muglia, L. J., D. S. Bae, T. T. Brown, S. K. Vogt, J. G. Alvarez, M. E. Sunday et J. A. Majzoub (1999). Proliferation and differentiation defects during lung development in corticotropin-releasing hormone-deficient mice. *Am J Respir Cell Mol Biol* 20(2): 181-188.

Munjal, A. et T. Lecuit (2014). Actomyosin networks and tissue morphogenesis. *Development* 141(9): 1789-1793.

Murdoch, J. N., D. J. Henderson, K. Doudney, C. Gaston-Massuet, H. M. Phillips, C. Paternotte, R. Arkell, P. Stanier et A. J. Copp (2003). Disruption of scribble (Scrb1) causes severe neural tube defects in the circletail mouse. *Hum Mol Genet* 12(2): 87-98.

Nakahara, S., K. Tsutsumi, T. Zuinen et Y. Ohta (2015). FilGAP, a Rho-ROCK-regulated GAP for Rac, controls adherens junctions in MDCK cells. *J Cell Sci* 128(11): 2047-2056.

Nakamura, F. (2013). FilGAP and its close relatives: a mediator of Rho-Rac antagonism that regulates cell morphology and migration. *Biochem J* 453(1): 17-25.

Navarro, C., S. Nola, S. Audebert, M. J. Santoni, J. P. Arsanto, C. Ginestier, S. Marchetto, J. Jacquemier, D. Isnardon, A. Le Bivic, D. Birnbaum et J. P. Borg (2005). Junctional recruitment of mammalian Scribble relies on E-cadherin engagement. *Oncogene* 24(27): 4330-4339.

Nayal, A., D. J. Webb, C. M. Brown, E. M. Schaefer, M. Vicente-Manzanares et A. R. Horwitz (2006). Paxillin phosphorylation at Ser273 localizes a GIT1-PIX-PAK complex and regulates adhesion and protrusion dynamics. *J Cell Biol* 173(4): 587-589.

Ngok, S. P., R. Geyer, A. Kourtidis, N. Mitin, R. Feathers, C. Der et P. Z. Anastasiadis (2013). TEM4 is a junctional Rho GEF required for cell-cell adhesion, monolayer integrity and barrier function. *J Cell Sci* 126(Pt 15): 3271-3277.

Ngok, S. P., W. H. Lin et P. Z. Anastasiadis (2014). Establishment of epithelial polarity--GEF who's minding the GAP? *J Cell Sci* 127(Pt 15): 3205-3215.

Nimnual, A. S., L. J. Taylor et D. Bar-Sagi (2003). Redox-dependent downregulation of Rho by Rac. *Nat Cell Biol* 5(3): 236-241.

Nishimura, T., T. Yamaguchi, K. Kato, M. Yoshizawa, Y. Nabeshima, S. Ohno, M. Hoshino et K. Kaibuchi (2005). PAR-6-PAR-3 mediates Cdc42-induced Rac activation through the Rac GEFs STEF/Tiam1. *Nat Cell Biol* 7(3): 270-277.

Nishiya, N., W. B. Kiosses, J. Han et M. H. Ginsberg (2005). An alpha4 integrin-paxillin-Arf-GAP complex restricts Rac activation to the leading edge of migrating cells. *Nat Cell Biol* 7(4): 343-352.

Nobes, C. D. et A. Hall (1995). Rho, rac, and cdc42 GTPases regulate the assembly of multimolecular focal complexes associated with actin stress fibers, lamellipodia, and filopodia. *Cell* 81(1): 53-62.

Nola, S., M. Sebbagh, S. Marchetto, N. Osmani, C. Nourry, S. Audebert, C. Navarro, R. Rachel, M. Montcouquiol, N. Sans, S. Etienne-Manneville, J. P. Borg et M. J. Santoni (2008). Scrib regulates PAK activity during the cell migration process. *Hum Mol Genet* 17(22): 3552-3565.

Ohta, Y., J. H. Hartwig et T. P. Stossel (2006). FilGAP, a Rho- and ROCK-regulated GAP for Rac binds filamin A to control actin remodelling. *Nat Cell Biol* 8(8): 803-814.

Osmani, N., N. Vitale, J. P. Borg et S. Etienne-Manneville (2006). Scrib controls Cdc42 localization and activity to promote cell polarization during astrocyte migration. *Curr Biol* 16(24): 2395-2405.

Otani, T., T. Ichii, S. Aono et M. Takeichi (2006). Cdc42 GEF Tuba regulates the junctional configuration of simple epithelial cells. *J Cell Biol* 175(1): 135-146.

Ouellette, M. H., E. Martin, G. Lacoste-Caron, K. Hamiche et S. Jenna (2015). Spatial control of active CDC-42 during collective migration of hypodermal cells in *Caenorhabditis elegans*. *J Mol Cell Biol*.

Page, B. D., W. Zhang, K. Steward, T. Blumenthal et J. R. Priess (1997). ELT-1, a GATA-like transcription factor, is required for epidermal cell fates in *Caenorhabditis elegans* embryos. *Genes Dev* 11(13): 1651-1661.

Pagliarini, R. A. et T. Xu (2003). A genetic screen in *Drosophila* for metastatic behavior. *Science* 302(5648): 1227-1231.

Park, E., M. Na, J. Choi, S. Kim, J. R. Lee, J. Yoon, D. Park, M. Sheng et E. Kim (2003). The Shank family of postsynaptic density proteins interacts with and promotes synaptic accumulation of the beta PIX guanine nucleotide exchange factor for Rac1 and Cdc42. *J Biol Chem* 278(21): 19220-19229.

Parri, M. et P. Chiarugi (2010). Rac and Rho GTPases in cancer cell motility control. *Cell Commun Signal* 8: 23.

Parrini, M. C., M. Lei, S. C. Harrison et B. J. Mayer (2002). Pak1 kinase homodimers are autoinhibited in trans and dissociated upon activation by Cdc42 and Rac1. *Mol Cell* 9(1): 73-83.

Peng, H., Z. Ruan, D. Atasoy et S. Sternson (2010). Automatic reconstruction of 3D neuron structures using a graph-augmented deformable model. *Bioinformatics* 26(12): i38-46.

Peng, H., Z. Ruan, F. Long, J. H. Simpson et E. W. Myers (2010). V3D enables real-time 3D visualization and quantitative analysis of large-scale biological image data sets. *Nat Biotechnol* 28(4): 348-353.

Peng, J., B. J. Wallar, A. Flanders, P. J. Swiatek et A. S. Alberts (2003). Disruption of the Diaphanous-related formin Drf1 gene encoding mDia1 reveals a role for Drf3 as an effector for Cdc42. *Curr Biol* 13(7): 534-545.

Perez-Moreno, M., C. Jamora et E. Fuchs (2003). Sticky business: orchestrating cellular signals at adherens junctions. *Cell* 112(4): 535-548.

Pertz, O. (2010). Spatio-temporal Rho GTPase signaling - where are we now? *J Cell Sci* 123(Pt 11): 1841-1850.

Peters, E. C., A. J. Gossett, B. Goldstein, C. J. Der et D. J. Reiner (2013). Redundant canonical and noncanonical *Caenorhabditis elegans* p21-activated kinase signaling governs distal tip cell migrations. *G3 (Bethesda)* 3(2): 181-195.

Petrie, R. J. et K. M. Yamada (2012). At the leading edge of three-dimensional cell migration. *J Cell Sci* 125(Pt 24): 5917-5926.

Pettitt, J., E. A. Cox, I. D. Broadbent, A. Flett et J. Hardin (2003). The *Caenorhabditis elegans* p120 catenin homologue, JAC-1, modulates cadherin-catenin function during epidermal morphogenesis. *J Cell Biol* 162(1): 15-22.

Piekny, A. J., J. L. Johnson, G. D. Cham et P. E. Mains (2003). The *Caenorhabditis elegans* nonmuscle myosin genes nmy-1 and nmy-2 function as redundant

components of the let-502/Rho-binding kinase and mel-11/myosin phosphatase pathway during embryonic morphogenesis. *Development* 130(23): 5695-5704.

Piekny, A. J., A. Wissmann et P. E. Mains (2000). Embryonic morphogenesis in Caenorhabditis elegans integrates the activity of LET-502 Rho-binding kinase, MEL-11 myosin phosphatase, DAF-2 insulin receptor and FEM-2 PP2c phosphatase. *Genetics* 156(4): 1671-1689.

Pilot, F. et T. Lecuit (2005). Compartmentalized morphogenesis in epithelia: from cell to tissue shape. *Dev Dyn* 232(3): 685-694.

Pirraglia, C. et M. M. Myat (2010). Genetic regulation of salivary gland development in *Drosophila melanogaster*. *Front Oral Biol* 14: 32-47.

Pirraglia, C., J. Walters et M. M. Myat (2010). Pak1 control of E-cadherin endocytosis regulates salivary gland lumen size and shape. *Development* 137(24): 4177-4189.

Plageman, T. F., Jr., B. K. Chauhan, C. Yang, F. Jaudon, X. Shang, Y. Zheng, M. Lou, A. Debant, J. D. Hildebrand et R. A. Lang (2011). A Trio-RhoA-Shroom3 pathway is required for apical constriction and epithelial invagination. *Development* 138(23): 5177-5188.

Plutoni, C., E. Bazellieres, M. Le Borgne-Rochet, F. Comunale, A. Brugues, M. Seveno, D. Planchon, S. Thuault, N. Morin, S. Bodin, X. Trepat et C. Gauthier-Rouviere (2016). P-cadherin promotes collective cell migration via a Cdc42-mediated increase in mechanical forces. *J Cell Biol* 212(2): 199-217.

Ponti, A., M. Machacek, S. L. Gupton, C. M. Waterman-Storer et G. Danuser (2004). Two distinct actin networks drive the protrusion of migrating cells. *Science* 305(5691): 1782-1786.

Priess, J. R. et D. I. Hirsh (1986). *Caenorhabditis elegans* morphogenesis: the role of the cytoskeleton in elongation of the embryo. *Dev Biol* 117(1): 156-173.

Priya, R., A. S. Yap et G. A. Gomez (2013). E-cadherin supports steady-state Rho signaling at the epithelial zonula adherens. *Differentiation* 86(3): 133-140.

Qin, Y., C. Capaldo, B. M. Gumbiner et I. G. Macara (2005). The mammalian Scribble polarity protein regulates epithelial cell adhesion and migration through E-cadherin. *J Cell Biol* 171(6): 1061-1071.

Quinn, C. C., D. S. Pfeil et W. G. Wadsworth (2008). CED-10/Rac1 mediates axon guidance by regulating the asymmetric distribution of MIG-10/lamellipodin. *Curr Biol* 18(11): 808-813.

Quintin, S., C. Gally et M. Labouesse (2008). Epithelial morphogenesis in embryos: asymmetries, motors and brakes. *Trends Genet* 24(5): 221-230.

Raich, W. B., C. Agbunag et J. Hardin (1999). Rapid epithelial-sheet sealing in the *Caenorhabditis elegans* embryo requires cadherin-dependent filopodial priming. *Curr Biol* 9(20): 1139-1146.

Ramani, A. K., T. Chuluunbaatar, A. J. Verster, H. Na, V. Vu, N. Pelte, N. Wannissorn, A. Jiao et A. G. Fraser (2012). The majority of animal genes are required for wild-type fitness. *Cell* 148(4): 792-802.

Rane, C. K. et A. Minden (2014). P21 activated kinases: structure, regulation, and functions. *Small GTPases* 5.

Ratheesh, A., G. A. Gomez, R. Priya, S. Verma, E. M. Kovacs, K. Jiang, N. H. Brown, A. Akhmanova, S. J. Stehbens et A. S. Yap (2012). Centralspindlin and alpha-catenin regulate Rho signalling at the epithelial zonula adherens. *Nat Cell Biol* 14(8): 818-828.

Rauzi, M., P. F. Lenne et T. Lecuit (2010). Planar polarized actomyosin contractile flows control epithelial junction remodelling. *Nature* 468(7327): 1110-1114.

Rauzi, M., P. Verant, T. Lecuit et P. F. Lenne (2008). Nature and anisotropy of cortical forces orienting *Drosophila* tissue morphogenesis. *Nat Cell Biol* 10(12): 1401-1410.

Ridley, A. J. (2011). Life at the leading edge. *Cell* 145(7): 1012-1022.

Ridley, A. J. (2015). Rho GTPase signalling in cell migration. *Curr Opin Cell Biol* 36: 103-112.

Ridley, A. J. et A. Hall (1992). The small GTP-binding protein rho regulates the assembly of focal adhesions and actin stress fibers in response to growth factors. *Cell* 70(3): 389-399.

Ridley, A. J., H. F. Paterson, C. L. Johnston, D. Diekmann et A. Hall (1992). The small GTP-binding protein rac regulates growth factor-induced membrane ruffling. *Cell* 70(3): 401-410.

Rosenfeldt, H., M. D. Castellone, P. A. Randazzo et J. S. Gutkind (2006). Rac inhibits thrombin-induced Rho activation: evidence of a Pak-dependent GTPase crosstalk. *J Mol Signal* 1: 8.

Row, R. H., J. L. Maitre, B. L. Martin, P. Stockinger, C. P. Heisenberg et D. Kimelman (2011). Completion of the epithelial to mesenchymal transition in zebrafish mesoderm requires Spadetail. *Dev Biol* 354(1): 102-110.

Rudel, T. et G. M. Bokoch (1997). Membrane and morphological changes in apoptotic cells regulated by caspase-mediated activation of PAK2. *Science* 276(5318): 1571-1574.

Sahai, E. et C. J. Marshall (2002). ROCK and Dia have opposing effects on adherens junctions downstream of Rho. *Nat Cell Biol* 4(6): 408-415.

Sailem, H., V. Bousgouni, S. Cooper et C. Bakal (2014). Cross-talk between Rho and Rac GTPases drives deterministic exploration of cellular shape space and morphological heterogeneity. *Open Biol* 4: 130132.

Saito, K., Y. Ozawa, K. Hibino et Y. Ohta (2012). FilGAP, a Rho/Rho-associated protein kinase-regulated GTPase-activating protein for Rac, controls tumor cell migration. *Mol Biol Cell* 23(24): 4739-4750.

Samakovlis, C., N. Hacohen, G. Manning, D. C. Sutherland, K. Guillemin et M. A. Krasnow (1996). Development of the *Drosophila* tracheal system occurs by a series of morphologically distinct but genetically coupled branching events. *Development* 122(5): 1395-1407.

Sanders, L. C., F. Matsumura, G. M. Bokoch et P. de Lanerolle (1999). Inhibition of myosin light chain kinase by p21-activated kinase. *Science* 283(5410): 2083-2085.

Sanz-Moreno, V., G. Gadea, J. Ahn, H. Paterson, P. Marra, S. Pinner, E. Sahai et C. J. Marshall (2008). Rac activation and inactivation control plasticity of tumor cell movement. *Cell* 135(3): 510-523.

Sawa, M., S. Suetsugu, A. Sugimoto, H. Miki, M. Yamamoto et T. Takenawa (2003). Essential role of the C. elegans Arp2/3 complex in cell migration during ventral enclosure. *J Cell Sci* 116(Pt 8): 1505-1518.

Sawyer, J. M., J. R. Harrell, G. Shemer, J. Sullivan-Brown, M. Roh-Johnson et B. Goldstein (2010). Apical constriction: a cell shape change that can drive morphogenesis. *Dev Biol* 341(1): 5-19.

Sayyad, W. A., L. Amin, P. Fabris, E. Ercolini et V. Torre (2015). The role of myosin-II in force generation of DRG filopodia and lamellipodia. *Sci Rep* 5: 7842.

Schock, F. et N. Perrimon (2002a). Cellular processes associated with germ band retraction in Drosophila. *Dev Biol* 248(1): 29-39.

Schock, F. et N. Perrimon (2002b). Molecular mechanisms of epithelial morphogenesis. *Annu Rev Cell Dev Biol* 18: 463-493.

Semplice, M., A. Veglio, G. Naldi, G. Serini et A. Gamba (2012). A bistable model of cell polarity. *PLoS One* 7(2): e30977.

Sharma, A. et B. J. Mayer (2008). Phosphorylation of p130Cas initiates Rac activation and membrane ruffling. *BMC Cell Biol* 9: 50.

Shaye, D. D. et I. Greenwald (2011). OrthoList: a compendium of *C. elegans* genes with human orthologs. *PLoS One* 6(5): e20085.

Sheffield, M., T. Loveless, J. Hardin et J. Pettitt (2007). C. elegans Enabled exhibits novel interactions with N-WASP, Abl, and cell-cell junctions. *Curr Biol* 17(20): 1791-1796.

Sheik, A. R., E. E. Muller, J. N. Audinot, L. A. Lebrun, P. Grysan, C. Guignard et P. Wilmes (2016). In situ phenotypic heterogeneity among single cells of the filamentous bacterium *Candidatus Microthrix parvicella*. *ISME J* 10(5): 1274-1279.

Shelton, C. A., J. C. Carter, G. C. Ellis et B. Bowerman (1999). The nonmuscle myosin regulatory light chain gene mlc-4 is required for cytokinesis, anterior-posterior polarity, and body morphology during *Caenorhabditis elegans* embryogenesis. *J Cell Biol* 146(2): 439-451.

Shewan, A. M., M. Maddugoda, A. Kraemer, S. J. Stehbens, S. Verma, E. M. Kovacs et A. S. Yap (2005). Myosin 2 is a key Rho kinase target necessary for the local concentration of E-cadherin at cell-cell contacts. *Mol Biol Cell* 16(10): 4531-4542.

Simoes, S., B. Denholm, D. Azevedo, S. Sotillos, P. Martin, H. Skaer, J. C. Hombria et A. Jacinto (2006). Compartmentalisation of Rho regulators directs cell invagination during tissue morphogenesis. *Development* 133(21): 4257-4267.

Simske, J. S., M. Koppen, P. Sims, J. Hodgkin, A. Yonkof et J. Hardin (2003). The cell junction protein VAB-9 regulates adhesion and epidermal morphology in *C. elegans*. *Nat Cell Biol* 5(7): 619-625.

So, S., K. Miyahara et Y. Ohshima (2011). Control of body size in *C. elegans* dependent on food and insulin/IGF-1 signal. *Genes Cells* 16(6): 639-651.

Solnica-Krezel, L. et D. S. Sepich (2012). Gastrulation: making and shaping germ layers. *Annu Rev Cell Dev Biol* 28: 687-717.

Spencer, A. G., S. Orita, C. J. Malone et M. Han (2001). A RHO GTPase-mediated pathway is required during P cell migration in *Caenorhabditis elegans*. *Proc Natl Acad Sci U S A* 98(23): 13132-13137.

Steven, R., T. J. Kubiseski, H. Zheng, S. Kulkarni, J. Mancillas, A. Ruiz Morales, C. W. Hogue, T. Pawson et J. Culotti (1998). UNC-73 activates the Rac GTPase and is required for cell and growth cone migrations in *C. elegans*. *Cell* 92(6): 785-795.

Stockholm, D., R. Benchaouir, J. Picot, P. Rameau, T. M. Neildez, G. Landini, C. Laplace-Builhe et A. Paldi (2007). The origin of phenotypic heterogeneity in a clonal cell population in vitro. *PLoS One* 2(4): e394.

Stockton, R., J. Reutershan, D. Scott, J. Sanders, K. Ley et M. A. Schwartz (2007). Induction of vascular permeability: beta PIX and GIT1 scaffold the activation of extracellular signal-regulated kinase by PAK. *Mol Biol Cell* 18(6): 2346-2355.

Sugimura, K. et S. Ishihara (2013). The mechanical anisotropy in a tissue promotes ordering in hexagonal cell packing. *Development* 140(19): 4091-4101.

Sulston, J. et J. Hodgkin (1988). The Nematode *Caenorhabditis elegans.* Methods. W. B. Wood. Cold Spring Harbor Laboratory, Cold Spring Harbor: 587-606.

Sulston, J. E. et H. R. Horvitz (1977). Post-embryonic cell lineages of the nematode, *Caenorhabditis elegans*. *Dev Biol* 56(1): 110-156.

Sulston, J. E., E. Schierenberg, J. G. White et J. N. Thomson (1983). The embryonic cell lineage of the nematode *Caenorhabditis elegans*. *Dev Biol* 100(1): 64-119.

Symons, M. et J. E. Segall (2009). Rac and Rho driving tumor invasion: who's at the wheel? *Genome Biol* 10(3): 213.

Takai, Y., T. Sasaki et T. Matozaki (2001). Small GTP-binding proteins. *Physiol Rev* 81(1): 153-208.

Tan, I., C. H. Ng, L. Lim et T. Leung (2001). Phosphorylation of a novel myosin binding subunit of protein phosphatase 1 reveals a conserved mechanism in the regulation of actin cytoskeleton. *J Biol Chem* 276(24): 21209-21216.

Tan, I., J. Yong, J. M. Dong, L. Lim et T. Leung (2008). A tripartite complex containing MRCK modulates lamellar actomyosin retrograde flow. *Cell* 135(1): 123-136.

Tan, L., S. Wang, Y. Wang, M. He et D. Liu (2015). Bisphenol A exposure accelerated the aging process in the nematode *Caenorhabditis elegans*. *Toxicol Lett* 235(2): 75-83.

Tavares, A.L., M.E. Mercado-Pimentel, R.B. Runyan, G.T. Kitten (2006). TGF beta-mediated RhoA expression is necessary for epithelial-mesenchymal transition in the embryonic chick heart. *Dev Dyn* 235(6): 1589-1598.

Tay, H. G., Y. W. Ng et E. Manser (2010). A vertebrate-specific Chp-PAK-PIX pathway maintains E-cadherin at adherens junctions during zebrafish epiboly. *PLoS One* 5(4): e10125.

Tcherkezian, J., E. I. Danek, S. Jenna, I. Triki et N. Lamarche-Vane (2005). Extracellular signal-regulated kinase 1 interacts with and phosphorylates CdGAP at an important regulatory site. *Mol Cell Biol* 25(15): 6314-6329.

Tcherkezian, J. et N. Lamarche-Vane (2007). Current knowledge of the large RhoGAP family of proteins. *Biol Cell* 99(2): 67-86.

ten Klooster, J. P., Z. M. Jaffer, J. Chernoff et P. L. Hordijk (2006). Targeting and activation of Rac1 are mediated by the exchange factor beta-Pix. *J Cell Biol* 172(5): 759-769.

Terry, S. J., C. Zihni, A. Elbediwy, E. Vitiello, I. V. Leefa Chong San, M. S. Balda et K. Matter (2011). Spatially restricted activation of RhoA signalling at epithelial junctions by p114RhoGEF drives junction formation and morphogenesis. *Nat Cell Biol* 13(2): 159-166.

Totsukawa, G., Y. Yamakita, S. Yamashiro, D. J. Hartshorne, Y. Sasaki et F. Matsumura (2000). Distinct roles of ROCK (Rho-kinase) and MLCK in spatial regulation of MLC phosphorylation for assembly of stress fibers and focal adhesions in 3T3 fibroblasts. *J Cell Biol* 150(4): 797-806.

Tsyganov, M. A., W. Kolch et B. N. Kholodenko (2012). The topology design principles that determine the spatiotemporal dynamics of G-protein cascades. *Mol Biosyst* 8(3): 730-743.

Turner, C. E., M. C. Brown, J. A. Perrotta, M. C. Riedy, S. N. Nikolopoulos, A. R. McDonald, S. Bagrodia, S. Thomas et P. S. Leventhal (1999). Paxillin LD4 motif binds PAK and PIX through a novel 95-kD ankyrin repeat, ARF-GAP protein: A role in cytoskeletal remodeling. *J Cell Biol* 145(4): 851-863.

Vaezi, A., C. Bauer, V. Vasioukhin et E. Fuchs (2002). Actin cable dynamics and Rho/Rock orchestrate a polarized cytoskeletal architecture in the early steps of assembling a stratified epithelium. *Dev Cell* 3(3): 367-381.

Van Aelst, L. et M. Symons (2002). Role of Rho family GTPases in epithelial morphogenesis. *Genes Dev* 16(9): 1032-1054.

van de Wijngaert, F. P., M. D. Kendall, H. J. Schuurman, L. H. Rademakers et L. Kater (1984). Heterogeneity of epithelial cells in the human thymus. An ultrastructural study. *Cell Tissue Res* 237(2): 227-237.

Vanneste, C. A., D. Pruyne et P. E. Mains (2013). The role of the formin gene fhod-1 in *C. elegans* embryonic morphogenesis. *Worm* 2(3): e25040.

Vargo-Gogola, T., B. M. Heckman, E. J. Gunther, L. A. Chodosh et J. M. Rosen (2006). P190-B Rho GTPase-activating protein overexpression disrupts ductal

morphogenesis and induces hyperplastic lesions in the developing mammary gland. *Mol Endocrinol* 20(6): 1391-1405.

Verster, A. J., A. K. Ramani, S. J. McKay et A. G. Fraser (2014). Comparative RNAi screens in *C. elegans* and *C. briggsae* reveal the impact of developmental system drift on gene function. *PLoS Genet* 10(2): e1004077.

Vial, E., E. Sahai et C. J. Marshall (2003). ERK-MAPK signaling coordinately regulates activity of Rac1 and RhoA for tumor cell motility. *Cancer Cell* 4(1): 67-79.

Vicente-Manzanares, M. et A. R. Horwitz (2011). Adhesion dynamics at a glance. *J Cell Sci* 124(Pt 23): 3923-3927.

Vicente-Manzanares, M., K. Newell-Litwa, A. I. Bachir, L. A. Whitmore et A. R. Horwitz (2011). Myosin IIA/IIB restrict adhesive and protrusive signaling to generate front-back polarity in migrating cells. *J Cell Biol* 193(2): 381-396.

Vicente-Manzanares, M., J. Zareno, L. Whitmore, C. K. Choi et A. F. Horwitz (2007). Regulation of protrusion, adhesion dynamics, and polarity by myosins IIA and IIB in migrating cells. *J Cell Biol* 176(5): 573-580.

Vlachos, S. et N. Harden (2011). Genetic evidence for antagonism between Pak protein kinase and Rho1 small GTPase signaling in regulation of the actin cytoskeleton during *Drosophila* oogenesis. *Genetics* 187(2): 501-512.

Walck-Shannon, E. et J. Hardin (2014). Cell intercalation from top to bottom. *Nat Rev Mol Cell Biol* 15(1): 34-48.

Walck-Shannon, E., D. Reiner et J. Hardin (2015). Polarized Rac-dependent protrusions drive epithelial intercalation in the embryonic epidermis of *C. elegans*. *Development* 142(20): 3549-3560.

Wang, Y. et V. Riechmann (2007). The role of the actomyosin cytoskeleton in coordination of tissue growth during *Drosophila* oogenesis. *Curr Biol* 17(15): 1349-1355.

Watabe-Uchida, M., N. Uchida, Y. Imamura, A. Nagafuchi, K. Fujimoto, T. Uemura, S. Vermeulen, F. van Roy, E. D. Adamson et M. Takeichi (1998). alpha-Catenin-vinculin interaction functions to organize the apical junctional complex in epithelial cells. *J Cell Biol* 142(3): 847-857.

Weber, G. F., M. A. Bjerke et D. W. DeSimone (2012). A mechanoresponsive cadherin-keratin complex directs polarized protrusive behavior and collective cell migration. *Dev Cell* 22(1): 104-115.

Weil, M., M. D. Jacobson et M. C. Raff (1997). Is programmed cell death required for neural tube closure? *Curr Biol* 7(4): 281-284.

Wilkinson, S., H. F. Paterson et C. J. Marshall (2005). Cdc42-MRCK and Rho-ROCK signalling cooperate in myosin phosphorylation and cell invasion. *Nat Cell Biol* 7(3): 255-261.

Williams-Masson, E. M., P. J. Heid, C. A. Lavin et J. Hardin (1998). The cellular mechanism of epithelial rearrangement during morphogenesis of the *Caenorhabditis elegans* dorsal hypodermis. *Dev Biol* 204(1): 263-276.

Williams-Masson, E. M., A. N. Malik et J. Hardin (1997). An actin-mediated two-step mechanism is required for ventral enclosure of the *C. elegans* hypodermis. *Development* 124(15): 2889-2901.

Williams, M., W. Yen, X. Lu et A. Sutherland (2014). Distinct apical and basolateral mechanisms drive planar cell polarity-dependent convergent extension of the mouse neural plate. *Dev Cell* 29(1): 34-46.

Winter-Vann, A. M. et P. J. Casey (2005). Post-prenylation-processing enzymes as new targets in oncogenesis. *Nat Rev Cancer* 5(5): 405-412.

Wissmann, A., J. Ingles et P. E. Mains (1999). The *Caenorhabditis elegans* mel-11 myosin phosphatase regulatory subunit affects tissue contraction in the somatic gonad and the embryonic epidermis and genetically interacts with the Rac signaling pathway. *Dev Biol* 209(1): 111-127.

Wissmann, A., J. Ingles, J. D. McGhee et P. E. Mains (1997). *Caenorhabditis elegans* LET-502 is related to Rho-binding kinases and human myotonic dystrophy kinase and interacts genetically with a homolog of the regulatory subunit of smooth muscle myosin phosphatase to affect cell shape. *Genes Dev* 11(4): 409-422.

Withee, J., B. Galligan, N. Hawkins et G. Garriga (2004). *Caenorhabditis elegans* WASP and Ena/VASP proteins play compensatory roles in morphogenesis and neuronal cell migration. *Genetics* 167(3): 1165-1176.

Wu, X., P. S. Tanwar et L. A. Raftery (2008). *Drosophila* follicle cells: morphogenesis in an eggshell. *Semin Cell Dev Biol* 19(3): 271-282.

Wu, Y. I., D. Frey, O. I. Lungu, A. Jaehrig, I. Schlichting, B. Kuhlman et K. M. Hahn (2009). A genetically encoded photoactivatable Rac controls the motility of living cells. *Nature* 461(7260): 104-108.

Yamazaki, D., S. Kurisu et T. Takenawa (2009). Involvement of Rac and Rho signaling in cancer cell motility in 3D substrates. *Oncogene* 28(13): 1570-1583.

Yashiro, H., A. J. Loza, J. B. Skeath et G. D. Longmore (2014). Rho1 regulates adherens junction remodeling by promoting recycling endosome formation through activation of myosin II. *Mol Biol Cell* 25(19): 2956-2969.

Yates, L. L., C. Schnatwinkel, L. Hazelwood, L. Chessum, A. Paudyal, H. Hilton, M. R. Romero, J. Wilde, D. Bogani, J. Sanderson, C. Formstone, J. N. Murdoch, L. A. Niswander, A. Greenfield et C. H. Dean (2013). Scribble is required for normal epithelial cell-cell contacts and lumen morphogenesis in the mammalian lung. *Dev Biol* 373(2): 267-280.

Yin, Z., A. Sadok, H. Sailem, A. McCarthy, X. Xia, F. Li, M. A. Garcia, L. Evans, A. R. Barr, N. Perrimon, C. J. Marshall, S. T. Wong et C. Bakal (2013). A screen for morphological complexity identifies regulators of switch-like transitions between discrete cell shapes. *Nat Cell Biol* 15(7): 860-871.

Yonemura, S., Y. Wada, T. Watanabe, A. Nagafuchi et M. Shibata (2010). alpha-Catenin as a tension transducer that induces adherens junction development. *Nat Cell Biol* 12(6): 533-542.

Yu, J. S., W. J. Chen, M. H. Ni, W. H. Chan et S. D. Yang (1998). Identification of the regulatory autophosphorylation site of autophosphorylation-dependent protein kinase (auto-kinase). Evidence that auto-kinase belongs to a member of the p21-activated kinase family. *Biochem J* 334 (Pt 1): 121-131.

Yu, W., L. E. O'Brien, F. Wang, H. Bourne, K. E. Mostov et M. M. Zegers (2003). Hepatocyte growth factor switches orientation of polarity and mode of movement during morphogenesis of multicellular epithelial structures. *Mol Biol Cell* 14(2): 748-763.

Yu, Z., D. Yin et H. Deng (2015). The combinational effects between sulfonamides and metals on nematode *Caenorhabditis elegans*. *Ecotoxicol Environ Saf* 111: 66-71.

Zaidel-Bar, R., C. Ballestrem, Z. Kam et B. Geiger (2003). Early molecular events in the assembly of matrix adhesions at the leading edge of migrating cells. *J Cell Sci* 116(Pt 22): 4605-4613.

Zaidel-Bar, R. et B. Geiger (2010). The switchable integrin adhesome. *J Cell Sci* 123(Pt 9): 1385-1388.

Zaidel-Bar, R., S. Itzkovitz, A. Ma'ayan, R. Iyengar et B. Geiger (2007). Functional atlas of the integrin adhesome. *Nat Cell Biol* 9(8): 858-867.

Zallen, J. A. (2007). Planar polarity and tissue morphogenesis. *Cell* 129(6): 1051-1063.

Zallen, J. A. et E. Wieschaus (2004). Patterned gene expression directs bipolar planar polarity in *Drosophila*. *Dev Cell* 6(3): 343-355.

Zarnescu, D. C. et G. H. Thomas (1999). Apical spectrin is essential for epithelial morphogenesis but not apicobasal polarity in *Drosophila*. *J Cell Biol* 146(5): 1075-1086.

Zegers, M. M., M. A. Forget, J. Chernoff, K. E. Mostov, M. B. ter Beest et S. H. Hansen (2003). Pak1 and PIX regulate contact inhibition during epithelial wound healing. *EMBO J* 22(16): 4155-4165.

Zegers, M. M. et P. Friedl (2014). Rho GTPases in collective cell migration. *Small GTPases* 5: e28997.

Zenke, F. T., C. C. King, B. P. Bohl et G. M. Bokoch (1999). Identification of a central phosphorylation site in p21-activated kinase regulating autoinhibition and kinase activity. *J Biol Chem* 274(46): 32565-32573.

Zhan, Q., Q. Ge, T. Ohira, T. Van Dyke et J. A. Badwey (2003). p21-activated kinase 2 in neutrophils can be regulated by phosphorylation at multiple sites and by a variety of protein phosphatases. *J Immunol* 171(7): 3785-3793.

Zhang, H., C. Gally et M. Labouesse (2010). Tissue morphogenesis: how multiple cells cooperate to generate a tissue. *Curr Opin Cell Biol* 22(5): 575-582.

Zhang, H., F. Landmann, H. Zahreddine, D. Rodriguez, M. Koch et M. Labouesse (2011). A tension-induced mechanotransduction pathway promotes epithelial morphogenesis. *Nature* 471(7336): 99-103.

Zhang, H., A. Maximov, Y. Fu, F. Xu, T. S. Tang, T. Tkatch, D. J. Surmeier et I. Bezprozvanny (2005). Association of CaV1.3 L-type calcium channels with Shank. *J Neurosci* 25(5): 1037-1049.

Zhang, H., D. J. Webb, H. Asmussen, S. Niu et A. F. Horwitz (2005). A GIT1/PIX/Rac/PAK signaling module regulates spine morphogenesis and synapse formation through MLC. *J Neurosci* 25(13): 3379-3388.

Zhao, Z. S. et E. Manser (2005). PAK and other Rho-associated kinases--effectors with surprisingly diverse mechanisms of regulation. *Biochem J* 386(Pt 2): 201-214.

Zhao, Z. S., E. Manser, T. H. Loo et L. Lim (2000). Coupling of PAK-interacting exchange factor PIX to GIT1 promotes focal complex disassembly. *Mol Cell Biol* 20(17): 6354-6363.

Zihni, C., P. M. Munro, A. Elbediwy, N. H. Keep, S. J. Terry, J. Harris, M. S. Balda et K. Matter (2014). Dbl3 drives Cdc42 signaling at the apical margin to regulate junction position and apical differentiation. *J Cell Biol* 204(1): 111-127.